# BOOSTING STABILITY AND EFFICIENCY IN PEROVSKITE SOLAR CELLS BY UTILIZATION OF PASSIVATORS AND ORGANIC CHARGE CARRIERS

A THESIS SUBMITTED TO
THE GRADUATE SCHOOL OF NATURAL AND APPLIED SCIENCES
OF
MIDDLE EAST TECHNICAL UNIVERSITY

BY

ZEYNEP GÖZÜKARA KARABAĞ

IN PARTIAL FULFILLMENT OF THE REQUIREMENTS
FOR
THE DEGREE OF DOCTOR OF PHILOSOPHY
IN
CHEMISTRY

NOVEMBER 2024

Approval of the thesis:

**BOOSTING STABILITY AND EFFICIENCY IN PEROVSKITE SOLAR CELLS BY UTILIZATION OF PASSIVATORS AND ORGANIC CHARGE CARRIERS**

submitted by **ZEYNEP GÖZÜKARA KARABAĞ** in partial fulfillment of the requirements for the degree of **Doctor of Philosophy** i**n Chemistry, Middle East Technical University** by,

Prof. Dr. Naci Emre Altun
Dean, **Graduate School of Natural and Applied Sciences** _____

Prof. Dr. Ali Çırpan
Head of the Department, **Chemistry** _____

Prof. Dr. Emrullah Görkem Günbaş
Supervisor, **Chemistry, METU** _____

**Examining Committee Members:**

Prof. Dr. Ali Çırpan
Chemistry, METU _____

Prof. Dr. Emrullah Görkem Günbaş
Chemistry, METU _____

Prof. Dr. Serap Güneş
Physics, Yıldız Technical University _____

Assoc. Prof. Dr. Safacan Kölemen
Chemistry, Koç University _____

Assist. Prof. Dr. Erol Yıldırım
Chemistry, METU _____

Date: 21.11.2024

**I hereby declare that all information in this document has been obtained and presented in accordance with academic rules and ethical conduct. I also declare that, as required by these rules and conduct, I have fully cited and referenced all material and results that are not original to this work.**

Name Last name : Zeynep Gözükara Karabağ

Signature :

# ABSTRACT

## BOOSTING STABILITY AND EFFICIENCY IN PEROVSKITE SOLAR CELLS BY UTILIZATION OF PASSIVATORS AND ORGANIC CHARGE CARRIERS

Gözükara Karabağ, Zeynep
Doctor of Philosophy, Chemistry
Supervisor: Prof. Dr. Emrullah Görkem Günbaş

November 2024, 169 pages

Lead-based perovskite materials are promising in photovoltaics due to exceptional properties such as high absorption coefficients, carrier mobility, and tunable bandgap. However, enhancing the stability of perovskite solar cells (PSCs) is a critical challenge. One effective strategy is surface passivation, mainly using 2D perovskites based on phenylethylammonium ($PEA^+$) salts. Systematic studies conducted in this thesis revealed that halogenated $PEA^+$ salts, like *meta*-bromo phenylethylammonium iodide (***m*-BrPEAI**), yield high efficiencies (23.42%). In contrast, *meta*-chloro phenylethylammonium iodide (***m*-ClPEAI)**-treated cells provide superior stability and reproducibility. Methoxylated $PEA^+$ salts, particularly *ortho*-methoxy phenylethylammonium iodide (***o*-OMe-PEAI)**, reduce defect densities and nonradiative recombination rates, leading to power conversion efficiencies (PCEs) over 23%. Density functional theory (DFT) suggests these improvements result from favorable formation energies and optimal molecular orientations.

Furthermore, the design and synthesis of thermally evaporable **DFH** ($N^2$,$N^2$,$N^7$,$N^7$-tetra-ptolylspiro[fluorene-9,2′-[1,3]dioxolane]-2,7-diamine)-based $NiO_x$ passivation

molecules and naphthalene diimide (**NDI**) derivatives as fullerene alternatives were realized. Their preliminary performance was demonstrated in inverted PSCs.

Polymeric passivation layers have great potential to enhance the performance of PSCs. Diketopyrrolopyrrole (DPP)-based polymers integrated into cesium formamidinium methylammonium (CsFAMA)-based perovskites improve crystallization, defect management, ambient and thermal stability. In this work, PSCs utilizing novel polymeric additive 1 (***poly*-ADD1**) achieve efficiencies of nearly 21%, significantly surpassing those of unmodified cells. It retains 67% of its efficiency after 1600 hours of storage at 85 °C in an ambient environment compared to reference devices, retaining 29% of its initial PCE.

This research provides critical insights into the development of innovative passivation techniques. It offers solutions to the stability challenges of PSCs and extends their longevity within the industry.

Keywords: Perovskite Solar Cells, 2D Perovskite Passivation, Stability, DPP-Based Polymeric Passivation, Organic Charge Transport Materials.

# ÖZ

## PASSİVATORLAR VE ORGANİK YÜK TAŞIYICILARIN KULLANIMIYLA PEROVSKİT GÜNEŞ HÜCRELERİNDE STABİLİTE VE VERİMLİLİĞİN ARTIRILMASI

Gözükara Karabağ, Zeynep
Doktora, Kimya
Tez Yöneticisi: Prof. Dr. Emrullah Görkem Günbaş

Kasım 2024, 169 sayfa

Kurşun bazlı perovskit malzemeler, yüksek absorpsiyon katsayısı, taşıyıcı hareketliliği ve ayarlanabilir bant aralığı gibi olağanüstü özellikleri nedeniyle fotovoltaikler için umut verici bir seçenektir. Ancak, perovskit güneş hücrelerinin (PGH'lerinin) kararlılığını artırmak önemli bir zorluktur. Bu zorluğa yönelik etkili stratejilerden biri, ağırlıklı olarak feniletilamonyum ($PEA^+$) tuzlarına dayalı 2D perovskitlerin kullanıldığı yüzey pasivasyonudur. Bu tezde gerçekleştirilen sistematik çalışmalar, ***m*-BrPEAI** gibi halojenlenmiş $PEA^+$ tuzlarının yüksek verimlilikler (%23,42) sağladığını, ancak ***m*-ClPEAI** ile işlem görmüş hücrelerin üstün kararlılık ve yeniden üretilebilirlik sunduğunu ortaya koymuştur. Özellikle metoksile edilmiş $PEA^+$ tuzları, ***o*-OMe-PEAI** gibi, kusur yoğunluğunu ve ışıma olmayan rekombinasyon oranlarını azaltarak %23'ün üzerinde güç dönüşüm verimliliklerine (PCE) ulaşılmasını sağlamaktadır. Yoğunluk fonksiyonel teorisi (DFT) bu iyileştirmelerin, uygun oluşum enerjilerinden ve optimal moleküler yönelimlerden kaynaklandığını öne sürmektedir.

Ayrıca, DFH tabanlı $NiO_x$ pasivasyon molekülleri ve fullerene alternatif termal olarak buharlaştırılabilir NDI türevlerinin tasarımı ve sentezi gerçekleştirilmiş ve tersinir PGH'lerindeki ön performansları gösterilmiştir.

Polimerik pasivasyon katmanları, PGH'lerinin performansını artırma potansiyeline sahiptir. Diketopirolopirol (DPP) bazlı polimerlerin, sezyum formamidinyum metilamonyum (CsFAMA) bazlı perovskitlere entegrasyonu, kristalizasyon, kusur yönetimi ve termal kararlılığı iyileştirmektedir. Bu çalışmada, polimerik katkı malzemesi 1 (***poly*-ADD1)** polimerini içeren PGH'leri, modifiye edilmemiş hücrelere kıyasla %21 oranında daha yüksek verimlilik sağlamıştır. Bu hücreler, ortam koşullarında 85 °C'de 1600 saat depolama sonrası verimliliklerinin %67'sini korurken, referans hücrenin başlangıç veriminin %29'unu koruduğu gözlenmiştir.

Bu araştırma, yenilikçi pasivasyon tekniklerinin geliştirilmesine ilişkin kritik bilgiler sunmaktadır. PGH'lerinin kararlılık sorunlarına çözümler sunarak ticari uygulamaları için önemli bir adım atmaktadır

Anahtar Kelimeler: Perovskit Güneş Hücreleri, 2D Perovskit Pasivasyonu, Kararlılık, DPP Tabanlı Polimer Pasivasyonu, Organik Yük Taşıyıcı Tabakalar.

To my family: my darling husband Aliekber Karabağ and my sweet daughter Kumsal Karabağ

## ACKNOWLEDGMENTS

I thank my supervisor, Prof. Dr. E. Görkem Günbaş, for his invaluable guidance, encouragement, and patience. His assistance throughout my academic research has significantly enhanced my critical thinking skills, and I profoundly appreciate his unwavering support during my Ph.D. journey.

I want to express my gratitude to Assoc. Prof. Selçuk Yerci has provided invaluable guidance, support, and encouragement throughout my doctoral journey. It has been a privilege to work under his mentorship, and his dedication to science and research will continue to inspire me in my future endeavours.

I want to extend my sincere thanks to the members of my dissertation committee: Prof. Dr. Ali Çırpan, Prof. Dr. Serap Güneş, Assoc. Prof. Dr. Safacan Kölemen, and Assist. Prof. Dr. Erol Yıldırım, for their scientific guidance and support and for providing me with critical feedback on my research.

I want to express my sincere gratitude to my collaborators, lab mates, colleagues, and all members of our research team, particularly Muhammed Mustafa Çodur, Konstantin Tsoi, Elsen Ashadi, M. Cem Şahiner, and Doğuşcan Dönmez for their endless friendship and support. I would also like to thank Cem Maden, Ahmed Javed and Amir Zarean Ashford for their invaluable assistance with the AFM, XPS analysis and NDI-based ETLs deposition for my perovskite studies, respectively.

I appreciate Figen Varlıoğlu Yaylalı, Büşra İleri, Bahri Eren Uzuner, Mustafa Yaşa, and Amir Zarean Ashford for their unforgettable friendships, enjoyable moments, the moral support we shared, and the many valued experiences in the lab and during our social gatherings with sincerity. I will always hold dear the wonderful times and great memories created with each of you.

I sincerely thank my dedicated students, Elif Sude Çamkıran and Yağmur Yaren Kurnaz, for their invaluable assistance in the laboratory work. I consider myself fortunate to have such diligent and delightful students.

I want to express my heartfelt gratitude to Ümmügülsüm Güneş for her remarkable friendship and support during our ten-month visit to EPFL in Switzerland. I would also like to thank Dr. Xiao-Xin Gao and Prof. Dr. Muhammad Khaja Nazeeruddin for their invaluable collaboration and support during my research at EPFL. It has been a true privilege to conduct my research on perovskite photovoltaics under Prof. Dr. Mohammad Khaja Nazeeruddin's exceptional mentorship.

I want to express my profound appreciation to my husband, Dr. Aliekber Karabağ, who has made my life meaningful since we met during my master's years. He is always there for me whenever I feel discouraged and require assistance in research with his endless support and invaluable love. I would also like to extend my deepest gratitude for his help and efforts in creating exceptional illustrations and conceptualizing the figures in my thesis.

My deepest gratitude goes to my beloved daughter, Kumsal Karabağ, 19 months old. Since birth, she has brought joy and meaning to our lives. As her mother, my love for her is beyond measure.

I want to extend my heartfelt gratitude to my family, Ahmet Gözükara, Leyla Gözükara, Mehmet Efe Gözükara, Beyza Gürsoy, Haluk Gürsoy, and my dear nephew, Bulut Gürsoy, whom I adore. I also want to thank my husband's family members. Their unwavering belief in me, support, and patience throughout my PhD journey have been invaluable whenever I needed them.

Finally, I sincerely thank TÜBİTAK (Project No: 118C063, 20AG002, 121C250, and 123F373) for financial support and the opportunity to join the 2244-Industrial PhD Fellowship Program with Şişecam.

## TABLE OF CONTENTS

ABSTRACT ..... v

ÖZ ..... vii

ACKNOWLEDGMENTS ..... x

TABLE OF CONTENTS ..... xiii

LIST OF TABLES ..... xvii

LIST OF FIGURES ..... xix

LIST OF ABBREVIATIONS ..... xxv

LIST OF SYMBOLS ..... xxvii

CHAPTERS

1 INTRODUCTION ..... 1

1.1 Discovery of Perovskite Materials ..... 1

1.2 Organic-Inorganic Perovskite Solar Cells ..... 3

1.2.1 Electrodes ..... 5

1.2.2 Charge Transport Layers ..... 5

1.2.3 Absorber Layer ..... 6

1.3 Perovskite Solar Cell Architectures and Working Mechanism ..... 8

1.4 Hole Transport Materials for Perovskite Solar Cells ..... 9

1.4.1 Inorganic HTMs ..... 10

1.4.2 Chemically Doped Organic Small Molecule-Based HTMs ..... 11

1.4.3 Polymeric HTMs ..... 14

1.5 Electron Transporting Materials for Perovskite Solar Cells ..... 16

1.5.1 Organic ETMs ..... 17

1.5.2 Polymeric ETMs ..... 19

1.5.3 Inorganic ETMs ..... 20
1.6 Passivation Strategies in Perovskite Solar Cells ..... 20
1.6.1 3D/2D Perovskite Solar Cells ..... 21
1.6.2 Small Organic Molecules ..... 25
1.6.3 Inorganic Additives ..... 26
1.7 Challenges in Perovskite Solar Cells ..... 26
1.8 Motivation and Strategy ..... 28
2 2D PEROVSKITE PASSIVATION STUDIES BY IMPLEMENTING METHOXY AND HALOGEN UNITS ON PEAI RING FOR THE FABRICATION OF HIGH PERFORMANCE AND STABLE N-I-P-BASED 3D PEROVSKITE SOLAR CELLS ..... 31
2.1 Tuning the 2D Perovskite Passivation: Impact of Electronic and Steric Effects on the Performance of 3D/2D Perovskite Solar Cells ..... 31
2.1.1 Introduction ..... 32
2.1.2 Experimental ..... 37
2.1.3 Results and Discussion ..... 41
2.1.4 Conclusion ..... 59
2.2 The Drastic Influence of Substituent Position on the Orientation of 2D Layers Enables Efficient and Stable 3D/2D Perovskite Solar Cells ..... 60
2.2.1 Introduction ..... 61
2.2.2 Experimental ..... 63
2.2.3 Results and Discussion ..... 66
2.2.4 Conclusion ..... 80
3 SYNTHESIS OF NON-FULLERENE ELECTRON TRANSPORT AND $NiO_x$ LAYER PASSIVATION MOLECULES SUITABLE FOR THERMAL EVAPORATION TO FABRICATE HIGH-PERFORMANCE INVERTED PSCS ..... 83

3.1 Synthesis of Naphthalene Diimide-Based Electron Transport Layers Suitable for Thermal Evaporation to Fabricate High-Performance Inverted PSCs 84

3.1.1 Experimental Procedure for the Synthesis of NDI Derivatives ..... 89

3.1.2 Optical and Electrochemical Properties ..... 90

3.1.3 Inverted Perovskite Solar Cells Fabrication and Efficiency Results with **NDI-pT** Derivative ..... 91

3.2 Synthesis of Fluorene-Based $NiO_x$ Layer Passivation Molecules for Inverted PSCs ..... 94

3.2.1 Experimental Procedure for the Synthesis of DFH Derivatives ..... 95

3.2.2 Optical and Electrochemical Properties ..... 98

3.2.3 Inverted Perovskite Solar Cells Fabrication and Efficiency Results with **DFHD2** Derivative ..... 99

4 EFFECT OF POLYMERIC ADDITIVES ON THE EFFICIENCY AND STABILITY OF N-I-P STRUCTURED PSCS ..... 103

4.1 Introduction ..... 103

4.2 Results and Discussion ..... 105

4.3 Experimental ..... 113

4.4 Conclusion ..... 114

REFERENCES ..... 117

A. NMR DATA ..... 161

CURRICULUM VITAE ..... 167

## LIST OF TABLES

TABLES

**Table 1.1.** Summary of *spiro*-OMeTAD pristine material properties ..... 12

**Table 2.1.** Fitting parameters of TRPL spectra of reference and ***x*-XPEAI**-treated films, $A1$ and $A2$ are the fractions of the two decay processes, and $\tau_1$ and $\tau_2$ are shorter and longer lifetimes, respectively. ..... 48

**Table 2.2.** PV parameters of 2D–3D PSCs with varying ***o*-XPEAI**, ***m*-XPEAI**, and ***p*-XPEAI** contents compared to the control device. ..... 50

**Table 2.3.** Formation energies of **(*x*-XPEA)$_2$PbI$_4$** 2D films on 3D perovskite layer. ..... 53

**Table 2.4.** Interfacial Dipole values of the entire interface between the $FAPbI_3$ perovskite and 2D **(*x*-XPEA)$_2$PbI$_4$** perovskite. ..... 54

**Table 2.5.** Hammett parameters for halogen substituents[176] ..... 55

**Table 2.6.** Fitting parameters of TRPL spectra of reference and **OMe-PEAI**-treated films, $A1$ and $A2$ are the fractions of the two decay processes and $\tau_1$ and $\tau_2$ are shorter and longer lifetimes, respectively. ..... 71

**Table 2.7.** Reverse scan (R.S.) and Forward Scan (F.S.) *J-V* device parameters and hysteresis Index (%) results of the reference and **OMe-PEI** treated PSCs ..... 74

**Table 2.8.** $V_{OC}$, $J_{SC}$, FF, and PCE statistics of reference (3D) and 3D/2D solar cells ..... 74

**Table 2.9.** The formation energies of neutral I vacancies at the respective interfaces. ..... 76

**Table 3.1.** Detailed cost analysis and material requirements for the synthesis of 1 gram of NDI-based ETMs. ..... 86

**Table 3.2.** Optical and electrochemical properties of **NDI-pT, NDI-Ph,** and **$C_{60}$.** 91

**Table 3.3.** Photovoltaic parameters of the reference and the target devices. ..... 93

**Table 3.4.** Optical and electrochemical properties of **DFHD1, DFHD2,** and $NiO_x$. ..... 99

**Table 3.5.** Photovoltaic parameters of the reference and the **DFHD2**-treated inverted PSCs. ..... 101
**Table 4.1.** Photovoltaic device parameters of unencapsulated reference, ***poly*-ADD1**- and ***poly*-ADD2**-treated champion PSCs (kept under ambient conditions for 21 days). ..... 105
**Table 4.2.** Optical and electrochemical properties of the pristine perovskite layer, ***poly*-ADD1** and ***poly*-ADD2** molecules. ..... 107

## LIST OF FIGURES

FIGURES

**Figure 1.1.** An ideal cubic 3D perovskite structure. ..... 1
**Figure 1.2.** Several applications of perovskite materials. ..... 3
**Figure 1.3**. Historical development of power conversion efficiency (PCE) in single junction inverted and regular PSCs. Data was retrieved from the National Renewable Energy Laboratory data sheet. ..... 4
**Figure 1.4.** The general perovskite solar cell architecture.[13] ..... 4
**Figure 1.5.** Various forms of defects in perovskite structure[41] ..... 8
**Figure 1.6.** Common Architectures of **a)** n-i-p and **b)** p-i-n structures PSCs.[42] ..... 9
**Figure 1.7.** General Charge Transfer Pathways in **a)** n-i-p and **b)** p-i-n structures PSCs ..... 9
**Figure 1.8.** Molecular structure of *spiro*-OMeTAD. ..... 13
**Figure 1.9.** Molecular structure of the dopants used for *spiro*-OMeTAD. ..... 13
**Figure 1.10.** Various small organic-based HTMs are used in the literature. ..... 14
**Figure 1.11.** Molecular structures of polymeric HTMs in the literature. ..... 16
**Figure 1.12.** Molecular structures of fullerene and its derivatives used as ETLs in the literature. ..... 17
**Figure 1.13.** Molecular Structures of NFA-based ETMs in the literature. ..... 18
**Figure 1.14.** Structure of NDI-core. ..... 19
**Figure 1.15.** Molecular structure of some polymeric ETMs in the literature.[96, 97, 98] ..... 19
**Figure 1.16.** Some examples of passivation materials for PSCs are in the literature. [113, 114, 115, 116, ..... 21
**Figure 1.17.** Molecular structures of some 2D forming salts in the literature. ..... 22
**Figure 1.18. A)** Selection of A cations that have facilitated significant breakthroughs in the PSCs domain, arranged according to their cationic radius and corresponding tolerance factor in the $APbI_3$ lattice model. The values in parentheses denote the cation radius. **B)** Molecular structures of the organic cations specified in **A)**.[117] ... 23

**Figure 1.19.** Layered Perovskite Configurations Derived from 3D Perovskites: **a)** (100)-Terminated, **b)** (110)-Terminated, **c)** (111)-Terminated.[118] ..... 24
**Figure 1.20.** Representation of the three phases of 2D perovskites Ruddlesden-Popper (**RP**), Dion-Jacobson (**DJ**), and alternating-cation-interlayer (**ACI**) 2D perovskites.[119] ..... 25
**Figure 1.21.** Structures of small organic molecules used in the passivation of PSCs in the literature. ..... 26
**Figure 1.22.** The molecular structure of **a)** halogen (F, Cl, Br)- and **b)** methoxy (OMe)-substituted **PEAI** type salts. ..... 29
**Figure 1.23.** The structures of p-i-n-based PSCs, NFET and $NiO_x$ passivation molecules. ..... 30
**Figure 1.24.** Structıres of polymeric additives. ..... 30
**Figure 2.1.** A comparison of halogen-containing phenylalkylammonium iodide salt-treated photovoltaic device efficiencies from various high-profile PSC papers from 2019 onwards. The related molecular structures are illustrated with their reported names and champion efficiencies. It should be noted that at various papers, different names are given to the same salts by publishers. To avoid confusion, each set of salt-treated PSC studies are demonstrated by different shapes. Also, three major colours are used to identify the device type (i.e., black colour identifies the control device; turquoise colour identifies 3D/2D PSCs; red colour identifies the direct passivation on 3D PSCs. All corresponding device architectures, stability details and references are additionally given in Table S5. Note: to avoid confusion, the same structured salts were identified by the same style (*x*-XPA*AI; x: *o, m, p*; X: F, Cl, Br; P: phenyl; A*: alkyl chain either methyl or ethyl; A: ammonium; I: iodide) in the Table 1.1 rather than original names given in Figure 2.1 (i.e., **PMAI**: BAI, BZAI; ***o*-FPMAI**: 2-F-PMAI; ***p*-FPMAI**: FBAI; ***p*-ClPMAI**: CBAI; ***o*-ClPMAI**: 2-CBAI; ***m*-ClPMAI**: 3-CBAI; ***p*-ClPMAI**: 4-CBAI, ***p*-BrPMAI**: BBAI; ***o*-FPEAI**: 2-FPEAI, oFPEAI, o-F-PEAI; ***m*-FPEAI**: 3-F-PEAI, mFPEAI, m-F-PEAI, 3F-PEAI; ***p*-FPEAI**: 4-F-PEAI, pFPEAI, p-F-PEAI, FPEAI, F-PEAI, 4-FPEAI, ***p*-ClPEAI**: Cl-PEAI; ***o*-BrPEAI**: 2-Br-PEAI; **$F_5$PEAI**: FEAI). ..... 36

**Figure 2.2. a)** Structures of the nine different halogenated **PEAI** salts synthesized and used in this study; **b)** XRD patterns of ***m*-XPEAI**-treated perovskite films; **c)** GIWAXS images (with 2.0° incident angle); and **d)** SEM images of the reference and *meta*-substituted salt-treated 3D perovskite films. ..... 41
**Figure 2.3.** Reference and 3D/2D XRD spectra of perovskite films treated with **(a) *x*-FPEAI**, **(b) *x*-ClPEAI**, and **(c) *x*-BrPEAI**; Pure 2D (n = 1) **(d) (*x*-FPEA)$_2$PbI$_4$**, **(e) (*x*-ClPEA)$_2$PbI$_4$**, and **(f) (*x*-BrPEA)$_2$PbI$_4$** films. ..... 42
**Figure 2.4.** GIWAXS images of 3D/2D films with 0.12° incident angle. ..... 43
**Figure 2.5.** GIWAXS images of 3D/2D films with 0.4° incident angle. ..... 43
**Figure 2.6.** GIWAXS images of 3D/2D films with 2.0° incident angle. ..... 44
**Figure 2.7.** Top-view SEM images of the 3D/2D PSCs treated with ***x*-XPEAI** salts. ..... 45
**Figure 2.8.** Cross-sectional SEM images of the 3D/2D PSCs treated with ***x*-XPEAI** salts. ..... 46
**Figure 2.9.** Atomic force microscopy images of the 3D reference and ***x*-XPEAI**-treated 2D films. ..... 46
**Figure 2.10. a)** Steady-state photoluminescence spectra; **b)** Time-resolved PL traces; **c)** Transmission spectra of reference and meta-halogenated **PEAI** salt-treated 3D perovskite films. ..... 46
**Figure 2.11.** PL spectra of 3D/2D films treated with **(a) *x*-FPEAI**, **(b) *x*-ClPEAI**, and **(c) *x*-BrPEAI**. ..... 47
**Figure 2.12.** Transmission spectra of 3D/2D films treated with **(a) *x*-FPEAI**, **(b) *x*-ClPEAI**, and **(c) *x*-BrPEAI**. ..... 48
**Figure 2.13. a–d)** Statistics of reference and 3D/2D films; **e)** *J–V* Curves of the pristine and halogenated **PEAI** treated devices simulated under 1 sun illumination; **f)** EQE spectra and calculated photocurrent values. ..... 49
**Figure 2.14.** Reverse and forward scans of halogenated-salt-treated champion solar cells. ..... 51
**Figure 2.15.** Theoretical modeling of all the halogenated salts at three different positions by DFT analysis. ..... 52

**Figure 2.16.** Optimized crystal structures of ***o*-XPEAI–$FAPbI_3$**, ***m*-XPEAI–$FAPbI_3$** and ***p*-XPEAI–$FAPbI_3$** interfaces: ac plane and bc plane views. .....55
**Figure 2.17.** Comparison between the reference 3D perovskite and ***m*-XPEAI**-treated 3D/2D films on: **a)** contact angle of a surface water droplet; **b)** ambient air stability (RH > 20%, T = 20–25 °C); **c)** thermal stability (RH = 60–70%, T = 60 °C); and **d)** long-term stability of unencapsulated ***m*-ClPEAI**-treated and reference device at maximum power point (MPP) tracking under continuous 1-sun illumination and nitrogen atmosphere. .....57
**Figure 2.18.** Ambient air stabilities for the reference and halogenated 3D/2D films. .....58
**Figure 2.19.** Solar device architecture and crystallographic features of the films. **A)** Illustration of the solar cell architecture. **B)** Schematics of the ***o*-OMe-PEAI**, ***m*-OMe-PEAI**, and ***p*-OMe-PEAI** structures. **C)** XRD pattern of the reference (ref.) 3D perovskite and perovskites treated with methoxy-substituted salts (***o*-OMe-PEAI**, ***m*-OMe-PEAI**, and ***p*-OMe-PEAI**). (002), (040), and (001) represent the diffraction peaks of 2D (n = 1), quasi 2D (n = 2), and $PbI_2$ (001), respectively. **D)** GIWAXS images of the 3D perovskite. **E)** GIWAXS images of the 3D/2D perovskite films. .....67
**Figure 2.20. a)** XRD pattern of the pure 2D films (n=1). **b)** XRD pattern of the quasi 2D film (n = 2).....68
**Figure 2.21.** GIWAXS spectra of the pure 2D films (n = 1). .....69
**Figure 2.22.** Film characterization. **A)** SEM top-view and cross-section images of the 3D film. **B)** 3D/2D films with ***o*-OMe-PEAI**. **C)** ***m*-OMe-PEAI**. **D)** ***p*-OMe-PEAI**.....69
**Figure 2.23. A)** Steady-state photoluminescence (PL) spectra. **B)** PL spectra of the pure 2D films (n = 1). **C)** TRPL traces. **D)** Absorption spectra of the 3D film and 3D films with **OMe-PEAI** treatment. .....70
**Figure 2.24**. Device parameters and molecular dynamics **(A–D). A)** $V_{OC}$, **B)** $J_{SC}$, **C)** FF, and **D)** PCE statistics of reference (3D) and 3D/2D solar cells (out of 5 devices). Box plot details: The bottom and top edges of the box indicate 25th and 75th

percentiles, respectively. The central horizontal line in the box indicates the median, whiskers extend to the most extreme data points, and the mean is indicated by open symbols. **E)** *J-V* curves of the champion ref. and 3D/2D solar cells. **F)** EQE spectra of the champion ref. and 3D/2D solar cells. **(G-I)** Optimized structures of interfaces between 3D $FAPbI_3$ perovskite and ***o*-OMe-PEAI**, ***m*-OMe-PEAI**, and ***p*-OMe-PEAI** 2D perovskites. ..... 72
**Figure 2.25.** Reverse and forward scans of champion solar cells. ..... 73
**Figure 2.26.** UPS spectra of the reference and OMe-treated 3D/2D films. ..... 78
**Figure 2.27.** Stability studies **A)** Contact angle images of ref. and 3D/2D films. **B)** Stability under 65% relative humidity at ambient air for 10 h. Solid lines are given to guide the eye. **C)** In situ stability for measuring the PCEs of unencapsulated PSC devices over 900 h under a nitrogen atmosphere. ..... 79
**Figure 3.1.** Molecule structures of NDI-based ETMs. ..... 88
**Figure 3.2.** Synthetic route of **NDI-Ph.** ..... 89
**Figure 3.3.** Synthetic route of **NDI-pT.** ..... 89
**Figure 3.4.** Cyclic Voltammograms of the **a) NDI-Ph** and **b) NDI-pT**, **c)** Uv-vis absorption spectra of **NDI-Ph** and **NDI-pT.** ..... 90
**Figure 3.5.** *J-V* curve of the thickness study of **NDI-pT**. ..... 93
**Figure 3.6.** Molecule structures of **DFH**-based molecules. ..... 94
**Figure 3.7.** Synthetic route of **2,7-dibromo-9H-fluoren-9-one**. ..... 95
**Figure 3.8.** Synthetic route of **2,7-dibromospiro[fluorene-9,2'-[1,3]dioxolane]**. 96
**Figure 3.9.** Synthetic route of **DFHD1**. ..... 96
**Figure 3.10.** Synthetic route of **DFHD2**. ..... 97
**Figure 3.11.** Cyclic voltammograms of the **a) DFHD1** and **b) DFHD2**, **c)** Uv-Vis absorption spectra of **DFHD1** and **DFHD2**. ..... 98
**Figure 3.12.** *J-V* curve of the thickness study of **DFHD2**. ..... 101
**Figure 4.1.** General n-i-p perovskite device architecture and the molecule structures of ***poly*-ADD1** and ***poly*-ADD2**. ..... 105
**Figure 4.2. a)** Transmission spectra of the reference, ***poly*-ADD1** and ***poly*-ADD2** films. **b)** PL spectrum of the reference, ***poly*-ADD1**, and ***poly*-ADD2** films..... 106

**Figure 4.3**. Cyclic voltammograms of the **a) *poly*-ADD1** and **b) *poly*-ADD2.**.....107
**Figure 4.4.** XRD Spectrum of the reference, ***poly*-ADD1**, and ***poly*-ADD2**-treated films.....108
**Figure 4.5.** SEM images of the resulting reference, ***poly*-ADD1**, and ***poly*-ADD2**-treated films.....108
**Figure 4.6.** AFM images of the reference and polymer-treated films.....109
**Figure 4.7.** XPS spectra of Pb 4f and I 3d in reference and polymer-treated films. .....110
**Figure 4.8.** Contact angle results of the prepared reference and polymer-treated films.....110
**Figure 4.9.** Thermal stability test results of unencapsulated PSCs kept on a hot plate at 85℃ for 1600 h under ambient conditions. .....111
**Figure 4.10.** Ambient air stability test results of unencapsulated PSCs at ~35% RH for 1320 h under ambient conditions.....112

## LIST OF ABBREVIATIONS

| ABBREVIATIONS | |
|---|---|
| PSC | Perovskite Solar Cell |
| HOMO | Highest Occupied Molecular Orbital |
| LUMO | Lowest Unoccupied Molecular Orbital |
| CBM | Conduction Band Minimum |
| VBM | Valence Band Maximum |
| TCO | Transparent Conductive Oxide |
| ITO | Indium-Doped Tin Oxide |
| FTO | Fluorine-Doped Tin Oxide |
| $TiO_2$ | Titanium (IV) Oxide |
| *cp*-$TiO_2$ | Compact Titanium (IV) Oxide |
| *mp*-$TiO_2$ | Mesoporous $TiO_2$ (IV) Oxide |
| HTL | Hole Transport Layer |
| ETL | Electron Transport Layer |
| *spiro*-OMeTAD | 2,2′,7,7′-Tetrakis[*N*,*N*-Di(4-Methoxyphenyl)amino]-9,9′-Spirobifluorene |
| PTAA | Poly(triaryl Amine) |
| P3HT | Poly(3-Hexylthiophene) |
| PEDOT: PSS | Poly(3,4-Ethylenedioxythiophene) Polystyrene Sulfonate |
| CuSCN | Copper(I) Thiocyanate |

| | |
|---|---|
| $C_{60}$ | Fullerene |
| $PC_{61}BM$ | [6,6]-Phenyl-$C_{61}$-Butyric Acid Methyl Ester |
| ICBA | Indene-$C_{60}$ bisadduct |
| NFA | Non-Fullerene Acceptor |
| NDI | Naphthalene Diimide |
| PDI | Perylene Diimide |
| DSSC | Dye Sensitized Solar Cell |
| $SnO_2$ | Tin (IV) Oxide |
| UV | Ultraviolet |
| PCE | Power Conversion Efficiency |
| PEAI | Phenylethylammonium Iodide |
| Li-TFSI | Lithium-Bis(trifluoromethanesulfonyl)imide |
| FK209 | Tris(2-(1H-Pyrazol-1-yl)-4-*tert*-Butylpyridine)-Cobalt(III)tris(bis(trifluoromethylsulfonyl)imide)) |
| *t*-BP | 4-*tert*-Butylpyridine |
| BCP | Bathocuproine |
| *J-V* | Current Density-Voltage |
| HI | Hysteresis Index |
| NMR | Nuclear Magnetic Resonance |
| DPP | Diketopyrrolopyrrole |
| CV | Cyclic Voltammetry |
| RH | Relative Humidity |

## LIST OF SYMBOLS

SYMBOLS

| | |
|---|---|
| D | Donor |
| A | Acceptor |
| J | Coupling Constant |
| br | Broad |
| dd | Doublet of Doublets |
| t | Triplet |
| s | Singlet |
| d | Doublet |
| q | Quartet |
| *o-* | *Ortho-* |
| *m-* | *Meta-* |
| *p-* | *Para-* |
| Å | Angstrom |
| $\lambda_{max}$ | Maximum Absorption |
| $E_g$ | Bandgap |
| $V_{OC}$ | Open-Circuit Voltage |
| $J_{SC}$ | Short-Circuit Current Density |

# CHAPTER 1

# INTRODUCTION

## 1.1 Discovery of Perovskite Materials

Gustav Rose first discovered perovskite materials in the Ural Mountains in 1839. It was named in honor of Lev Alekseevich Perovski, a Russian mineralogist and a nobleman count.[1] The structure of a perovskite material generally refers to oxides having the same crystal structure as $CaTiO_3$, namely $ABX_3$. For the organic-inorganic halide perovskites, A is the organic or inorganic cation with different sizes ($(CH_3NH_3)^+$, $(HC(NH_2)_2)^+$, $Cs^+$, $K^+$, etc.); B is the inorganic cation ($Pb^{2+}$, $Sn^{2+}$, etc.), and X is the halogen ($Cl^-$, $Br^-$, $I^-$). In an ideal stable cubic 3D (3-Dimensional) perovskite structure, B cations and X anions are placed at the corners and the midpoints of edges, respectively, and A cations are located at the center of the skeleton **(Figure 1.1.)**.

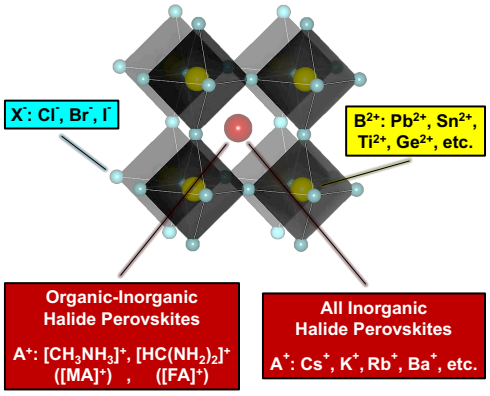



**Figure 1.1.** An ideal cubic 3D perovskite structure.

There are some deviations from this ideal cubic structure when the size of the ions does not satisfy the Goldschmidt tolerance factor (*t*) requirement.[2] Under optimum situations, ideal 3D cubic perovskite structures have a *t* value close to 1, as shown in

**Equation 1.1,** where the $R_A$, $R_B$, and $R_X$ are the ionic radius of the ions in the $ABX_3$ design. In the opposite case, some deviations from the 3D cubic structure occur, and crystal symmetry is lowered to 2D (2-dimensional) and/or 1D (1-dimensional) structures.

$$\frac{r_A + r_X}{\sqrt{2}(r_B + r_X)} \qquad \textbf{Equation 1.1}$$

Various application areas of perovskite materials have been placed in the field, such as sensors, solar cells, supercapacitors, photodetectors, and hydrogen evolution reactions, since they show superconductivity, piezoelectricity, and magnetic properties.[2] Among the perovskite materials, halide perovskites where halides replace the X anions show remarkable light-emitting and photovoltaic properties [3,4]. Halide perovskites are subdivided further into hybrid organic-inorganic perovskite halides (HOIPH) and all-inorganic perovskites. Weber et al. first introduced the physical properties and the structures of hybrid organic-inorganic based $CH_3NH_3MX_3$ (M = Pb or Sn, X = I, Br or I) perovskites in 1978 [5,6]. Since then, HOIPH has dominated the area of optoelectronics due to their remarkable optical absorption properties, tunable bandgap (E*g*), carrier mobility, long diffusion length, defect tolerance, and easy synthesis. Applying HOIPH varies from solar cells and light-emitting diodes (LEDs) to photodetectors **(Figure 1.2)**.[7–9]

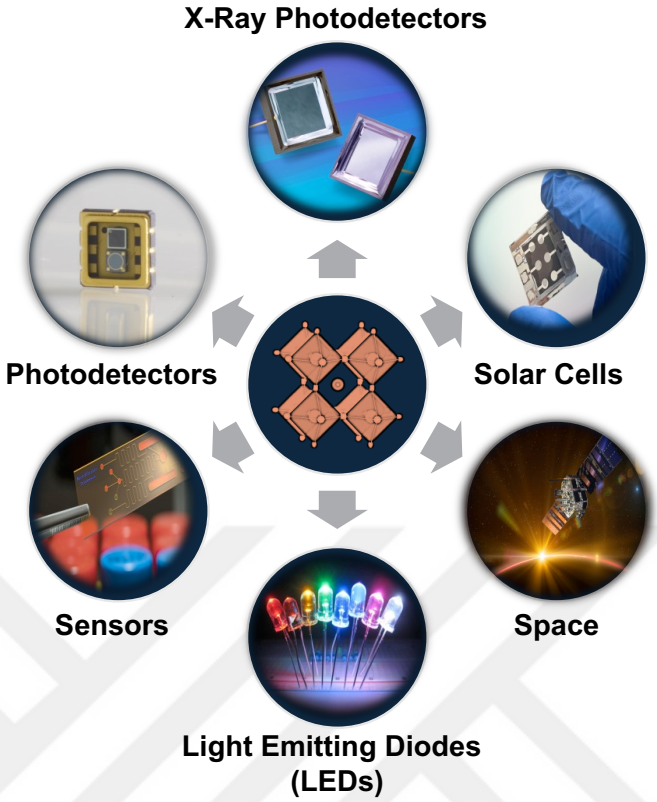



**Figure 1.2.** Several applications of perovskite materials.

## 1.2 Organic-Inorganic Perovskite Solar Cells

The first solar cell report based on organic-inorganic perovskites was published by Kojima et al. in 2009.[10] This paper achieved 3.9% PCE by preparing thin film solar cells with hybrid organic-inorganic perovskite material. Since then, perovskite materials have attracted much attention from researchers working in the photovoltaic area. Through the years, the best-certified perovskite solar cell efficiency has reached over 26% PCE in 2024 and taken its place in the National Renewable Energy Laboratory (NREL) chart.[11,12]

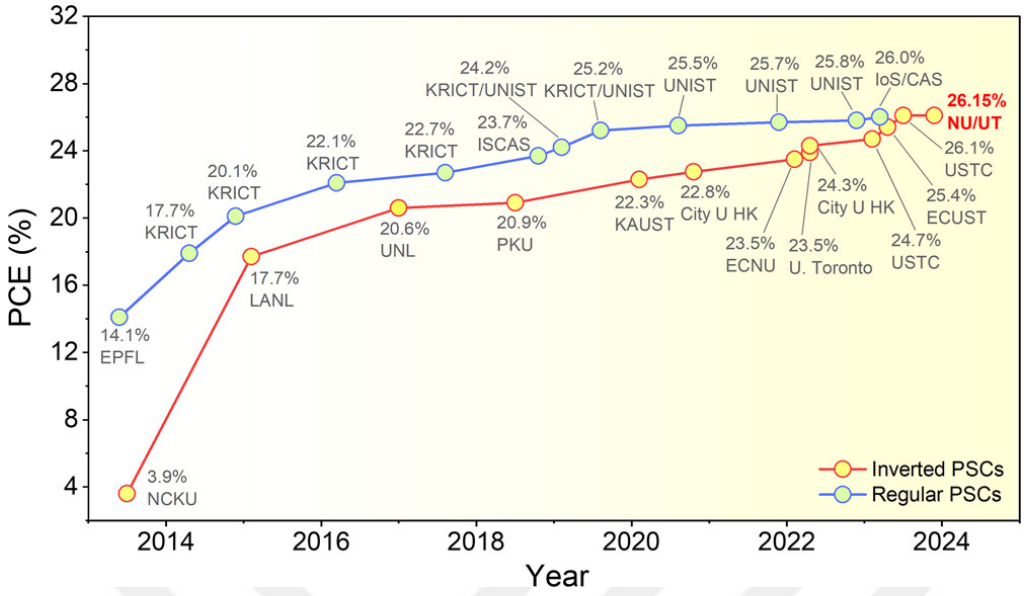



**Figure 1.3**. Historical development of PCE in single junction inverted and regular PSCs. Data was retrieved from the National Renewable Energy Laboratory (NREL) data sheet.

A typical perovskite solar cell consists of several functional layers: charge transport layers (CTL) where the electron (ETL) or hole (HTL) transport layer takes place; an absorbing layer where the perovskite structure takes place, and an electrode (**Figure 1.4**). Each functional layer should provide the essential optoelectronic properties for an active PSC design.

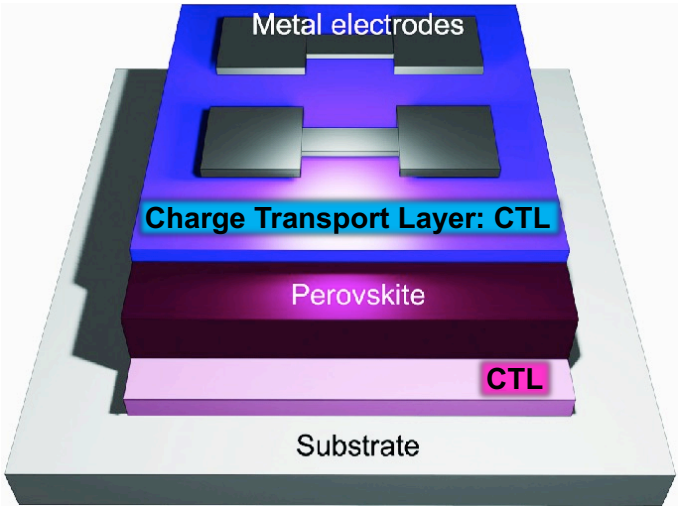



**Figure 1.4.** The general perovskite solar cell architecture.[13]

### 1.2.1 Electrodes

Electrodes are necessary constituents of PSCs and affect the solar cell's PCE and stability. Metal electrodes (Ag, Au), carbon nanotubes (CNTs), and transparent conducting oxides (TCOs) are some examples of electrodes used in PSC design in the literature.[14] Metal electrodes are generally used as a back contact in perovskite photovoltaics since they have high reflectivity and conductivity. An appropriate metal electrode should have a well-matched work function and a suitable resistivity with a charge transport layer for a high PCE in the solar cell. Generally, thermal evaporation is applied to deposit metal electrodes on the transport layer. Gold (Au), silver (Ag), aluminum (Al), copper (Cu), and nickel (Ni) are the most used metal electrodes. Among them, Au is the best choice for high PCE. Ag is cheaper than gold; in 2012, Snaith and coworkers used Ag as a metal electrode for the first time.[15] Apart from metal electrodes, TCOs are used as electrodes in PSCs. FTO (fluorine-doped tin oxide), ITO (Indium-doped tin oxide), and AZO (aluminum-doped zinc oxide) are the TCOs that are mainly used as electrodes. An ideal TCO should have an optimum work function, optical transparency, conductivity, and low resistivity to be applied in PSCs.[16] The choice of TCOs depends on their work function, surface roughness, and electrical and optical characteristics.

### 1.2.2 Charge Transport Layers

Charge transport layers extract holes and electrons from the absorber layer and transfer them to the corresponding electrodes in a PSC. HTLs play a critical role in the performance and efficiency of PSCs by facilitating the extraction of holes from the perovskite absorber layer and transporting them to the corresponding electrode. These layers improve charge selectivity and suppress recombination at the interface, contributing to enhanced device efficiency and stability.

Based on their material composition, HTLs can be divided into three main types: organic, inorganic, and polymeric. Each type has unique advantages and challenges

regarding processability, stability, and compatibility with the perovskite layer. To give an example of these hole transport layers, $NiO_x$ (Nickel Oxide), *spiro*-OMeTAD (2,2',7,7'-Tetrakis[N,N-di(4-methoxyphenyl)amino]-9,9'-spirobifluorene), PTAA (polytriarylamine) are some of them. S*piro*-OMeTAD is a widely used HTM in n-i-p type high-efficiency PSCs due to its optimum glass transition temperature, favorable band alignment with the perovskite, and superior transparency.[17,18] The properties and the various kinds of electron and hole transport layers are given in the following sections.

Electrons are extracted from the perovskite layer by ETLs. PSCs employ organic, inorganic, and polymeric ETLs. $SnO_2$ (Tin Oxide), fullerene ($C_{60}$) and its derivatives such as PCBM (Phenyl-C61-butyric acid methyl ester), and NDI-based polymers are a few examples of them. The ETL selection significantly impacts the photovoltaic performance of PSCs. Careful consideration must be given to material stability, processing temperature, energy level alignment, and electron mobility. For example:

- Inorganic ETMs like $SnO_2$ are preferred for their robustness and scalability, especially for commercial applications.
- Organic ETMs like PCBM are favored when low-temperature processing and flexibility are required.

In conclusion, optimizing electron transport layers is vital to advancing PSCs' efficiency, stability, and scalability. Research continues to explore novel ETMs and configurations to address the challenges of large-scale production and long-term operational stability.

### 1.2.3 Absorber Layer

The perovskite material acts as an absorber layer, absorbing light from the source and generating free electrons and holes. Then, the generated free electrons and holes are injected into the corresponding transport layers. Perovskite material is a promising candidate due to its high absorption coefficient, adjustable bandgap, long

carrier lifetime, high carrier mobility, low exciton binding energy, direct bandgap, and low-cost production compared to its silicon counterparts.[19]

Light absorption is crucial for a best-performing perovskite solar cell since electron and hole carriers are formed during absorption. Therefore, there are several methods to enhance the light-harvesting property of the perovskite material and reduce the possible defects (**Figure 1.5**), such as additive engineering, passivation of the perovskite layer, and compositional engineering in perovskite material by variation of the halogen and organic cation.[20] In 2015, Seok and coworkers reported the efficiency and stability dependence on the $(FAPbI_3)_{1-x}(MAPbBr_3)_x$ composition, where the x represents the mole ratio between 0 and 0.3. The ideal composition is formed when X-ray diffraction (XRD) ensures x = 0.15 and 3D perovskite material phase stability.[21] You and coworkers utilized the **PEAI** (phenethyl ammonium iodide) salt on top of $FA_{(1-x)}MA_xPbI_3$ perovskite to passivate the surface defects. After utilizing **PEAI** salt, the open-circuit voltage ($V_{OC}$) increased from 1.12V to 1.18V due to decreased non-radiative recombination, and defects were suppressed.[22] Several groups reported the addition of excess $PbI_2$ as a Lewis acid on perovskite composition to ameliorate the device performances.[23–25] Besides, fullerene derivatives are also employed in PSCs.[26–29] Wang and coworkers indicated a high fill factor (FF: 86.7%) upon the addition of water-soluble fullerene derivatives in the perovskite precursor solution.[30] Lewis bases are also incorporated into perovskite solution for defect passivation in the literature.[31–33] In 2017, urea as a Lewis base additive was reported to enhance the PSC device performance. With the addition of urea, perovskite crystallinity was increased, and non-radiative recombination was suppressed.[34] In other respects, excess ammonium salts are added to the perovskite solution to enhance the crystallinity and morphology of the absorber layer.[35–37] Ionic liquids (IL) are liquid forms of salts, and they are added to the perovskite composition to improve the crystallization and passivate the defects in the absorber film.[38,39] Wang and coworkers added three triazolium-based ILs into the methylammonium lead iodide ($MAPbI_3$) perovskite to observe the passivation and stability effect.[40] Consequently, the lone pair on the $-NH_2$ group on ILs interacts with

the $Pb^{2+}$ to attain surface passivation. Self-assembled monolayers (SAMs) were formed on the perovskite layer, making the perovskite surface hydrophobic and enhancing humidity stability.

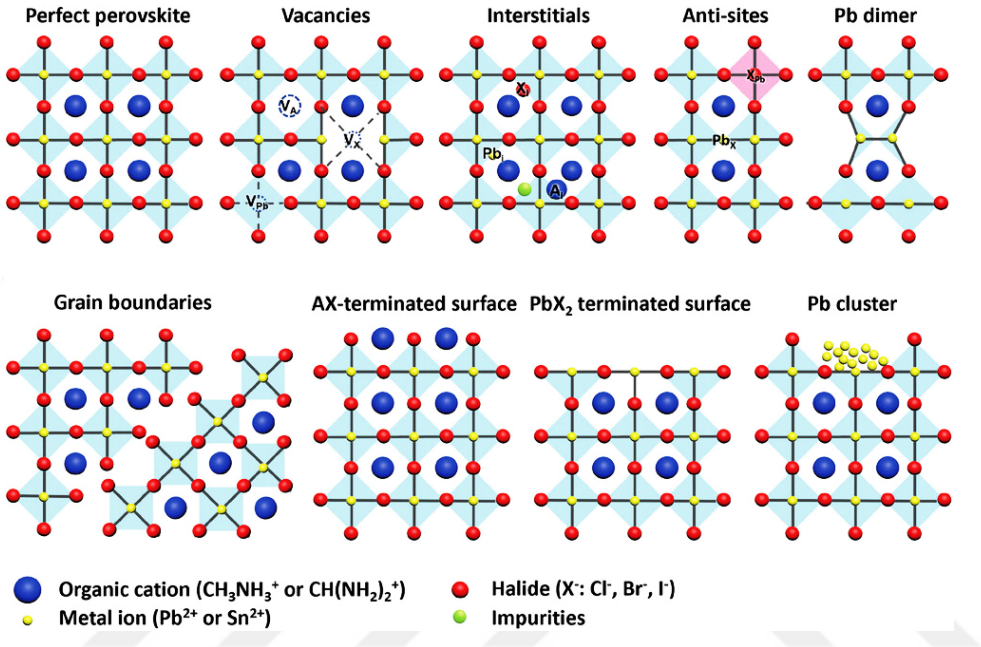



**Figure 1.5.** Various forms of defects in perovskite structure.[41]

## 1.3 Perovskite Solar Cell Architectures and Working Mechanism

In a primary perovskite solar cell, the active perovskite layer is sandwiched between an electron transport layer and a hole transport layer. There are two types of PSC architectures: mesoporous and planar **(Figure 1.6).** The planar structure is further divided into n-i-p and p-i-n, depending on the penetration side of light. In the n-i-p configuration, the light enters from the ETL side, and in the p-i-n design, the light enters from the HTL side. The mesoporous structure has the n-i-p configuration, where the mesoporous layer is used as ETL. In the case of planar structures, flexible and large-area devices can be produced at low temperatures, which is impossible in mesoporous architecture since it requires high sintering temperatures. On the other

hand, the mesoporous layer is essential for the repeatability of the device performance and for controlling the perovskite layer morphology.

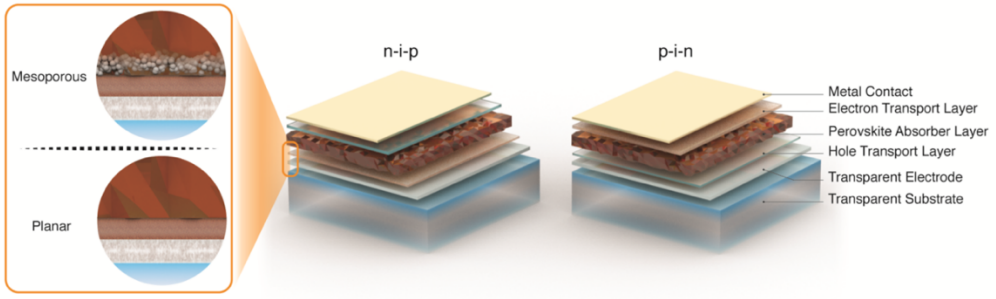



**Figure 1.6.** Common Architectures of **a)** n-i-p and **b)** p-i-n structures PSCs.[42]

Light conversion occurs in three steps in a perovskite solar device: charge generation, separation, and transportation. The active perovskite layer absorbs sunlight, then generates electron-hole pairs, which are charge carriers. The electron and hole transport layers collect these charge carriers and then transport them to the electrodes **(Figure 1.7).** Since the charge transport layers significantly affect PSCs' performance and stability, selecting or designing the best electron/hole transport material for the perovskite solar device is essential.

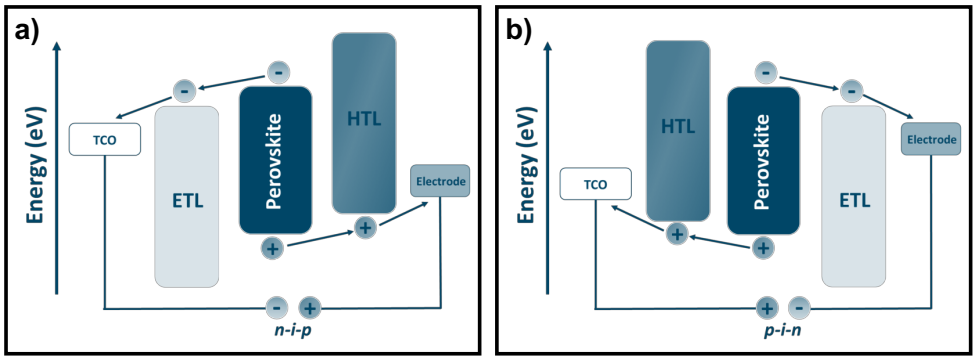



**Figure 1.7.** General Charge Transfer Pathways in **a)** n-i-p and **b)** p-i-n structures PSCs

## 1.4 Hole Transport Materials for Perovskite Solar Cells

A hole transport layer is positioned between the perovskite layer and the electrode and plays a crucial role in PSCs. The hole transport layer is in charge to extract and transport the holes to the electrode without charge recombination. HTL should have

the optimum valence band with the perovskite to transport holes without energy loss and high glass transition temperature ($T_g$). High hole mobility and adequate conductivity are also desired to have a high PCE for the hole transport materials. In an n-i-p type perovskite device, since HTL is placed on top of the absorber layer, it is expected that the HTL will preserve the perovskite layer from external factors such as oxygen and humidity. In p-i-n type perovskite devices, transparency in the visible range is needed for the HTLs for light penetration.[43] From a chemistry point of view, an ideal HTM should have a compact morphology, and the perovskite/HTL interface should be chemically settled for a stable perovskite solar cell. Furthermore, while designing HTMs, short synthetic routes and facile purifying methods should be considered for the industrialization of PSCs.

The literature identifies three main types of HTMs: inorganic, organic, and polymeric. The following section will discuss their advantages and disadvantages.

### 1.4.1 Inorganic HTMs

Inorganic hole transport materials are widely used in PSCs. Although they have high hole mobility, stability, and low-cost production, the solvent used to dissolve the inorganic HTM dissolves the perovskite layer during deposition, venturing the stability.[44] In 2014, Kamat and coworkers reported the first utilization of CuI on top of $MAPbI_3$ ($CH_3NH_3PbI_3$) perovskite as an alternative to *spiro*-OMeTAD HTM. They reported a 6.0% PCE with enhanced stability and FF (0.70).[45] Although CuI has superior conductivity compared to *spiro*-OMeTAD demonstrated by impedance spectroscopy, $V_{OC}$ is still lower than *spiro*-OMeTAD resulting from high recombination in the CuI-based perovskite devices. Other than CuI, CuSCN, a p-type semiconductor with optimum transparency in the visible and near-infrared region and high hole mobility, is also used as HTM in the literature.[44,46,47] Among the inorganic hole transport materials, $NiO_x$ is the most widely used in organic photovoltaics (OPV)[48], dye-sensitized solar cells (DSSCs)[49,50] and p-i-n type PSCs. The first paper regarding $NiO_x$ in perovskite devices was published in 2014 by Hsu

and coworkers. They demonstrated the application of $NiO_x$ as an electrode interlayer for the fabrication of $CH_3NH_3PbI_3$ – based planar PSC. Enhanced device parameters are obtained with the utilization of $NiO_x$ instead of PEDOT:PSS which is an organic hole transport material ($V_{OC}$ = 0.92 V, a short-circuit current ($J_{SC}$) = 12.43 mA/cm$^2$, FF = 0.68, and a PCE of 7.8%) in place of PEDOT:PSS ($V_{OC}$ = 0.62 V, a $J_{SC}$ = 9.39 mA/cm$^2$, FF = 0.66, and a PCE of 3.9%).[51] Later, many papers were published using $NiO_x$ as a hole transport layer in PSCs.[52–54] Although there are many endeavours to enhance the performance of $NiO_x$-based p-i-n type PSC, commercialization of inverted $NiO_x$-based PSC has some adversities because of energy-level mismatch between $NiO_x$ HTLs and perovskite, interfacial defects, poor contact, and improper phase orientation.[55]

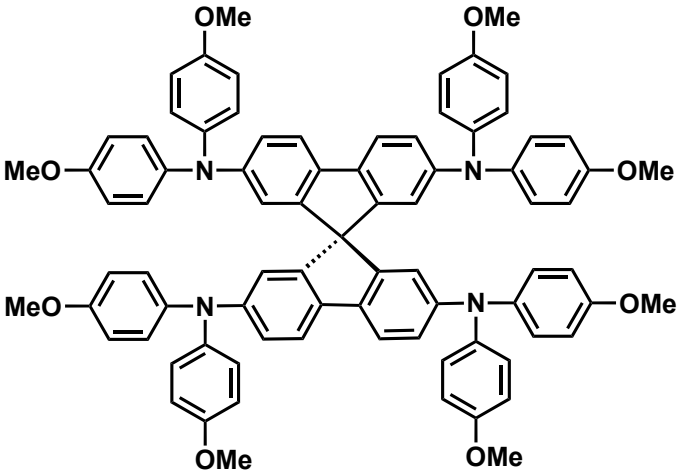
### 1.4.2 Chemically Doped Organic Small Molecule-Based HTMs

HTMs in PSCs are doped to improve their structural and electrical characteristics, eventually raising the device's overall performance. The intrinsic hole conductivity of HTMs is frequently low. Dopants provide charge carriers, or holes, significantly boosting the HTL's electrical conductivity. They can also slightly modify the HTL's energy levels or work function, which maximizes its alignment with the electrode and the perovskite absorber layer. This alignment makes charge separation and collection more effective, which lowers energy barriers for hole extraction and transit. Among the chemically doped organic small molecules, 2,2',7,7'-Tetrakis[N,N-di(4-methoxyphenyl)amino]-9,9'-spirobifluorene (*spiro*-OMeTAD) attracts much attention due to its higher performance as a small molecule in n-i-p type PSCs, as shown in **Figure 1.8.** Other than the efficiency parameter, being easy-processed and having a convenient HOMO level with the perovskite make it the most preferred organic small HTM. Other characteristics are summarized in **Table 1.1**.[56]

**Table 1.1.** Summary of *spiro*-OMeTAD pristine material properties

| Properties | Values |
|---|---|
| HOMO (eV) | -5.07 |
| LUMO (eV) | -2.09 |
| $E_{opt.}g$ (eV) | 2.98 |
| UV (nm) | 309,389 |
| $T_g$ (°C) | 121 - 125 |
| $T_m$(°C) | 244 - 248 |
| Conductivity (S $cm^{-1}$) | $1\times10^{-8}$ to $2.5\times10^{-7}$ |
| Hole Mobility ($cm^2$ $V^{-1}$ $s^{-1}$) | $2\times10^{-4}$ |
| Intrinsic Carrier Density ($cm^{-3}$) | $8.67\times10^{14}$ |

*spiro*-OMeTAD was first utilized in light-emitting diode devices and then broadened to DSSC and PSC with a $T_g$ passes beyond 120°C.[57] It gives a 9.7% PCE when first used as HTL in PSCs in 2012[58] and recently improved over 25% PCE.[59] Despite primarily being used in organic HTM, it needs to be doped with hydrophilic additives to enhance its conductivity within the device. Lithium bistrifluoromethanesulfonimidate (LiTFSI) and FK209 (tris[2-(*1H*-pyrazol-1-yl)-4-*tert*-butylpyridine)cobalt(III) tris(bis(trifluoromethylsulfonyl)imide)] are the mainly used p-dopants for the fast doping of *spiro*-OMeTAD to *spiro*-$OMeTAD^+$ **(Figure 1.9)**.




***Spiro*-OMeTAD**

**Figure 1.8.** Molecular structure of *spiro*-OMeTAD.

Doing so provides better band alignment between the perovskite and HTL interface.[60] These hydrophilic p-dopants easily absorb water, resulting in the degradation of the perovskite layer. Furthermore, *tert*-butylpyridine (*t*-BP) is also used as an additive along with p-dopants. The primary role of *t*-BP in *spiro*-OMeTAD is to regulate the morphology while controlling the distribution of p-dopants within the HTL. However, *t*-BP vaporizes quickly and erodes the perovskite layer.[61]

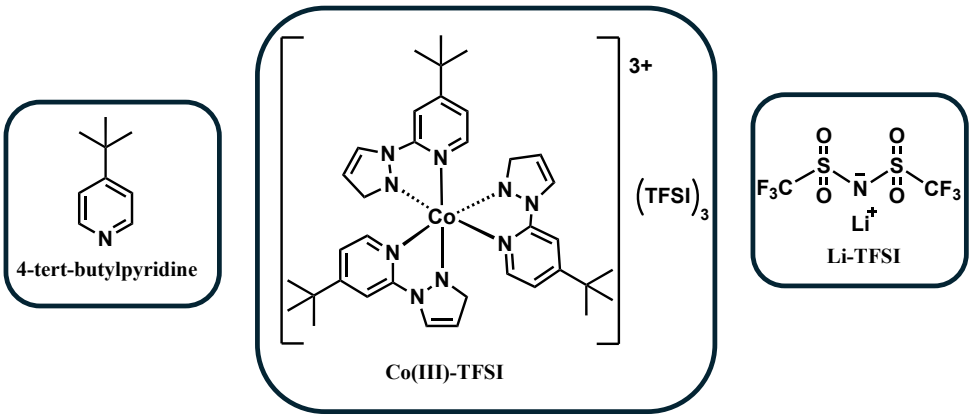



**Figure 1.9.** Molecular structure of the dopants used for *spiro*-OMeTAD.

Other than *spiro*-OMeTAD, different types of small organic-based HTMs used in the literature must be doped with the p-dopants mentioned above **(Figure 1.10)**.[62–72]

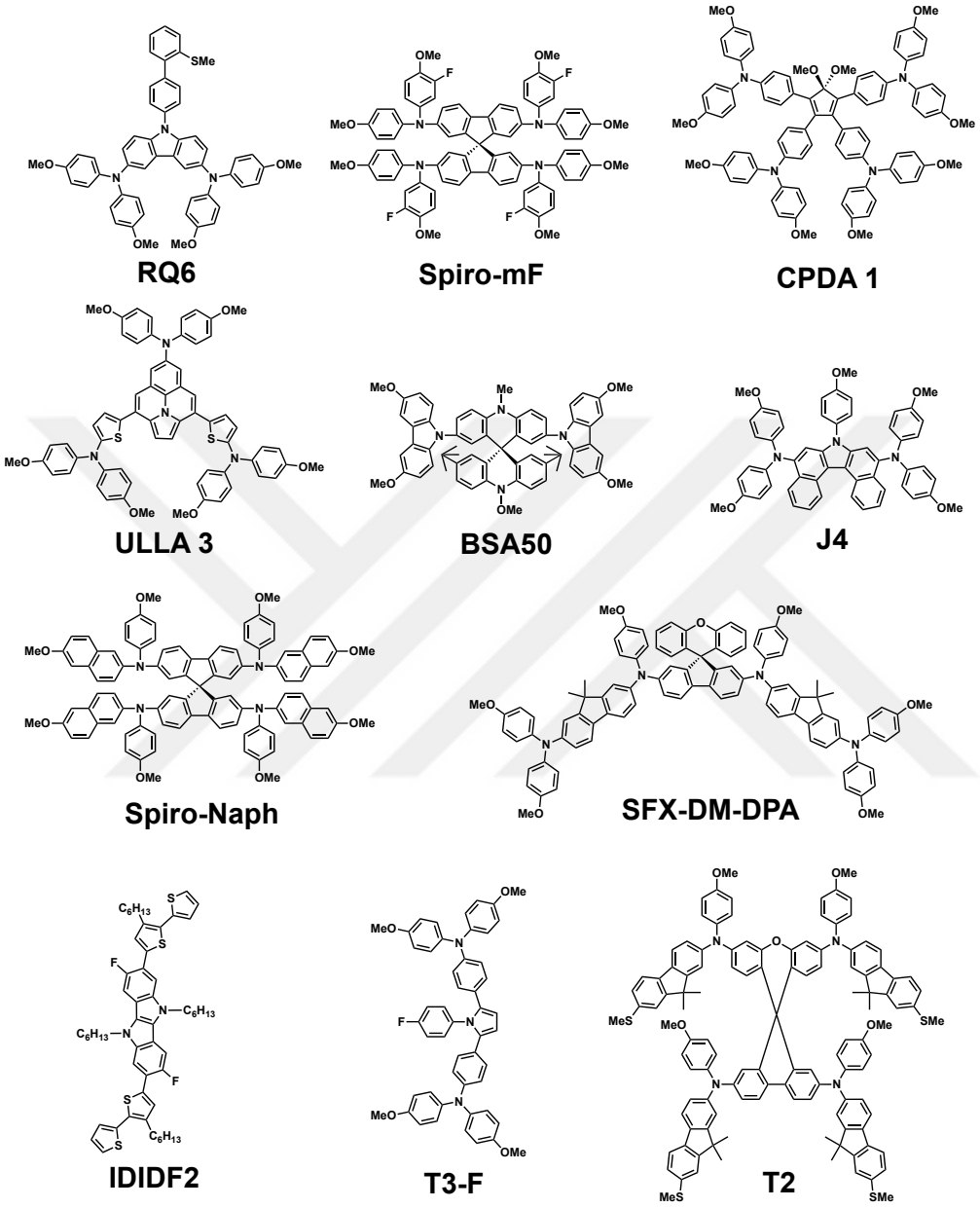



**Figure 1.10.** Various small organic-based HTMs are used in the literature.

### 1.4.3 Polymeric HTMs

$\pi$-Conjugated polymeric HTMs have superior film-forming ability with almost no grain boundaries and thermal and moisture stability due to their hydrophobic nature

and higher $T_g$ value compared to the small organic HTMs. Polymers have high conductivity compared to small organic molecules and can be used instead of *spiro*-OMeTAD in PSCs.[73] The efficiency of PSC can be improved by using thinner polymeric HTLs since polymeric HTLs give shorter pathways for the holes through the metal electrode.[74] In PSCs, poly-(triarylamine) (PTAA) was first used as a polymeric HTL in 2013 by Seok et al.[75] It is reported that with the incorporation of PTAA in n-i-p type mesoscopic perovskite device, a maximum of 12% PCE was achieved with an attractive reproducibility compared to other polymeric HTMs. Several $\pi$-conjugated polymers like poly(3-hexylthiophene) (P3HT), poly[N-9-heptadecanyl-2,7-carb-azole-alt-3,6-bis(thiophen-5-yl)-2,5-dioctyl-2,5-dihydropyrrolo-[3,4]pyrrole-1,4-dione] (PCBTDPP), poly[2,1,3-benzothia-diazole-4,7-diyl[4,4-bis(2-ethylhexyl)-4H-cyclopenta[2,1-b:3,4-b′]dithiophene-2,6-diyl]] (PCPDTBT), and poly[[9-(1-octyl-nonyl)-9H-carbazole-2,7-diyl]-2,5-thiophenediyl-2,1,3-benzo-thiadiazole-4,7-diyl-2,5-thiophenediyl] (PCDTBT) and the rest have been used as HTLs[76–80], and the molecule structures are given in **Figure 1.11**. Among these over numerous polymeric HTMs, PTAA still takes the lead in terms of efficiency in PSCs due to its suitable HOMO level (-5.20 eV), adequate hole mobility (3-6 x $10^{-4}$ $cm^2V^{-1}s^{-1}$), enhanced stability, transparency, and ease of deposition in PSCs.[81] Recently, Zhu et al. reported 24.89% PCE (certified 24.5%) with the utilization of PTAA-based HTMs in inverted PSCs with enhanced long-term stability (93% of initial PCE retained after 800h).[82] Although polymeric HTMs have superior features over small organic molecule-based HTMs, they suffer in synthetic reproducibility, which may affect the device's reproducibility at the same time.

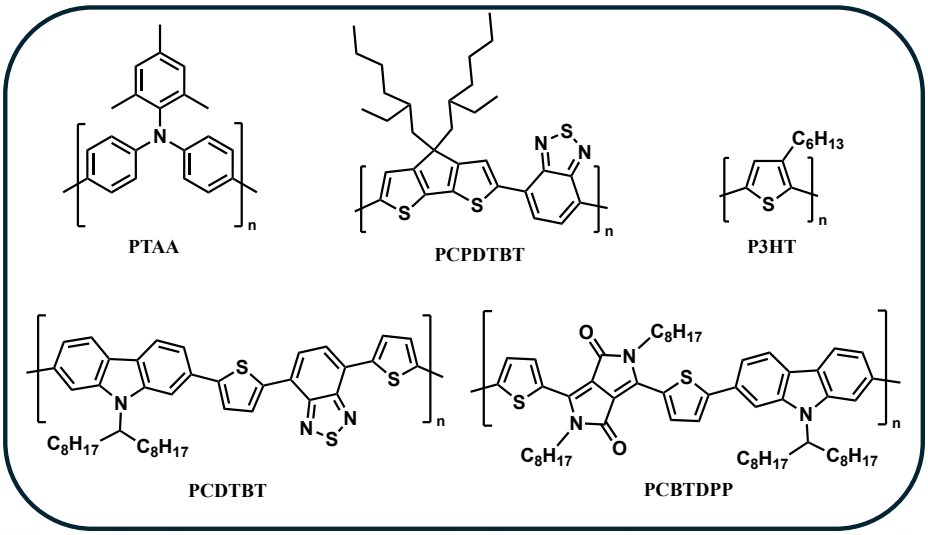



**Figure 1.11.** Molecular structures of polymeric HTMs in the literature.[83]

## 1.5 Electron Transporting Materials for Perovskite Solar Cells

An ideal electron transport layer has two distinct roles. One is to extract negatively charged carriers (electrons) from the perovskite layer and deliver them to the cathode without charge accumulation. The second role is to act as a hole-blocking layer between the perovskite and the cathode by reducing electron-hole recombination leaning. There are also some other criteria for an ideal ETL: (i) an optimum conduction band level for the secure transportation of electrons to the corresponding electrode, (ii) a wide band gap for high transparency to allow more light absorption by perovskite layer, (iii) homogeneous and compact film morphology to prevent current leakage via direct contact between the perovskite and transparent conducting oxide and high electron mobility to enable electrons transport from perovskite through cathode via electron transport layer.[84] The chosen ETL should not react with the absorber layer and the TCO. This thesis classifies the electron transport layers into organic and inorganic-based ETMs.

Despite their close relationship and frequent interchangeability, the words ETL and electron transport material (ETM) refer to different characteristics of PSCs and other optoelectronic devices. The term "ETM" refers to the material itself, which facilitates electron transport. On the other hand, an ETL is the functional layer of a device

comprising an ETM. The device architecture's physical layer is responsible for electron transit and collection.

### 1.5.1 Organic ETMs

Fullerene ($C_{60}$) and its derivatives, such as Phenyl-$C_{61}$-butyric acid methyl ester (PCBM), and Indene-$C_{60}$ bisadduct (ICBA) have been widely employed as ETL in PSCs since 2013 (**Figure 1.12)**.[85] They show appropriate energy levels within the perovskite, low-temperature preparation process, and decent electron acceptor properties.[86] The literature also reported that fullerenes can minimize or eliminate the hysteresis phenomenon in PSCs.[87] In 2014, Shao et al. reported the passivation of charge trap states and annihilation of hysteresis by including PCBM in $MAPbI_3$-based PCS.[26] Fullerenes are primarily used in p-i-n type PSCs due to their abovementioned properties. The first certified inverted PSC efficiency above 25% where fullerene was used as ETL was reported by Jiang et al. in 2022.[88] While fullerene and its derivatives lead in efficiency for inverted PSCs, their industrialization face some challenges such as high costs, poor morphological stability, doping requirements, and difficulties in modification.

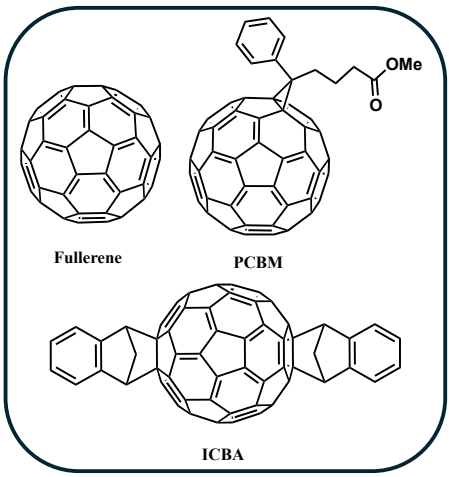



**Figure 1.12.** Molecular structures of fullerene and its derivatives used as ETLs in the literature.[89]

Other than fullerene and its derivatives, non-fullerene electron acceptors (NFAs), such as rylene diimide derivatives, which are perylene diimides (PDIs) and NDIs, azaacene derivatives, and indacenodithiophene (IDT) derivatives are emerging materials as ETMs in the solar field (**Figure 1.13**).[90] NFAs have authentic advantages over fullerene and its derivatives, such as low fabrication costs, high solubility in common organic solvents, easily adjustable energy levels, and high absorption in the visible spectrum. Since designing molecules and substituent effects play a significant role in the electron transport layers in PSCs, NFAs are good competitors in terms of fullerene and its derivatives as ETMs in perovskite photovoltaics.

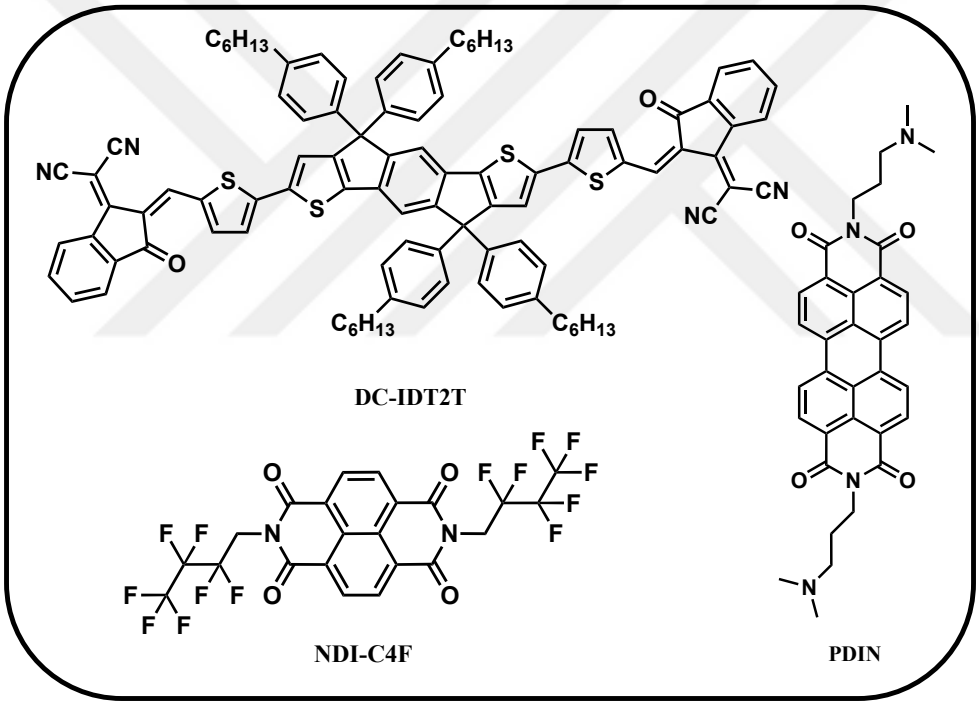



**Figure 1.13.** Molecular Structures of NFA-based ETMs in the literature.[91–93]

Among NFAs, rylene diimide derivatives are promising material alternatives to $PC_{61}BM$ in planar PSCs. NDI-based rylene diimide derivatives have submitted the highest efficiencies so far (>23.0% PCE).[94] NDI unit is a powerful acceptor, and solubility can be enhanced by substituting diverse groups (lipophilic, aliphatic, and hydrophilic groups) at imide/core positions **(Figure 1.14).** Additionally, the NDI

unit possesses superior thermal, photo, and chemical stability than fullerene derivatives at room temperature, which makes NDI derivatives more favored as ETMs.[95]

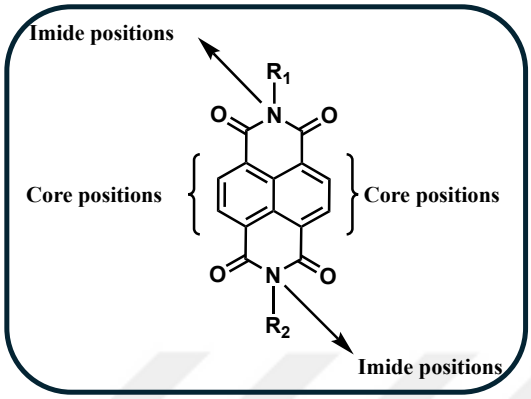



**Figure 1.14.** Structure of NDI-core.

### 1.5.2 Polymeric ETMs

n-type polymeric materials can provide uniform morphologies and robust moisture stability as an electron transport material for the absorber layer in PSC. Also, polymers can form a dipole layer between the ETL and perovskite by impairing the charge recombination **(Figure 1.15)**.[96–98] NDI and PDI-based polymers are widely utilized as ETLs in PSCs. NDI-based polymeric ETLs have unique properties like intense electron mobility and enhanced stability, conducive to modification for solubility.[99,100]

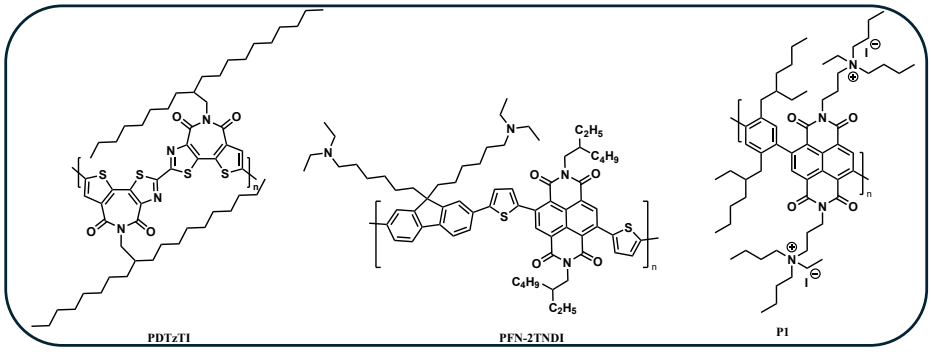



**Figure 1.15.** Molecular structure of some polymeric ETMs in the literature. [101–103]

### 1.5.3 Inorganic ETMs

Many n-type inorganic materials, especially metal oxides ($TiO_2$, $SnO_2$, ZnO, etc.), are engaged as ETLs in PSCs. They possess low-cost fabrication, enhanced electronic properties, and physicochemical stability compared to their organic counterparts. Among the inorganic ETMs, $TiO_2$ is the one that is used primarily due to its generation in dye-sensitized solar cells (DSSCs). Thanks to its wide bandgap, it acts as a hole-blocking layer (3.2 eV). The electron injection from the absorber layer to the ETL is higher when $TiO_2$ is used as an ETL.[104] Nevertheless, high deposition temperatures (~500°C), which restrain the application on both flexible and tandem solar cells, nominal electron mobility, and high trap states because of the photocatalytic activity of $TiO_2$ hinder the high performance and stability of PSCs. Another preferred ETM is $SnO_2$, which is more stable than $TiO_2$ under UV illumination due to its high transparency, electron mobility, and low-temperature process. Although the $SnO_2$ compact electron transport layer shows enhanced electrical and optical properties, it shows hysteresis behaviour, which needs to be solved.[105] Other types of inorganic materials used as ETLs differ from the aforementioned electron transport materials in the literature, such as Mxenes, metal sulfides/oxides, etc.[106]

## 1.6 Passivation Strategies in Perovskite Solar Cells

During perovskite crystallization, lattice mismatches and vacancies are formed within the crystal lattice due to the non-thermodynamic equilibrium, resulting in some defects at the interface or bulk. The non-uniform dispersion of defects in the perovskite or at the grain boundaries, surfaces, and interfaces affects carrier transport negatively, leads to the formation of nonradiative recombination centers, and reduces the further improvement of the PCE. Several techniques in the literature diminish the number of defects within the perovskite layer.[107] One of the most popular techniques is passivation, using additives in perovskite films or coating on the surface of

perovskite films. The defects or energy level mismatches between the perovskite and charge transport interface can be ameliorated by passivation. Passivation can be utilized by introducing low-dimensional (2D) materials (organic ammonium salts and MXenes)[108–110] small organic molecules (derivatives of pyridine and thiophene, etc.)[111–116], inorganic additives (incorporation of metal cations and anions, inorganic salts, etc.)[117] where the structures of some of them are shown in **Figure 1.16.**

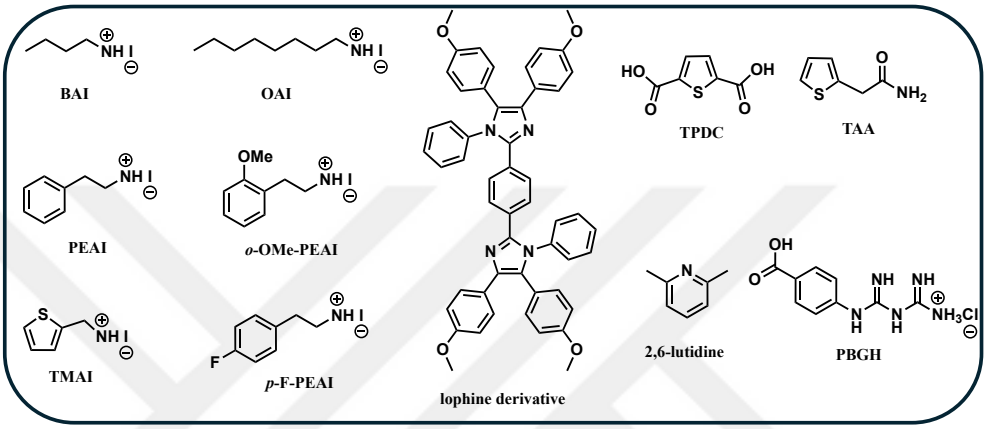



**Figure 1.16.** Some examples of passivation materials for PSCs are in the literature.[118–123]

### 1.6.1 3D/2D Perovskite Solar Cells

Performing 2D passivation on top of 3D PSCs is an effective strategy for passivating the interface and suppressing surface defects. 2D perovskites have a large, bulky organic cation, rendering them hydrophobic. This hydrophobic nature prevents water molecules from infiltrating the perovskite structure and causing degradation. The bulky organic cation acts as a barrier, effectively blocking the intrusion of water molecules and thus improving the overall stability of the perovskite-based devices. This feature is particularly crucial for these devices' long-term stability and reliability, especially in real-world environmental conditions where exposure to moisture can be a significant challenge. Several 2D-forming salts (aromatic, aliphatic, and alicyclic) are reported in the literature, and they show excellent stability when coated on 3D PSCs **(Figure 1.17)**.[124, 125]

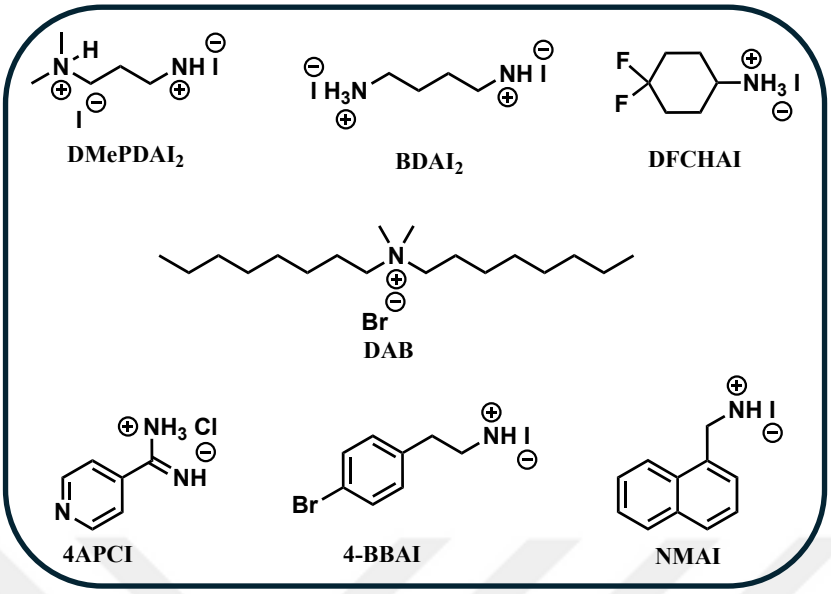



**Figure 1.17.** Molecular structures of some 2D forming salts in the literature.[126–132]

The Goldschmidt tolerance factor, which is mentioned, can predict the structure of a 2D perovskite. When the A site cations in the 3D structure become too large to fit within the octahedral cavity, the structure of 3D perovskites can transform into a layered 2D structure, leading to deviations from the typical range of t values (0.8 to 1.1), as illustrated in **Figure 1.18**.

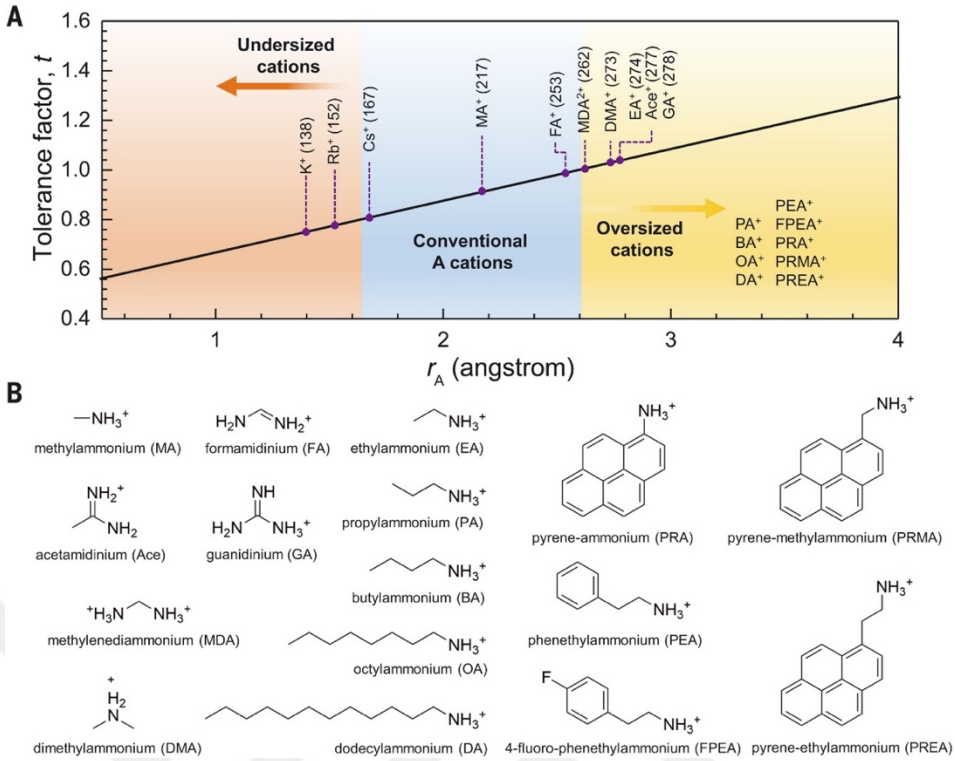



**Figure 1.18. A)** Selection of A cations that have facilitated significant breakthroughs in the PSCs domain, arranged according to their cationic radius and corresponding tolerance factor in the $APbI_3$ lattice model. The values in parentheses denote the cation radius. **B)** Molecular structures of the organic cations specified in **A)**.[133]

In this process, large organic spacers separate the inorganic layered octahedra and closely connect the layers through hydrogen bonding and van der Waals forces. Based on the arrangement of these unit cells in the 3D perovskite structure, 2D perovskites can be classified into different orientations, such as (100), (110), and (111). These orientations refer to the direction in which the perovskite layers are stacked, as shown in **Figure 1.19.**

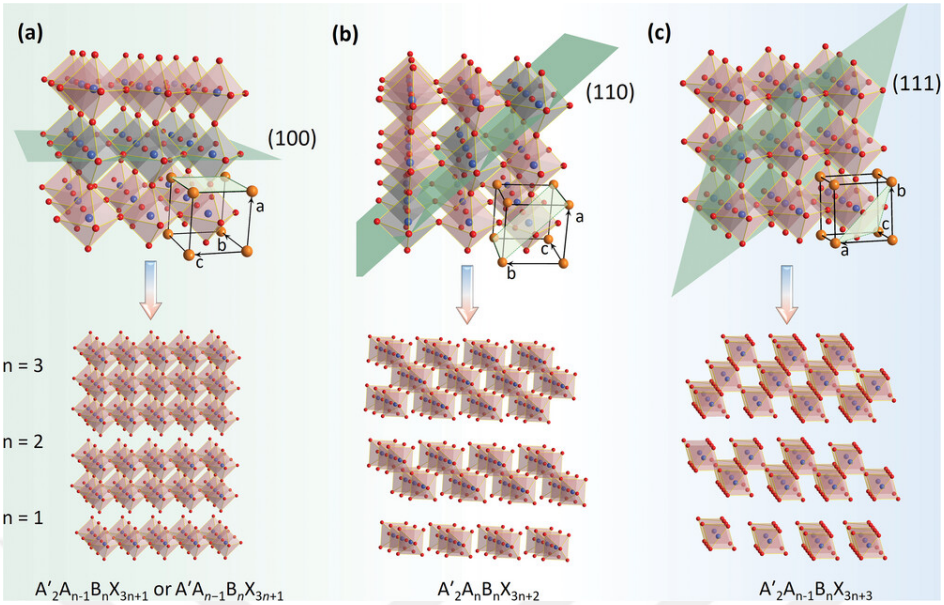



**Figure 1.19.** Layered Perovskite Configurations Derived from 3D Perovskites: **a)** (100)-Terminated, **b)** (110)-Terminated, **c)** (111)-Terminated.[134]

Furthermore, depending on the types of organic spacers used, 2D perovskites can be categorized into three main classifications **(Figure 1.20)**:

1. **The RP Phase** refers to the Ruddlesden-Popper phase, in which organic spacers separate the layers and weak forces connect the inorganic layers.
2. **Dion-Jacobson (DJ) Phase,** named after Dion and Jacobson, who first described it; the organic spacers connect the inorganic layers differently than the RP phase, resulting in a different stacking arrangement.
3. **Alternating Cations in the interlayer space (ACl)** where the cations in the interlayer space alternate between different types, contributing to the stability and unique properties of the 2D perovskite structure.

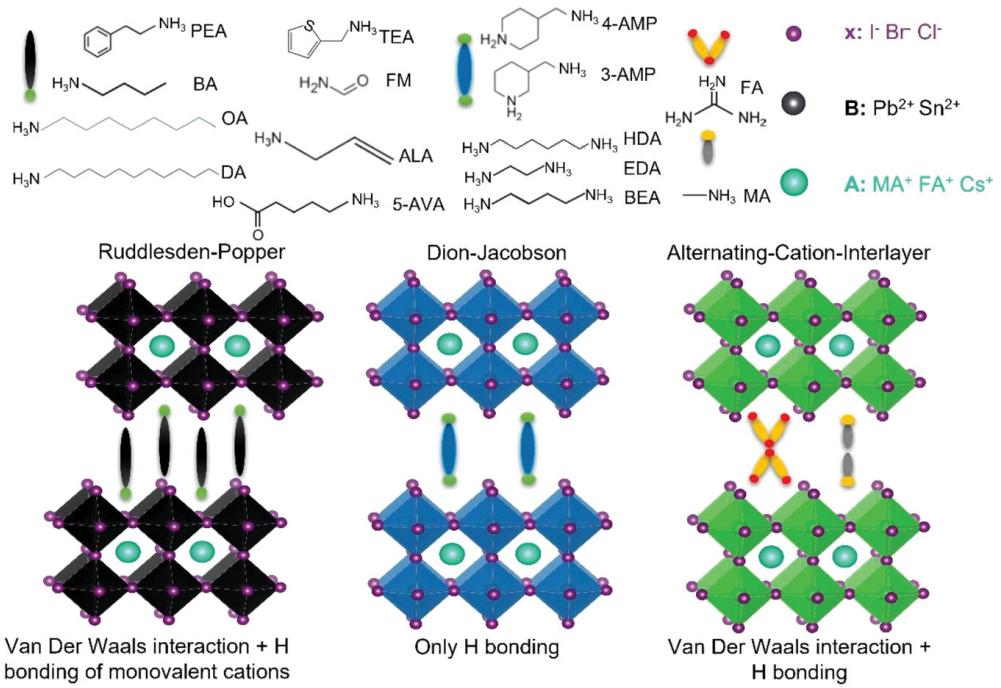



**Figure 1.20.** Representation of the three phases of 2D perovskites Ruddlesden-Popper (**RP**), Dion-Jacobson (**DJ**), and alternating-cation-interlayer (**ACI**) 2D perovskites.[135]

Overall, selecting interlayer spacers and their specific orientations and interactions is thus a key design strategy for tuning the overall performance of 2D perovskite-based solar cells, making these materials highly versatile for future photovoltaic applications.[136–138]

### 1.6.2 Small Organic Molecules

Various structural imperfections are found in perovskite materials due to their ionic nature, which can significantly impact the performance of PSCs. Low-molecular-weight organic compounds can effectively passivate these imperfections in the perovskite material. They often have functional groups that can interact with the surface of the perovskite and reduce non-radiative recombination. Examples include various organic ligands and small aromatic compounds shown in **Figure 1.21**.[139] These molecules can help improve the resistance to humidity, electron and hole

extraction, and light absorption, control the electron density range, and promote lattice distortions when modified by suitable functional groups.

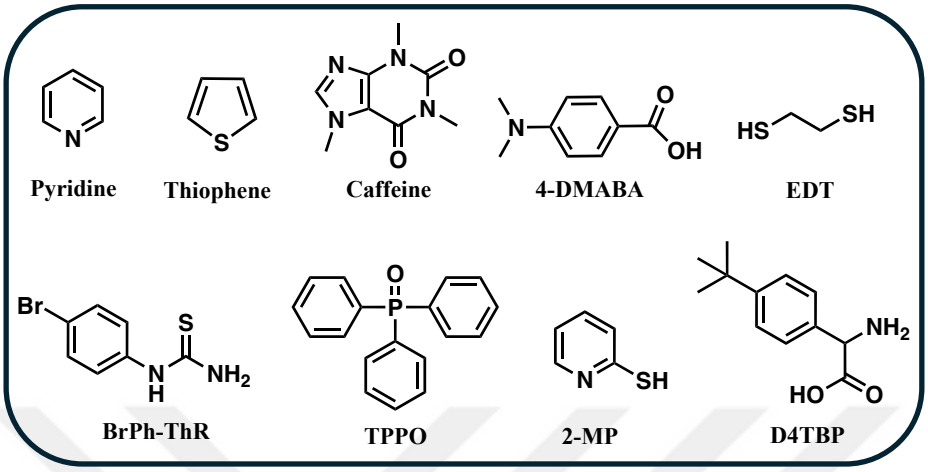



**Figure 1.21.** Structures of small organic molecules used in the passivation of PSCs in the literature.

### 1.6.3 Inorganic Additives

Inorganic materials can form strong covalent or ionic bonds with the surface of the perovskite material, providing more durable passivation than organic molecules. These bonds can effectively passivate defects within the perovskite lattice, reducing non-radiative recombination and improving PSCs' overall stability and performance. Various inorganic salts in the literature are utilized as additives in the perovskite layer or applied on a 3D perovskite surface.[140,141]

## 1.7 Challenges in Perovskite Solar Cells

PSCs offer impressive efficiencies and have shown great potential in recent years. However, their commercialization still needs to be improved, with long-term durability being one of the most critical issues.

- **Stability and Durability:** Perovskite materials are susceptible to moisture, oxygen, and light, which can degrade their performance over time. This degradation can reduce efficiency and ultimately limit the solar cell's

lifetime. Researchers are actively working on developing encapsulation techniques and improving the stability of perovskite materials to address this issue. In addition, understanding the intrinsic and extrinsic degradation mechanisms would also help enhance the long-term stability problem.[142]

- **Upscaling Production:** Attempting to scale up production to commercial levels while maintaining efficiency and stability remains a challenge for PSCs. Manufacturing processes must be optimized to ensure consistent performance and reliability over large areas.[143]
- **Lead Toxicity:** Research and development efforts have focused heavily on the potential environmental impact of lead (Pb) in PSCs. Lead is a toxic heavy metal, and its presence in PSCs raises concerns about environmental pollution and possible health hazards, especially during the manufacturing, operation, and disposal phases. Researchers and industry partners have been working to address this issue through several approaches, such as fabricating lead-free perovskites, encapsulation, and recycling.[144]
- **Cost:** PSCs' competitiveness compared to established technologies like silicon photovoltaics (PV) is crucial for their widespread adoption and commercial success in terms of cost. While PSCs offer the advantage of potentially lower manufacturing costs due to solution-based processing techniques and abundant raw materials, several factors contribute to the overall cost of PSCs that must be addressed, such as manufacturing processes, material efficiency, and scalability.[145]
- **Standardization and Certification:** Establishing standardized testing protocols and certification procedures for PSCs ensures reliability and performance consistency across different manufacturers. This will facilitate widespread adoption and market acceptance of PSCs.

## 1.8 Motivation and Strategy

This thesis utilizes passivation and organic charge carriers to achieve high-performance and stable PSCs.

For passivation strategies, twelve distinct 2D-forming **PEAI**-based salts were systematically designed and applied in n-i-p structured PSCs to deepen the understanding of structure-activity relationships by varying different substituents on the phenyl ring in the first part of the thesis. **(Figure 1.22**). The specific aims of this strategy were:

- To analyse the impact of structural modifications on the **PEAI** phenyl ring by introducing electron-withdrawing and electron-donating groups-namely halogens (-F, -Cl, -Br) and methoxy (-OMe) groups at *ortho* (-*o*), *meta* (-*m*), and *para* (-*p*) positions. This enables a systematic investigation of the structure-activity relationship in passivation.
- To decrease trap-assisted nonradiative recombination, thereby minimizing energy losses in the perovskite devices.
- To achieve highly stable, high-performance PSCs by leveraging the benefits of optimized 2D passivation.

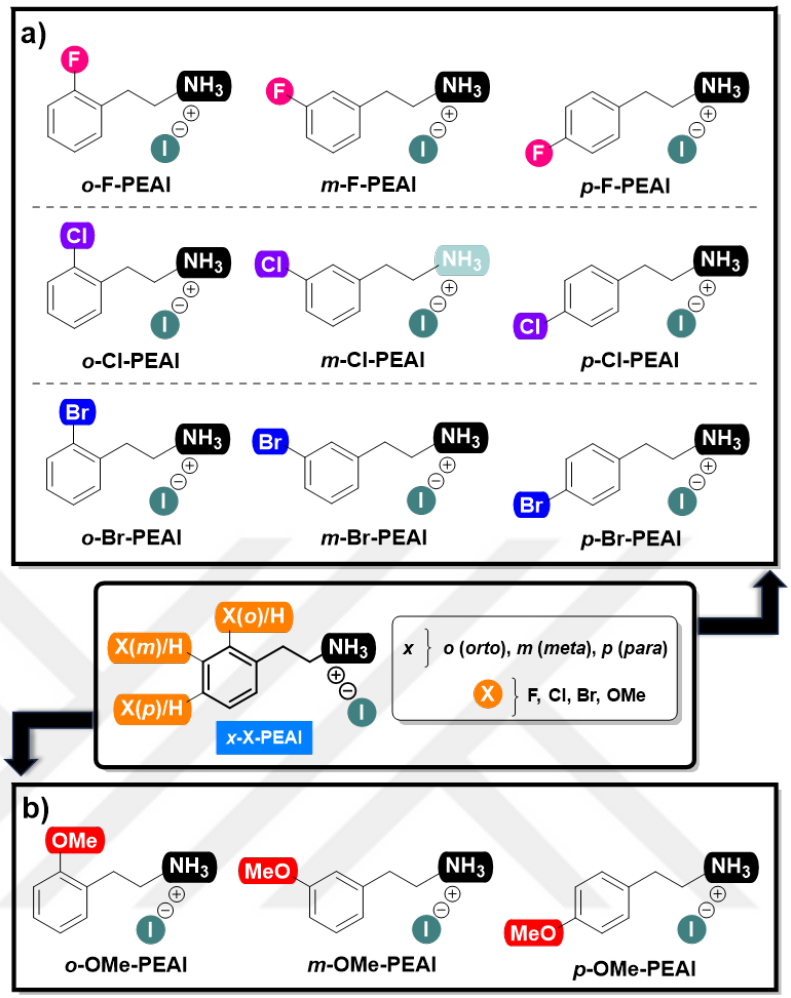



**Figure 1.22.** The molecular structure of **a)** halogen (F, Cl, Br)- and **b)** methoxy (OMe)-substituted **PEAI** type salts.

While organic charge carriers in current research achieve high PCEs, their high costs and vulnerability to external conditions limit their commercial viability. Additionally, these materials often require time-consuming and complicated synthesis and purification procedures. Therefore, alternative organic charge carriers with improved stability and cost-effectiveness are being actively pursued. In the second part of this thesis, non-fullerene electron transport (NFET) molecules and $NiO_x$ layer passivation molecules — designed for compatibility with thermal evaporation — were synthesized through a straightforward, efficient method and incorporated into the fabrication of inverted PSCs **(Figure 1.23.)**.

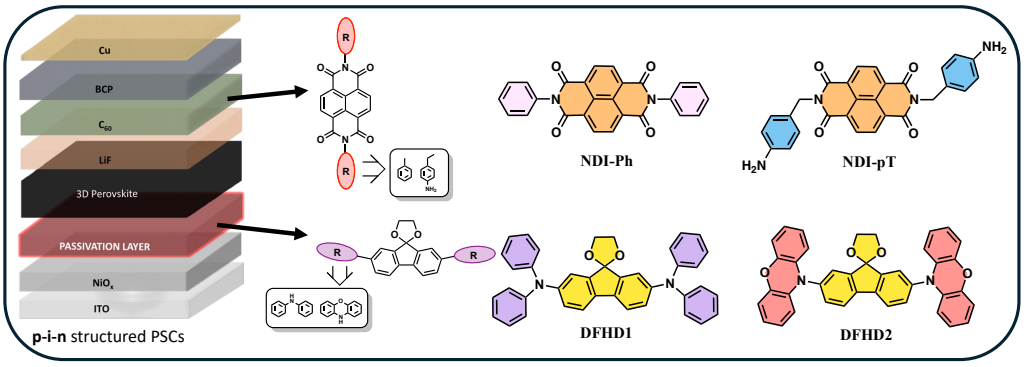



**Figure 1.23.** The structures of p-i-n-based PSCs, NFET, and $NiO_x$ passivation molecules.

Another effective passivation strategy for PSCs involves introducing a polymer layer on the perovskite surface or in the bulk to improve stability and performance. Conjugated polymers based on DPP have shown promise in organic field effect transistors (OFETs) and OPVs due to their high charge mobility and broad absorption spectrum.[146,147] Studies on DPP-based polymers in PSC architectures are emerging, with particular attention to thiophene-substituted derivatives that have been well-characterized in OFETs[148,149]. Nonetheless, a thorough knowledge of the impact of DPP-based polymers on several PSC aspects is missing in the literature. In this work, high-quality n-i-p perovskite films are developed by incorporating donor units — biselenophene (***poly*-ADD1**) and thienothiophene (***poly*-ADD2**) — into the DPP backbone (**Figure 1.24**). These DPP-based polymers are incorporated into the PSC by dissolving them in chlorobenzene, which serves as an antisolvent, and applying them onto the perovskite layer during spin-coating.

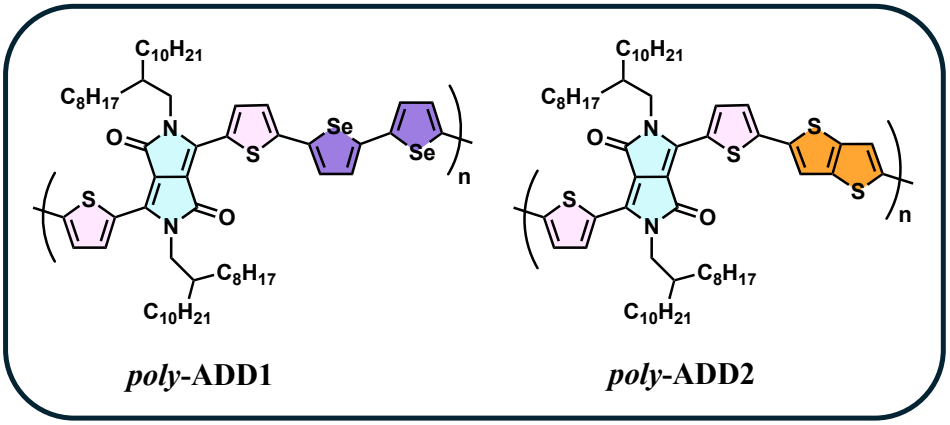



**Figure 1.24.** Structures of polymeric additives

# CHAPTER 2

# 2D PEROVSKITE PASSIVATION STUDIES BY IMPLEMENTING METHOXY AND HALOGEN UNITS ON PEAI RING FOR THE FABRICATION OF HIGH PERFORMANCE AND STABLE N-I-P-BASED 3D/2D PEROVSKITE SOLAR CELLS

This chapter reports the strong impact of substituent position in **PEAI**-based cations on attaining efficient and stable 3D/2D PSCs. Both parts of this chapter are based on two published works.

## 2.1 Tuning the 2D Perovskite Passivation: Impact of Electronic and Steric Effects on the Performance of 3D/2D Perovskite Solar Cells

*The first part of this chapter is based on the published work of Gozukara Karabag et al. Adv. Energy Mater., 2023, 13(45), 2302038. DOI: 10.1002/aenm.202302038.*

*Authors: **Zeynep Gozukara Karabag**, Aliekber Karabag, Ummugulsum Gunes, Xiao-Xin Gao, Olga A. Syzgantseva, Maria A. Syzgantseva, Figen Varlioglu Yaylali, Naoyuki Shibayama, Hiroyuki Kanda, Alwani Imanah Rafieh, Roland C. Turnell-Ritson, Paul J. Dyson, Selcuk Yerci, Mohammad Khaja Nazeeruddin, and Gorkem Gunbas*

*I contributed as the first author of this work, working in equal collaboration with Aliekber Karabag, Ummugulsum Gunes, and Xiao-Xin Gao. I performed the initial device optimizations, characterized the optimized fabricated Perovskite Solar Cells, and analyzed data.*

Surface passivation with 2D perovskites is a powerful strategy to achieve improved stability and performance in PSCs. Various large organic cations have been successfully implemented, led by phenylethylammonium (**$PEA^+$**) and its derivatives. However, systematic studies on large sets of cations to understand the effect of substituent position on 2D perovskite passivation and device performance still need

to be included. Herein, a collection of halogenated **PEA**$^{+}$ iodide salts (***x*-XPEAI** where ***x***: *ortho* (*o*), *meta* (*m*), *para* (*p*), **X**: F, Cl, Br) are synthesized by a facile method and deposited on top of 3D perovskite. The 2D perovskite layer formation is confirmed by XRD and grazing-incidence wide-angle X-ray scattering (GIWAXS) analyses for all cations, regardless of the nature and position of the halogen. Density functional theory (DFT) analysis reveals that lower formation energies and higher interfacial dipoles achieved by *m*-substituted cations are responsible for enhanced performance compared to their *o*-and *p*-counterparts. While the ***m*-BrPEAI**-treated device shows a champion efficiency of 23.42% ($V_{OC}$ = 1.13 V, FF = 81.2%), considering average efficiencies, stability, and reproducibility, the treatment with ***m*-ClPEAI** salt yields the best overall performance. This comprehensive study provides guidelines for understanding the influence of large cation modification on the performance and stability of 3D/2D PSCs.

### 2.1.1 Introduction

The search for low-cost, efficient, and stable solar technology has been central to energy research and development over the last three decades. The best research cell efficiency chart demonstrates how 3D hybrid PSCs have dominated the field in the last decade, owing to their excellent optoelectronic properties.[12] Additionally, perovskites have demonstrated immense potential to be utilized in silicon/perovskite tandem solar cells to achieve efficiencies over the Shockley-Queisser limit for single junction devices, paving the way for unheard lows in the levelized cost of electricity. The conventional cubic 3D perovskite structure is formed by the combination of three different components with a general formula $ABX_3$, where A is an organic/inorganic cation such as formamidinium iodide (FAI), methylammonium iodide (MAI) or cesium (Cs), B is a metal cation (typically $Pb^{2+}$), and X is a halide anion (i.e., $Cl^{-}$, $Br^{-}$, $I^{-}$). The cubic 3D perovskite structure reveals excellent photovoltaic performance due to its high absorption coefficient, tunable band gap by halide substitution, low exciton binding energy (≈10–50 meV), easy photo-

generation of free charges, long carrier diffusion length (0.1–1 μm), low trap density, and low non-radiative recombination rate, resulting in PCEs exceeding 25%, comparable to their silicon counterparts.[150–152] Additionally, the perovskite structure can be realized through straightforward, low-cost processes resulting in high crystallinity materials.[153] While the $J_{SC}$ and FF of PSCs are already close to their theoretical limits (≈26 mA cm$^{-2}$ and 88% for a band gap of 1.55 eV), recent studies have been mainly focused on the improvement of the $V_{OC}$ of PSCs.[22]

Unfortunately, the anticipated commercialization of PSCs is challenged by their limited long-term stability. Conventional 3D PSCs are liable to degradation from extrinsic factors such as moisture, temperature, UV light, and intrinsic ones, including ion migration and interface defects.[154] Low-dimensional 2D perovskites are more stable than their 3D counterparts due to the introduction of larger hydrophobic organic groups in the crystal structure, improving water tolerance and suppressing ion migration.[155] However, 2D perovskites lack efficient charge transport due to the presence of an insulating organic layer and display poor light absorption owing to their high band gap.[156] Additionally, these materials tend to possess high exciton binding energy, resulting in diminished charge extraction to the transport layers.[157] To combine the advantages of 3D and 2D perovskites into a single device, 2D perovskite films are employed on the surface of 3D perovskite films to enhance stability without compromising PCE. Recently, it has been demonstrated that in addition to improved stability, performance enhancement can be achieved in 3D/2D perovskites.[158] Different types of bulky organic cations have been widely reported in the literature and used for various purposes (i.e., 2D PSCs,[159] interfacial passivation layer(s) on bottom and/or top of 3D perovskite[160,161] or 3D/2D PSCs[162] to fabricate highly stable and efficient PSCs over the last decade. Among them, multi-functional halogen-containing phenyl alkylammonium cations (**XPA*A**$^+$; **X**: F, Cl, Br; **P**: phenyl; **A***: alkyl chain either methyl or ethyl; **A**$^+$: ammonium) have an excellent reputation for developing high-performing PSCs via introducing these cations as either 2D Ruddlesden-Popper (RP) layer or interfacial protective layer on top of 3D perovskite. Gao et al. introduced the 2D layer formed by 2-(2-

fluorophenyl)ethylamine iodide (***o*-FPEAI**), 2-(3-fluorophenyl)ethylamine iodide (***m*-FPEAI**), and 2- (4 fluorophenyl)ethylamine iodide (***p*-FPEAI**) atop their 3D perovskite to construct 3D/2D PSCs and reported over 20% PCE with improved stability under continuous illumination for 1440 h.[163] In 2019, You et al. reported the fabrication of only 2D PSCs using a set of mono-fluorinated **PEAI** salts, namely ***o*-FPEAI**, ***m*-FPEAI**, and ***p*-FPEAI**.[164] Concerning the control device based on **PEAI** salt (7.67% PCE), the photovoltaic device efficiencies were improved by over 10% upon utilization of ***m*-FPEAI** (10.17%) and ***p*-FPEAI** (10.55%) salts. In the case of ***o*-FPEAI**-treated 2D PSC, the device efficiency drastically decreased to 0.50%. Among these 2D PSCs, non-encapsulated ***m*-FPEAI**-based 2D PSC showed the highest stability under 45% humidity at room temperature for 30 days.

You and Liu et al. have examined the effect of molecular polarity on the performance of 3D/2D PSCs using fluorinated 2D-forming salts, namely ***o*-FPEAI** and (2-fluorophenyl)methylammonium iodide (***o*-FPMAI**).[165] They reported that the longer carbon chain between the ***o*-FPEA$^+$** and ***o*-FPMA$^+$** cations reduced the inductive effect between amino and fluorine units. Hence, there is a larger dipole for ***o*-FPEAI** than ***o*-FPMAI**, which results in better band alignment and charge transport at the interface. The authors also indicated that the significant molecular polarity enhances the passivation effect by improving the interactions between the 2D passivator and the $PbI_2$, enabling a device performance higher than 23% PCE with an impressive $V_{OC}$ of 1.16 V and FF of 81.36%. The cells retained 82.5% of the initial PCE with high stability for 2000 h at 40% relative humidity and room temperature. In 2021, a set of fluorinated **PEAI** salts (***o*-FPEAI**, ***m*-FPEAI**, and ***p*-FPEAI**) on 3D perovskite film were employed as a direct passivation layer instead of forming a 2D perovskite layer. These salts improved the efficiency and long-term stability at a relative humidity of 15–25% after 430 h. The *meta*-substituted **FPEAI**-treated PSC gave an efficiency of over 23%.[166]

Besides fluorine substitution, chlorine and bromine substitution on the phenyl ring of the $PEA^+$ cation has also been reported to impact the performance of the resulting devices. Liu, Xing, Zhao, and Zheng et al. examined the effect of F, Cl, and Br

substitution on the crystal orientation and phase distribution of the quasi-2D (Q-2D) RP perovskite films.[167] Q-2D RP PSC based on **(*p*-FPEA)$_2$MA$_3$Pb$_4$I$_{12}$** (n = 4) was reported to demonstrate higher efficiency of 18.10% than that of **(PEA)$_2$MA$_3$Pb$_4$I$_{12}$** (12.23%), **(*p*-ClPEA)$_2$MA$_3$Pb$_4$I$_{12}$** (7.93%) and **(*p*-BrPEA)$_2$MA$_3$Pb$_4$I$_{12}$** (6.08%) structured counterparts and also exhibited greater stability after aging 30 days with relative humidity (RH) of 40–50% at room temperature.[168] The reports showed primarily that the addition of electron-withdrawing halogen substituents to the phenyl ring of **PEAI** salts induces higher polarity, leading to lower exciton binding energy and more effective exciton dissociation in the 2D-perovskite structures.[168–170] Several other critical works related to halogen-substituted phenyl alkylammonium iodide salts are detailed in **Figure 2.1** and the supporting information part in the related paper.[171]

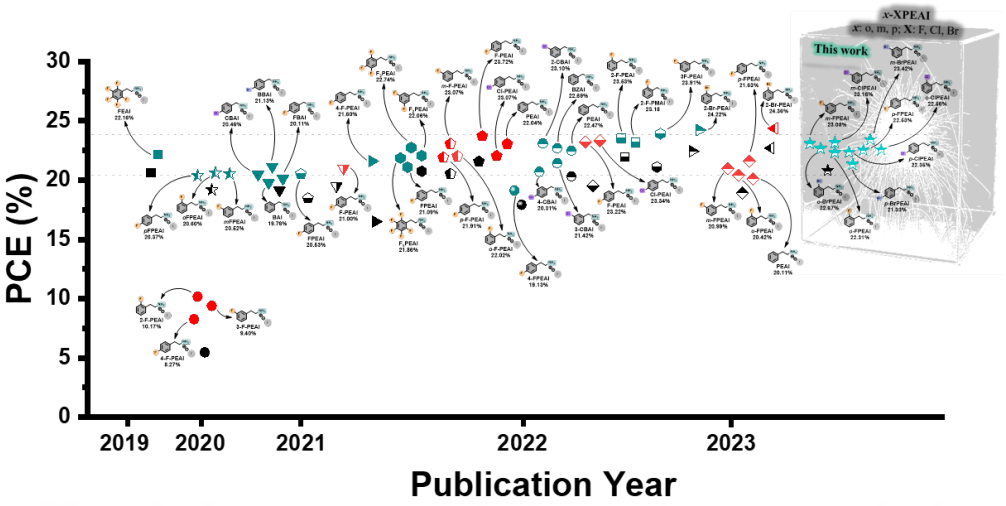



**Figure 2.1.** A comparison of halogen-containing phenylalkylammonium iodide salt-treated photovoltaic device efficiencies from various high-profile PSC papers from 2019 onwards. The related molecular structures are illustrated with their reported names and champion efficiencies. It should be noted that at various papers, different names are given to the same salts by publishers. To avoid confusion, each set of salt-treated PSC studies are demonstrated by different shapes. Also, three major colours are used to identify the device type (i.e., black colour identifies the control device; turquoise colour identifies 3D/2D PSCs; red colour identifies the direct passivation on 3D PSCs. All corresponding device architectures, stability details and references are additionally given in Table S5. Note: to avoid confusion, the same structured salts were identified by the same style (***x*-XPA*AI**; ***x***: *o, m, p*; **X**: F, Cl, Br; **P**: phenyl; **A***: alkyl chain either methyl or ethyl; **A**: ammonium; **I**: iodide) in the Table 1.1 rather than original names given in Figure 2.1 (i.e., **PMAI**: BAI, BZAI; ***o*-FPMAI**: 2-F-PMAI; ***p*-FPMAI**: FBAI; ***p*-ClPMAI**: CBAI; ***o*-ClPMAI**: 2-CBAI; ***m*-ClPMAI**: 3-CBAI; ***p*-ClPMAI**: 4-CBAI, ***p*-BrPMAI**: BBAI; ***o*-FPEAI**: 2-FPEAI, oFPEAI, o-F-PEAI; ***m*-FPEAI**: 3-F-PEAI, mFPEAI, m-F-PEAI, 3F-PEAI; ***p*-FPEAI**: 4-F-PEAI, pFPEAI, p-F-PEAI, FPEAI, F-PEAI, 4-FPEAI, ***p*-ClPEAI**: Cl-PEAI; ***o*-BrPEAI**: 2-Br-PEAI; **F$_5$PEAI**: FEAI).

Despite the large number of studies exploring the effect of **PEAI**-type salts on the performance of PSCs in the literature, detailed systematic analysis and a fundamental understanding of the nature (electronic effects), the size, and the position (steric effects) of the substituents of 2D-perovskite-forming salts on the performance of 3D/2D PSCs is lacking.[172] We recently demonstrated the positional effect of methoxy (-OMe) substituents on the orientation of 2D-forming **PEAI** salts (***x*-OMe-PEAI** salts) on 3D/2D perovskite films.[173] In the present work, a series of bulky organic

cations based on the **PEA** framework with 3 different halogens (F, Cl, and Br) that vary significantly in their size and electronegativity were realized. For all halogens, the substituent position also varied (*o*, *m*, and *p*) on the aromatic ring, yielding nine different ***x*-XPEAI** salts toward understanding the effects of electronic and steric on the performance of resulting 3D/2D PSCs. The salts were deposited on the surface of CsFAMA-based 3D triple cation perovskites, and we successfully demonstrated the formation of 2D perovskite layers for all nine salts via XRD and GIWAXS analyses. Photoluminescence (PL) and time-resolved photoluminescence (TRPL) spectroscopy results showed that a 2D perovskite layer based on ***m*-XPEA$_2$PbI$_4$** suppresses nonradiative carrier recombination more effectively than both its *ortho* or *para*-analogues and the untreated reference. Among these nine different 2D perovskites, ***m*-XPEA$_2$PbI$_4$** had higher interfacial dipoles and lower formation energies on the 3D perovskite surface, as demonstrated by detailed DFT analyses. While halogen substitution at the meta-position of the phenyl ring of 2D PEAI salts results in higher $V_{OC}$ (1.13 V) and FF (over 81%), furnishing an enhanced PCE exceeding 23% the identity of the halogen showed a limited effect. Hence, regarding halogen substitution in **PEAI**-based salts, we demonstrated that steric effects, which dictated the orientation and thus the surface dipole, are the basis for the enhanced performance. For clarity, data related to meta-substituted **PEAI**-based salts are shared together in the main text, and data of *ortho* and *para*-substituted counterparts are given separately.

### 2.1.2 Experimental

#### 2.1.2.1 Materials

Titanium dioxide paste (30NR-D), formamidinium iodide (FAI), and methylammonium bromide (MABr) were purchased from Greatcell Solar. Lead iodide ($PbI_2$) was purchased from Tokyo Chemical Company (TCI). Titanium diisopropoxide bis-(acetylacetonate) solution (75% in IPA), *spiro*-OMeTAD,

bis(trifluoromethane)sulfonimide lithium salt (Li-TFSI), 4-tert-butylpyridine (*t*-BP), and chlorobenzene (CB) were provided from Sigma Aldrich. Isopropyl alcohol (IPA, 99.8%), $SnCl_4$ aqueous (99%), dimethylformamide (DMF, 99.9%), and dimethyl sulfoxide (DMSO, 99.9%) were purchased from Acros Organics.

#### 2.1.2.2 Solar Cell Fabrication

The FTO glass substrates (TEC9AX) were cleaned with detergent, deionized water, acetone, and isopropanol by ultrasonication for 10 min, respectively. The cleaning procedure was followed by the UV-ozone treatment of substrates for 10 min. The compact $TiO_2$ (*cp*-$TiO_2$) was deposited onto the clean FTO substrates by spray pyrolysis using a titanium diisopropoxide bis-(acetylacetonate) solution diluted in IPA at 1:15 volume ratio on 450 °C and followed by in situ annealing for 30 min. The mesoporous $TiO_2$ (*mp*-$TiO_2$) solution was composed of 1 g of $TiO_2$ paste diluted in 10 mL of anhydrous ethanol solution; then, the *mp*-$TiO_2$ layer was deposited onto the FTO/*cp*-$TiO_2$ substrate by a one-step spin-coating process at 4500 rpm for 20 s. After annealing at 125 °C for 30 min, the *mp*-$TiO_2$ films were gradually heated to 500 °C in air, and then, they were baked at the same temperature for 20 min to remove organic components. $SnO_2$ layers were prepared by spin coating 0.1 M $SnCl_4$ aqueous solution by a one-step process at 3000 rpm for 20 s; then, the substrates were transferred onto a hot plate and heated between 150 and 190 °C for 1 h. Before use, the FTO/*cp*-$TiO_2$/*mp*-$TiO_2$/$SnO_2$ substrates were treated with UV/ozone for 30 min. The precursor solution was prepared by dissolving $PbI_2$ (1.35 M), CsI (0.05 M), FAI (1.12 M) MABr (0.05 M), and MACl (0.10 M) in a mixed solvent of DMF: DMSO (4:1, volume ratio). Then, 25 µL perovskite precursors were coated onto the FTO/*cp*-$TiO_2$/*mp*-$TiO_2$/$SnO_2$ substrates (around 1.4 cm × 2.4 cm) by spin-coating; the procedure was performed through a two-step program running at 1000 and 4000 rpm for 12 and 25 s, respectively. During the second step, 750 µL of CB as an anti-solvent was dropped quickly onto the center of the substrates after 11 s into the second step was dispensed. Afterward, the films were transferred to a 100 °C annealing plate and left for 45 min to allow optimum crystallization. After cooling

to room temperature, a solution of ***x*-XPEAI** diluted in IPA (10 mg/1 mL) was spin-coated on the substrate at 4000 rpm for 15 s. Then, The HTM solution was prepared by mixing a stock solution of *spiro*-OMeTAD in CB with solutions of *t*-BP, Li-TFSI, and Co(*t*-BuPyPz)$_3$(TFSI)$_3$ (FK209, Dyesol) in acetonitrile with a molar ratio of *spiro*-OMeTAD: FK209:Li(TFSI):*t*-BP at 1:0.03:0.5:3.3. 40 µL of the *spiro*-OMeTAD solution was deposited at 4000 rpm for 20 s on the perovskite film as the hole-transport layer. Finally, a 70 nm-thick Au layer was thermally evaporated as a counter electrode to complete the device fabrication.

#### 2.1.2.3 Film Cell Characterization

The morphology and particle size of obtained samples were investigated by using a scanning electron microscope (SEM: FEI Sirion-200). 1D XRD analysis was carried out (D8 Advance diffractometer, Bruker) with Cu Kα radiation by measuring the diffraction angle (2θ) from 3° to 60°. GIWAXS patterns represented in reciprocal lattice space were conducted at beamline BL46XU of SPring-8. The sample was irradiated with an X-ray energy of 12.39 keV ($\lambda$ = 1 Å) at a fixed incident angle on the order of 0.12°, 0.4° and 2.0° through a Huber diffractometer. The GIWAXS patterns were recorded with a 2D image detector (Pilatus 300 K).

PL spectroscopy measurements (PerkinElmer LS 55) were carried out from the film side with an excitation wavelength of 450 nm. TRPL spectroscopy analysis (HORIBA) was performed using a Fluorolog TCSPC with an excitation wavelength of 640 nm. The carrier lifetime was calculated by using the following **Equation 1.1** with a biexponential decay function:

$$R(t) = A1e^{\frac{-t}{\tau 1}} + A2e^{\frac{-t}{\tau 2}} \qquad \textbf{Equation 1.1}$$

UV–vis absorption spectra (PerkinElmer) were obtained using a lambda 950S with an integrating sphere.

#### 2.1.2.4 Computational Details

Density functional theory (DFT) with Perdew–Burke–Ernzerhof (PBE)[174] density functional along with Grimme's D3 dispersion correction[175] was used to model the interfaces of $FAPbI_3$and $(\boldsymbol{x}\textbf{-XPEA})_2PbI_4$, where X stands for F, Cl, Br, and *x* for *ortho*, *meta*, *para*, fully relaxing both atomic positions and cell parameters. The wavefunctions were described using the DZVP-MOLOPT[176] basis set, while the charge density was expanded in the auxiliary plane wave basis set with the 600 Ry cutoff. Core region and core-valence interactions were described with the Goedecker-Teter-Hutter (GHT) pseudopotentials.[177] The first Brillouin zone was sampled in the Γ-point. The interaction between $\boldsymbol{x}\textbf{-XPEA}^+$ cations and perovskite surfaces were assessed using Born-Oppenheimer molecular dynamics (BOMD) simulations with 1 fs timestep and the constant temperature of 343 K maintained using the velocity rescaling algorithm. All the simulations were accomplished with the CP2K code.[178] The structures are visualized using VESTA[179] and VMD[180] software.

#### 2.1.2.5 Solar Cell Characterization

Solar cell measurements were performed using an Oriel solar simulator (450 W xenon, AAA class) and a Keithley model 2400 digital source meter at room temperature. The light intensity was calibrated, and the solar cells' current density-voltage (*J–V*) characteristics were obtained under the same conditions reported in the previous work. The active areas of solar cells were masked with a metal aperture of 0.09 $cm^2$ to reduce the influence of the scattered light. The voltage scan rate was 100 mV $s^{-1}$ with no device preconditioning. The EQEs were measured with an IQE 200B (Oriel) for devices without bias light. The long-term stability test was performed as maximum power tracking under 100 mW $cm^{-2}$ illumination with a LED power source, encapsulating samples in a measurement box purged with nitrogen gas kept at 25 °C by a cooling system.

### 2.1.3 Results and Discussion

The *o*-, *m*-, and *p*-halogenated phenylethylammonium cations (***x*-XPEA**$^{+}$) were synthesized by a robust and facile method in good yields (>80% over three steps), and the details are given in the supporting information part in the related paper and Ph.D. thesis of Dr. Aliekber Karabag.[171,181] For all device architectures, the $[(Cs_{0.04}FA_{0.85}MA_{0.11})Pb(I_{0.96}Br_{0.01}Cl_{0.03})_3]$-based triple cation 3D perovskite composite was utilized and deposited via the traditional spin coating method. The synthesized ***x*-XPEAI** salts were individually coated on top of the 3D perovskite to construct 3D/2D hybrid structures using the same process. The chemical structures of each ***x*-XPEAI**-based salt are represented in **Figure 2.2.a**.

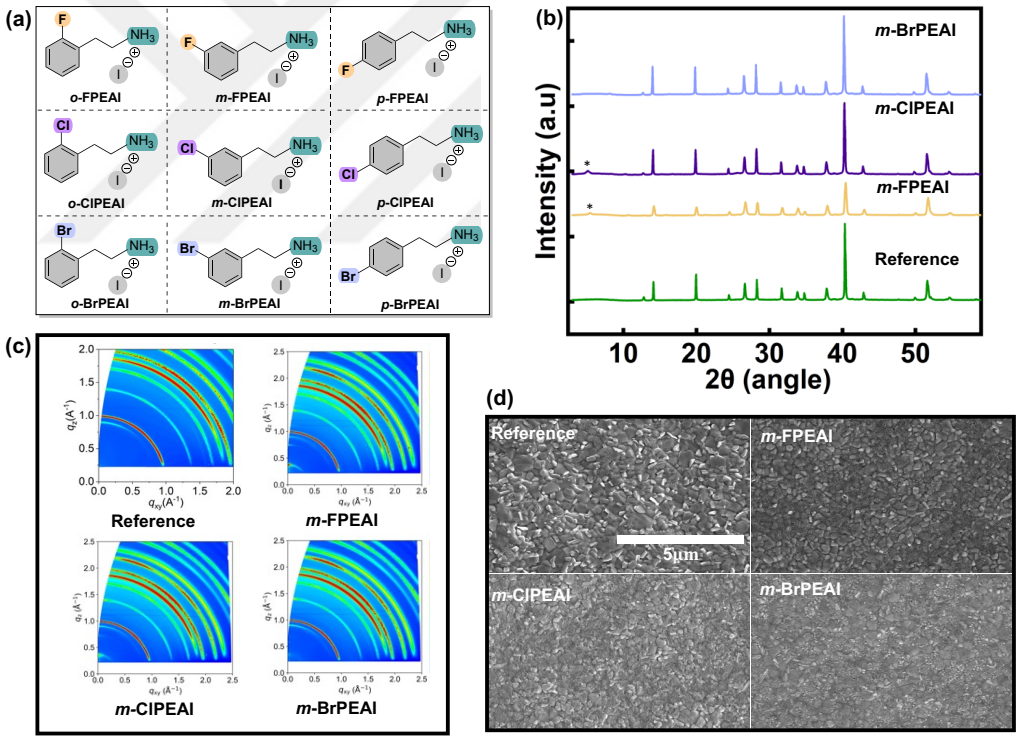



**Figure 2.2. a)** Structures of the nine different halogenated PEAI salts synthesized and used in this study; **b)** XRD patterns of ***m*-XPEAI**-treated perovskite films; **c)** GIWAXS images (with 2.0° incident angle); and **d)** SEM images of the reference and *meta*-substituted salt-treated 3D perovskite films.

XRD diffraction patterns of the ***m*-XPEAI** salt-treated 3D perovskites are shown in **Figure 2.2.b**, as well as the untreated 3D perovskite as a reference. XRD peaks lower than 10° ($2\theta$) are typically assigned to 2D perovskite crystals.[182] The observed 2D peaks are located at 5.13° and 5.40°, indicating the formation of the {002} plane of the 2D (n = 1) films[154,183,184] for ***m*-ClPEAI** and ***m*-FPEAI**, respectively, which are consistent with XRD peaks of the pure 2D (n = 1) material (5.16° and 5.33° for ***m*-ClPEAI** and ***m*-FPEAI**, respectively; (**Figure 2.3**).

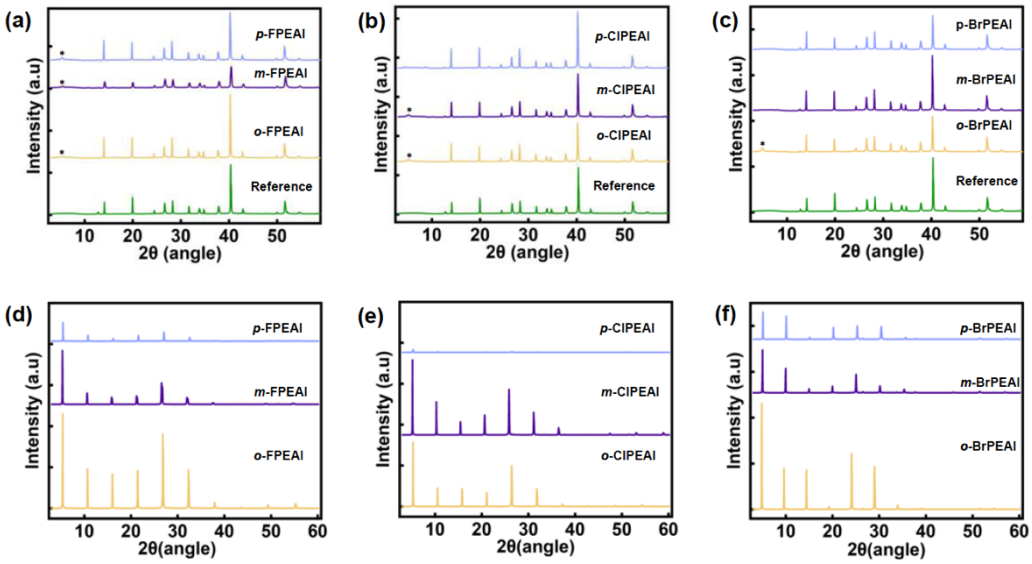



**Figure 2.3.** Reference and 3D/2D XRD spectra of perovskite films treated with **(a)** ***x*-FPEAI**, **(b)** ***x*-ClPEAI**, and **(c)** ***x*-BrPEAI**; Pure 2D (n = 1) **(d)** (***x*-FPEA**)$_2$PbI$_4$, **(e)** (***x*-ClPEA**)$_2$PbI$_4$, and **(f)** (***x*-BrPEA**)$_2$PbI$_4$ films.

The 3D perovskite film (reference) has a $PbI_2$ peak around 12.6°, almost disappearing after ***m*-XPEAI** salts treatment. This suggests that the organic ammonium salts react with excess $PbI_2$ on the surface of 3D perovskite to form a 2D layer.[185] GIWAXS measurements were performed to investigate the orientation of the 2D films on the 3D perovskite with three different incident angles: 0.12°, 0.4°, and 2.0° (**Figures 2.4–2.6**).

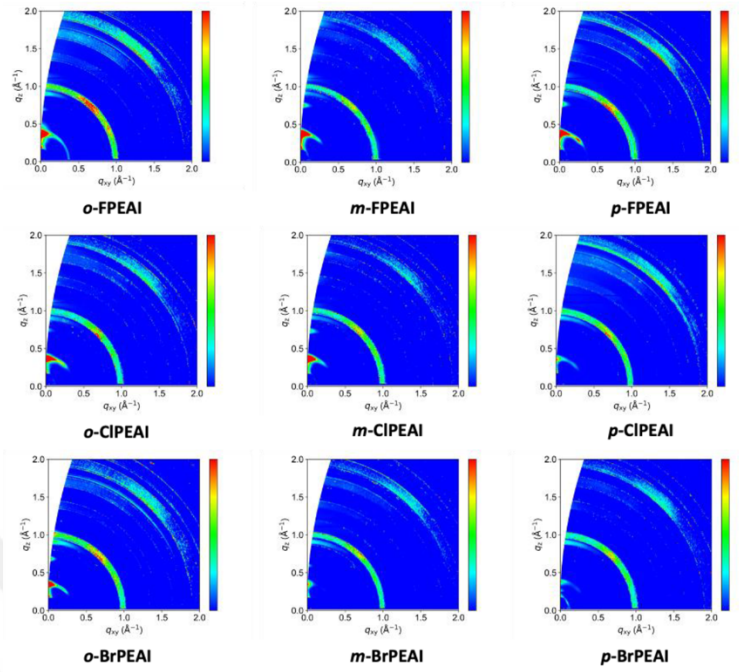



**Figure 2.4.** GIWAXS images of 3D/2D films with 0.12° incident angle.

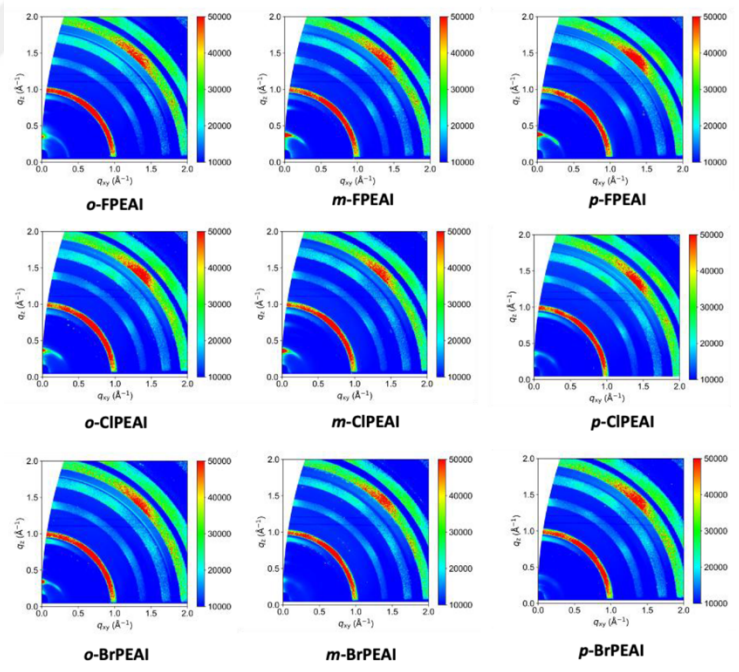



**Figure 2.5.** GIWAXS images of 3D/2D films with 0.4° incident angle.

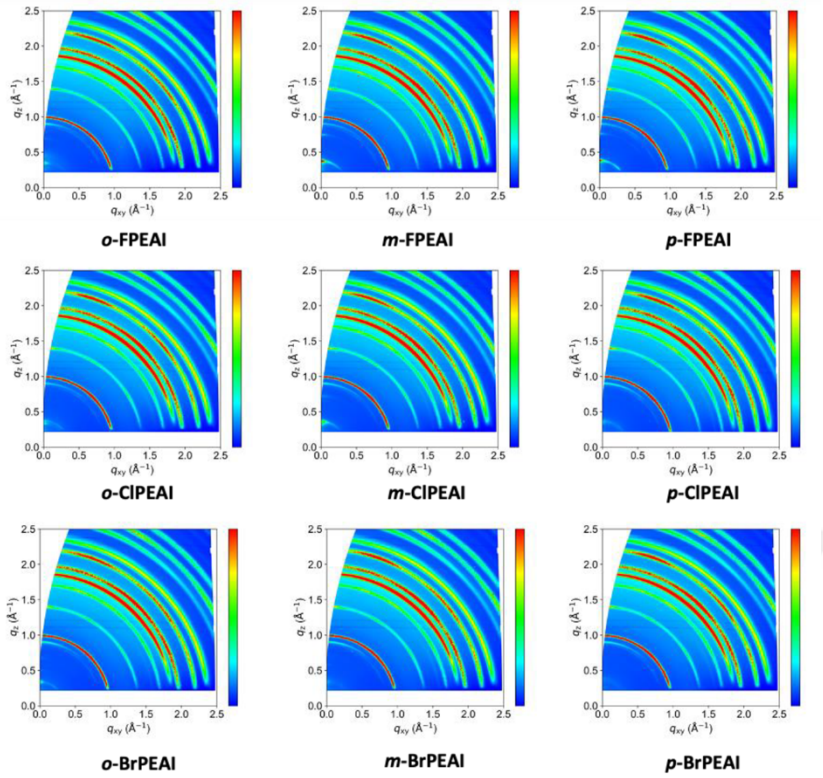



**Figure 2.6.** GIWAXS images of 3D/2D films with 2.0° incident angle.

GIWAXS images, performed with an incident angle of 2.0° for the ***m*-XPEAI**-doped 2D films and the reference, are shown in **Figure 2.2.c**. The corresponding Debye-Scherrer rings at $q_z$ = 1.0 Å$^{-1}$ and $q_z$ = 0.9 Å$^{-1}$ represent the preferential orientation for the {110} crystal plane of 3D perovskite and {001} crystal plane of $PbI_2$, respectively.[186,187] For all the GIWAXS films, there is a decrease in the $PbI_2$ peak at {001} crystal plane with the inclusion of halogenated salts, which indicates the reaction of $PbI_2$ with **PEAI** salts.[188] As a result, a new spot appears below $q_z$ = 0.5 Å$^{-1}$ for all the salt-treated films, which refers to the formation of the 2D perovskite layer. The Bragg spots in a low incident angle measurement (0.12°), which is more surface sensitive, show strong preferential orientation for the nine 2D films on the surface where the 2D perovskite films are oriented parallel to the substrate (**Figure 2.4-2.6**).[189] As the incident angle increases, 2D perovskite Debye-Scherrer rings weaken, and the rings related to 3D perovskite films with a random orientation

become more apparent, proving that the 2D films are formed on the surface of the 3D film.[190,191]

Top-view SEM studies were performed to investigate the morphology of the perovskite films, with and without the addition of halogenated **PEAI** salts (**Figure 2.2.d**; **Figure 2.7**).

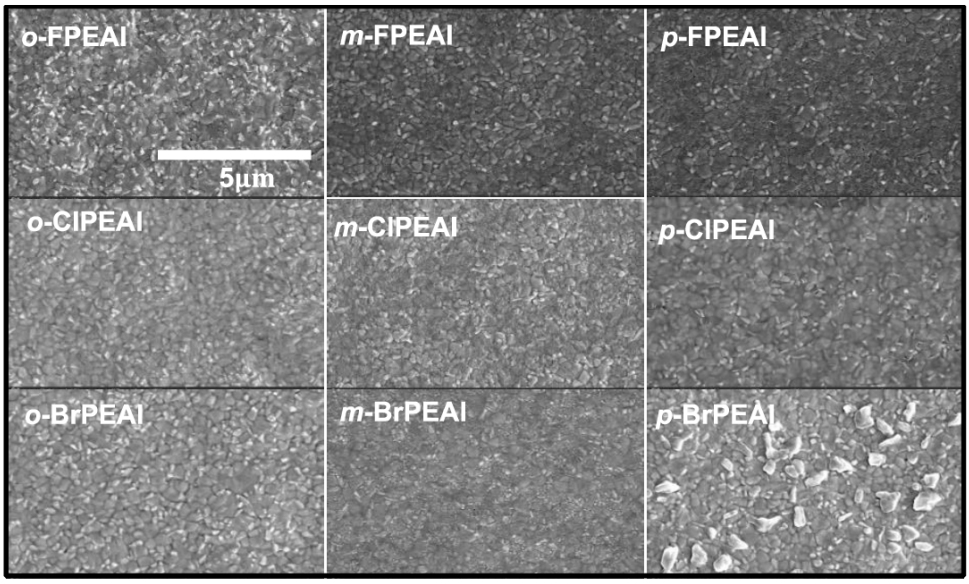



**Figure 2.7.** Top-view SEM images of the 3D/2D PSCs treated with ***x*-XPEAI** salts.

As shown in **Figure 2.2.d**, the reference film displays significant white contrast at the grain boundaries, which is generally attributed to excess $PbI_2$ on 3D perovskite films.[192–194] After treatment with *meta*-halogenated **PEAI** salts, the white $PbI_2$ flakes decrease on the films, which further proves the reaction between the $PbI_2$ and ammonium salts.[195] Cross-section SEM images of all 3D/2D films are given in **Figure 2.8**.

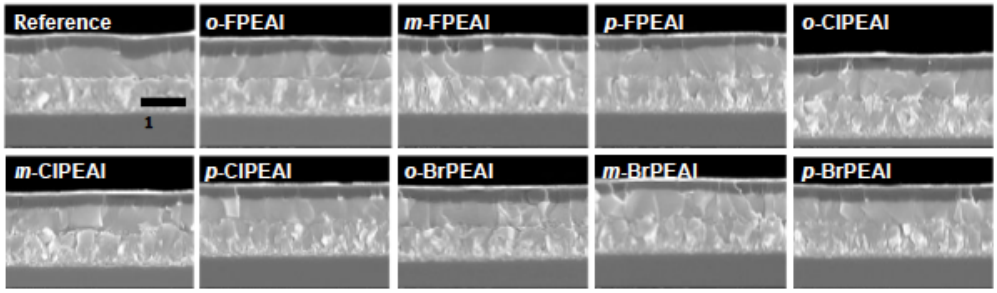



**Figure 2.8.** Cross-sectional SEM images of the 3D/2D PSCs treated with ***x*-XPEAI** salts.

Due to their extremely thin nature, 2D films are not visible on top of 3D perovskite films.[196] Atomic force microscopy (AFM) images of 3D and 3D/2D films are shown in **Figure 2.9**. The formation of all the 2D layers results in smoother surfaces than the reference film, as given by the lower root mean square (RMS) values of the films generated from the addition of the *meta*-halogenated ammonium salts, ***m*-FPEAI**, ***m*-ClPEAI**, and ***m*-BrPEAI**, are 18.18, 23.97, and 15.54 nm, respectively. In contrast, the RMS value for the reference film is 46.13 nm.

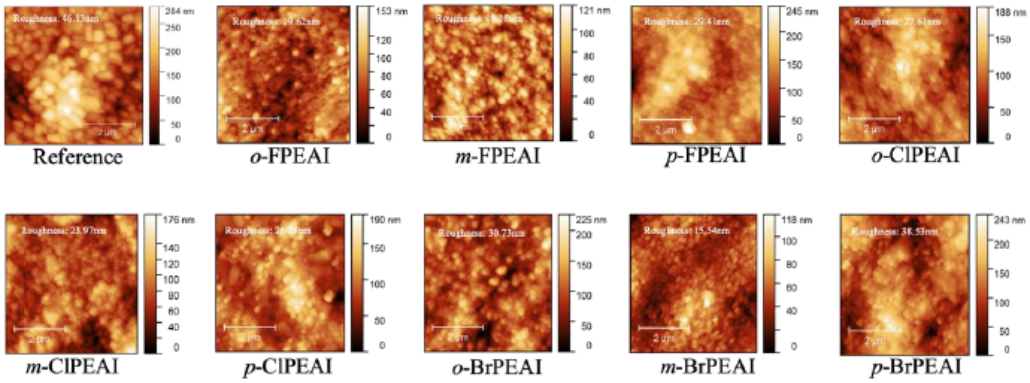



**Figure 2.9.** Atomic force microscopy images of the 3D reference and *x*-XPEAI-treated 2D films.

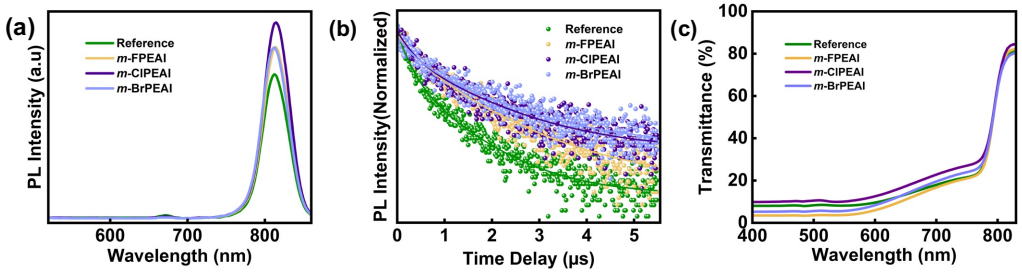



**Figure 2.10. a)** Steady-state photoluminescence spectra; **b)** Time-resolved PL traces; **c)** Transmission spectra of reference and meta-halogenated **PEAI** salt-treated 3D perovskite films.

The optical properties of the reference film and ***x*-XPEAI**-treated perovskite films were investigated by PL, TRPL, and Transmission spectroscopy (**Figure 2.10**). PL measurements were performed using a 450 nm excitation from the film side. The greater PL intensity of the 2D treated 3D films at 812 nm was observed compared to the reference film, commonly associated with decreased nonradiative recombination.[197] There is no PL emission from 2D perovskites at shorter wavelengths due to the low concentration of 2D precursor solutions; thus, highly thin films are produced in the process (**Figure 2.10.a**).[198] In correlation, the PL spectra of all the salt-treated films are shown in **Figure 2.11**, among which the *meta* positions have the most enhanced PL intensity of all halogen substituents. This demonstrates that suppression of nonradiative carrier recombination is superior in *meta*-substituted **XPEAI** derivatives.

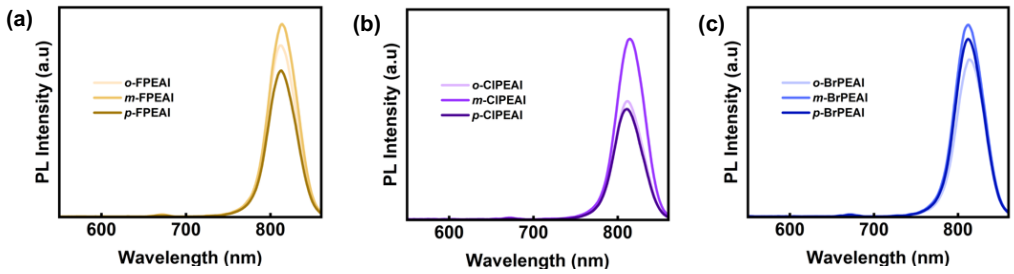



**Figure 2.11.** PL spectra of 3D/2D films treated with **(a) *x*-FPEAI**, **(b) *x*-ClPEAI**, and **(c) *x*-BrPEAI**.

The 3D/2D perovskite film's average carrier lifetime is significantly longer than the reference device, as shown by the TRPL spectra (**Figure 2.10.b**). It is envisioned that 2D perovskite films reduce defect density, thereby decreasing nonradiative recombination. The carrier lifetimes are calculated from the TRPL spectra, and data are given in **Table 2.1**. All the halogenated salts treated perovskites have longer carrier lifetimes than the reference film, confirming the suppressed nonradiative recombination and enhanced defect passivation, thereby increasing $V_{OC}$.[199]

**Table 2.1.** Fitting parameters of TRPL spectra of reference and ***x*-XPEAI**-treated films, $A1$ and $A2$ are the fractions of the two decay processes, and $\tau_1$ and $\tau_2$ are shorter and longer lifetimes, respectively.

| | $A_1$ | $\tau_1$ | $A_2$ | $\tau_2$ | $R^2$ |
|---|---|---|---|---|---|
| *Reference* | 0.503 | 232.60 | 0.398 | 1129.6 | 0.972 |
| *o-FPEAI* | 0.362 | 463.26 | 0.496 | 1641.9 | 0.963 |
| *m-FPEAI* | 0.318 | 442.34 | 0.531 | 1683.8 | 0.962 |
| *p-FPEAI* | 0.399 | 212.35 | 0.515 | 1232.0 | 0.976 |
| *o-ClPEAI* | 0.386 | 332.27 | 0.475 | 1389.4 | 0.973 |
| *m-ClPEAI* | 0.349 | 306.67 | 0.492 | 1667.2 | 0.930 |
| *p-ClPEAI* | 0.419 | 351.38 | 0.493 | 1244.3 | 0.982 |
| *o-BrPEAI* | 0.383 | 447.19 | 0.461 | 1620.8 | 0.971 |
| *m-BrPEAI* | 0.282 | 345.08 | 0.492 | 1794.2 | 0.923 |
| *p-BrPEAI* | 0.539 | 261.45 | 0.379 | 1199.4 | 0.975 |

Among these nine salts, the *meta*-halogenated derivatives show longer lifetimes than their ortho and para counterparts. The transmission data demonstrate that placing a 2D layer on top of the 3D perovskite does not affect the transmittance of the 3D/2D hybrid structure (**Figure 2.10.c**; **Figure 2.12**).

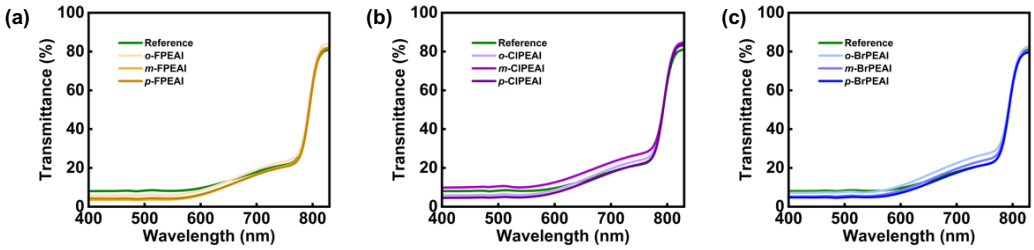



**Figure 2.12.** Transmission spectra of 3D/2D films treated with **(a) *x*-FPEAI**, **(b) *x*-ClPEAI**, and **(c) *x*-BrPEAI**.

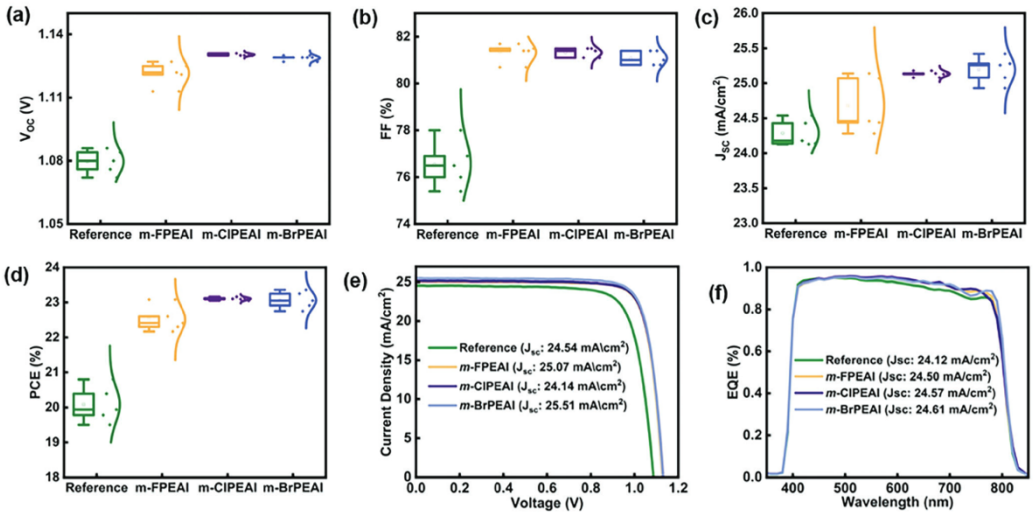



**Figure 2.13. a–d)** Statistics of reference and 3D/2D films; **e)** *J–V* Curves of the pristine and halogenated **PEAI** treated devices simulated under 1 sun illumination; **f)** EQE spectra and calculated photocurrent values.

The PSCs with and without 2D layers were fabricated and characterized under 1 sun illumination. Remarkable improvements in $V_{OC}$ (in the absence of band gap change with the salt treatment) and FF (together with reduced series resistance) were observed in salt-treated 3D perovskite films, indicating superior surface passivation and enhanced hole extraction, respectively, as shown in **Figure 2.13**.[200,201] The increase in the $J_{SC}$ for salt-treated films (**Figure 2.13.c**) results in enhanced PCE (**Figure 2.13.d**), and the very thin 2D films do not increase absorption in 3D perovskite.

**Table 2.2.** PV parameters of 2D–3D PSCs with varying ***o*-XPEAI**, ***m*-XPEAI**, and ***p*-XPEAI** contents compared to the control device.

| | | $V_{OC}$ (V) | $J_{SC}$ (mA/cm$^2$) | FF (%) | PCE (%) | HI (%) |
|---|---|---|---|---|---|---|
| Ref | Best | 1.09 | 24.54 | 78.0 | **20.80** | **6.7** |
| | Average | 1.08 | 24.28 | 76.6 | **20.08** | |
| *o*-FPEAI | Best | 1.12 | 25.07 | 79.7 | 22.31 | 3.9 |
| | Average | 1.12 | 24.88 | 80.2 | 22.28 | |
| *m*-FPEAI | Best | 1.13 | 25.07 | 81.7 | **23.08** | **3.8** |
| | Average | 1.12 | 24.68 | 81.3 | **22.51** | |
| *p*-FPEAI | Best | 1.13 | 24.50 | 81.6 | 22.53 | 6.3 |
| | Average | 1.10 | 24.38 | 80.7 | 21.66 | |
| *o*-ClPEAI | Best | 1.13 | 24.78 | 80.1 | 22.56 | 5.1 |
| | Average | 1.13 | 24.70 | 80.7 | 22.44 | |
| *m*-ClPEAI | Best | 1.13 | 25.14 | 81.5 | **23.16** | **5.0** |
| | Average | 1.13 | 25.13 | 81.3 | **23.10** | |
| *p*-ClPEAI | Best | 1.12 | 24.84 | 80.4 | 22.35 | 4.9 |
| | Average | 1.12 | 24.74 | 80.2 | 22.20 | |
| *o*-BrPEAI | Best | 1.13 | 24.71 | 81.2 | 22.67 | 5.0 |
| | Average | 1.13 | 24.57 | 81.3 | 22.55 | |
| *m*-BrPEAI | Best | 1.13 | 25.51 | 81.2 | **23.42** | **5.3** |
| | Average | 1.13 | 25.19 | 81.1 | **23.06** | |
| *p*-BrPEAI | Best | 1.11 | 24.23 | 79.1 | 21.33 | 5.2 |
| | Average | 1.11 | 24.24 | 78.4 | 21.10 | |

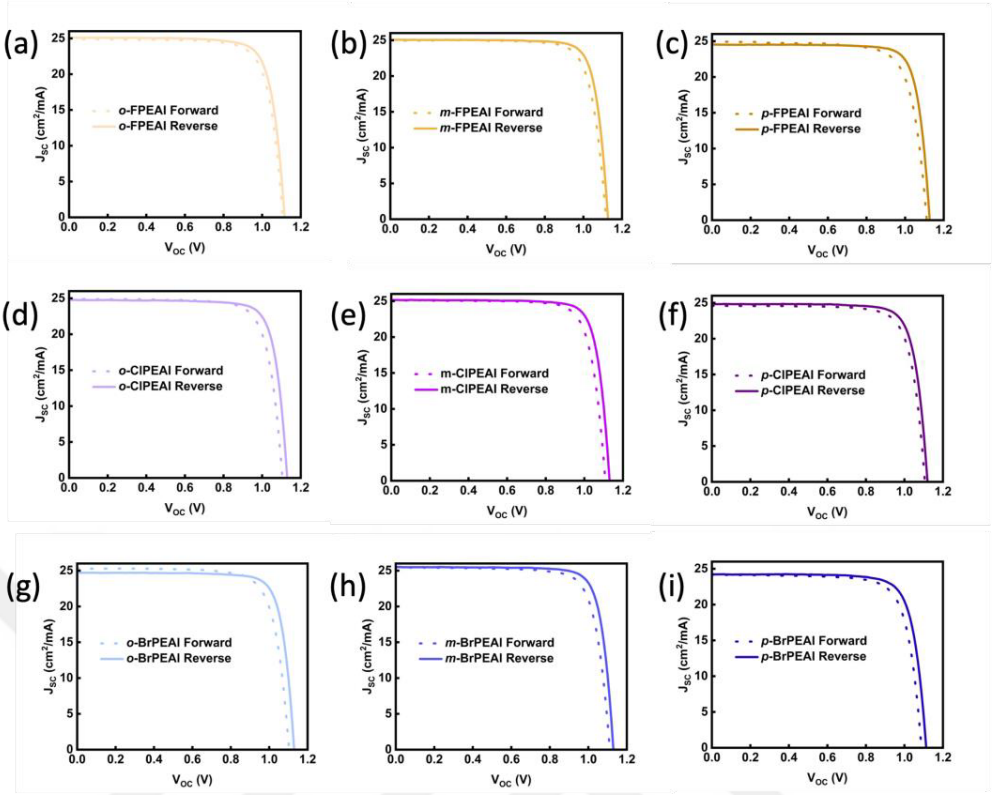



**Figure 2.14.** Reverse and forward scans of halogenated-salt-treated champion solar cells.

**Table 2.2** and **Figure 2.14** outline the detailed device parameters for all salts. 2D passivated films show lower hysteresis than the reference film, indicating reduced ion migration and enhanced charge extraction.[202–205] The reference 3D device showed a maximum PCE of 20.80%, with a $V_{OC}$ of 1.09 V, a $J_{SC}$ of 24.54 mAcm$^{-2}$, and an FF of 79.7% lower in all cases compared to the 3D/2D counterparts. Introducing 2D layers on top of 3D perovskite films significantly improves the device performance. The average $V_{OC}$ for the 3D/2D PSCs is around 1.13 V, which implies that the formation of 2D layers by ***x*-XPEAI** salts effectively passivates the recombination centers.[206] Better device parameters are observed by inserting the ***m*-XPEAI** 2D layer (PCE: >23%), consistent with PL and TRPL studies. The integrated $J_{SC}$ from the external quantum efficiency (EQE) measurements align with the current density-voltage (*J–V*) curve in **Figure 2.13.e-f**.

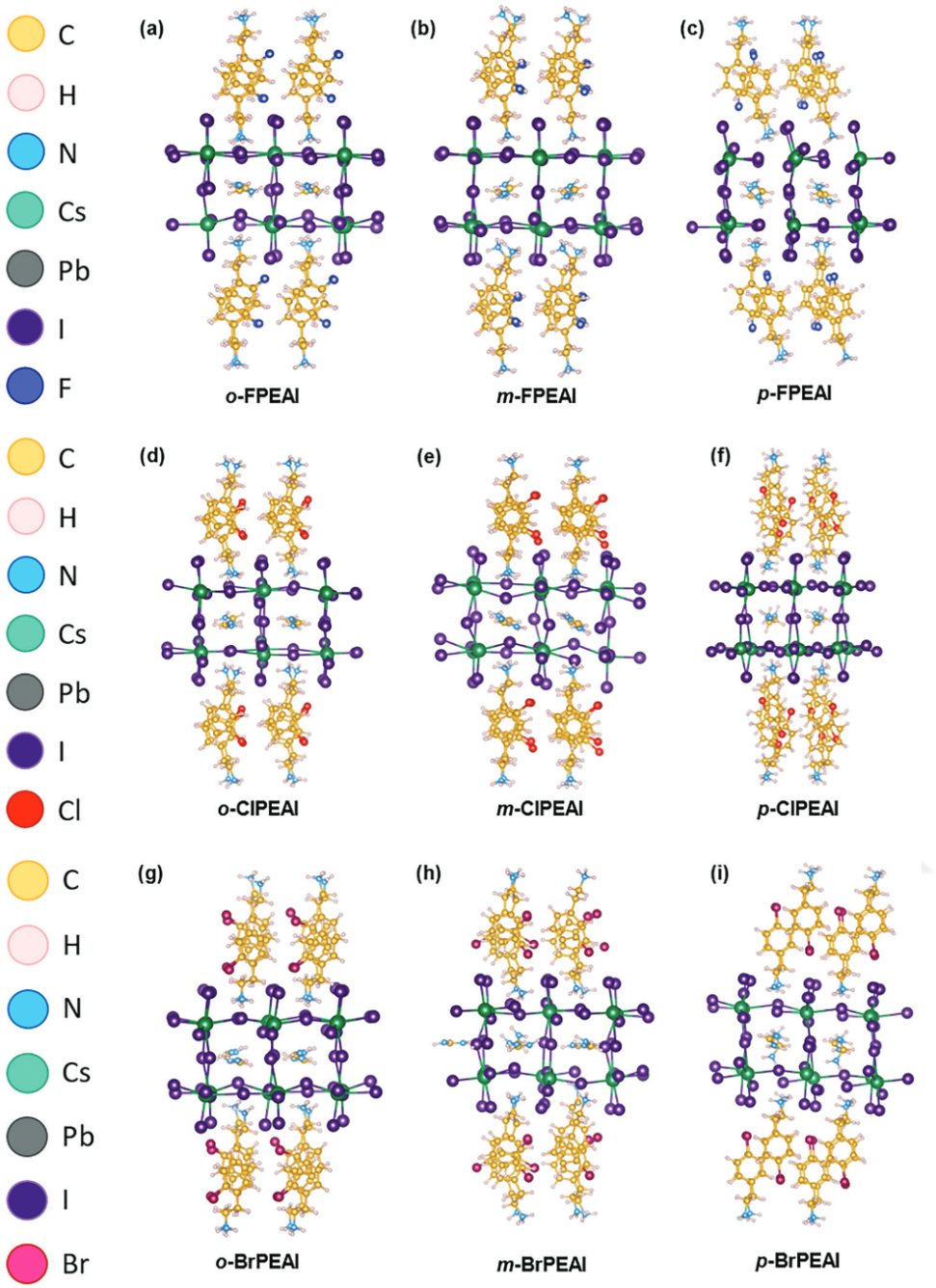



**Figure 2.15.** Theoretical modelling of all the halogenated salts at three different positions by DFT analysis.

**Figure 2.15.** shows the optimized structures for the 2D cations on the 3D perovskite surface. The formation energies of the **(*x*-XPEA)$_2$PbI$_4$** layers are calculated by DFT calculations (**Table 2.3**). It is shown that the formation energy of **(*m*-FPEA)$_2$PbI$_4$**, **(*m*-ClPEA)$_2$PbI$_4$**, and **(*m*-BrPEA)$_2$PbI$_4$** on 3D perovskite films is lower than the

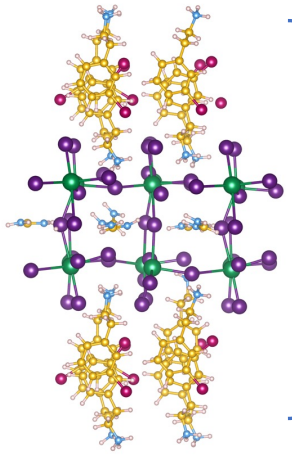
2D perovskites formed from *ortho* or *para*-substituted **XPEAI** salts. This lower formation energy correlates with the observed high device performances with ***m*-XPEAI** salts. With more favorable formation energy, forming large domains that result in a more compact film is relatively easier.[206]

**Table 2.3.** Formation energies of **(*x*-XPEA)$_2$PbI$_4$** 2D films on 3D perovskite layer.

| Cation type | $\Delta_f E$, eV |
|---|---|
| (***o*-FPEA**)$_2$PbI$_4$ | -9.06 |
| (***m*-FPEA**)$_2$PbI$_4$ | -9.22 |
| (***p*-FPEA**)$_2$PbI$_4$ | -9.02 |
| (***o*-ClPEA**)$_2$PbI$_4$ | -9.15 |
| (***m*-ClPEA**)$_2$PbI$_4$ | -9.39 |
| (***p*-ClPEA**)$_2$PbI$_4$ | -9.55 |
| (***o*-BrPEA**)$_2$PbI$_4$ | -9.19 |
| (***m*-BrPEA**)$_2$PbI$_4$ | -9.50 |
| (***p*-BrPEA**)$_2$PbI$_4$ | -9.44 |

The interfacial dipole of the 3D/2D interface is determined using DFT calculations, and the 3D layer treated with 2D **(*m*-XPEA)$_2$PbI$_4$** perovskite forms a surface with a higher interfacial dipole (**Table 2.4**). This result is consistent with our device performance data, indicating that higher interfacial dipole implies better hole extraction from perovskite to hole transport layer.[163]

**Table 2.4.** Interfacial Dipole values of the entire interface between the $FAPbI_3$ perovskite and 2D **(*x*-XPEA)$_2$PbI$_4$** perovskite.



| Structure | Interfacial dipole |
|---|---|
| *o*-FPEAI | 21.29505 |
| p-FPEAI | 20.95391 |
| ***m*-FPEAI** | **31.34773** |
| *o*-ClPEAI | 10.48717 |
| p-ClPEAI | 24.74725 |
| ***m*-ClPEAI** | **29.98106** |
| *o*-BrPEAI | 22.37343 |
| p-BrPEAI | 32.33824 |
| ***m*-BrPEAI** | **41.47651** |

The position of halogen atoms on the phenyl ring affects the strength of the $\sigma$-electron withdrawing inductive effect, the $\pi$-electron resonance, and the molecular dipole moment. The combination of the first two of these parameters can be estimated from the Hammett parameters, $\sigma_{meta}$ and $\sigma_{para}$, given in **Table 2.5**. These parameters are calculated from the effect of meta and para substituents on the *p*Ka of substituted benzoic acid, relative to the unsubstituted acid. The $\sigma_{meta}$ parameter indicates the electron-withdrawing power of the substituent, as no resonance structure adds (or removes) significant electron density onto the *ipso* carbon. The three halogen atoms display similar net inductive effects in the *meta* position. The $\sigma_{para}$ parameter, on the other hand, is affected by $\pi$ donation due to resonance, and this effect is much greater for F than Cl or Br. As the *ortho* position has similar resonance structures to the para position but with slightly stronger negative induction due to proximity, a theoretical "$\sigma_{ortho}$" parameter (which cannot be experimentally determined due to steric effects) would be expected to have slightly more positive values than $\sigma_{para}$. It can, therefore, be seen clearly that halogen substituents in the meta position are most strongly electron-withdrawing.

**Table 2.5.** Hammett parameters for halogen substituents[207]

| Halogen Substituent | $\sigma_{meta}$ | $\sigma_{para}$ |
|---|---|---|
| F | +0.34 | +0.06 |
| Cl | +0.37 | +0.23 |
| Br | +0.39 | +0.23 |

The molecular dipole increases from the *ortho* to *para* position on the phenyl ring. The combination of electron distribution and the molecular polarity from the dipole moment results in a better passivation effect of the **(*m*-XPEA)$_2$PbI$_4$** 2D layer.[166] Furthermore, there is another structural factor affecting the performance. The formation of a 2D perovskite layer with ***x*-XPEA$^+$** cations affects the structure of $PbI_2$ layers differently. *Ortho* and *para* substituents cause the $PbI_6$ octahedral network's highest disruption compared to *meta*-substituted **XPEA$^+$**. This disruption is expressed in the significant elongation of inter-octahedral connections in the ac plane for *ortho*-substituted analogues. The Pb–I bond breakage is observed in the ac and *bc* planes for *para*-substituted analogues. In the *meta*-substituted cases, the distribution of bonds is the most homogeneous, which should result in the best polaronic mobility and conductivity and, hence, higher PSC performance (**Figure 2.16** and **Figure 2.15**).

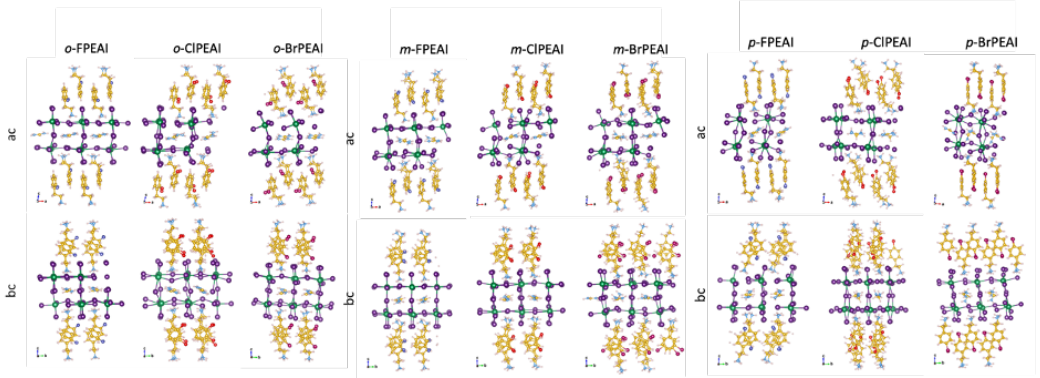



**Figure 2.16.** Optimized crystal structures of ***o*-XPEAI–FAPbI$_3$**, ***m*-XPEAI–FAPbI$_3$** and ***p*-XPEAI–FAPbI$_3$** interfaces: ac plane and bc plane views.

In addition to the static structural analysis, we have performed ab initio molecular dynamics simulations of the ***x*-XPEAI** cation behaviour on the FAI- and $PbI_2$ -terminated (001) surfaces of $FAPbI_3$ to unravel the possible interaction and passivation features as a function of organic cation structure and composition. Using this technique, it was observed that the ***m*-ClPEAI** cation has the most favorable configuration to interact through the halide atom with the surface, passivating under-coordinated $Pb^{2+}$ cations. This contrasts with the ***p*-ClPEAI** cation, which maintains a vertical orientation when interacting with both types of surfaces. As for the ***o*-ClPEAI** cation, the *ortho*-Cl hampers the bending of the molecule, which is responsible for the simultaneous halogen and amino-group interaction. The same scheme applies to all other ortho-substituted analogies. The resulting *meta*-passivation prevents the disruption of the Pb–I–Pb connection due to the migration of the I to the superficial position. In contrast, such migration is observed for the ***o*-BrPEAI**, ***o*-FPEAI**, and ***p*-BrPEAI**, resulting in a disconnection of the octahedral chains. ***p*-FPEAI** mainly interacts via $NH_3$ – groups with little interaction of the substituted benzene ring with the perovskite surface. These observations from ab initio molecular dynamics (MD) simulations correlate with the highest observed performance of the ***m*-ClPEAI** structures.

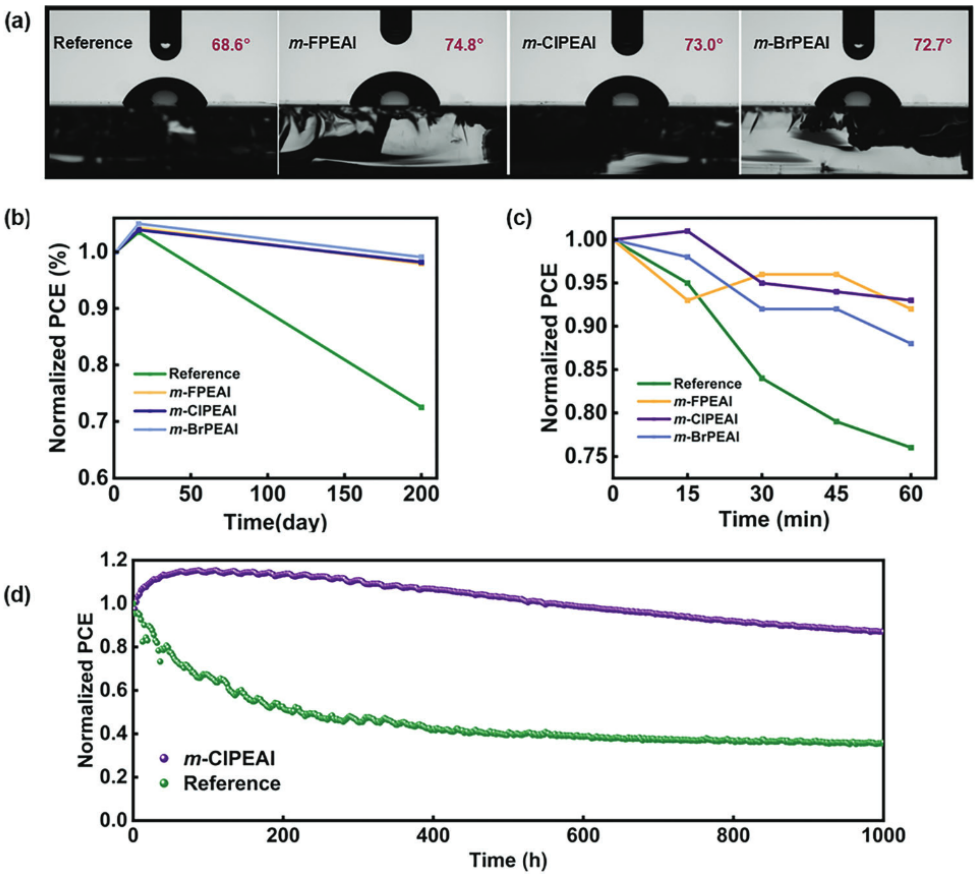



**Figure 2.17.** Comparison between the reference 3D perovskite and ***m*-XPEAI**-treated 3D/2D films on: **a)** contact angle of a surface water droplet; **b)** ambient air stability (RH > 20%, T = 20–25 °C); **c)** thermal stability (RH = 60–70%, T = 60 °C); and **d)** long-term stability of unencapsulated ***m*-ClPEAI**-treated and reference device at maximum power point (MPP) tracking under continuous 1-sun illumination and nitrogen atmosphere.

Contact angles of the reference and *meta*-halogenated salt-treated perovskite films with water are also measured, as shown in **Figure 2.17.a**. 3D/2D films exhibit more hydrophobic surfaces than the control 3D perovskite film due to the nature of the ***m*-XPEAI** salts, which are oriented so that the organic part of the molecule points away from the surface. An ambient air stability test was performed for all nine salt-treated and reference devices. Non-encapsulated devices were kept in a dry box with relative humidity (RH) of over 20% for 200 days at 20–25 °C (**Figure 2.17.b** and **Figure 2.18**).

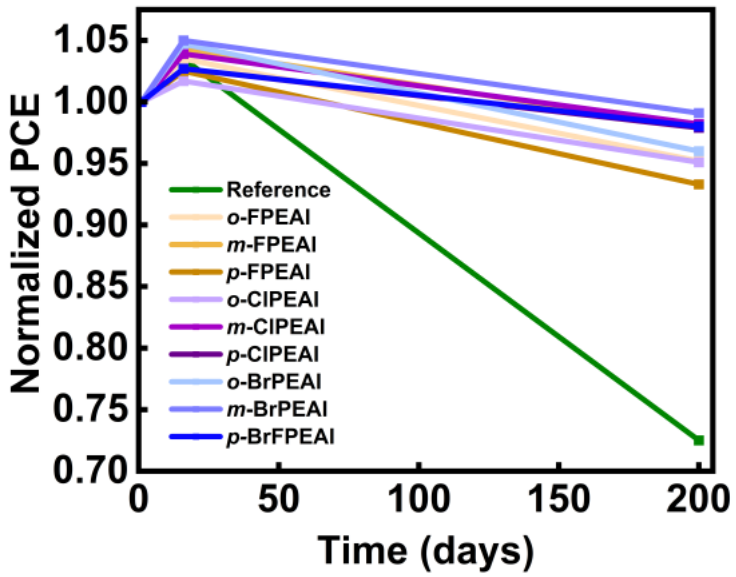



**Figure 2.18.** Ambient air stabilities for the reference and halogenated 3D/2D films.

The ***m*-XPEAI**-treated 3D/2D devices (**Figure 2.17.b**) showed superior ambient stability (average 98% of their original performances) compared to the control device (73% of its original performance). For the thermal stability test, non-encapsulated ***m*-XPEAI**-treated devices were kept in a glove box with an RH of 60–70% for 60 min at 60 °C (**Figure 2.17.c**). All 3D/2D devices containing only ***m*-XPEAI** salts (**Figure 2.17.c**) demonstrated greater thermal stability (average 91% of their original performances) compared to the control device (76% of its original performance). To get more reliable data, the photostability test under continuous 1-sun illumination was also conducted based on the overall best-performing **PEAI**-based salt (***m*-ClPEAI**) among the ***x*-XPEAI** family and the reference device (**Figure 2.17.d**). Both PSC devices were maintained in a nitrogen atmosphere under a constant illumination of 100 mW $cm^{-2}$. The current density-voltage (*J–V*) curves were recorded every 2 h. After 1000 hours of continuous illumination, the MPO (maximum power output) of the ***m*-ClPEAI**-treated device exhibited enhanced long-term stability (87% of its original performance) compared to the reference device (36% of its original performance). These results provide a clear perspective of the substantial benefit of

our passivation materials and pave the way toward the molecular design of functional passivation materials.

### 2.1.4 Conclusion

In conclusion, we introduced nine different halogenated **PEAI** salts, namely ***x*-XPEAI**, on 3D perovskite films. Three of these ***x*-XPEAI** salts (***o*-ClPEAI**, ***m*-ClPEAI**, and ***m*-BrPEAI**) had not previously been tested in PSCs. Our findings reveal that the *meta*-substituted salts ***m*-FPEAI**, ***m*-ClPEAI**, and ***m*-BrPEAI** significantly improved the PCE of the 3D/2D devices, surpassing 23%. DFT calculations demonstrate that the 2D **(*x*-XPEA)$_2$PbI$_4$** perovskites formed from *meta*-substituted ***m*-XPEAI** salts have a lower formation energy than their *ortho*- or *para*-substituted counterparts. PL spectroscopy indicates an enhanced $V_{OC}$ (1.13 V) and defect passivation on the 3D $FAPbI_3$ surface by adding a 2D **(*m*-XPEA)$_2$PbI$_4$** perovskite layer. Based on our results, the effect of the substitution position is more pronounced than the identity of the halogen in device performance. Due to the orientation of the organic cation, the 2D layer formed by PEAI salts on top of the 3D perovskite film provides a hydrophobic surface that significantly reduces moisture-induced degradation of the 3D perovskite layer. Among them, ***m*-XPEAI**-treated 3D films have superior thermal stability, surpassing the reference device. After 1000 h continuous light exposure, the ***m*-ClPEAI**-treated 3D perovskite devices showed excellent photostability. Considering all aspects of efficiency, stability, and reproducibility, the treatment with ***m*-ClPEAI** salt yielded the best performance in 3D/2D PSCs. Our study demonstrates the significant benefits of incorporating *meta*-substituted **PEAI** salts into 3D perovskite films, providing valuable insights for advancing perovskite-based solar cell technologies.

*The supporting information section, available at https://doi.org/10.1002/aenm.202302038, provides the synthetic details and methods involved in the device's manufacture.*

***This study is reproduced from Advanced Energy Materials, 2023, with the permission of Wiley Ltd.***

## 2.2 The Drastic Influence of Substituent Position on the Orientation of 2D Layers Enables Efficient and Stable 3D/2D Perovskite Solar Cells

*The second part of this chapter is based on the published work of Gunes et al. Cell Rep. Phys. Sci. 2023, **4**, 101380. DOI: 10.1016/j.xcrp.2023.101380.*

*Authors: Ummugulsum Gunes, Figen Varlioglu Yaylali, **Zeynep Gozukara Karabag**, Xiao-Xin Gao, Olga A. Syzgantseva, Aliekber Karabag, Gulsevim Bensu Yildirim, Konstantin Tsoi, Naoyuki Shibayama, Hiroyuki Kanda, Alwani Imanah Rafieh, Liping Zhong, Andreas Züttel, Paul Joseph Dyson, Selcuk Yerci, Mohammad Khaja Nazeeruddin, and Gorkem Gunbas.*

*I contributed as the third author in this work, working in equal collaboration with Ummugulsum Gunes, Figen Varlıoglu Yaylalı, and Xiao-Xin Gao. I characterized the optimized fabricated Perovskite Solar Cells and analysed data.*

The primary challenge to successfully commercializing PSCs lies in achieving reliable long-term stability and reproducibility. 3D/2D PSCs are one of the most prominent ways to address these issues. Various salts, primarily based on phenyl ethyl ammonium iodide (**PEAI**), have grown a 2D perovskite layer on 3D perovskites. Herein, we report the effect of substituting the methoxy (-OMe) group at the *ortho* (*o*), *meta* (*m*), and *para* (*p*) positions on **PEAI** salts. PL and TRPL show that ***o*-OMe-PEAI**-treated surfaces achieve reduced defect densities and nonradiative recombination rates compared with the other analogues. Devices with PCEs over 23% are achieved for ***o*-OMe-PEAI**-based 3D/2D PSCs, and the enhanced performance is attributed to the favorable formation energy and desired vertical orientation according to the density functional theory (DFT) analyses. Finally, the unique orientation of the ***o*-OMe-PEAI**-based 2D perovskite results in significantly enhanced long-term, moisture, and thermal stability.

### 2.2.1 Introduction

The interest in metal-halide hybrid PSCs has expeditiously increased due to their favorable properties, including long carrier diffusion length, band-gap tunability, high absorption coefficient, and low exciton binding energy.[208–211] While the first reported PCE only reached 3.8% in 2009,[10] the highest certified PCE is now over 26%.[11] Although this photovoltaic technology is almost on par with single heterojunction silicon solar cells in efficiency, it cannot provide sufficient long-term stability required for industrialization. Exposure of perovskite materials to external factors such as UV light, temperature, and humidity causes its structure to degrade irreversibly.[212–214] In addition, the point defects in the cell and the defects caused by the corrosion of the metal contact over time are also detrimental to long-term stability.[215] Several methods have been demonstrated to remedy these issues, and 2D perovskites have been proposed as one of the most promising groups of materials with increased stability compared with their 3D counterparts.[191,202] In the general representation of Ruddlesden-Popper 2D perovskites $(A')_2A_{(n-1)}B_nX_{(3n+1)}$, A', A, B, and X represent the bulky organic cation, small cation, inorganic cation, and halide species, respectively, and n represents the number of the inorganic $[BX_6]^{4-}$ octahedral layers.[216,217] 2D perovskites are formed by the presence of large ammonium salts with a size exceeding the tolerance factor of the inorganic crystal lattice, thus preventing the continuity of the 3D framework that results in well-defined 2D fragments.[218] Despite their remarkable stability, high exciton binding energies, poor charge separation characteristics, and large band gap, they have proved unfavourable for device performance in terms of efficiency.[219,220] Modifying 3D perovskites with a 2D counterpart (3D/2D) has been investigated to improve stability without compromising efficiency. Various organic ammonium salts have been used to produce efficient 3D/2D solar cells, but efforts have mainly concentrated on halogenated analogues of phenyl ethyl ammonium iodide (**PEAI**) salts.[221] Studies were also performed on the effect of functional group position on the aromatic moiety of **PEAI**-based salts. Zhou et al. employed *ortho* (*o*), *meta* (*m*), and *para* (*p*)

fluorine-substituted **PEAI** salts on 3D perovskite and achieved over 20% efficiency[222], with *ortho*-substituted **PEAI** leading the pack. A vital electron-releasing group substitution is used to design hole transport materials due to the group's ability to stabilize holes and defect-passivating character through their uncoordinated lone pairs. Taking these advantages into account, the electron-donating groups are also preferred in large organic ammonium salt design for 3D/2D perovskites, as they have the potential to enhance hole extraction and create favorable interaction sites with uncoordinated $Pb^{2+}$ ions on the surface of 3D perovskite.[223,224] To date, methoxy (OMe)-substituted organic ammonium salts have not been frequently utilized in 3D/2D PSCs. Meng et al. integrated 4-methoxy-**PEAI** (***p*-OMe-PEAI**) salt on 3D perovskite, achieving an efficiency of 19.64% with improved long-term stability.[225] The improved stability was attributed to the steric effect of methoxy moiety and electron repulsion between the -OMe unit and lone pair electrons of water molecules.[226] In the literature, one of the highest perovskite-based photovoltaic device efficiencies of 25.8% (certified efficiency of 25.5%) and remarkable long-term stability were achieved by forming a coherent interlayer between $SnO_2$ and the perovskite absorbing layer. At the same time, this notable device efficiency was attained by the ***p*-OMe-PEAI**-treated passivation layer on top of FA (Formamidinium)-based perovskite.[227] However, the effect of -OMe substitution positions (*ortho*, *meta*, and *para*) on 2D **PEAI** salts and their impact on the performance and long-term stability of 3D/2D PSC have not been investigated.

In this work, three methoxy-substituted organic ammonium salts named 2-methoxy-**PEAI** (***o*-OMe-PEAI**), 3-methoxy-**PEAI** (***m*-OMe-PEAI**), and 4-methoxy-**PEAI** (***p*-OMe-PEAI**) are synthesized with a straightforward synthetic methodology and utilized in 3D/2D PSCs with $(Cs_{0.04}FA_{0.85}MA_{0.11})Pb(I_{0.96}Br_{0.01}Cl_{0.03})_3$ triple-cation perovskites. The position effect of the methoxy-substituted ammonium salts on device performances and the stability of the 3D/2D PSCs are elucidated. XRD and GIWAXS results reveal that a 2D layer on the 3D perovskite is formed independently of the -OMe position. PL and TRPL analyses show that films treated with methoxy-substituent salts remarkably decrease trap density and enhance carrier lifetime.

Significant enhancement in PCE is achieved for all salts, with ***o*-OMe-PEAI** leading the pack (21.35%–23.34%). Enhancements of FF and $V_{OC}$ upon salt treatment are explained by drift-diffusion simulations. Density functional theory (DFT) analyses reveal that ***o*-OMe-PEAI**-treated films have the lowest formation energy, forming a super stable interface, thus enhancing device performance and long-term stability.

### 2.2.2 Experimental

#### 2.2.2.1 Solar Cell Fabrication

The FTO glass substrates (Nippon sheet glass, TEC9AX) were cleaned with Hellmanex, deionized water, acetone, and IPA for 15 min. Then, substrates were treated with UV-ozone for 15 min. $TiO_2$ solution was prepared by diluting titanium diisopropoxide bis(acetylacetonate) with IPA at a 1:15 vol ratio. The compact layer (*cp*-$TiO_2$) was deposited on the FTO substrates by spray pyrolysis at 450℃ and in situ annealing for 30 min. The *mp*-$TiO_2$ solution was prepared by dissolving 1 g $TiO_2$ paste in 10.5 mL ethanol and stirring overnight. Then, the *mp*-$TiO_2$ layer was deposited at 4,500 rpm for 20 s. After annealing at 125℃ for 30 min, the *mp*-$TiO_2$ films were gradually heated to 500℃ in air, then annealed at 500℃for 20 min. The $SnO_2$ layer was prepared by spin coating 0.1 M $SnCl_4$ solution at 3,000 rpm for 20 s; then, the substrates were annealed for 10 min at 150℃ and 1 h at 190℃. Before use, the FTO/*cp*-$TiO_2$/*mp*-$TiO_2$/$SnO_2$ substrates were treated with UV-ozone for 30 min. The precursor solution was prepared by dissolving $PbI_2$ (1.35 M), CsI (0.05 M), FAI (1.12 M), MABr (0.05 M), and MACl (0.10 M) in a mixed solvent of DMF:DMSO = 4:1 (volume ratio). Then, 25 mL perovskite precursors were coated onto the FTO/*cp*-$TiO_2$/*mp*-$TiO_2$/$SnO_2$ substrates (around 1.4 x 2.4 cm) by spin-coating method, and the coating procedure was performed through a two-step program running at 1,000 and 4,000 rpm for 12 and 25 s, respectively. During the second step (at the 11th second), 750 mL CB as an antisolvent was injected quickly onto the substrates. Afterward, the films were annealed at 100  C for 45 min. After cooling to

room temperature, a solution of ***x*-OMe-PEAI** in IPA (10 mg/mL) was spin-coated on the substrate at 4,000 rpm for 15 s. Then, the HTM solution was prepared by mixing a stock solution of *spiro*-OMeTAD in CB with solutions of 4-*tert*-butylpyridine, Li[TFSI] and Co[t-BuPyPz]$_3$[TFSI]$_3$ (FK209, Dyesol) in acetonitrile with a molar ratio of *spiro*-OMeTAD:FK209:Li[TFSI]:4-*tert*-butylpyridine (TBP) at 1:0.03:0.5:3.3. 40 mL *spiro*-OMeTAD solution was deposited at 3,500 rpm for 20 s on the perovskite film as the hole-transport layer. Finally, a 70-nm-thick gold layer was evaporated as a counter electrode to complete the device fabrication.

#### 2.2.2.2 Fabrication of 2D perovskite Films

For the fabrication of pure 2D films, the ***x*-OMe-PEAI** salts were mixed with $PbI_2$ in a 2:1 (molar) ratio and dissolved in DMF:DMSO mixture = 4:1 (volume ratio). For quasi-2D perovskite film, ***o*-OMe-PEAI** (2M), MAI (1M), and $PbI_2$ (2 M) were mixed and dissolved in DMF:DMSO = 4:1 (volume ratio). Then, all the substrates were coated at 1,000 and 4,000 rpm for 12 and 25 s, respectively, on ETLs. The films were annealed at 100℃ for 45 min.

#### 2.2.2.3 Film Characterization

The morphology of the films was analyzed by SEM (FEI Sirion-200). XRD diffraction peaks were obtained (D8 Advance diffractometer, Bruker) with a Cu K$\alpha$ radiation and a diffraction angle ($2\theta$) between 3° and 60°. GIWAXS patterns represented in reciprocal lattice space were conducted at beamline BL46XU of SPring-8. The sample was irradiated with an X-ray energy of 12.39 keV (l = 1A°) at a fixed incident angle on the order of 2 through a Huber diffractometer. The GIWAXS patterns were recorded with a 2D image detector (Pilatus 300 K). PL spectroscopy measurements (Perkin Elmer LS 55) were carried out from the film side of the substrates (FTO/*cp*-$TiO_2$/*mp*-$TiO_2$/$SnO_2$/perovskite/2D layer) with an excitation wavelength of 450 nm. TRPL spectroscopy analysis (HORIBA) was

performed using a Fluorolog TCSPC with an excitation wavelength of 640 nm from the film side of the substrates (glass/perovskite/2D layer). A biexponential decay function fits the carrier lifetime:

$$R(t) = A1e^{\frac{-t}{\tau 1}} + A2e^{\frac{-t}{\tau 2}} \quad \textbf{Equation 2.1}$$

UV-visible (UV-vis) absorption (PerkinElmer) analysis was done by using a Lambda 950S. UPS was used to determine the valence band energy and Fermi level. The measurements were measured on an Axis Supra (Kratos Analytical, Manchester, UK) using a He-I source (hv = 21.22 eV). All the samples were grounded to remove charging effects.

#### 2.2.2.4 Solar Cell Characterization

*J-V* measurements were carried out using an Oriel solar simulator (450 W Xenon, AAA class) and a Keithley 2400 digital source meter. The light intensity was calibrated by a silicon cell. A metal mask with a 0.09 $cm^2$ active area defined the active areas of solar cells. The scan rate was 100 mV $s^{-1}$ with no preconditioning. The EQEs were measured with an IQE 200B (Oriel) for devices without bias light.

#### 2.2.2.5 Computational Details

The simulation of $FAPbI_3$-2D-***x*-OMe-$PEA_2PbI_4$** interfaces was accomplished within DFT employing Perdew-Burke-Ernzerhof (PBE)[174] density functional along with Grimme's D3 dispersion correction[175], as implemented in CP2K code.[178] The wavefunctions and charge density were expanded using the atomic Gaussian-type double-z basis set (DZVP-MOLOPT)[176] and the plane wave auxiliary basis set with 600 Ry cutoffs, respectively. Norm-conserving Goedecker-Teter-Hutter (GHT) pseudopotentials[177] were used for the description of the core region and core-valence interactions. All structures were fully relaxed both in terms of atomic positions and cell parameters. The first Brillouin zone was sampled in the G-point. To assess the

interactions of the *x*-OMe-PEA cations with the FAI- and $PbI_2$-terminated perovskite surfaces, the first principles Born-Oppenheimer molecular dynamics (BOMD) simulations were accomplished for several picoseconds using 1 fs timestep and velocity rescaling algorithm for maintaining the temperature constant at 343 K. The structures are visualized using VESTA[179] and VMD[180] software.

### 2.2.3 Results and Discussion

The organic ammonium salts were synthesized in three high-yielding steps; details are given in the supporting information part in the related paper and Figen Varlioglu Yaylali's Ph.D. thesis.[173,228] The solar cells were fabricated in FTO/*cp*-$TiO_2$/*mp*-$TiO_2$/$SnO_2$/perovskite/***x*-OMe-PEAI**/*spiro*-OMeTAD/Au architecture, as shown in **Figure 2.19.A**. A 3D triple-cation perovskite absorber layer was employed, and a solution of methoxy-substituted salts in IPA was coated on it by spin coating to form the 3D/ 2D perovskite structure.

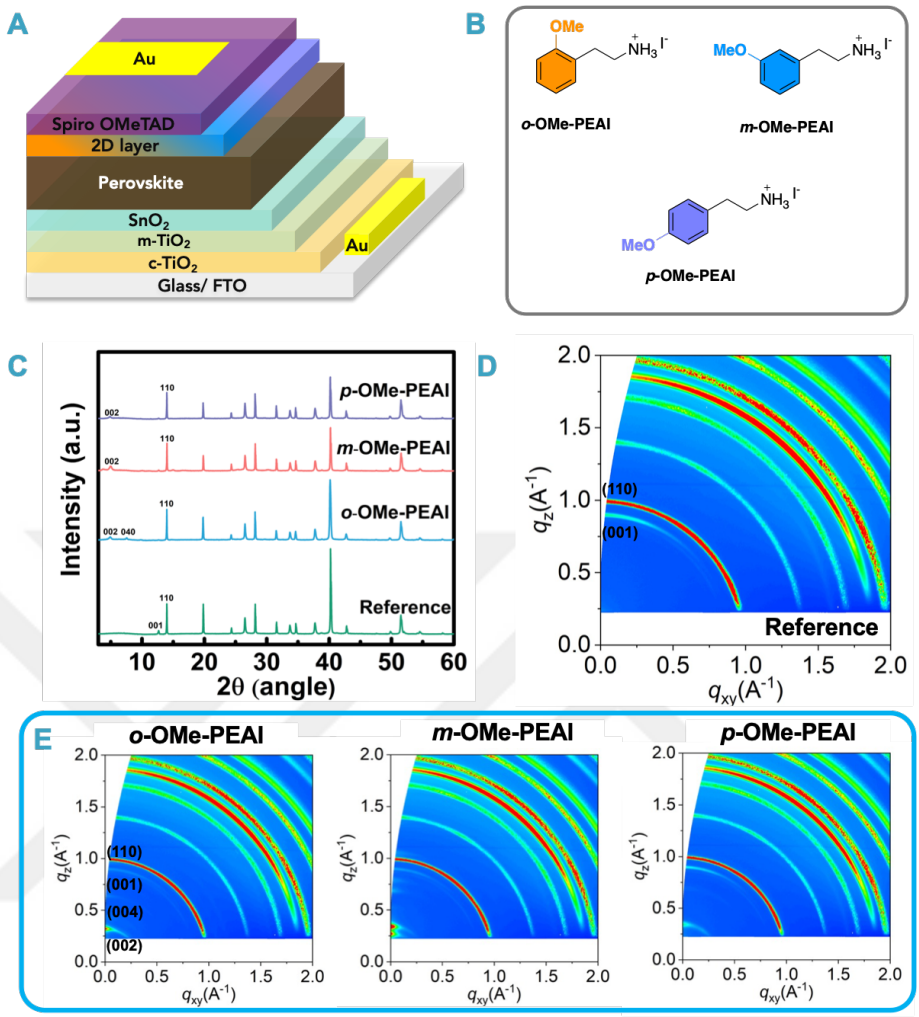



**Figure 2.19.** Solar device architecture and crystallographic features of the films. **A)** Illustration of the solar cell architecture. **B)** Schematics of the ***o*-OMe-PEAI**, ***m*-OMe-PEAI**, and ***p*-OMe-PEAI** structures. **C)** XRD pattern of the reference (ref.) 3D perovskite and perovskites treated with methoxy-substituted salts (***o*-OMe-PEAI**, ***m*-OMe-PEAI**, and ***p*-OMe-PEAI**). (002), (040), and (001) represent the diffraction peaks of 2D (n = 1), quasi 2D (n = 2), and $PbI_2$ (001), respectively. **D)** GIWAXS images of the 3D perovskite. **E)** GIWAXS images of the 3D/2D perovskite films.

The XRD spectra displayed a peak below 10° for all 3D/2D films, which is attributed to forming a low-dimensional top perovskite layer.[229] The observed peaks at $2\theta$=4.92°, 4.97°, and 4.90° for salt-treated 3D perovskites (**Figure 2.19.C.**) are consistent with pure **$(OMe\text{-}PEAI)_2PbI_4$** 2D perovskite (n = 1) peaks (4.97°, 4.91°, and 4.94°) with slight (<0.06) shifts (**Figure 2.20.a**). Moreover, a significant

decrease in $PbI_2$ peak intensity ($2\theta$ = 12.7°) was observed for films treated with **OMe-PEAI**, indicating that organic ammonium salts interact with excess $PbI_2$ on the 3D perovskite surface, providing further strong evidence of 2D layer formation.[230,231] Additional peak observed for ***o*-OMe-PEAI** at $2\theta$ = 7.55° ((040) oriented) arises from quasi-2D perovskite structure with n = 2 (**Figure 2.20.b**).[232]

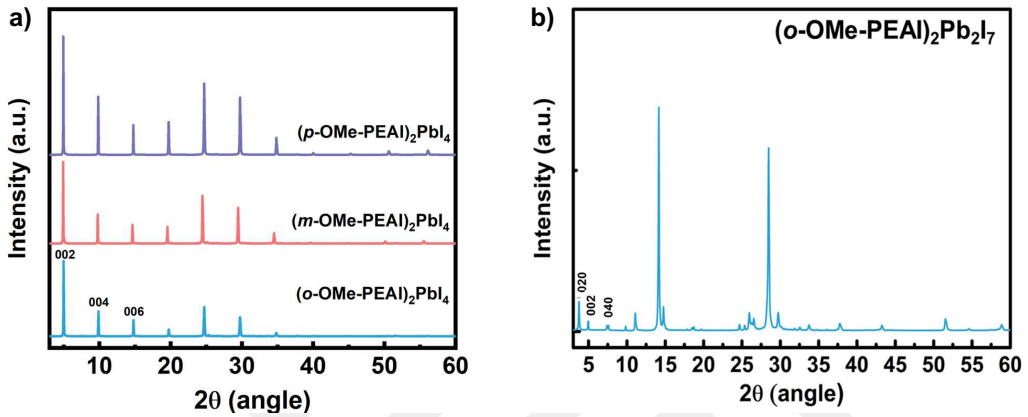



**Figure 2.20. a)** XRD pattern of the pure 2D films (n = 1). **b)** XRD pattern of the quasi 2D film (n = 2).

Since crystallographic orientation affects the optoelectronic properties and overall stability of devices[233], GIWAXS measurements were carried out with a 0.2° the incident angle reveals the crystal orientation of perovskite components. The strong scattering rings at $q_z$ = 1 and 0.9$Å^{-1}$ belong to the (110)-oriented crystal plane of the 3D perovskite[234], and the (001)-oriented $PbI_2$ crystal plane[235] (**Figure 2.19.D**), respectively. The scattering ring of $PbI_2$ decreases gradually, and a new spot appears at $q_z$ = 0.3$Å^{-1}$ upon insertion of an ***o*-OMe-PEAI** salt on the 3D perovskite (**Figure 2.19.E**). The GIWAXS spectra of the pure 2D film of ***o*-OMe-PEAI** (**(*o*-OMe-PEAI)$_2$PbI$_4$**) also has strong spots around $q_z$ = 0.3 and 0.6 $Å^{-1}$, which confirms the formation of the proposed 2D layer (**Figure 2.21**).[236,237]

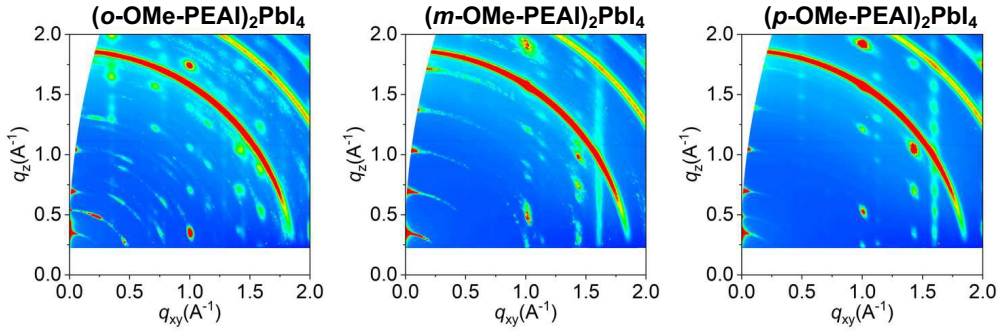



**Figure 2.21.** GIWAXS spectra of the pure 2D films (n = 1).

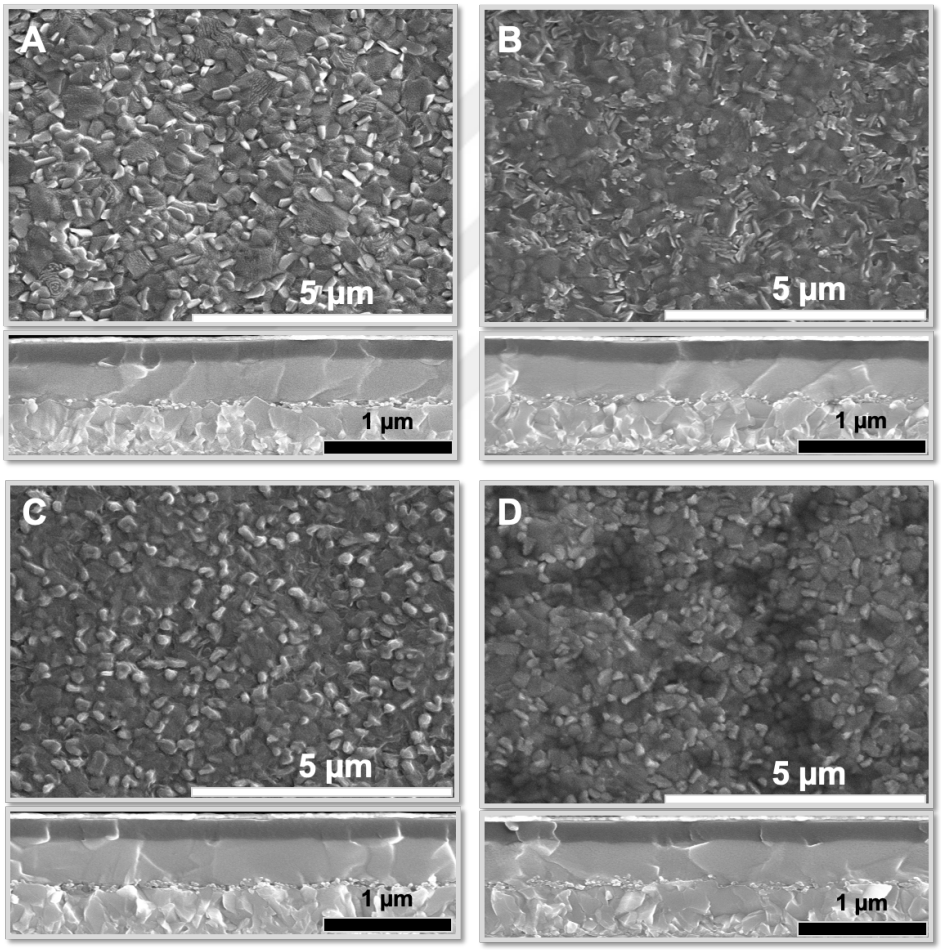



**Figure 2.22.** Film characterization. **A)** SEM top-view and cross-section images of the 3D film. **B)** 3D/2D films with ***o*-OMe-PEAI**. **C)** ***m*-OMe-PEAI**. **D)** ***p*-OMe-PEAI**.

The films' surface morphologies changed upon treatment with -OMe salts, as shown by top-view SEM images in **Figures 2.22.A–D**. The 3D film's higher contrast

(**Figure 2.22.A**) and the observation of bright grain sites refer to excess $PbI_2$ on the surface.[238] Contrarily, perovskite films treated with methoxy-substituent salts have fewer bright grains on the surface, indicating that **OMe-PEAI** salts react with excess $PbI_2$ on the 3D perovskite surface (**Figures 2.22.B–D**). It should be noted that the 2D layers are not distinguished in cross-section SEM due to their very thin nature (**Figures 2.22.B-D**).[223]

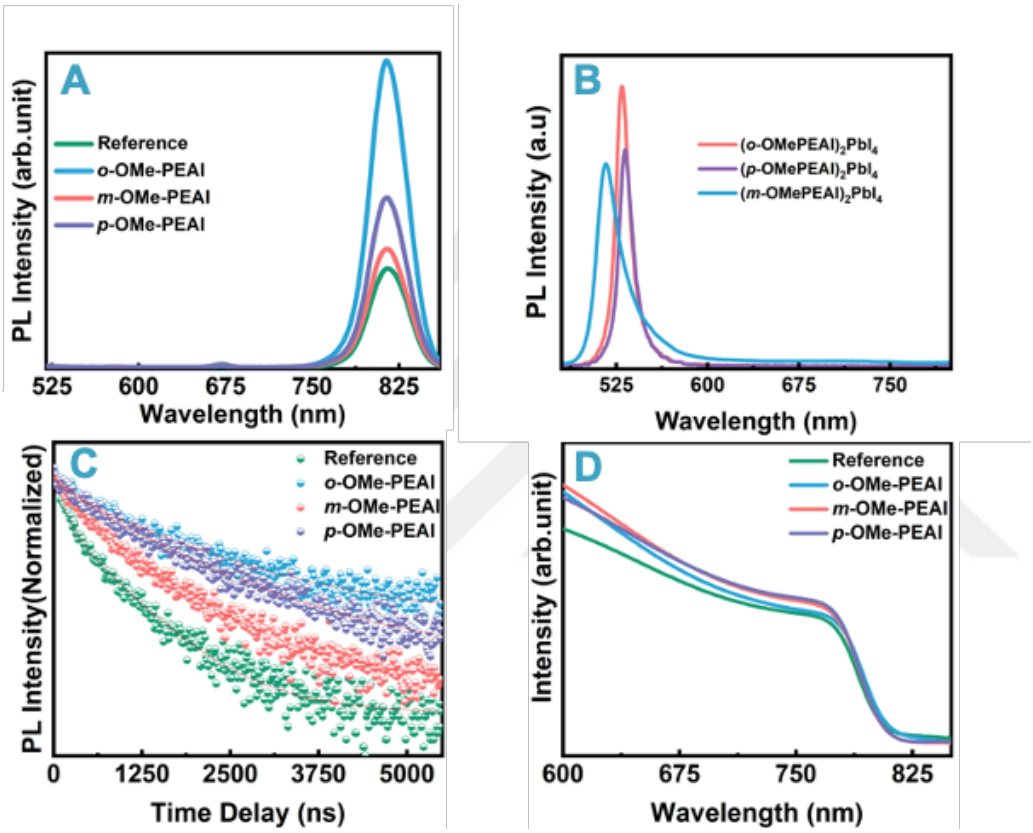



**Figure 2.23. A)** Steady-state PL spectra. **B)** PL spectra of the pure 2D films (n = 1). **C)** TRPL traces. **D)** Absorption spectra of the 3D film and 3D films with **OMe-PEAI** treatment.

**Table 2.6.** Fitting parameters of TRPL spectra of reference and **OMe-PEAI**-treated films, *A*1 and *A*2 are the fractions of the two decay processes and $\tau_1$ and $\tau_2$ are shorter and longer lifetimes, respectively.

| | $A_1$ | $\tau_1$ | $A_2$ | $\tau_2$ | $R^2$ |
|---|---|---|---|---|---|
| **Reference** | 0.505 | 137.98 | 0.428 | 823.59 | 0.993 |
| ***o*-OMe-PEAI** | 0.212 | 240.50 | 0.597 | 1712.5 | 0.963 |
| ***m*-OMe-PEAI** | 0.298 | 223.14 | 0.578 | 1098.7 | 0.991 |
| ***p*-OMe-PEAI** | 0.173 | 327.21 | 0.635 | 1569.9 | 0.978 |

All 3D/2D perovskites have higher PL intensities (**Figure 2.23.A**) and longer PL decay times (**Figure 2.23.C**; **Table 2.6**) compared with the 3D reference film, indicating that **OMe-PEAI** salts suppress the nonradiative recombination and decrease defect density in the perovskite layer and/or grain boundaries.[239] Particularly, film treated with ***o*-OMe-PEAI** salt shows a significant increase in PL intensity and lifetime, implying that *ortho*-positioned salt provides superior passivation of effects than the *meta* and *para* methoxy-substituted ammonium salts.

No PL signal was detected at the lower wavelengths for the corresponding high-bandgap 2D perovskites due to the low concentration of the salt in the solution, which results in a very thin layer of 2D perovskite.[240,241] Absorption spectra showed no significant change in absorption for 3D/2D films compared with 3D only, revealing that 2D materials do not incorporate into 3D perovskite bulk, which is also in line with XRD and GIWAXS analyses. See **Figure 2.23.B** for the PL spectra of pure 2D films.

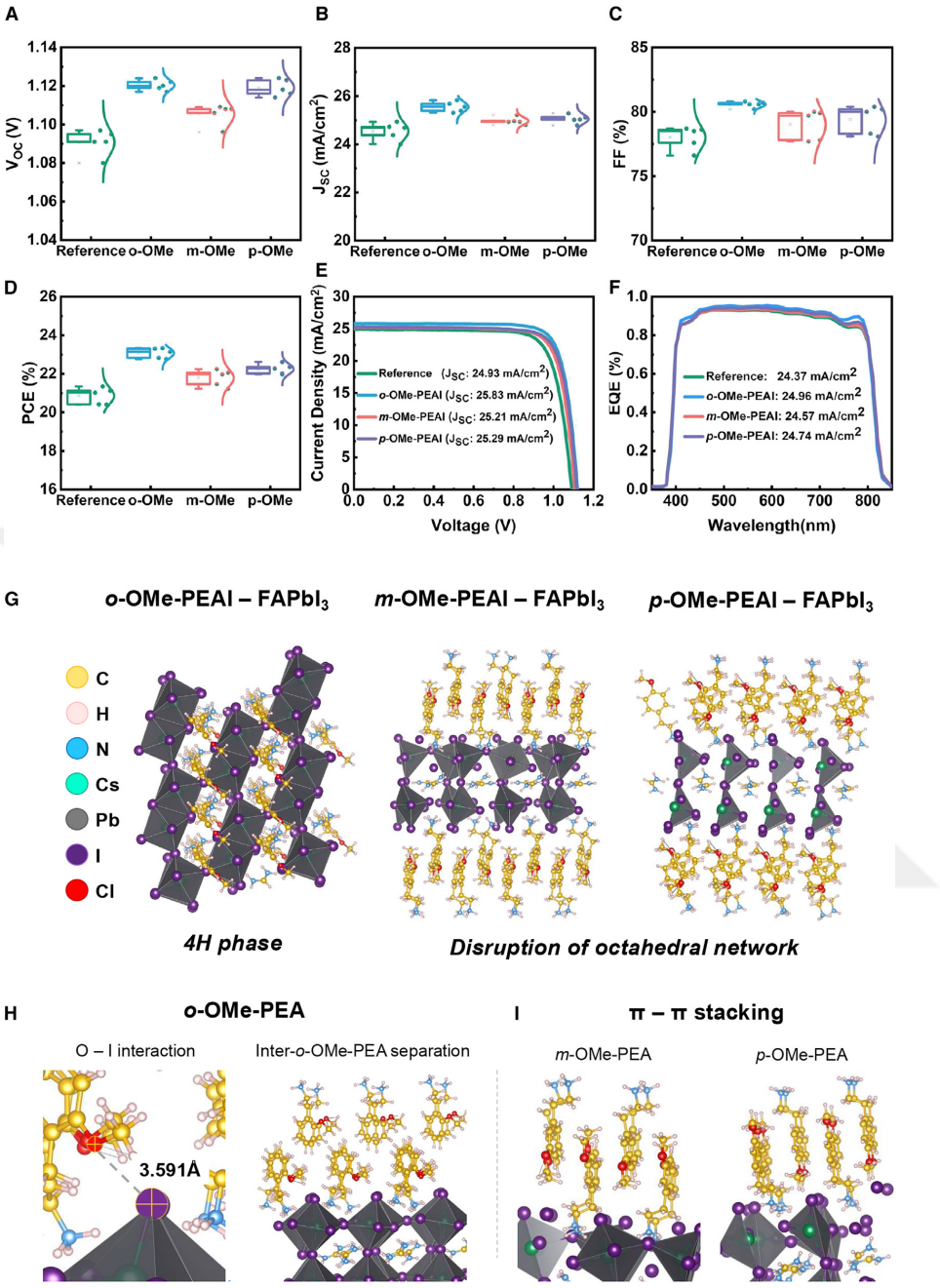



**Figure 2.24**. Device parameters and molecular dynamics **(A–D). A)** $V_{OC}$, **B)** $J_{SC}$, **C)** FF, and **D)** PCE statistics of reference (3D) and 3D/2D solar cells (out of 5 devices). Box plot details: The bottom and top edges of the box indicate 25th and 75th percentiles, respectively. The central horizontal line in the box indicates the median, whiskers extend to the most extreme data points, and the mean is indicated by open symbols. **E)** *J-V* curves of the champion ref. and 3D/2D solar cells. **F)** EQE spectra of the champion ref. and 3D/2D solar cells. **(G-I)** Optimized structures of interfaces between 3D $FAPbI_3$ perovskite and ***o*-OMe-PEAI**, ***m*-OMe-PEAI**, and ***p*-OMe-PEAI** 2D perovskites.

Significant improvements in $V_{OC}$ and FF were observed for 3D films treated with **OMe-PEAI** salts (**Figures 2.24.A and 2.24.C**), in line with the steady-state PL and TRPL studies and inferring superior charge transport, respectively.[242] In addition, a slight increase in the $J_{SC}$ was also observed for the 3D-/2D-based solar cells (**Figure 2.24.B**). Average efficiencies for the reference, ***o*-OMe-PEAI**, ***m*-OMe-PEAI**, and ***p*-OMe-PEAI** PSCs were obtained as 20.86%, 23.08%, 21.79%, and 22.25%, respectively (**Figure 2.24.D**). All solar cells fabricated in this work showed a limited deviation in all device parameters, showcasing the reproducibility of the device fabrication processes (**Table 2.8**).

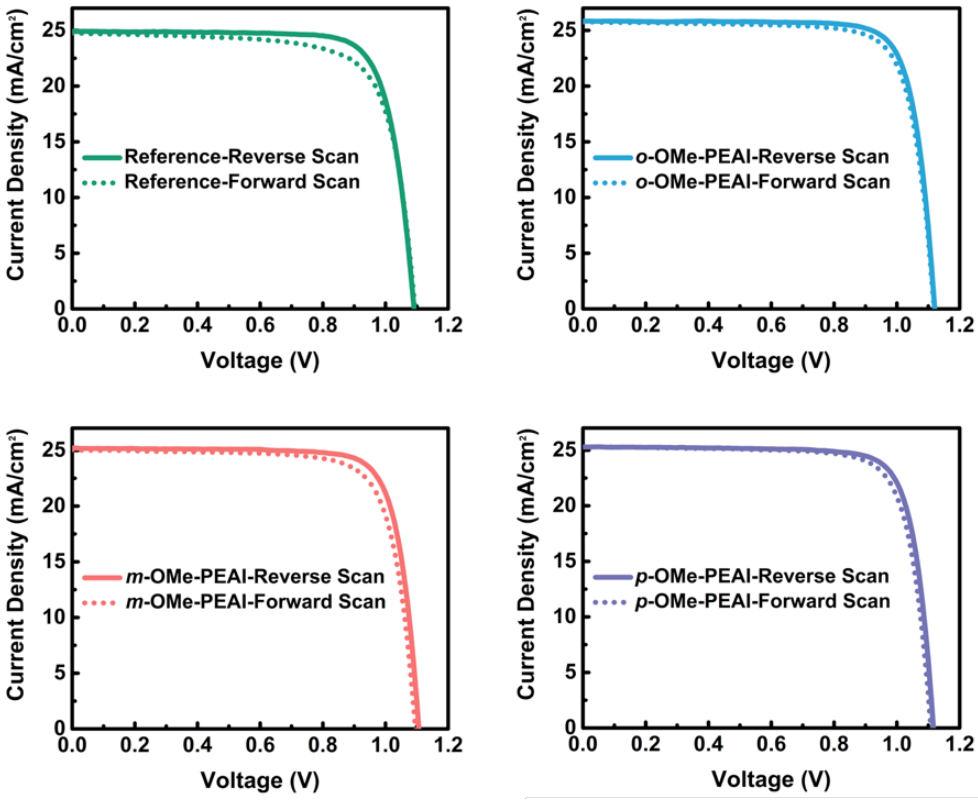



**Figure 2.25.** Reverse and forward scans of champion PSCs.

**Table 2.7.** Reverse scan (R.S.) and Forward Scan (F.S.) *J-V* device parameters and hysteresis Index (%) results of the reference and **OMe-PEAI**-treated PSCs.

| | $V_{oc}$ (V) | $J_{sc}$(mA/cm$^2$) | FF (%) | PCE (%) | HI (%) |
|---|---|---|---|---|---|
| ***Reference – R.S.*** | 1.09 | 24.93 | 78.5 | 21.35 | 6.37 |
| ***Reference – F.S.*** | 1.09 | 24.78 | 73.8 | 19.99 | - |
| ***o-OMe-PEAI – R.S.*** | 1.12 | 25.83 | 80.6 | 23.34 | 2.91 |
| ***o-OMe-PEAI – F.S.*** | 1.12 | 25.76 | 78.4 | 22.66 | - |
| ***m-OMe-PEAI – R.S.*** | 1.11 | 25.21 | 79.7 | 22.25 | 4.94 |
| ***m-OMe-PEAI – F.S.*** | 1.10 | 25.06 | 77.0 | 21.15 | - |
| ***p-OMe-PEAI – R.S.*** | 1.12 | 25.29 | 80.2 | 22.62 | 3.18 |
| ***p-OMe-PEAI – F.S.*** | 1.11 | 25.31 | 78.2 | 21.90 | - |

The highest PCEs of PSCs with 3D perovskite treated by ***o*-OMe-PEAI**, ***m*-OMe-PEAI**, and ***p*-OMe-PEAI** and of the reference are 23.34%, 22.25%, 22.62%, and 21.35%, respectively (**Figure 2.24.E** and **Figure 2.25**; **Table 2.7**). All 3D/2D PSCs treated with methoxy-substituted salts showed lower hysteresis than the reference solar cell (**Table 2.7**), indicating suppressed ion migration and accumulation by passivating the defects on the perovskite surface.[243] It should be noted that the $J_{SC}$ values obtained from the current-voltage (*J-V*) curves and external quantum efficiency (EQE) spectra agree well, as shown in **Figures 2.24.E and 2.24.F**

**Table 2.8.** $V_{OC}$, $J_{SC}$, FF, and PCE statistics of reference (3D) and 3D/2D PSCs.

| Cell label | $V_{OC}$ (V) | $J_{SC}$ (mA/cm$^2$) | FF (%) | PCE (%) |
|---|---|---|---|---|
| Ref. | 1.091 ± 0.007 | 24.55 ± 0.36 | 78.0 ± 0.9 | 20.86 ± 0.43 |
| *o*-OMe-PEAI | 1.120 ± 0.003 | 25.55 ± 0.21 | 80.6 ± 0.2 | 23.08 ± 0.27 |
| *m*-OMe-PEAI | 1.105 ± 0.005 | 24.97 ± 0.15 | 79.0 ± 1.2 | 21.79 ± 0.43 |
| *p*-OMe-PEAI | 1.119 ± 0.004 | 25.05 ± 0.18 | 79.4 ± 1.1 | 22.25 ± 0.26 |

To rationalize the better performance of the ***o*-OMe-PEAI** treatment, which results in the formation of a low-dimensional ***o*-OMe-PEA$_2$PbI$_2$** layer, the formation energies of the interfaces FAPbI$_{3-x}$-**OMe-PEA$_2$PbI$_4$** were computed within the DFT applying PBE-D3[244,245] functional as in **Equation 2.2**.

$$\Delta_f E = E_{interface} - xE_{FAI} - (x + y)E_{PbI2} - 2yE_{nOMe\text{-}PEAI} \qquad \textbf{Equation 2.2}$$

***o*-OMe-PEA$_2$PbI$_4$** forms a remarkably stable interface with $FAPbI_3$ compared with *m*-OMe- and *p*-OMe-based 2D layers, as shown in **Figures 2.24.G-I**. Indeed, the formation energies of ***o*-OMe-PEA$_2$PbI$_4$-FAPbI$_3$** interfaces are 0.70 and 0.65 eV lower than that of ***p*-OMe-PEA$_2$PbI$_4$-FAPbI$_3$** and ***m*-OMe-PEA$_2$PbI$_4$-FAPbI$_3$**, respectively. Calculations reveal that shifting the -OMe group from the *ortho* to the *para* position induces elongation of Pb...I lengths, i.e., breaking the integrity of $PbI_6$ octahedra, which hinders the charge transfer along the $PbI_2$ layer. The structural optimization of these interfaces reveals that for the ***o*-OMe-PEA** case, the stable 4H phase, which is one of the well-known precursors of the perovskite crystallization process[246], is spontaneously formed (**Figure 2.24.G**). It has both the corner-sharing and edge-sharing connections of the $PbI_6$ octahedra and forms a continuous 2D network in the plane perpendicular to the crystal growth direction. This phase is stabilized at the interface with the 3D perovskite by 0.9 eV when the organic cation ***o*-OMe-PEA** is used. The topology of this phase allows for the passivation of iodine vacancies on the perovskite surface, reducing the concentration of trap centers and thus improving the performance of the device. Indeed, the 4.5–4.6 Å I-I distance on FAI-terminated and $PbI_2$-terminated surfaces of 4H-$FAPbI_3$ are compatible with the topology of the iodine sites on the 3D $FAPbI_3$ surfaces, making structurally possible the passivation of the vacancy sites.

Moreover, stabilizing the 4H phase as a precursor in forming cubic $FAPbI_3$ perovskites inherently passivates the defective $FAPbI_3$ perovskite surfaces and grain boundaries by simply preventing their formation. The interaction between organic cations in this structure is weakened due to the increased distance, which prevents their p-p stacking, unlike ***m*-OMe-PEA**- and ***p*-OMe-PEA**-based structures (**Figure 2.24.H**), in which the last one is present (**Figure 2.24.I**). The methoxy groups in the *ortho* positions can noncovalently interact with the iodine atoms, enhancing the binding of bulky organic cations. This weakened interaction within the bulky organic cation layer implies that ***o*-OMe-PEA** cations can serve not only to form the 2D layered structure but also as an organic surface capping layer. Notably, the ***o*-OMe-**

**PEA**-based interface is the most stable among the three configurations considered:-9.98 (*ortho*) vs. -9.33 (*meta*) vs. -9.28 eV (*para*).

In contrast to ***o*-OMe-PEA**, ***m*-OMe-PEA** and ***p*-OMe-PEA** (**Figure 2.24.G**) do not spontaneously form the 4H phase in the DFT simulations. What is more, the connections of perovskite octahedra at ***m*-OMe-PEA**- and ***p*-OMe-PEA**-based interfaces become disrupted in one or two dimensions, transforming the original octahedra to tetrahedra (**Figure 2.24.G**), that is, unfavourable for the lateral electron and hole mobility and results in a decreased device performance, compared with the ***o*-OMe-PEA**-based device. In the case of the ***p*-OMe-PEA** cation, weak noncovalent interactions between O and I atoms are possible as well, similar to the *ortho*-substituted cation, constituting an additional factor in line with the observed performance order ***o*-OMe-PEA** > ***p*-OMe-PEA** > ***m*-OMe-PEA**.

According to the TRPL data, the highest lifetime is observed for the ***o*-OMe-PEA** interface, which is in line with the hypothesis about the passivation of iodine traps by the 4H phase and the consequent reduction of trap concentration compared with the reference, ***m*-OMe-PEA**, and ***p*-OMe-PEA** compounds. Besides, the SEM images evidence the most homogeneous morphology of the ***o*-OMe-PEA**-based samples, which is also in line with the hypothesized role of the 4H phase in the formation process of a homogeneous film.

Finally, the DFT calculations confirm that ***o*-OMe-PEA** has the highest energy of iodine vacancy formation among the three tested interfaces, which is also in line with the hypothesis on the reduced concentration of trap states (**Table 2.9**). The order of iodine vacancy formation energy correlates with the device performance, supporting the hypotheses as mentioned above.

**Table 2.9.** The formation energies of neutral I vacancies at the respective interfaces.

| *Interface* | $\Delta_f E_{vac}I$, eV |
|---|---|
| *o*-OMe-PEAI | 3.83 |
| *m*-OMe-PEAI | 3.03 |
| *p*-OMe-PEAI | 3.41 |

The ionization energies of the reference and 3D/2D films were extracted using the ultraviolet photoelectron spectroscopy (UPS) as -5.49, -6.03, -6.19, and -6.03 eV for the reference, ***o*-OMe-PEAI**, ***m*-OMe-PEAI**, and ***p*-OMe-PEAI**, respectively **(Figure 2.26)**. The highest occupied molecular orbital (HOMO) level energy of the 3D/2D films is lower than the HOMO level of the reference film, which results in an improved solar cell performance despite a stronger mismatch with the transport layer. Two possible explanations for these observations are that (1) the lowered energy levels imply a decrease in n-character upon salt treatment and cause band bending, thus improving charge transport properties[247,248], and/or (2) holes are tunnelling through the 2D layers to reach the hole transport layer, as evidenced by increased $V_{OC}$ and FF. Our observations align with the literature, where it has been shown that inserting a very thin layer of an even insulating layer into PSCs improves device performance through enhanced charge carrier lifetime and FF.[249]

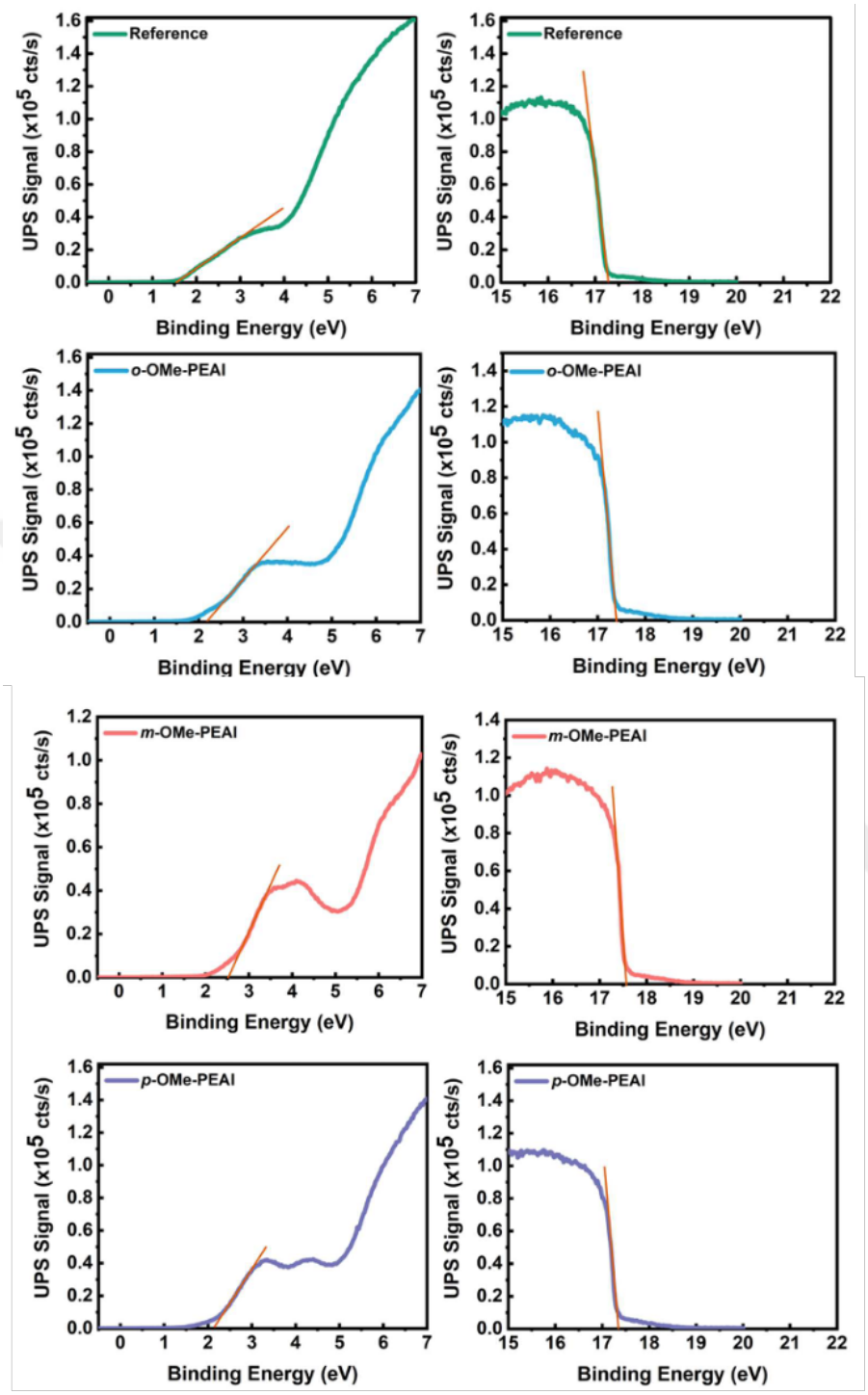



**Figure 2.26.** UPS spectra of the reference and ***x*-OMe-PEAI**-treated 3D/2D films.

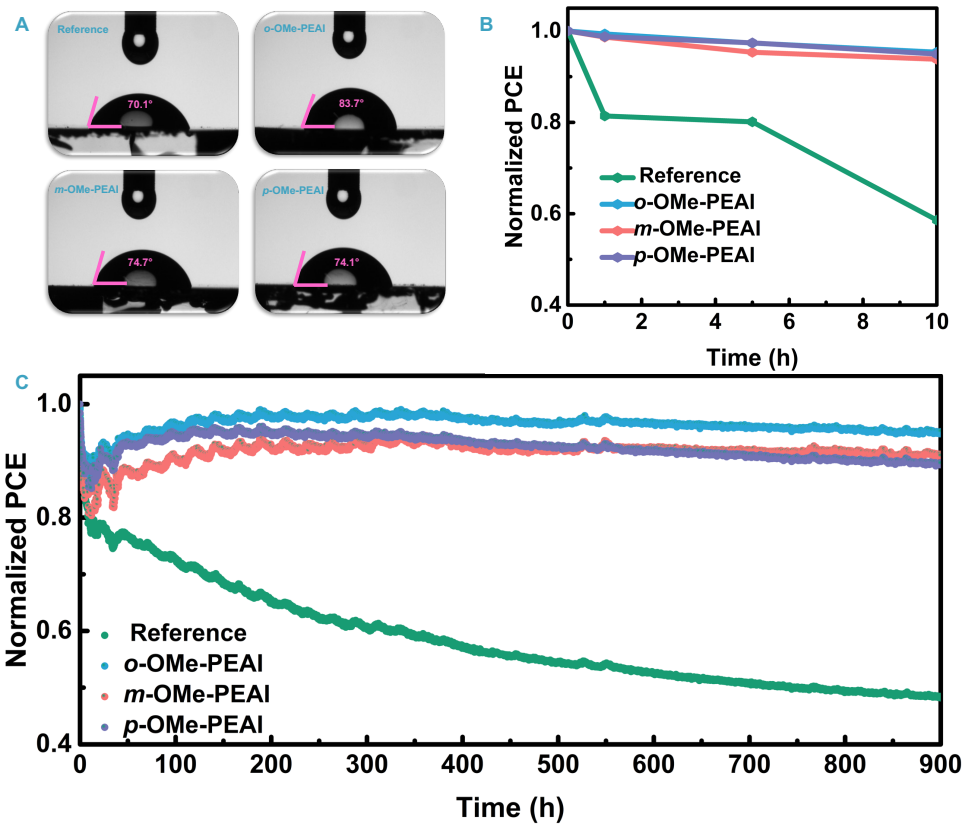



**Figure 2.27.** Stability studies **A)** Contact angle images of reference and ***x*-OMe-PEAI**-treated 3D/2D films. **B)** Stability tests for ***x*-OMe-PEAI**-treated PSCs under 65% relative humidity at ambient air for 10 h. Solid lines are given to guide the eye. **C)** In situ stability for measuring the PCEs of unencapsulated ***x*-OMe-PEAI**-treated PSCs over 900 h under a nitrogen atmosphere.

According to contact angle measurements, all 3D/2D films revealed a higher hydrophobic character than the 3D reference film (**Figure 2.27.A**). Due to its configurational geometry, the film with the ***o*-OMe-PEAI** layer showed the highest hydrophobicity. In addition, the ***x*-OMe-PEAI** treatment improved stability under high humidity conditions (65%). After 10 h exposure to humidity, devices with ***x*-OMe-PEAI** showed superior stability compared with the reference device (**Figure 2.27.B**). The device treated with ***o*-OMe-PEAI** maintained 95.3% of its initial yield (***m*-OMe-PEAI** retained 93.8%, and ***p*-OMe-PEAI** retained 94.9%). In comparison, the reference device only retained 58.6% of its initial efficiency. All devices were evaluated at the maximum power output (MPO) decay while being maintained under

a nitrogen atmosphere under a constant illumination of 100 mW $cm^{-2}$. The *J-V* curves were recorded at intervals of 2 h. The devices treated with ***x*-OMe-PEAI** salts were more stable than the reference device (**Figure 2.27.C**), with ***o*-OMe-PEAI** showing the highest stability. After 900 h continuous irradiation, the MPO values of the devices maintained 95% (with ***o*-OMe-PEAI**), 91% (with ***m*-OMe-PEAI**), and 90% (with ***p*-OMe-PEAI**) of their initial values. In contrast, the loss of MPO for the reference device is considerably higher, with only 49% of the initial MPO maintained after 900 h. A thermal stability test was also performed at 60℃[250] heating for 30 min under 30% relative humidity. The reference device showed a 13.3% decrease in PCE after 30 min, while ***o*-OMe-PEAI**-, ***m*-OMe-PEAI**-, and ***p*-OMe-PEAI**-treated devices showed 3.3%, 4.7%, and 4.8% decreases in their efficiencies, respectively.

### 2.2.4 Conclusion

In summary, we report 3D/2D PSCs based on *ortho*, *meta*, and *para* methoxy-substituted **PEAI** salts on 3D (triple cation [$Cs^+$, $FA^+$, $MA^+$]) perovskites. The formation of 2D films on 3D perovskite for all salts was confirmed by XRD, GIWAXS, and SEM analyses. PL and TRPL studies revealed that ***o*-OMe-PEAI** achieved lower point defect densities, and reduced nonradiative recombination rates compared with the reference, as well as ***m*-OMe-PEAI** and ***p*-OMe-PEAI** analogues. This observation translated well into the device performance, and PCEs of over 23% with excellent $V_{OC}$ (1.12 V) and FF (80%) were achieved utilizing an ***o*-OMe-PEAI**-treated triple-cation perovskite as the absorber. The stronger performance of these devices was attributed to the favorable formation energy, desired vertical orientation, and optimal surface coating of the ***o*-OMe-PEAI** salt according to the DFT analyses and lower SRV revealed by electrical simulations.[173] The unique orientation of the ***o*-OMe-PEAI** on the 3D perovskite surface revealed higher hydrophobicity compared with other salts (and the reference), which in turn reflected the higher stability of the resulting devices. PSCs fabricated with ***x*-OMe-**

**PEAI** salts showed that devices retained 95% (*o*-OMe), 91% (*m*-OMe), and 90% (*p*-OMe) of their original efficiencies after 900 h. In contrast, reference cells retained only 49% of their initial efficiency.

*The supporting information section, available at https://doi.org/10.1016/j.xcrp.2023.10138, provides the synthetic details and methods for manufacturing the device.*

***This study is reproduced from Cell Reports Physical Science, 2023, 101380, with the permission of Elsevier Ltd.***

# CHAPTER 3

## SYNTHESIS OF NON-FULLERENE ELECTRON TRANSPORT AND $NiO_x$ LAYER PASSIVATION MOLECULES SUITABLE FOR THERMAL EVAPORATION TO FABRICATE HIGH-PERFORMANCE INVERTED PSCS

PSCs can be fabricated using different processing methods, such as spin coating, inkjet printing, spray coating, thermal evaporation, chemical vapor deposition, etc.[251] Among them, thermal evaporation is a considerable effort for depositing organic-inorganic PSCs since it has several benefits.

- Fine-tuning of the growth environment and the rate at which perovskite precursors grow is crucial for achieving desired material properties.
- The ability to consistently produce films with uniform thickness is vital to ensuring that the material performs reliably in its intended application.
- The technique enables uniform deposition across large areas, which is essential for scaling up production, especially in applications like solar cells or displays.
- This technique's applicability across different technologies expands by allowing it to be applied to various substrates, including TCO-coated glass, flexible foils, and textured silicon.

This chapter of the thesis describes the design and synthesis of fluorene-based $NiO_x$ passivation molecules and thermally evaporable various NDI derivatives as electron transport layers for use in the creation of inverted PSCs.

## 3.1 Synthesis of Naphthalene Diimide-Based Electron Transport Layers Suitable for Thermal Evaporation to Fabricate High-Performance Inverted PSCs

The majority of high-performing organic ETL materials are conjugated structures, either by a combination of multiple building blocks, such as donor (D) and acceptor (A), or by having an elongated interconnected ring structure, and they possess strong acceptor functionalities. Selecting an acceptor functionality is crucial when designing new ETL materials. Considering the demanding structural requirements, such as the presence of heteroatoms that can interact with $Pb^{2+}$ ions in the perovskite layer and polar groups that can regulate the work function of electrodes, it is clear that ETL materials with an NDI core should lead the way in efficient and rational material design. The NDI unit is resistant to oxidation and contains electron-withdrawing imide fragments that facilitate simple reduction into stable anionic radicals, making NDI a stable n-type semiconducting backbone. Moreover, NDI-based molecules have splendid film-forming abilities without crystalization.[252] Changes at the NDI core and imide locations result in differences in the resulting NDI molecules' solubility, bandgap tuning, optoelectronic characteristics, and light-harvesting abilities.

A continuous pathway for electron mobility is produced by the stacked arrangement of the electron-transporting cores encouraged by the lamellar orientation of NDI molecules.[253] Effective charge extraction from the perovskite active layer to the electrode is made possible by this ordered stacking, primarily driven by π-π interactions. This reduces recombination losses and increases current density. Using this orientated structure, the energy levels of the NDI-based ETL can be adjusted. Lamellar orientation can help create a stable interface that maximizes alignment with the perovskite conduction band, which is necessary for effective electron transfer. Moreover, through chemical modifications, the energy levels of the NDI-based layers can be adjusted to better match the conduction band of the perovskite layer, reducing energy loss during charge transfer. Additionally, lamellar orientation

provides a smoother and more uniform ETL interface, which contributes to better film coverage over the perovskite layer.

Commercially available fullerenes and their derivatives offer excellent electron transport and interface passivation properties, making them the most demanded ETLs for high-performance PSCs. However, the main drawback in the photovoltaic field is the high cost of high-purity fullerenes and their derivatives. This can increase the overall cost of manufacturing PSCs, challenging their scalability and cost competitiveness with other photovoltaic technologies. On the contrary, NDI-based ETLs designed and synthesized in this study are highly cost-effective regarding fullerene, and the detailed cost analysis is given in **Table 3.1.** According to **Table 3.1**, while fullerene has a price of 681.00€/g, **NDI-Ph,** and **NDI-pT** can be synthesized at a dramatically lower cost of 15.04€/g and 17.50€/g, respectively.

**Table 3.1.** Detailed cost analysis and material requirements for the synthesis of 1 gram of NDI-based ETMs.

| Chemical Name | Supplier | Size of Chemical | Price of Chemical | Amount of Reagent | Material Cost |
|---|---|---|---|---|---|
| **NDI-Ph** | | | | | |
| 1,4,4,8-Naphthalene tetracarboxylic dianhydride (**NDA**) | Sigma-Aldrich | 100 G | €621.00 | 5 G | €31.05 |
| Aniline | Sigma-Aldrich | 100 ML | €48.50 | 3.47 ML | €1.68 |
| Dimethylformamide (**DMF**) | Sigma-Aldrich | 1000 ML | €200.00 | 87 ML | €17.40 |
| Ethanol (**EtOH**) | Sigma-Aldrich | 2500 ML | €71.80 | 200 ML | €5.74 |
| Dichloromethane (**DCM**) | Sigma-Aldrich | 2500 ML | €70.00 | 25 ML | €0.70 |
| TOTAL COST OF **NDI-Ph/3.76 G** | | | | | €56.57 |
| SYNTETIC COST OF **NDI-Ph/1 G** | | | | | €15.04 |
| COMMERCIAL COST OF **$C_{60}$ /1 G (Sigma-Aldrich)** | | | | | €681.00 |
| | | | | | |
| **NDI-pT** | | | | | |
| 1,4,4,8-Naphthalene tetracarboxylic dianhydride (**NDA**) | Sigma-Aldrich | 100 G | €621.00 | 2 G | €12.42 |
| 4-Aminobenzylamine | Sigma-Aldrich | 10 G | €110.00 | 1.72 ML | €18.92 |
| Dimethylformamide (**DMF**) | Sigma-Aldrich | 1000 ML | €200.00 | 35 ML | €7.00 |
| Hexane | Sigma-Aldrich | 2500 ML | €137.00 | 100 ML | €5.48 |
| Diethyl ether (**$Et_2O$**) | Sigma-Aldrich | 2500 ML | €121.00 | 100 ML | €4.84 |
| Ethyl acetate (**EtOAc**) | Sigma-Aldrich | 2500 ML | €96.50 | 100 ML | €3.86 |
| TOTAL COST OF **NDI-pT/3.00 G** | | | | | €52.52 |
| SYNTETIC COST OF **NDI-pT/1 G** | | | | | €17.50 |
| COMMERCIAL COST OF **$C_{60}$ /1 G (Sigma-Aldrich)** | | | | | €681.00 |

$C_{60}$'s spherical shape allows it to generate homogenous, isotropic films. Because of their spherical symmetry, $C_{60}$ molecules can pack well in various orientations

without needing to be aligned in a particular way. Strong contact with the perovskite layer is ensured by the continuous and compact layer development made possible by $C_{60}$'s isotropic nature during heat evaporation. This enhances electron extraction efficiency. However, anisotropic interactions with the perovskite layer are less likely to occur due to the absence of directional bonding sites on $C_{60}$, which results in lacking molecular orientation.

On the other hand, NDI molecules' rigid, planar shapes prefer to align themselves either parallel or perpendicular to the substrate during deposition. Depending on the surface characteristics of the substrate, NDI molecules may show preferential alignment during thermal evaporation. Proper alignment can facilitate charge transport, but misalignment may lead to increased resistance. The planar structure provides directional π-π stacking interactions and allows for better tuning of interfacial properties. However, uneven alignment might hinder uniform charge extraction. In conclusion, NDI-based ETLs provide tunability and stability benefits, despite the difficulty of attaining ideal molecule orientation during deposition, whereas $C_{60}$ is desirable for its uniform film formation.

The literature has not mentioned a perovskite solar cell produced using NDI-based ETLs through the evaporation method. Considering the advantages of NDI molecules over fullerene derivatives, two different NDI derivatives were synthesized in this part to be used as an alternative to the $C_{60}$ layer in p-i-n type PSCs. The structures of the molecules are given in **Figure 3.1**. The synthesized NDI-based ETLs were thermally evaporated on the perovskite layer, and we achieved functioning cells even with low performance.

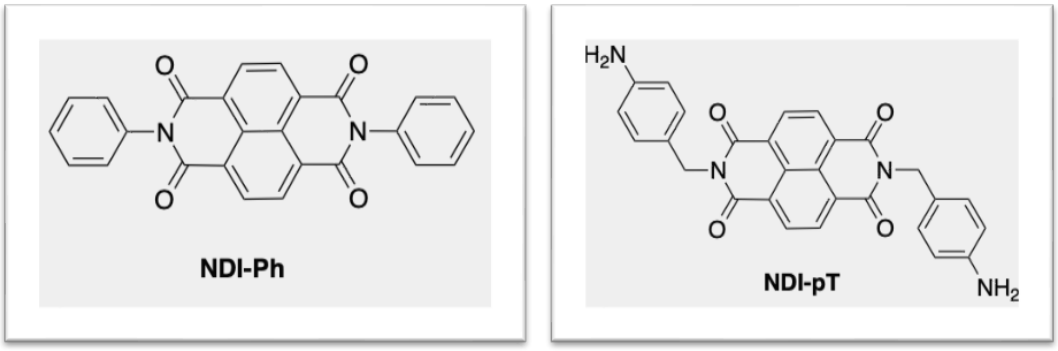



**Figure 3.1.** Molecule structures of NDI-based ETMs.

**NDI-pT** was engineered to promote lead alignment within the perovskite matrix via its two nitrogen atoms, aiding film passivation and orientation during evaporation. The 4-(aminomethyl)aniline group acts as an electron donor, featuring an amine (-$NH_2$) functionality. It lowers the NDI's LUMO level and improves energy alignment with the perovskite, facilitating efficient electron transfer to the ETL. The amine group also forms hydrogen bonds with the perovskite, enhancing interface contact and reducing recombination losses, thus boosting $V_{OC}$ and overall cell performance. Furthermore, 4-(aminomethyl)aniline can encourage NDI's lamellar ordering, improving electron mobility and minimizing ETL resistance.

The direct phenyl attached system in **NDI-Ph** was also designed to be tried in an evaporation system. The presence of a phenyl group on the axial position of NDI improves intermolecular interactions and helps create smoother, more uniform films. This quality improves the coverage and contact between the ETL and the perovskite layer. Furthermore, the phenyl group increases the steric bulk around the NDI core, enhancing molecular rigidity. This rigidity improves the structural integrity of the NDI layer during evaporation, preventing unwanted aggregation or structural collapse. This stability is crucial in vacuum-deposited layers, where uniform molecular packing is necessary for effective electron transport.

### 3.1.1 Experimental Procedure for the Synthesis of NDI Derivatives

To synthesize NDI derivatives, commercially available 1,4,4,8-naphthalene tetracarboxylic dianhydride (NDA) was reacted with the desired amine in a one-step reaction using dimethylformamide (DMF) as a solvent.

#### 3.1.1.1 Synthesis of NDI-Ph

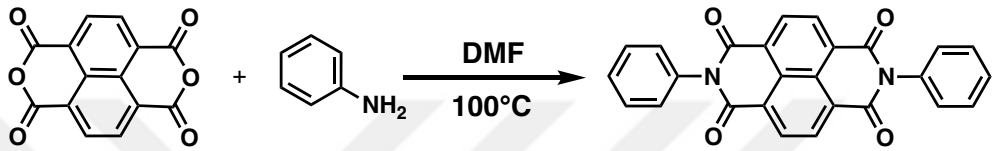



**Figure 3.2.** Synthetic route of **NDI-Ph.**

The commercially available NDA molecule (5.00 g, 18.6 mmol) for **NDI-Ph** was heated at 100 °C in 87 mL DMF solvent in the presence of the aniline (3.47 mL, 38.0 mmol) for 13 hours (**Figure 3.2**). After 13 hours, the reaction was poured into cold ethanol, and the solids that formed were filtered off. These solids were then dissolved in DCM and washed with water. The desired **NDI-Ph** structure was obtained in a 48% yield and confirmed by NMR spectroscopy.

**NDI-Ph**: $^{1}$H NMR (400 MHz, $CDCl_3$): $\delta$ 8.86 (s, 4H), 7.67 – 7.48 (m, 6H), 7.41 – 7.30 (m, 4H); $^{13}$C NMR (100 MHz, DMSO-$d_6$): $\delta$ 163.3, 135.9, 130.8, 129.4, 129.3, 128.8, 127.3, 127.0.

#### 3.1.1.2 Synthesis of NDI-pT

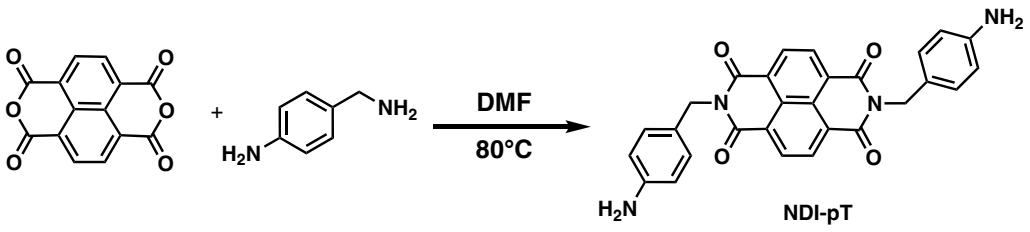



**Figure 3.3.** Synthetic route of **NDI-pT.**

The commercially available NDA molecule (2.00 g, 7.46 mmol) for **NDI-pT** was heated at 80 °C in 35 mL DMF solvent in the presence of 4-aminobenzylamine (1.72 mL, 15.2 mmol) for 13 hours (**Figure 3.3**). After 13 hours, DMF was removed from the system, and the remaining solids were washed with hexane, diethyl ether, and ethyl acetate, respectively. The desired **NDI-pT** structure was obtained in an 84% yield and confirmed by NMR spectroscopy.

**NDI-pT**: $^{1}$H NMR (400 MHz, DMSO-$d_6$): $\delta$ 8.58 (s, 4H), 7.11 (d, $J$ = 8.3 Hz, 4H), 6.49 (d, $J$ = 8.3 Hz, 4H), 5.06 (s, 4H), 5.02 (s, 4H); $^{13}$C NMR (100 MHz, DMSO): $\delta$ 162.6, 148.4, 130.8, 129.8, 126.4, 124.1, 121.1, 113.9, 43.3.

### 3.1.2 Optical and Electrochemical Properties

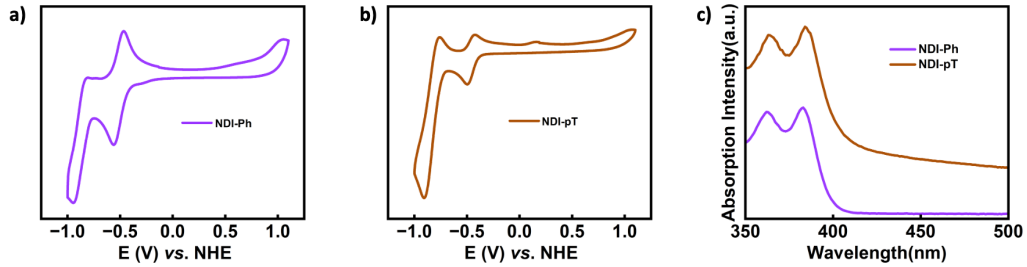



**Figure 3.4.** Cyclic Voltammograms of the **a) NDI-Ph** and **b) NDI-pT**, **c)** Uv-vis absorption spectra of **NDI-Ph** and **NDI-pT.**

The electrochemical properties of the **NDI-Ph** and **NDI-pT** were investigated by Cyclic Voltammetry (CV) measurements, which were carried out in a 0.1 M solution of tetra-*n*-butylammonium hexafluorophosphate (*n*-$Bu_4NPF_6$) in anhydrous DMF using glassy carbon working electrode, Pt reference electrode and Pt counter electrode calibrated by $Fc/Fc^+$ as an external reference (**Figure 3.4.a and Figure 3.4.b**). Potentials were converted to the normal hydrogen electrode (NHE) by adding +0.624 V and -4.44 eV to the vacuum, respectively (**Table 3.1**). The experimental $E_{LUMO}$ values are obtained from **Equation 3.1**, where the $E_{HOMO}$ values are calculated from cyclic voltammetry measurement. UV-vis spectroscopy in DMF

solvent was used to examine the optical characteristics of NDI-based ETMs; the spectra are shown in **Figure 3.2.b**. The produced NDI-based molecules show two maximal absorptions in the 350–400 nm range, which are consistent with the NDI core's π–π* transition (**Figure 3.4.c**).[254] Since NDI is a conjugated aromatic system, it displays π-π* transitions, usually between 300 and 400 nm in the ultraviolet-visible spectrum. **Table 3.1** provides an overview of the information gathered from the optical and electrochemical studies.

$$E_{LUMO} = E_{HOMO} + \Delta E_g; \quad \textbf{Equation 3.1}$$

$$\Delta E_g = 1240/\lambda_{onset} \quad \textbf{Equation 3.2}$$

**Table 3.2.** Optical and electrochemical properties of **NDI-pT, NDI-Ph,** and **$C_{60}$.**

| Compound | $\lambda_{max}$ [nm] | HOMO [eV] | LUMO [eV] | $\Delta E_g$ [eV] |
|---|---|---|---|---|
| **NDI-Ph** | 383 | -6.93 | -3.83 | 3.10 |
| **NDI-pT** | 384 | -6.91 | -3.89 | 3.02 |
| **$C_{60}$** | 348 | -6.30 | -4.10 | 2.00 |

### 3.1.3 Inverted Perovskite Solar Cells Fabrication and Efficiency Results with NDI-pT Derivative

#### 3.1.3.1 Device Fabrication

ITO-coated glasses were first etched with Zn powder and 4M HCl solution, and then they were trimmed to a size of 2 cm by 2 cm to create p-i-n type PSCs. The etched substrates were sonicated for ten minutes using diluted detergent, DI water, acetone, and IPA in that order. The substrates were then placed into an $N_2$-glovebox for the $NiO_x$ deposition process. A 15 nm thick layer of $NiO_x$ was then sputtered from a Ni metal target using RF sputtering with a power of 215W, employing $O_2$ plasma at a pressure of 6 mTorr on the substrate, and it was then annealed at 300 °C for 15 minutes in air. The same thermal evaporator was used to co-evaporate the $PbI_2$-CsBr seed layer at a pressure of about $1x10^{-7}$ Torr, 4 Å/s rate for $PbI_2$, thickness of 230

nm, and rate of 0.6 Å/s for CsBr. Afterward, the seed layer was spin-coated with 2100 rpm for 30 seconds to create a perovskite layer in the glove box using an organic solution containing FAI (0.31 M), MACl (0.08 M), and absolute ethanol. The organic solution was then moved to the air for post-annealing at 130°C for 15 minutes. The substrates were moved into the thermal evaporator for ETL deposition. At $10^{-6}$-$10^{-7}$ Torr base pressure, 100 nm of Cu was thermally evaporated as the top contact after 0.8 nm of LiF, 30 nm of $C_{60}$ for the reference device, 25 nm and 30 nm **NDI-pT** as the target devices and 7 nm of bathocuproine (BCP) were first evaporated.

#### 3.1.3.2 Results and Discussion

NDI-based n-type molecules were synthesized via a one-step reaction starting from a commercially available NDA precursor. This process involved coupling with the desired amine, successfully obtaining the target molecule with a high yield at a lower cost than their literature counterpart, which is fullerene. The absorption and electronic properties of the synthesized NDI derivatives align well with those reported in the literature, supporting their potential application as ETLs in inverted PSCs. Furthermore, NDI derivatives can show hole-blocking properties due to their deeper HOMO level than $C_{60}$. These findings suggest that NDI derivatives could be effectively employed as ETLs in p-i-n-type device architectures. Two thicknesses of the **NDI-pT** derivative were investigated, with the resulting *I-V* characteristics and device parameters presented in **Figure 3.5** and **Table 3.3**. Devices with a reference $C_{60}$ ETL and 25 nm and 30 nm **NDI-pT** layers as $C_{60}$ alternatives were fabricated via thermal evaporation. Initial studies on p-i-n-type devices indicate that, without optimization, **NDI-pT** demonstrates inferior performance compared to $C_{60}$. The *I-V* curve reveals high resistance for both thicknesses of **NDI-pT**, suggesting that a thinner **NDI-pT** layer may mitigate this issue.

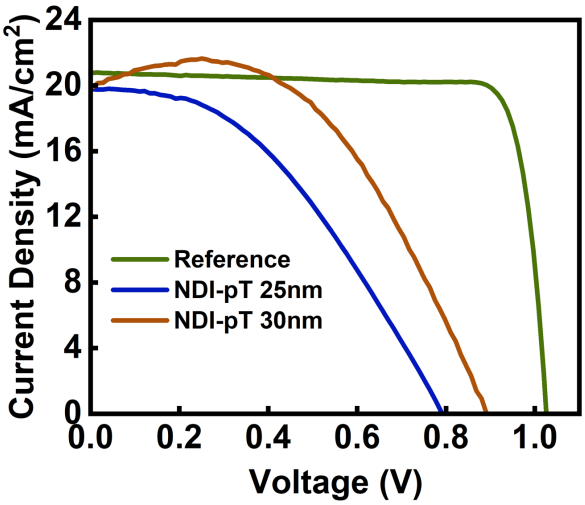



**Figure 3.5.** *J-V* curve of the thickness study of **NDI-pT**.

**Table 3.3.** Photovoltaic parameters of the reference and the target devices.

| Device | $J_{SC}$ (mA/cm²) | $V_{OC}$ (V) | FF (%) | PCE (%) |
|---|---|---|---|---|
| **Reference** | 20.79 | 1.03 | 83.98 | 18.66 |
| **NDI-pT 25 nm** | 19.76 | 0.79 | 41.52 | 6.77 |
| **NDI-pT 30 nm** | 19.91 | 0.89 | 53.85 | 9.96 |

In addition to reducing film thickness, optimizing deposition parameters, such as the evaporation rate that affects crystallinity, and implementing structural modifications to the NDI unit are crucial for enhancing device performance. The synthesized NDI-based molecules could also serve as an alternative buffer layer to BCP in the reference cell architecture. Therefore, considering their potential for more cost-competitive synthesis, these NDI derivatives show promise as effective ETLs compared to fullerene and represent a promising area of investigation. Further analysis of these molecules' structural and electronic properties, especially optimizing parameters such as energy levels and carrier mobilities, could offer valuable insights for future applications.

## 3.2 Synthesis of Fluorene-Based $NiO_x$ Layer Passivation Molecules for Inverted PSCs

Despite being the primary hole transport layer in p-i-n type PSCs, $NiO_x$ has a complex surface chemistry that can include $Ni(OH)_2$, NiO(OH), and $Ni_2O_3$. Interactions between these elements and the perovskite layer may result in faster deterioration and interfacial charge carrier recombination, reducing PCE and stability. This interface can be stabilized, and the deterioration of the perovskite film can be lessened by adding another organic layer.[255] Compared to PTAA, **DFH**, a fluorene-based hole transport layer, is a low-cost, high-performance material proposed in an inverted perovskite solar cell structure and synthesized in literature.[256] **DFH** can be made for as little as 3$/g, compared to PTAA's price of 2000$/g. Furthermore, the **DFH** structure will be useful for a straightforward thermal evaporation procedure because of its low molecular weight. **Figure 3.3** shows the architectures of the innovative materials influenced by the **DFH** molecules.

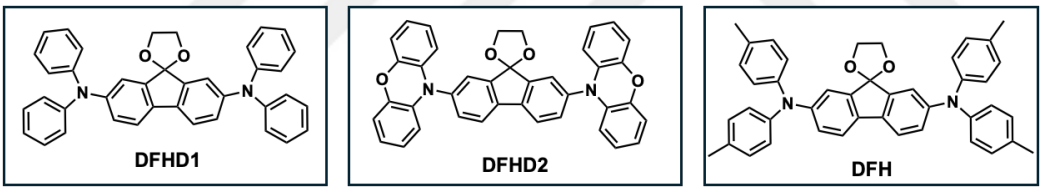



**Figure 3.6.** Molecule structures of **DFH**-based molecules.

The reasons behind adding methyl groups to the **DFH** structure in the literature were assumed to be improved molecule solubility and film-forming capabilities. Given that this chapter will employ thermal evaporation for coating, the only phenyl group-containing structure is anticipated to exhibit comparable performance at a reduced expense in the design of the **DFHD1** structure. The phenyl structures with free rotation in the **DFH** structure are fixed in the derivative intended for **DFHD2**. The more rigid variant of the structure is anticipated to improve the hole transfer characteristics. Additionally, the oxygen atoms in the **DFHD2** structure can passivate the undercoordinated $Pb^{+2}$ ions in the perovskite film via electron transfer.

### 3.2.1 Experimental Procedure for the Synthesis of DFH Derivatives

DFH molecules are synthesized by a three-step reaction that starts with brominating the fluorenone core from *meta* positions and then protecting the carbonyl unit in the brominated fluorenone structure. This is followed by coupling the desired amine unit with the brominated carbonyl-protected fluorenone core by the Buchwald-Hartwig reaction.

#### 3.2.1.1 Synthesis of 2,7-dibromo-9*H*-fluoren-9-one

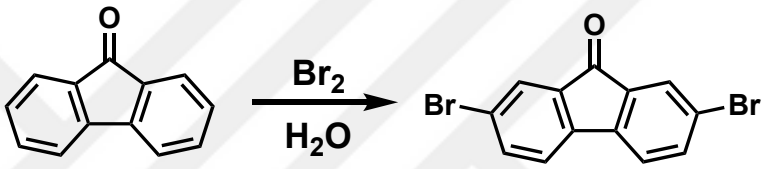



**Figure 3.7.** Synthetic route of **2,7-dibromo-9*H*-fluoren-9-one**.

For the synthesis of **2,7-dibromospiro[fluorene-9,2'-[1,3] dioxolane]**, neat $Br_2$ (7.00 mL, 138 mmol) was added to a solution of fluorenone (5.00 g, 27.7 mmol) in $H_2O$ (70 mL) over 10 min at 0 °C, then heated to 80 °C and stirred for 10 h. After 10 hours, the reaction was cooled to room temperature, and additional $H_2O$ (150 mL) was added, followed by a saturated $Na_2SO_3$ solution (150 mL). The crude residue was filtered and washed with $H_2O$ to yield a solid yellow product (**2,7-dibromo-9*H*-fluoren-9-one**) of 96% yield. The desired product was purified by column chromatography and confirmed by NMR spectroscopy.

**2,7-dibromo-9*H*-fluoren-9-one**: $^1$H NMR (400 MHz, $CDCl_3$): $\delta$ 7.77 (s, 2H), 7.71 – 7.62 (m, 2H), 7.39 (d, $J$ = 7.9 Hz, 2H); $^{13}$C NMR (100 MHz, $CDCl_3$): $\delta$ 142.1, 137.4, 135.1, 127.7, 123.2, 121.7.

### 3.2.1.2 Carbonyl Protection in the 2,7-dibromo-9*H*-fluoren-9-one unit

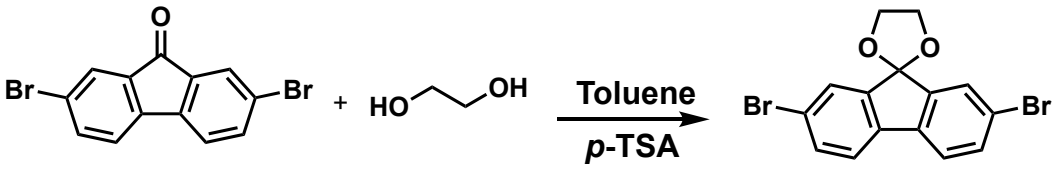



**Figure 3.8.** Synthetic route of **2,7-dibromospiro[fluorene-9,2'-[1,3]dioxolane]**.

For the synthesis of **2,7-dibromospiro[fluorene-9,2'-[1,3] dioxolane]**, dibromo fluorenone unit (5.00 g, 14.8 mmol) and *p*-TSA (280 mg, 1.48 mmol) were put in a double neck round bottom flask and was linked to Dean-Stark apparatus via a condenser and Schenk line. The flask was recycled between vacuum and Ar 3 times. Then dry toluene (90 mL) was added and stirred for 5-10 mins. After stirring, ethylene glycol (7.45 mL, 133 mmol) was added.
The reaction was placed in an oil bath with a temperature of 135 °C and left for overnight at 130 °C. TLC showed a new spot after an overnight stirring, indicating the synthesis of **2,7-dibromospiro[fluorene-9,2'-[1,3] dioxolane]** with a 44% yield. The desired product was purified by column chromatography and confirmed by NMR spectroscopy.

**2,7-dibromospiro[fluorene-9,2'-[1,3] dioxolane]:** $^{1}$H NMR (400 MHz, $CDCl_3$): $\delta$ 7.54 (s, 2H), 7.50 (dd, $J$ = 8.0, 1.7 Hz, 2H), 7.38 (d, $J$ = 8.0 Hz, 2H), 4.42 (s, 4H); $^{13}$C NMR (100 MHz, $CDCl_3$): $\delta$ 145.7, 137.5, 133.3, 127.3, 122.2, 121.4, 111.4, 66.0.

### 3.2.1.3 Synthesis of DFHD1

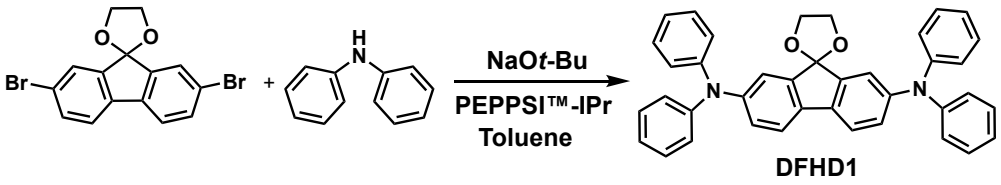



**Figure 3.9.** Synthetic route of **DFHD1**.

Using a palladium catalyst, the Buchwald-Hartwig reaction was utilized to link diphenylamine and **2,7-dibromospiro[fluorene-9,2'-[1,3]dioxalane]** to obtain **DFHD1** derivative. In a two-neck Schlenk tube attached to the Schlenk line, the protected dibromo fluorenone (400 mg, 1.05 mmol), diphenyl amine (372 mg, 2.20 mmol), NaO*t*-Bu (211 mg, 2.20 mmol), and PEPPSI$^{TM}$-*i*Pr (0.01 mmol, 7 mmol) were added to initiate the reaction. Three cycles of the combination were performed using argon and vacuum. After adding 5.00 mL of anhydrous toluene to the reaction mixture as a reaction solvent, the reaction was heated to 100 °C and allowed to sit overnight. The next day, TLC showed a new spot. Methanol was added to the reaction mixture to precipitate, filtered, and collected. Column chromatography was used to purify the intended product, yielding a 54% yield, and was validated by NMR spectroscopy.

**DFHD1**: $^{1}$H NMR (400 MHz, $CDCl_3$): $\delta$ 7.31 (d, $J$ = 8.1 Hz, 2H), 7.25 – 7.21 (m, 8H), 7.14 (d, $J$ = 1.7 Hz, 2H), 7.10 (d, $J$ = 7.6 Hz, 8H), 7.04 – 6.96 (m, 6H), 4.16 (s, 4H); $^{13}$C NMR (100 MHz, $CDCl_3$): $\delta$ 147.6, 147.3, 145.4, 134.1, 129.2, 126.0, 124.0, 122.7, 120.1, 119.7, 111.7, 65.5.

### 3.2.1.4 Synthesis of DFHD2

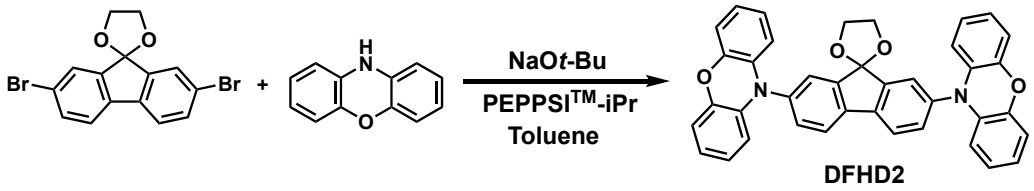



**Figure 3.10.** Synthetic route of **DFHD2**.

The Buchwald-Hartwig reaction was utilized to link 10*H*-phenoxazine and **2,7-dibromospiro[fluorene-9,2'-[1,3]dioxalane]** using a palladium catalyst. In a two-neck Schlenk tube attached to the Schlenk line, the protected dibromo fluorenone (400 mg, 1.05 mmol), phenoxazine (403 mg, 2.20 mmol), NaO*t*-Bu (211 mg, 2.20 mmol), and PEPPSI$^{TM}$-*i*Pr (0.01 mmol, 7 mmol) were added to initiate the reaction.

Three cycles of the combination were performed using argon and vacuum. After adding 4.2 mL of anhydrous toluene to the reaction mixture as a reaction solvent, the reaction was heated to 100 °C and allowed to sit overnight. The next day, TLC showed a new spot. Methanol was added to the reaction mixture to precipitate, filtered, and collected. Column chromatography was used to purify the intended product, yielding a 49% yield, and was validated by NMR spectroscopy.

**DFHD2**: $^{1}$H NMR (400 MHz, $CDCl_3$): $\delta$ 7.85 (d, $J$ = 7.9 Hz, 2H), 7.49 (s, 2H), 7.43 (d, $J$ = 7.9 Hz, 2H), 6.76 – 6.62 (m, 12H), 6.06 (d, $J$ = 7.7 Hz, 4H), 4.39 (s, 4H); $^{13}$C NMR (100 MHz, $CDCl_3$): $\delta$ 147.9, 143.8, 139.1, 138.8, 134.0, 133.2, 126.7, 123.2, 122.6, 121.4, 115.4, 113.2, 111.3, 66.0.

### 3.2.2 Optical and Electrochemical Properties

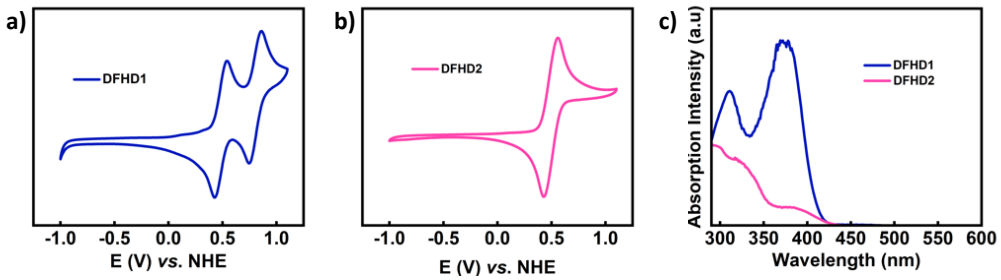



**Figure 3.11.** Cyclic voltammograms of the **a) DFHD1** and **b) DFHD2**, **c)** Uv-Vis absorption spectra of **DFHD1** and **DFHD2**.

The electrochemical properties of the **DFHD1** and **DFHD2** were investigated by Cyclic Voltammetry (CV) measurements, which were carried out in a 0.1 M solution of tetra-n-butylammonium hexafluorophosphate ($n$-$Bu_4NPF_6$) in anhydrous DCM using glassy carbon working electrode, Pt reference electrode and Pt counter electrode calibrated by $Fc/Fc^+$ as an external reference (**Figure 3.3.a** and **Figure 3.3.b**). Potentials were converted to the normal hydrogen electrode (NHE) by adding +0.624 V and -4.44 eV to the vacuum, respectively (**Table 3.2**). The experimental $E_{LUMO}$ values are obtained from **Equation 3.1**, where the $E_{HOMO}$ values are

calculated from cyclic voltammetry measurement. The synthesized DFH derivatives show absorption maximum at 317 and 372 nm for the **DFHD1** and **DFHD2** molecules, respectively. The HOMO energy levels of the DFH molecules are well-aligned with those of the $NiO_x$ HTL, facilitating efficient hole transfer from the $NiO_x$ to the perovskite layer without introducing an energy barrier.

**Table 3.4.** Optical and electrochemical properties of **DFHD1**, **DFHD2**, and $NiO_x$.

| Compound | $\lambda_{max}$ [nm] | HOMO [eV] | LUMO [eV] | $\Delta E_g$ [eV] |
|---|---|---|---|---|
| **DFHD1** | 372 | -5.31 | -2.30 | 3.01 |
| **DFHD2** | 317 | -5.40 | -2.02 | 3.38 |
| **NiOx** | 305 | -5.40 | -1.79 | 3.60 |

The initial passivation study in inverted PSCs was conducted using the **DFHD2** molecule. The subsequent fabrication steps and results are detailed in the following section. Future studies will involve the **DFHD1** molecule.

### 3.2.3 Inverted Perovskite Solar Cells Fabrication and Efficiency Results with DFHD2 Derivative

#### 3.2.3.1 Device Fabrication

ITO-coated glasses were first etched with Zn powder and 4M HCl solution, and then they were trimmed to a size of 2 cm by 2 cm to create p-i-n type PSCs. The etched substrates were sonicated for ten minutes using diluted detergent, DI water, acetone, and IPA in that order. The substrates were then placed into an $N_2$-glovebox for the $NiO_x$ deposition process. A 15 nm thick layer of $NiO_x$ was then sputtered from a Ni metal target using RF sputtering with a power of 215W, employing $O_2$ plasma at a pressure of 6 mTorr on the substrate, and it was then annealed at 300 °C for 15

minutes in air. The passivation **DFHD2** layer was then deposited on the samples by placing them within the thermal vacuum chamber (NANOVAK) housed in a glovebox filled with $N_2$. The passivation layer was evaporated to the required thicknesses after the vacuum chamber was adjusted to $1x10^{-7}$ Torr pressure. The same thermal evaporator was used to co-evaporate the $PbI_2$-CsBr seed layer at a pressure of about $1x10^{-7}$ Torr, 4 Å/s rate for $PbI_2$, thickness of 230 nm, and rate of 0.6 Å/s for CsBr. Afterward, the seed layer was spin-coated with 2100 rpm for 30 seconds to create a perovskite layer in the glove box using an organic solution containing FAI (0.31 M), MACl (0.08 M), and absolute ethanol. The organic solution was then moved to the air for post-annealing at 130°C for 15 minutes. The substrates were moved into the thermal evaporator for ETL deposition. At $10^{-6}$-$10^{-7}$ Torr base pressure, 100 nm of Cu was thermally evaporated as the top contact after 0.8 nm of LiF, 30 nm of $C_{60}$, and 7 nm of bathocuproine (BCP) were first evaporated.

#### 3.2.3.2 Results and Discussion

DFH-based molecules are synthesized via a three-step reaction sequence that begins with the fluorenone precursor unit. In the first step, fluorenone undergoes bromination at the meta positions, followed by the protection of its carbonyl group, resulting in the formation of the intermediate compound **2,7-dibromospiro[fluorene-9,2'-[1,3]dioxolane]**. In the subsequent step, this intermediate is coupled with the target amine to produce the DFH derivative. Initial experiments incorporating these DFH derivatives into inverted PSCs via co-evaporation have shown promising results, especially with the **DFHD2** variant.

To optimize the film thickness of **DFHD2**, it was deposited atop $NiO_x$ layers at varying thicknesses of 1 nm, 3 nm, and 5 nm. The *J-V* characterization of the different **DFHD2** thicknesses on $NiO_x$ is presented in **Figure 3.11**. Among the tested thicknesses, the 1 nm **DFHD2** layer exhibited superior performance in $V_{OC}$ and FF compared to the reference and the 3 nm and 5 nm **DFHD2** layers. These findings suggest that fine-tuning the **DFHD2** layer thickness could enhance charge transport

and device efficiency in inverted PSCs, with 1 nm appearing optimal for maximizing $V_{OC}$ and FF values.

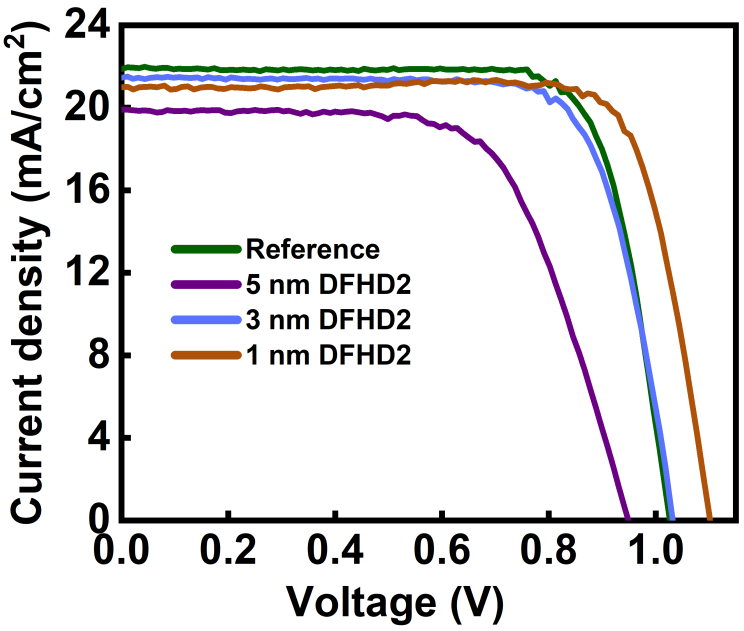



**Figure 3.12.** *J-V* curve of the thickness study of **DFHD2**.

By adding the **DFHD2** layer, the hysteresis index is also less than the reference device's, indicating better ion transportation. The better $V_{OC}$ demonstrates that the **DFHD2** layer functions as an interlayer to passivate the recombination centers (**Table 3.3**).

**Table 3.5.** Photovoltaic parameters of the reference and the **DFHD2**-treated inverted PSCs.

| Device | $J_{SC}$ (mA/cm²) | $V_{OC}$ (V) | FF % | PCE % | HI % |
|---|---|---|---|---|---|
| **Reference-reverse** | 20.40 | 1.06 | 79.40 | 17.17 | 12.5 |
| **Reference-forward** | 19.90 | 1.09 | 69.23 | 15.02 | |
| **DFHD2-reverse** | 20.57 | 1.10 | 81.47 | 18.43 | 11.9 |
| **DFHD2-forward** | 19.90 | 1.10 | 74.20 | 16.24 | |

# CHAPTER 4

# EFFECT OF POLYMERIC ADDITIVES ON THE EFFICIENCY AND STABILITY OF N-I-P STRUCTURED PSCS

## 4.1 Introduction

Due to their adaptable qualities, polymers are excellent choices for various uses, including solar energy. PSCs can be optimized using their ease of modification and optical tuning capabilities. Polymer encapsulation, due to its flexibility, hydrophobicity, and transparency, is a commonly used approach to prevent moisture infiltration in PSC systems. PMMA, PDMS, and PEG are commonly utilized encapsulating materials that have improved PSC stability.[257] In addition to encapsulation, attempts to improve performance and lengthen the stability of devices have been made continuously in recent years with polymer additives in CTL and perovskite layers. Jones et al. examined polymer utilization options to enhance PSC performance and stability in 2021.[258] The polymer can be added to the perovskite precursor solution[259] to form the active layer. Alternatively, it can be used as an encapsulant to improve PSC stability by blocking moisture diffusion[260], or as a passivation layer on top of 3D perovskite.[261] The electron distribution of the passivating molecules is the paramount consideration in the design guidelines for creating an effective passivation layer for perovskites. Adopting a donor-π-acceptor (D-π-A) configuration is a frequently employed tactic that suppresses the trap states by using the moiety's tendency toward electron withdrawal or donation. Extended π spacer groups between the passivator molecule's D and A derivatives display molecular planarity throughout the passivated surface and cause electron delocalization due to the conjugated π bonds. Wu et al. discovered that a significant electron density would be produced on the carboxyl functional group at the acceptor end of D-π-A molecules due to their strong dipole nature. By coordinating with the

undercoordinated $Pb^{2+}$ sites, this electron-rich area can eventually prevent the harmful formation of metallic $Pb^0$.[262]

When employed in OFETs and OPVs, conjugated polymers based on DPP have garnered interest because of their remarkable mobility and wide-ranging absorption properties.[146,147] PSC architecture incorporates a few publications from the literature that discuss DPP-based polymers. Thiophene-substituted derivatives of DPP-based polymers are the most widely used ones; these have been thoroughly examined in OFETs[148,149] When employed as hole transport materials (HTMs), DPP-based polymers, which are hydrophobic, demonstrate better stability and efficiency than the widely used HTM *spiro*-OMeTAD. When they are utilized as an interlayer or additive in the perovskite layer, they can protect the perovskite layer by creating a moisture barrier.[263–265] By switching from sulphur to selenium, two chalcogens with distinct atomic radii can modify the resulting polymers' optoelectronic characteristics and enhance the stability and performance of PSCs. Nonetheless, a thorough knowledge of the impact of DPP-based polymers on several PSC aspects still needs to be improved in the literature.

Here, high-quality perovskite films with high stability and efficiency of n-i-p type PSC are formed by introducing donor units of biselenophene (***poly*-ADD1**) and thienothiophene (***poly*-ADD2**) into the perovskite layer in CB as an antisolvent. This is achieved by using DPP-based polymeric materials. The PSC containing ***poly*-ADD1** exhibits a higher PCE of approximately 21% and stability (retaining 67% of its initial PCE after 1600 hours of storage in a humid ambient air condition without any encapsulation at 85 °C) than the reference and ***poly*-ADD2**-containing device, which maintain 29% and 23% under the same conditions. The ***poly*-ADD1**-treated device's $V_{OC}$, $J_{SC}$, and FF are 1.11 V, 23.23 mA/cm$^2$, and 81.23%, respectively. Further evidence of reduced crystal defects and improved ***poly*-ADD1** passivation was provided by the hysteresis index (HI), which decreased from 0.07 for the reference device to 0.048 for the ***poly*-ADD1**-treated device.

## 4.2 Results and Discussion

The synthetic details of DPP-based polymeric passivators are reported in the Ph.D. theses of Dr. Aliekber Karabag and Dr. Figen Varlioglu Yaylali for the ***poly*-ADD1** and ***poly*-ADD2**, respectively[181,228]. The PSC device architecture and the molecular structures of ***poly*-ADD1** and ***poly*-ADD2** are displayed in **Figure 4.1**. The PSC in use is composed of a typical n-i-p type structure with a bottom electrode of FTO, a *cp*-$TiO_2$ layer, a *mp*-$TiO_2$ layer, a $SnO_2$ layer, an active layer of perovskite, a HTL of *spiro*-OMeTAD, and a top electrode of Au. The experiment section reports the specific fabrication steps.

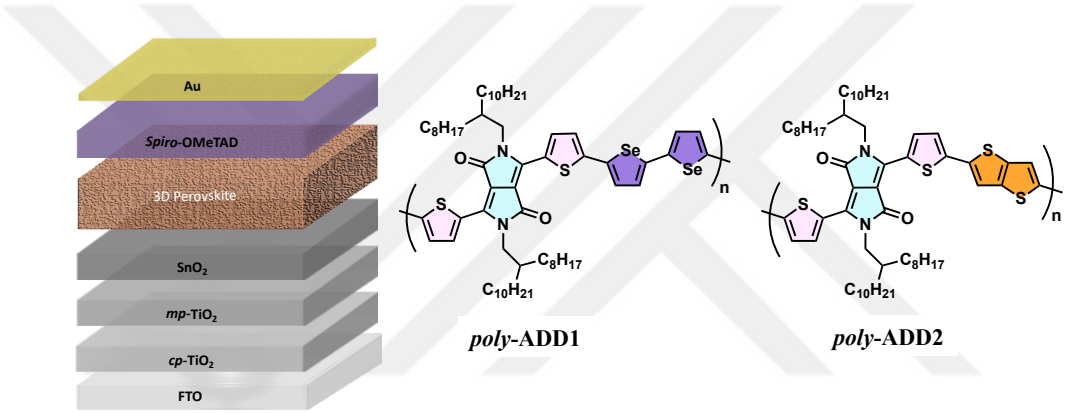



**Figure 4.1.** General n-i-p perovskite device architecture and the molecule structures of ***poly*-ADD1** and ***poly*-ADD2**.

**Table 4.1.** Photovoltaic device parameters of unencapsulated reference, ***poly*-ADD1**- and ***poly*-ADD2**-treated champion PSCs (kept under ambient conditions for 21 days).

| | $V_{OC}$ (V) | $J_{SC}$ (mA/cm²) | FF (%) | PCE (%) (avg.) | HI (%) |
|---|---|---|---|---|---|
| **Reference** | 1.11 | 22.92 | 80.35 | 20.51 (18.53) | 7.0 |
| ***poly*–ADD1** | 1.11 | 23.23 | 81.23 | 20.97 (19.89) | 4.8 |
| ***poly*–ADD2** | 1.11 | 22.59 | 81.62 | 20.57 (19.47) | 6.2 |

The PSC device parameters, fabricated by utilizing polymeric additives at the optimal concentration, are compiled in **Table 4.1.** along with the reference device. With an 81.23% FF, 23.23 mA/cm$^2$ $J_{SC}$, 1.11 V $V_{OC}$, and less hysteresis (4.8%), ***poly*-ADD1**-treated PSC exhibits a champion efficiency of 20.97% where the reference device displays a PCE of 20.51%, 80.35% FF, 22.92 mA/cm$^2$ $J_{SC}$, 1.11V $V_{OC}$, and a 7.0% hysteresis. Adding ***poly*-ADD1** and ***poly*-ADD2** does not change the transmission properties of the resulting films as shown in **Figure 4.2.a**. PL intensity is decreased upon the addition of the DPP-based polymers, pointing to the enhanced charge extraction from perovskite to the hole transport layer (**Figure 4.2.b**).

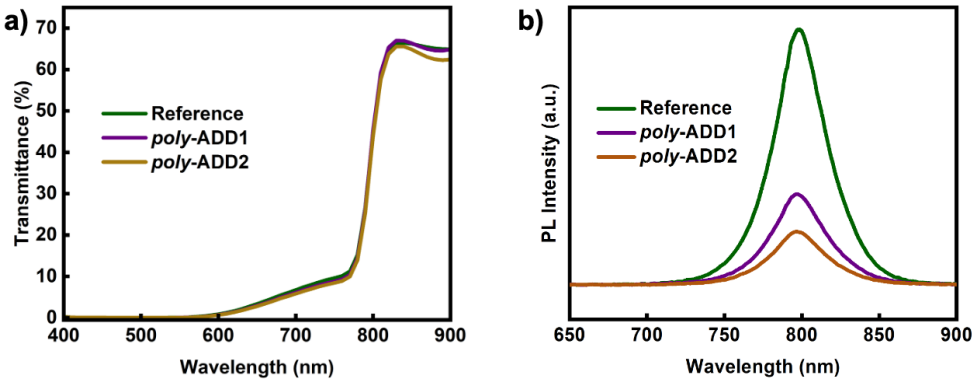



**Figure 4.2. a)** Transmission spectra of the reference, ***poly*-ADD1** and ***poly*-ADD2** films. **b)** PL spectrum of the reference, ***poly*-ADD1**, and ***poly*-ADD2** films.

According to the single scan cyclic voltammetry analysis, the HOMO energy levels of ***poly*-ADD1** and ***poly*-ADD2** are well aligned with the VB of perovskite film which are -5.51 eV, -5.58 eV, and -5.49 eV, respectively (**Figure 4.3.** and **Table 4.2**). That means the photogenerated holes can be transported to the HTL through the perovskite/hole transport layer. Furthermore, the higher LUMO energy level of the ***poly*-ADD1** (-3-73 eV) than the CB of the perovskite film itself (-3.94 eV) could hinder the electron transport to the hole transport layer, which is not the case in ***poly*-ADD2** whose $E_{LUMO}$ is much lower (-4.25 eV).

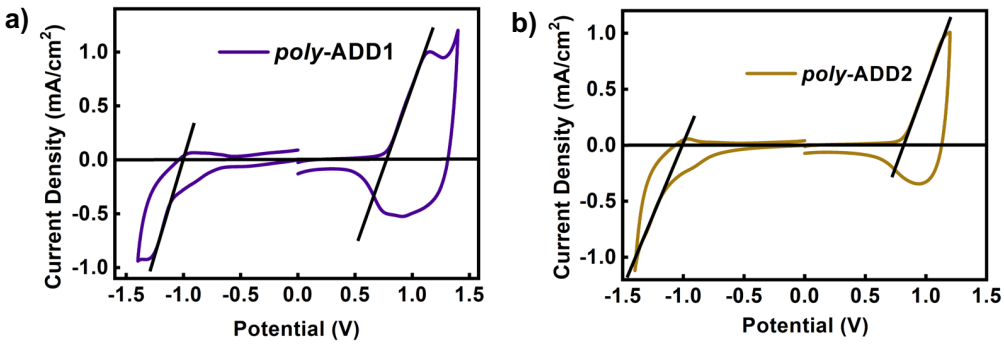



**Figure 4.3**. Cyclic voltammograms of the **a) *poly*-ADD1** and **b) *poly*-ADD2.**

**Table 4.2.** Optical and electrochemical properties of the pristine perovskite layer, ***poly*-ADD1** and ***poly*-ADD2** molecules.

| Material | HOMO [eV] | LUMO [eV] | $\Delta E_g$ [eV] |
|---|---|---|---|
| ***poly*-ADD1** | -5.51 | -3.73 | 1.78 |
| ***poly*-ADD2** | -5.58 | -4.25 | 1.33 |
| **Perovskite** | -5.49 | -3.94 | 1.55 |

The reference and the polymer-treated perovskite films are analysed using XRD, SEM, and AFM to elucidate the efficiency increase. **Figure 4.4** displays the XRD patterns of the reference, ***poly*-ADD1**, and ***poly*-ADD2** treated films. The primary diffraction peaks of the 3D perovskite and $PbI_2$ phases appear at 14.00° and 12.6°, respectively. The $PbI_2$ diffraction peak decreases with the application of the polymer. When ***poly*-ADD1** is added, the $PbI_2$ peak decreases far more quickly, demonstrating the polymer's and perovskite's interaction.[266]

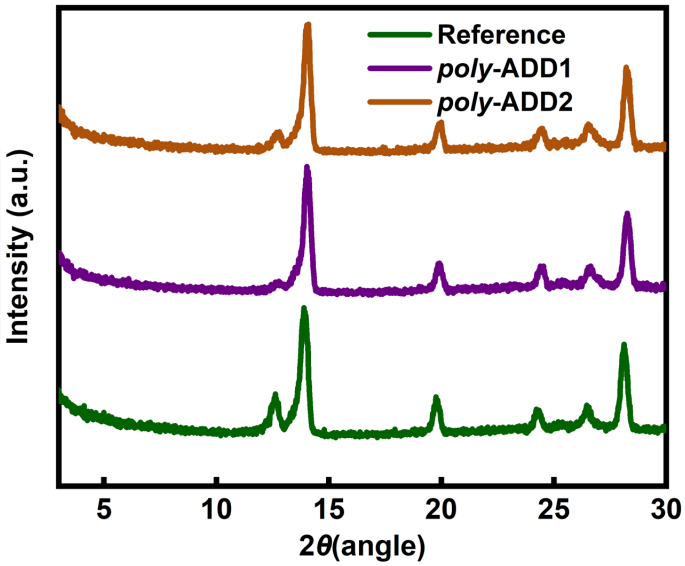



**Figure 4.4.** XRD Spectrum of the reference, ***poly*-ADD1**, and ***poly*-ADD2**-treated films.

Following treatment with ***poly*-ADD1** and ***poly*-ADD2**, the resulting perovskite films have different surface morphologies, as shown in SEM images in **Figure 4.5**. Due to the clear white contrast, extra $PbI_2$ is visible on the surface of the reference film. Nonetheless, the films treated with ***poly*-ADD1** and ***poly*-ADD2** showed a decrease in the $PbI_2$ phase.

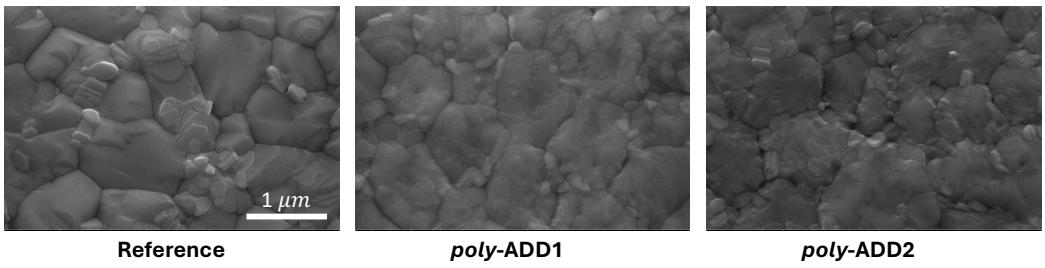



**Figure 4.5.** SEM images of the resulting reference, ***poly*-ADD1**, and ***poly*-ADD2**-treated films.

**Figure 4.6** displays AFM images of the reference and the films treated with polymer. Compared to the reference film, the surfaces of the ***poly*-ADD1** and ***poly*-ADD2** films are smoother. The films produced by adding ***poly*-ADD1** and ***poly*-ADD2** exhibit lower root mean square (RMS) values of 18.86 nm and 19.33 nm, respectively, and for the reference film is 24.09 nm.

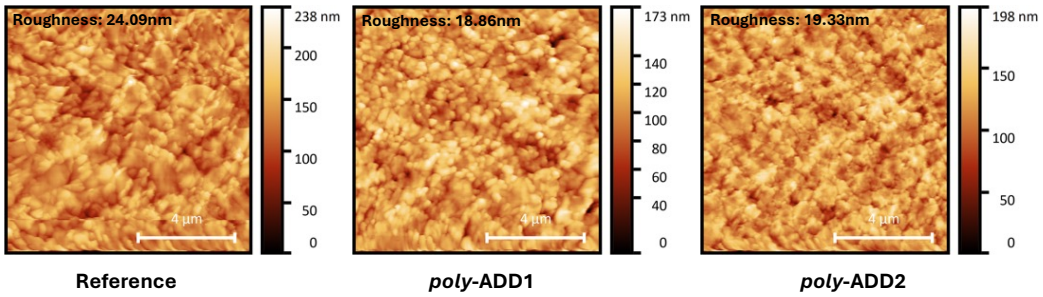



**Figure 4.6.** AFM images of the reference and polymer-treated films.

X-ray photoelectron spectroscopy (XPS) analysis was conducted to investigate the interaction between the polymers and the perovskite film. The presence of $Pb^0$ negatively impacts device performance, as it can create recombination sites due to the unsaturated nature of Pb.[267] A reduction in the metallic lead ($Pb^0$) peak is observed at low polymer concentrations, and this peak nearly vanishes when a higher concentration of polymers is introduced. This reduction in the $Pb^0$ ratio has been linked to enhanced stability in polymer-passivated PSCs. Adding ***poly*-ADD1** and ***poly*-ADD2** passivation layers results in a slight shift to lower binding energy (BE) for Pb 4f and I 3d, suggesting a change in surface bonding within the perovskite as shown in **Figure 4.7**. This observation is consistent with findings from existing literature.[268,269]

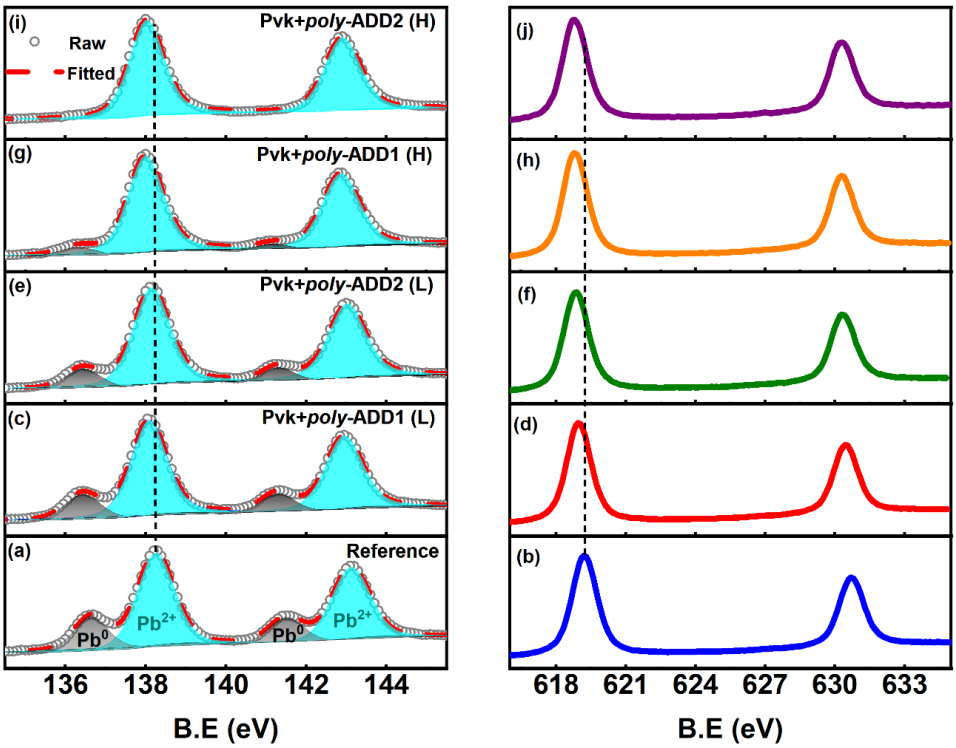



**Figure 4.7.** XPS spectra of Pb 4f and I 3d in reference and polymer-treated films.

As seen in **Figure 4.8**, contact angles between the polymer-treated perovskite films and the reference are also measured with water. Because the polymers are water-repellent and can shield the perovskite surface from moisture, polymer-treated films have higher hydrophobic surfaces than the control perovskite film, enhancing their moisture stability.

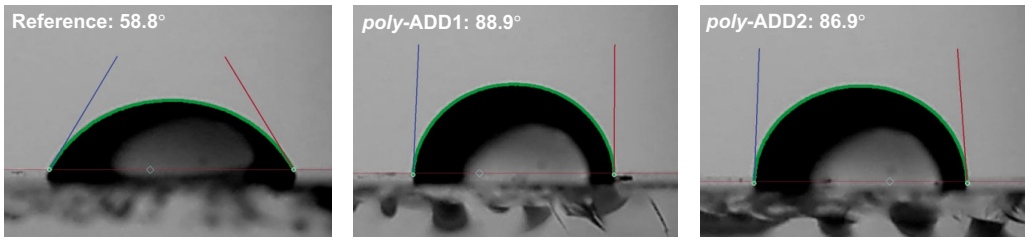



**Figure 4.8.** Contact angle results of the prepared reference and polymer-treated films.

Long-term stability is one of the most critical characteristics of PSCs used in commercial applications. The unencapsulated device's stability was assessed at 85 °C in ambient conditions, as shown in **Figure 4.9**. After 1600 hours, the ***poly*-ADD1-**

containing champion PSC exhibits excellent thermal stability, retaining 67% of its initial PCE. Under the same conditions, the pristine and ***poly*-ADD2** devices show more substantial degradation, losing 29% and 27% of their initial PCE, respectively. This difference in stability highlights the effectiveness of ***poly*-ADD1** in improving the thermal robustness of PSCs. The underlying reason of the reduced thermal stability in ***poly*-ADD2**-treated PSCs is currently under investigation. Further characterizations are planned to provide clarification on this matter.

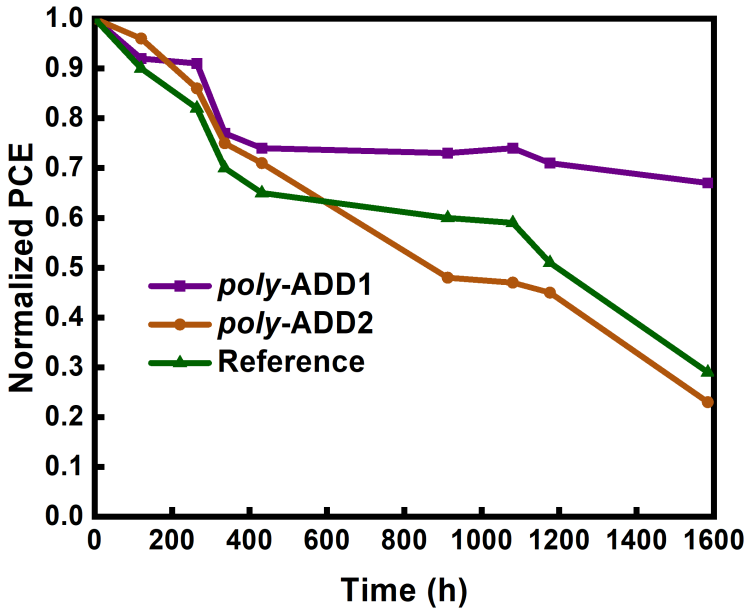



**Figure 4.9.** Thermal stability test results of unencapsulated ***poly*-ADD1**- and ***poly*-ADD1**-treated PSCs kept on a hot plate at 85℃ for 1600 h under ambient conditions.

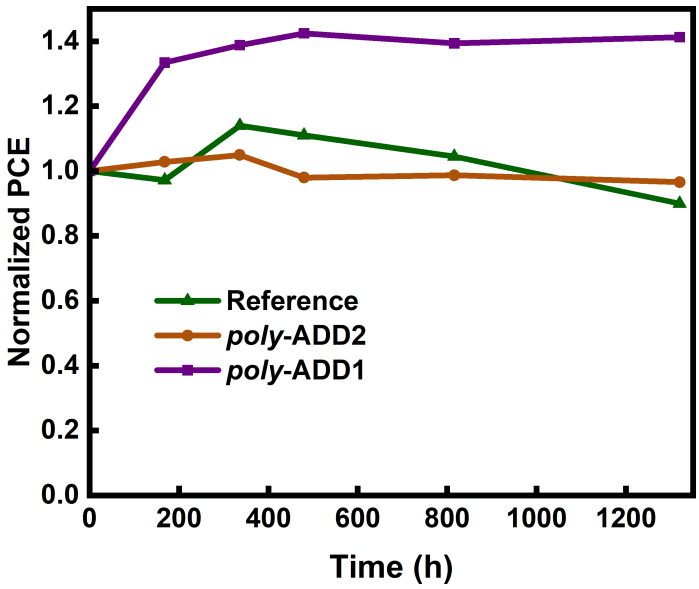



**Figure 4.10.** Ambient air stability test results of unencapsulated ***poly*-ADD1**- and ***poly*-ADD1**-treated PSCs at ~35% RH for 1320 h under ambient conditions.

Ambient air stability testing revealed significant durability enhancements with ***poly*-ADD**-treated devices (**Figure 4.10**). The devices were kept at laboratory and exposed to oxygen and humidity. After 1320 hours, devices treated with ***poly*-ADD2** retained 96% of their initial PCE, outperforming the reference devices, which retained 89%. Notably, devices treated with ***poly*-ADD1** exhibited no detectable degradation, indicating superior stability. The increase in the efficiency, especially for the ***poly*-ADD1** treated device, is hypothesized to result from the prolonged doping of *spiro*-OMeTAD over time, which maintains effective charge transport properties in the perovskite solar cell. These results suggest that ***poly*-ADD** treatments, particularly ***poly*-ADD1**, can effectively enhance device longevity under ambient conditions.

## 4.3 Experimental

Using detergent, deionised water, acetone, and isopropanol, the FTO glass substrates (TEC7) were ultrasonically cleaned for ten minutes each. After washing, the substrates were exposed to UV-ozone for 30 minutes. Using spray pyrolysis with a titanium diisopropoxide bis-(acetylacetonate) solution diluted in IPA at a 1:15 volume ratio, the *cp*-$TiO_2$ was deposited onto the clean FTO substrates at 450 °C and then in situ annealed for 30 minutes. The *mp*-$TiO_2$ layer was deposited onto the FTO/*cp*-$TiO_2$ substrate using a one-step spin-coating technique at 6000 rpm for 20 s. The *mp*-$TiO_2$ solution was made up of 0.5 g of $TiO_2$ paste diluted in 5 mL of anhydrous ethanol solution. Following a 30-minute annealing process at 125°C, the *mp*-$TiO_2$ films were progressively heated to 500 °C in air before being baked for 20 minutes at the same temperature to eliminate organic materials. The substrates were placed onto a hot plate and heated to 150 °C for 30 minutes after the $SnO_2$ layers were created by spin coating a $SnO_2$ colloidal solution that had been diluted to a 1:5 ratio with deionized water in a one-step procedure at 3000 rpm for 20 s. The prepared FTO/*cp*-$TiO_2$/*mp*-$TiO_2$/$SnO_2$ substrates were exposed to UV/ozone for 30 minutes prior to usage. The precursor solution was prepared by dissolving $PbI_2$ (1.35 M), CsI (0.05 M), FAI (1.12 M), MABr (0.05 M), and MACl (0.10 M) in a mixed solvent of DMF: DMSO (3:1, volume ratio). Then, 50 µL perovskite precursors were coated onto the FTO/*cp*-$TiO_2$/*mp*-$TiO_2$/$SnO_2$ substrates (around 2.0 cm × 2.0 cm) by spin-coating; the procedure was performed through a two-step program running at 1000 and 4000 rpm for 12 and 25 s, respectively. For the control sample, during the second step, 200 µL of CB as an anti-solvent was dropped quickly onto the center of the substrates after 11 s into the second step was dispensed. For the polymer (***poly*-ADD1** and ***poly*-ADD2**)-treated films, 0.25 mg/mL polymer solutions in CB were used as an anti-solvent simultaneously during the coating. Subsequently, the films were moved to an annealing plate set at 100 °C and allowed to crystallize for 40 minutes. The HTM solution was made by combining a stock solution of spiro-OMeTAD in CB with solutions of *t*-BP, Li-TFSI, and Co(*t*-BuPyPz)$_3$(TFSI)$_3$

(FK209, Dyesol) in acetonitrile with a molar ratio of spiro-OMeTAD:FK209:Li(TFSI):*t*-BP at 1:0.03:0.5:3.3. 60 µL of the spiro-OMeTAD solution was then deposited on the perovskite film as the hole-transport layer. The manufacturing of the gadget was finally finished by thermally evaporating a 70 nm thick layer of Au as a counter electrode.

## 4.4 Conclusion

DPP-based polymers containing biselenophene (***poly*-ADD1**) and thienothiophene (***poly*-ADD2**) donor units are incorporated individually into cesium formamidinium methylammonium (CsFAMA)-based 3D perovskite materials as passivation agents via anti-solvent treatment. Their bulky, well-ordered molecular structures enable significant improvements in crystallization, defect modulation, overall efficiency, ambient stability, and thermal stability of n-i-p structured PSCs. PSCs incorporating ***poly*-ADD1** achieved a peak PCE of approximately 21%, surpassing the pristine cells (20.51%) after 21 days of aging, and exhibited improved thermal stability. The electron-blocking properties of ***poly*-ADD1** effectively hinder charge recombination at the perovskite/HTL interface and facilitate improved charge extraction. The interaction between the polymers and the perovskite film was analyzed using XPS and XRD techniques. Film morphology was examined through SEM and AFM analyses, revealing more uniform and smoother film formation with the inclusion of polymers. The slight difference in the $\pi$-linker results in a fundamental difference in the stability. Namely, the variation of heteroatoms within the structure holds intrinsic significance for the stability of solar cells. To gain insights into the influence of heteroatoms, advanced characterization and analysis methods, including Time of Flight-Secondary Ion Mass Spectrometry (ToF-SIMS), will be employed which will provide a comprehensive understanding of the heteroatom's effects on the system. This comprehensive study is anticipated to serve as a guideline for developing novel, durable DPP-modified polymeric passivation, which could play a pivotal role in

overcoming the stability challenges PSCs face and expedite their path toward commercial viability.

## REFERENCES


(1) Wang, Y.; Lv, Z.; Zhou, L.; Chen, X.; Chen, J.; Zhou, Y.; Roy, V. A. L.; Han, S. T. Emerging Perovskite Materials for High Density Data Storage and Artificial Synapses. *Journal of Materials Chemistry C*. Royal Society of Chemistry 2018, pp 1600–1617. https://doi.org/10.1039/c7tc05326f.

(2) Peña, M. A.; Fierro, J. L. G. Chemical Structures and Performance of Perovskite Oxides. *Chemical Reviews*. July 2001, pp 1981–2017. https://doi.org/10.1021/cr980129f.

(3) Grancini, G.; Marras, S.; Prato, M.; Giannini, C.; Quarti, C.; De Angelis, F.; De Bastiani, M.; Eperon, G. E.; Snaith, H. J.; Manna, L.; Petrozza, A. The Impact of the Crystallization Processes on the Structural and Optical Properties of Hybrid Perovskite Films for Photovoltaics. *Journal of Physical Chemistry Letters* **2014**, *5* (21), 3836–3842. https://doi.org/10.1021/jz501877h.

(4) Kim, Y. H.; Cho, H.; Heo, J. H.; Kim, T. S.; Myoung, N. S.; Lee, C. L.; Im, S. H.; Lee, T. W. Multicolored Organic/Inorganic Hybrid Perovskite Light-Emitting Diodes. *Advanced Materials* **2015**, *27* (7), 1248–1254. https://doi.org/10.1002/adma.201403751.

(5) Weber, D. *CH3NH3PbX3, Ein Pb(II)-System Mit Kubischer Perowskitstruktur CH3NH3PbX3, a Pb(II)-System with Cubic Perovskite Structure*; 1978; Vol. 33.

(6) Weber, D. *CH3NH3SnBrxl3 x (x = 0-3), Ein Sn(II)-System Mit Kubischer Perowskitstruktur CHsNHsSnBraJa-z = 0-3), a Sn(II)-System with Cubic Perovskite Structure*; 1978; Vol. 33.

(7) Wang, G.; Liao, L. P.; Elseman, A. M.; Yao, Y. Q.; Lin, C. Y.; Hu, W.; Liu, D. B.; Xu, C. Y.; Zhou, G. D.; Li, P.; Chen, L. J.; Han, J. J.; De Yang, X.; Wu, R.; Rao, X.; Song, Q. L. An Internally Photoemitted Hot Carrier Solar Cell

Based on Organic-Inorganic Perovskite. *Nano Energy* **2020**, *68*. https://doi.org/10.1016/j.nanoen.2019.104383.

(8) Kim, T.; Kim, J. H.; Park, J. W. All-Solution-Processed Organic–Inorganic Hybrid Perovskite Light-Emitting Diodes under Ambient Air. *Physica Status Solidi (A) Applications and Materials Science* **2019**, *216* (22). https://doi.org/10.1002/pssa.201900642.

(9) Xie, C.; Liu, C. K.; Loi, H. L.; Yan, F. Perovskite-Based Phototransistors and Hybrid Photodetectors. *Advanced Functional Materials*. Wiley-VCH Verlag May 1, 2020. https://doi.org/10.1002/adfm.201903907.

(10) Kojima, A.; Teshima, K.; Shirai, Y.; Miyasaka, T. Organometal Halide Perovskites as Visible-Light Sensitizers for Photovoltaic Cells. *J Am Chem Soc* **2009**, *131* (17), 6050–6051. https://doi.org/10.1021/ja809598r.

(11) Chen, P.; Xiao, Y.; Li, S.; Jia, X.; Luo, D.; Zhang, W.; Snaith, H. J.; Gong, Q.; Zhu, R. The Promise and Challenges of Inverted Perovskite Solar Cells. *Chemical Reviews*. American Chemical Society 2024. https://doi.org/10.1021/acs.chemrev.4c00073.

(12) Renewable Energy Laboratory, N. *NREL Best Research-Cell PV Efficiency Chart*; 1976.

(13) Azmi, R.; Zhumagali, S.; Bristow, H.; Zhang, S.; Yazmaciyan, A.; Pininti, A. R.; Utomo, D. S.; Subbiah, A. S.; De Wolf, S. Moisture-Resilient Perovskite Solar Cells for Enhanced Stability. *Advanced Materials*. John Wiley and Sons Inc March 21, 2024. https://doi.org/10.1002/adma.202211317.

(14) Nath, B.; Ramamurthy, P. C.; Hegde, G.; Roy Mahapatra, D. Role of Electrodes on Perovskite Solar Cells Performance: A Review. *ISSS J Micro Smart Syst* **2022**, *11* (1), 61–79. https://doi.org/10.1007/s41683-021-00089-y.

(15) Michael M. Lee, J. T. T. M. T. N. M. H. J. S. Efficient Hybrid Solar Cells Based on Meso-Superstructured Organometal Halide Perovskites. *Science (1979)* **2012**, *338*, 643–647.

(16) Habis, C.; Zaraket, J.; Aillerie, M. Transparent Conductive Oxides. Part II. Specific Focus on ITO, ZnO-AZO, $SnO_2$-FTO Families for Photovoltaics Applications. **2022**, https://doi.org/10.4028/p-6fqmfiï.

(17) Gangala, S.; Misra, R. Spiro-Linked Organic Small Molecules as Hole-Transport Materials for Perovskite Solar Cells. *Journal of Materials Chemistry A*. Royal Society of Chemistry. **2018**, pp 18750–18765. https://doi.org/10.1039/c8ta08503j.

(18) Jeyakumar, R.; Bag, A. Methylammonium Lead Bromide Based Planar Perovskite Solar Cells Using Various Electron Transport Layers. *Solar Energy* **2021**, *221*, 456–467. https://doi.org/10.1016/j.solener.2021.04.029.

(19) Wang, R.; Mujahid, M.; Duan, Y.; Wang, Z. K.; Xue, J.; Yang, Y. A Review of Perovskites Solar Cell Stability. *Advanced Functional Materials*. Wiley-VCH Verlag November 1, 2019. https://doi.org/10.1002/adfm.201808843.

(20) Zhang, H.; Ji, X.; Yao, H.; Fan, Q.; Yu, B.; Li, J. Review on Efficiency Improvement Effort of Perovskite Solar Cell. *Solar Energy*. Elsevier Ltd February 1, 2022, pp 421–434. https://doi.org/10.1016/j.solener.2022.01.060.

(21) Jeon, N. J.; Noh, J. H.; Yang, W. S.; Kim, Y. C.; Ryu, S.; Seo, J.; Seok, S. Il. Compositional Engineering of Perovskite Materials for High-Performance Solar Cells. *Nature* **2015**, *517* (7535), 476–480. https://doi.org/10.1038/nature14133.

(22) Jiang, Q.; Zhao, Y.; Zhang, X.; Yang, X.; Chen, Y.; Chu, Z.; Ye, Q.; Li, X.; Yin, Z.; You, J. Surface Passivation of Perovskite Film for Efficient Solar Cells. *Nat Photonics* **2019**, *13* (7), 460–466. https://doi.org/10.1038/s41566-019-0398-2.

(23) Bi, D.; Tress, W.; Dar, M. I.; Gao, P.; Luo, J.; Renevier, C.; Schenk, K.; Abate, A.; Giordano, F.; Correa Baena, J. P.; Decoppet, J. D.; Zakeeruddin, S. M.; Nazeeruddin, M. K.; Grätzel, M.; Hagfeldt, A. Efficient Luminescent Solar Cells Based on Tailored Mixed-Cation Perovskites. *Sci Adv* **2016**, *2* (1). https://doi.org/10.1126/sciadv.1501170.

(24) Jacobsson, T. J.; Correa-Baena, J. P.; Halvani Anaraki, E.; Philippe, B.; Stranks, S. D.; Bouduban, M. E. F.; Tress, W.; Schenk, K.; Teuscher, J.; Moser, J. E.; Rensmo, H.; Hagfeldt, A. Unreacted PbI2 as a Double-Edged Sword for Enhancing the Performance of Perovskite Solar Cells. *J Am Chem Soc* **2016**, *138* (32), 10331–10343. https://doi.org/10.1021/jacs.6b06320.

(25) Jesper Jacobsson, T.; Correa-Baena, J. P.; Pazoki, M.; Saliba, M.; Schenk, K.; Grätzel, M.; Hagfeldt, A. Exploration of the Compositional Space for Mixed Lead Halogen Perovskites for High Efficiency Solar Cells. *Energy Environ Sci* **2016**, *9* (5), 1706–1724. https://doi.org/10.1039/c6ee00030d.

(26) Shao, Y.; Xiao, Z.; Bi, C.; Yuan, Y.; Huang, J. Origin and Elimination of Photocurrent Hysteresis by Fullerene Passivation in CH3NH3PbI3 Planar Heterojunction Solar Cells. *Nat Commun* **2014**, *5*. https://doi.org/10.1038/ncomms6784.

(27) Xu, J.; Buin, A.; Ip, A. H.; Li, W.; Voznyy, O.; Comin, R.; Yuan, M.; Jeon, S.; Ning, Z.; McDowell, J. J.; Kanjanaboos, P.; Sun, J. P.; Lan, X.; Quan, L. N.; Kim, D. H.; Hill, I. G.; Maksymovych, P.; Sargent, E. H. Perovskite-Fullerene Hybrid Materials Suppress Hysteresis in Planar Diodes. *Nat Commun* **2015**, *6*. https://doi.org/10.1038/ncomms8081.

(28) Liu, Y.; Jia, R.; Wang, Y.; Hu, Z.; Zhang, Y.; Pang, T.; Zhu, Y.; Luan, S. Inhibition of Zero Drift in Perovskite-Based Photodetector Devices via [6,6]-Phenyl-C61-Butyric Acid Methyl Ester Doping. *ACS Appl Mater Interfaces* **2017**, *9* (18), 15638–15643. https://doi.org/10.1021/acsami.7b02413.

(29) Chiang, C. H.; Wu, C. G. Bulk Heterojunction Perovskite-PCBM Solar Cells with High Fill Factor. *Nat Photonics* **2016**, *10* (3), 196–200. https://doi.org/10.1038/nphoton.2016.3.

(30) Wang, K.; Liu, C.; Du, P.; Zheng, J.; Gong, X. Bulk Heterojunction Perovskite Hybrid Solar Cells with Large Fill Factor. *Energy Environ Sci* **2015**, *8* (4), 1245–1255. https://doi.org/10.1039/c5ee00222b.

(31) Jeon, N. J.; Noh, J. H.; Kim, Y. C.; Yang, W. S.; Ryu, S.; Seok, S. Il. Solvent Engineering for High-Performance Inorganic-Organic Hybrid Perovskite Solar Cells. *Nat Mater* **2014**, *13* (9), 897–903. https://doi.org/10.1038/nmat4014.

(32) Gao, L.; Zhang, F.; Xiao, C.; Chen, X.; Larson, B. W.; Berry, J. J.; Zhu, K. Improving Charge Transport via Intermediate-Controlled Crystal Growth in 2D Perovskite Solar Cells. *Adv Funct Mater* **2019**, *29* (47). https://doi.org/10.1002/adfm.201901652.

(33) Gao, L.; Huang, S.; Chen, L.; Li, X.; Ding, B.; Huang, S.; Yang, G. Excellent Stability of Perovskite Solar Cells by Passivation Engineering. *Solar RRL* **2018**, *2* (8). https://doi.org/10.1002/solr.201800088.

(34) Lee, J. W.; Bae, S. H.; Hsieh, Y. T.; De Marco, N.; Wang, M.; Sun, P.; Yang, Y. A Bifunctional Lewis Base Additive for Microscopic Homogeneity in Perovskite Solar Cells. *Chem* **2017**, *3* (2), 290–302. https://doi.org/10.1016/j.chempr.2017.05.020.

(35) Son, D. Y.; Lee, J. W.; Choi, Y. J.; Jang, I. H.; Lee, S.; Yoo, P. J.; Shin, H.; Ahn, N.; Choi, M.; Kim, D.; Park, N. G. Self-Formed Grain Boundary Healing Layer for Highly Efficient CH3 NH3 PbI3 Perovskite Solar Cells. *Nat Energy* **2016**, *1* (7). https://doi.org/10.1038/nenergy.2016.81.

(36) Lai, H.; Kan, B.; Liu, T.; Zheng, N.; Xie, Z.; Zhou, T.; Wan, X.; Zhang, X.; Liu, Y.; Chen, Y. Two-Dimensional Ruddlesden-Popper Perovskite with Nanorod-like Morphology for Solar Cells with Efficiency Exceeding 15%. *J*

*Am Chem Soc* **2018**, *140* (37), 11639–11646. https://doi.org/10.1021/jacs.8b04604.

(37) Rong, Y.; Hou, X.; Hu, Y.; Mei, A.; Liu, L.; Wang, P.; Han, H. Synergy of Ammonium Chloride and Moisture on Perovskite Crystallization for Efficient Printable Mesoscopic Solar Cells. *Nat Commun* **2017**, *8*. https://doi.org/10.1038/ncomms14555.

(38) Seo, J. Y.; Matsui, T.; Luo, J.; Correa-Baena, J. P.; Giordano, F.; Saliba, M.; Schenk, K.; Ummadisingu, A.; Domanski, K.; Hadadian, M.; Hagfeldt, A.; Zakeeruddin, S. M.; Steiner, U.; Grätzel, M.; Abate, A. Ionic Liquid Control Crystal Growth to Enhance Planar Perovskite Solar Cells Efficiency. *Adv Energy Mater* **2016**, *6* (20). https://doi.org/10.1002/aenm.201600767.

(39) Salado, M.; Ramos, F. J.; Manzanares, V. M.; Gao, P.; Nazeeruddin, M. K.; Dyson, P. J.; Ahmad, S. Extending the Lifetime of Perovskite Solar Cells Using a Perfluorinated Dopant. *ChemSusChem* **2016**, *9* (18), 2708–2714. https://doi.org/10.1002/cssc.201601030.

(40) Wang, S.; Li, Z.; Zhang, Y.; Liu, X.; Han, J.; Li, X.; Liu, Z.; (Frank) Liu, S.; Choy, W. C. H. Water-Soluble Triazolium Ionic-Liquid-Induced Surface Self-Assembly to Enhance the Stability and Efficiency of Perovskite Solar Cells. *Adv Funct Mater* **2019**, *29* (15). https://doi.org/10.1002/adfm.201900417.

(41) Min, J.; Choi, Y.; Kim, D.; Park, T. Beyond Imperfections: Exploring Defects for Breakthroughs in Perovskite Solar Cell Research. *Advanced Energy Materials*. John Wiley and Sons Inc February 9, 2024. https://doi.org/10.1002/aenm.202302659.

(42) Aydin, E.; De Bastiani, M.; De Wolf, S. Defect and Contact Passivation for Perovskite Solar Cells. *Advanced Materials*. Wiley-VCH Verlag June 20, 2019. https://doi.org/10.1002/adma.201900428.

(43) Cheng, M.; Zuo, C.; Wu, Y.; Li, Z.; Xu, B.; Hua, Y.; Ding, L. Charge-Transport Layer Engineering in Perovskite Solar Cells. *Science Bulletin*. Elsevier B.V. August 15, 2020, pp 1237–1241. https://doi.org/10.1016/j.scib.2020.04.021.

(44) Qin, P.; Tanaka, S.; Ito, S.; Tetreault, N.; Manabe, K.; Nishino, H.; Nazeeruddin, M. K.; Grätzel, M. Inorganic Hole Conductor-Based Lead Halide Perovskite Solar Cells with 12.4% Conversion Efficiency. *Nat Commun* **2014**, *5*. https://doi.org/10.1038/ncomms4834.

(45) Christians, J. A.; Fung, R. C. M.; Kamat, P. V. An Inorganic Hole Conductor for Organo-Lead Halide Perovskite Solar Cells. Improved Hole Conductivity with Copper Iodide. *J Am Chem Soc* **2014**, *136* (2), 758–764. https://doi.org/10.1021/ja411014k.

(46) Ito, S.; Tanaka, S.; Vahlman, H.; Nishino, H.; Manabe, K.; Lund, P. Carbon-Double-Bond-Free Printed Solar Cells from TiO2/CH 3NH3PbI3/CuSCN/Au: Structural Control and Photoaging Effects. In *ChemPhysChem*; Wiley-VCH Verlag, 2014; Vol. 15, pp 1194–1200. https://doi.org/10.1002/cphc.201301047.

(47) Ito, S.; Tanaka, S.; Manabe, K.; Nishino, H. Effects of Surface Blocking Layer of Sb2S3 on Nanocrystalline TiO2 for CH3NH3PbI3 Perovskite Solar Cells. *Journal of Physical Chemistry C* **2014**, *118* (30), 16995–17000. https://doi.org/10.1021/jp500449z.

(48) Irwin, M. D.; Servaites, J. D.; Buchholz, D. B.; Leever, B. J.; Liu, J.; Emery, J. D.; Zhang, M.; Song, J. H.; Durstock, M. F.; Freeman, A. J.; Bedzyk, M. J.; Hersam, M. C.; Chang, R. P. H.; Ratner, M. A.; Marks, T. J. Structural and Electrical Functionality of NiO Interfacial Films in Bulk Heterojunction Organic Solar Cells. *Chemistry of Materials* **2011**, *23* (8), 2218–2226. https://doi.org/10.1021/cm200229e.

(49) Powar, S.; Daeneke, T.; Ma, M. T.; Fu, D.; Duffy, N. W.; Götz, G.; Weidelener, M.; Mishra, A.; Bäuerle, P.; Spiccia, L.; Bach, U. Highly Efficient P-Type Dye-Sensitized Solar Cells Based on Tris(1,2-Diaminoethane)Cobalt(II)/(III) Electrolytes. *Angewandte Chemie - International Edition* **2013**, *52* (2), 602–605. https://doi.org/10.1002/anie.201206219.

(50) Odobel, F.; Pellegrin, Y. Recent Advances in the Sensitization of Wide-Band-Gap Nanostructured p-Type Semiconductors. Photovoltaic and Photocatalytic Applications. *Journal of Physical Chemistry Letters* **2013**, *4* (15), 2551–2564. https://doi.org/10.1021/jz400861v.

(51) Jeng, J. Y.; Chen, K. C.; Chiang, T. Y.; Lin, P. Y.; Tsai, T. Da; Chang, Y. C.; Guo, T. F.; Chen, P.; Wen, T. C.; Hsu, Y. J. Nickel Oxide Electrode Interlayer in CH3NH3PbI 3 Perovskite/PCBM Planar-Heterojunction Hybrid Solar Cells. *Advanced Materials* **2014**, *26* (24), 4107–4113. https://doi.org/10.1002/adma.201306217.

(52) Ru, P.; Bi, E.; Zhang, Y.; Wang, Y.; Kong, W.; Sha, Y.; Tang, W.; Zhang, P.; Wu, Y.; Chen, W.; Yang, X.; Chen, H.; Han, L. High Electron Affinity Enables Fast Hole Extraction for Efficient Flexible Inverted Perovskite Solar Cells. *Adv Energy Mater* **2020**, *10* (12). https://doi.org/10.1002/aenm.201903487.

(53) Chen, M.; Qiao, H. W.; Zhou, Z.; Ge, B.; He, J.; Yang, S.; Hou, Y.; Yang, H. G. Homogeneous Doping of Entire Perovskite Solar Cellsviaalkali Cation Diffusion from the Hole Transport Layer. *J Mater Chem A Mater* **2021**, *9* (14), 9266–9271. https://doi.org/10.1039/d1ta01061a.

(54) Chen, H.; Teale, S.; Chen, B.; Hou, Y.; Grater, L.; Zhu, T.; Bertens, K.; Park, S. M.; Atapattu, H. R.; Gao, Y.; Wei, M.; Johnston, A. K.; Zhou, Q.; Xu, K.; Yu, D.; Han, C.; Cui, T.; Jung, E. H.; Zhou, C.; Zhou, W.; Proppe, A. H.; Hoogland, S.; Laquai, F.; Filleter, T.; Graham, K. R.; Ning, Z.; Sargent, E. H.

Quantum-Size-Tuned Heterostructures Enable Efficient and Stable Inverted Perovskite Solar Cells. *Nat Photonics* **2022**, *16* (5), 352–358. https://doi.org/10.1038/s41566-022-00985-1.

(55) Zhu, R.; Guan, N.; Wang, D.; Bao, Y.; Wu, Z.; Song, L. Review of Defect Passivation for $NiO_x$-Based Inverted Perovskite Solar Cells. *ACS Applied Energy Materials*. American Chemical Society February 27, 2023, pp 2098–2121. https://doi.org/10.1021/acsaem.2c03127.

(56) Ouedraogo, N. A. N.; Odunmbaku, G. O.; Guo, B.; Chen, S.; Lin, X.; Shumilova, T.; Sun, K. Oxidation of Spiro-OMeTAD in High-Efficiency Perovskite Solar Cells. *ACS Applied Materials and Interfaces*. American Chemical Society August 3, 2022, pp 34303–34327. https://doi.org/10.1021/acsami.2c06163.

(57) Nakka, L.; Cheng, Y.; Aberle, A. G.; Lin, F. Analytical Review of Spiro-OMeTAD Hole Transport Materials: Paths Toward Stable and Efficient Perovskite Solar Cells. *Advanced Energy and Sustainability Research*. John Wiley and Sons Inc August 1, 2022. https://doi.org/10.1002/aesr.202200045.

(58) Kim, H. S.; Lee, C. R.; Im, J. H.; Lee, K. B.; Moehl, T.; Marchioro, A.; Moon, S. J.; Humphry-Baker, R.; Yum, J. H.; Moser, J. E.; Grätzel, M.; Park, N. G. Lead Iodide Perovskite Sensitized All-Solid-State Submicron Thin Film Mesoscopic Solar Cell with Efficiency Exceeding 9%. *Sci Rep* **2012**, *2*. https://doi.org/10.1038/srep00591.

(59) Ye, L.; Wu, J.; Catalán-Gómez, S.; Yuan, L.; Sun, R.; Chen, R.; Liu, Z.; Ulloa, J. M.; Hierro, A.; Guo, P.; Zhou, Y.; Wang, H. Superoxide Radical Derived Metal-Free Spiro-OMeTAD for Highly Stable Perovskite Solar Cells. *Nature Communications* **2024**, *15* (1). https://doi.org/10.1038/s41467-024-52199-4.

(60) Fantacci, S.; De Angelis, F.; Nazeeruddin, M. K.; Grätzel, M. Electronic and Optical Properties of the Spiro-MeOTAD Hole Conductor in Its Neutral and Oxidized Forms: A DFT/TDDFT Investigation. *Journal of Physical*

*Chemistry C* **2011**, *115* (46), 23126–23133. https://doi.org/10.1021/jp207968b.

(61) Wang, S.; Sina, M.; Parikh, P.; Uekert, T.; Shahbazian, B.; Devaraj, A.; Meng, Y. S. Role of 4-Tert-Butylpyridine as a Hole Transport Layer Morphological Controller in Perovskite Solar Cells. *Nano Lett* **2016**, *16* (9), 5594–5600. https://doi.org/10.1021/acs.nanolett.6b02158.

(62) Wang, J.; Shi, H.; Xu, N.; Zhang, J.; Yuan, Y.; Lei, M.; Wang, L.; Wang, P. Aza[5]Helicene Rivals N-Annulated Perylene as π-Linker of D−π−D Typed Hole-Transporters for Perovskite Solar Cells. *Adv Funct Mater* **2020**, *30* (30). https://doi.org/10.1002/adfm.202002114.

(63) Jeong, M.; Woo Choi, I.; Min Go, E.; Cho, Y.; Kim, M.; Lee, B.; Jeong, S.; Jo, Y.; Won Choi, H.; Lee, J.; Bae, J.-H.; Kyu Kwak, S.; Suk Kim, D.; Yang, C. *Stable Perovskite Solar Cells with Efficiency Exceeding 24.8% and 0.3-V Voltage Loss*; 2020. https://www.science.org.

(64) Bauer, M.; Zhu, H.; Baumeler, T.; Liu, Y.; Eickemeyer, F. T.; Lorenz, C.; Mena-Osteritz, E.; Hertel, D.; Olthof, S.; Zakeeruddin, S. M.; Meerholz, K.; Grätzel, M.; Bäuerle, P. Cyclopentadiene-Based Hole-Transport Material for Cost-Reduced Stabilized Perovskite Solar Cells with Power Conversion Efficiencies Over 23%. *Adv Energy Mater* **2021**, *11* (30). https://doi.org/10.1002/aenm.202003953.

(65) Xia, J.; Cavazzini, M.; Igci, C.; Momblona, C.; Orlandi, S.; Ding, B.; Zhang, Y.; Kanda, H.; Klipfel, N.; Khan, S. B.; Asiri, A. M.; Dyson, P. J.; Pozzi, G.; Nazeeruddin, M. K. Molecular Engineering of Thienyl Functionalized Ullazines as Hole-Transporting Materials for Perovskite Solar Cells. *Solar RRL* **2022**, *6* (4). https://doi.org/10.1002/solr.202100926.

(66) Xia, J.; Zhang, Y.; Cavazzini, M.; Orlandi, S.; Ding, B.; Kanda, H.; Klipfel, N.; Gao, X. X.; Ul Ain, Q.; Jankauskas, V.; Rakstys, K.; Hu, R.; Qiu, Z.; Asiri, A. M.; Kim, H.; Dyson, P. J.; Pozzi, G.; Khaja Nazeeruddin, M.

Asymmetrically Substituted 10H,10′H-9,9′-Spirobi[Acridine] Derivatives as Hole-Transporting Materials for Perovskite Solar Cells. *Angewandte Chemie - International Edition* **2022**, *61* (48). https://doi.org/10.1002/anie.202212891.

(67) Wang, H.; Wu, C.; Zhai, M.; Chen, C.; Tao, L.; Ding, X.; Miao, Y.; Cheng, M. Constructing Efficient Hole Transport Material through π-Conjunction Extension for Perovskite Solar Cell. *ACS Appl Energy Mater* **2022**, *5* (11), 13261–13268. https://doi.org/10.1021/acsaem.2c01798.

(68) Jeong, M.; Choi, I. W.; Yim, K.; Jeong, S.; Kim, M.; Choi, S. J.; Cho, Y.; An, J. H.; Kim, H. B.; Jo, Y.; Kang, S. H.; Bae, J. H.; Lee, C. W.; Kim, D. S.; Yang, C. Large-Area Perovskite Solar Cells Employing Spiro-Naph Hole Transport Material. *Nat Photonics* **2022**, *16* (2), 119–125. https://doi.org/10.1038/s41566-021-00931-7.

(69) Wang, R.; Wu, C.; Qi, J.; Shen, W.; Wu, F.; Li, M.; He, R.; Liu, X. Side-Chain Methylthio-Based Position Isomerism of Hole-Transport Materials for Perovskite Solar Cells: From Theoretical Simulation to Experimental Characterization. *Adv Funct Mater* **2023**, *33* (14). https://doi.org/10.1002/adfm.202213843.

(70) Kim, D. W.; Choi, K. H.; Hong, S. H.; Kang, H. S.; Kwon, J. E.; Park, S.; An, B. K.; Park, S. Y. Indoloindole-Based Hole Transporting Material for Efficient and Stable Perovskite Solar Cells Exceeding 24% Power Conversion Efficiency. *Adv Energy Mater* **2023**, *13* (26). https://doi.org/10.1002/aenm.202300219.

(71) Zhou, J.; Li, H.; Tan, L.; Liu, Y.; Yang, J.; Hua, R.; Yi, C. Tuning Hole Transport Properties via Pyrrole Derivation for High-Performance Perovskite Solar Cells. *Angewandte Chemie - International Edition* **2023**, *62* (15). https://doi.org/10.1002/anie.202300314.

(72) Zhou, J.; Tan, L.; Liu, Y.; Li, H.; Liu, X.; Li, M.; Wang, S.; Zhang, Y.; Jiang, C.; Hua, R.; Tress, W.; Meloni, S.; Yi, C. Highly Efficient and Stable Perovskite Solar Cells via a Multifunctional Hole Transporting Material. *Joule* **2024**, *8* (6), 1691–1706. https://doi.org/10.1016/j.joule.2024.02.019.

(73) Zhao, X.; Wang, M. Organic Hole-Transporting Materials for Efficient Perovskite Solar Cells. *Materials Today Energy*. Elsevier Ltd March 1, 2018, pp 208–220. https://doi.org/10.1016/j.mtener.2017.09.011.

(74) Kim, G. W.; Shinde, D. V.; Park, T. Thickness of the Hole Transport Layer in Perovskite Solar Cells: Performance versus Reproducibility. *RSC Adv* **2015**, *5* (120), 99356–99360. https://doi.org/10.1039/c5ra18648j.

(75) Heo, J. H.; Im, S. H.; Noh, J. H.; Mandal, T. N.; Lim, C. S.; Chang, J. A.; Lee, Y. H.; Kim, H. J.; Sarkar, A.; Nazeeruddin, M. K.; Grätzel, M.; Seok, S. Il. Efficient Inorganic-Organic Hybrid Heterojunction Solar Cells Containing Perovskite Compound and Polymeric Hole Conductors. *Nat Photonics* **2013**, *7* (6), 486–491. https://doi.org/10.1038/nphoton.2013.80.

(76) Noh, J. H.; Im, S. H.; Heo, J. H.; Mandal, T. N.; Seok, S. Il. Chemical Management for Colorful, Efficient, and Stable Inorganic-Organic Hybrid Nanostructured Solar Cells. *Nano Lett* **2013**, *13* (4), 1764–1769. https://doi.org/10.1021/nl400349b.

(77) Kim, G. W.; Lee, J.; Kang, G.; Kim, T.; Park, T. Donor–Acceptor Type Dopant-Free, Polymeric Hole Transport Material for Planar Perovskite Solar Cells (19.8%). *Adv Energy Mater* **2018**, *8* (4). https://doi.org/10.1002/aenm.201701935.

(78) Liao, H. C.; Tam, T. L. D.; Guo, P.; Wu, Y.; Manley, E. F.; Huang, W.; Zhou, N.; Soe, C. M. M.; Wang, B.; Wasielewski, M. R.; Chen, L. X.; Kanatzidis, M. G.; Facchetti, A.; Chang, R. P. H.; Marks, T. J. Dopant-Free Hole Transporting Polymers for High Efficiency, Environmentally Stable

Perovskite Solar Cells. *Adv Energy Mater* **2016**, *6* (16). https://doi.org/10.1002/aenm.201600502.

(79) Kwon, Y. S.; Lim, J.; Yun, H. J.; Kim, Y. H.; Park, T. A Diketopyrrolopyrrole-Containing Hole Transporting Conjugated Polymer for Use in Efficient Stable Organic-Inorganic Hybrid Solar Cells Based on a Perovskite. In *Energy and Environmental Science*; Royal Society of Chemistry, 2014; Vol. 7, pp 1454–1460. https://doi.org/10.1039/c3ee44174a.

(80) Kim, G. W.; Kang, G.; Kim, J.; Lee, G. Y.; Kim, H. Il; Pyeon, L.; Lee, J.; Park, T. Dopant-Free Polymeric Hole Transport Materials for Highly Efficient and Stable Perovskite Solar Cells. *Energy Environ Sci* **2016**, *9* (7), 2326–2333. https://doi.org/10.1039/c6ee00709k.

(81) Wang, Y.; Duan, L.; Zhang, M.; Hameiri, Z.; Liu, X.; Bai, Y.; Hao, X. PTAA as Efficient Hole Transport Materials in Perovskite Solar Cells: A Review. *Solar RRL*. John Wiley and Sons Inc August 1, 2022. https://doi.org/10.1002/solr.202200234.

(82) Wu, X.; Gao, D.; Sun, X.; Zhang, S.; Wang, Q.; Li, B.; Li, Z.; Qin, M.; Jiang, X.; Zhang, C.; Li, Z.; Lu, X.; Li, N.; Xiao, S.; Zhong, X.; Yang, S.; Li, Z.; Zhu, Z. Backbone Engineering Enables Highly Efficient Polymer Hole-Transporting Materials for Inverted Perovskite Solar Cells. *Advanced Materials* **2023**, *35* (12). https://doi.org/10.1002/adma.202208431.

(83) Sun, X.; Yu, X.; Li, Z. Recent Advances of Dopant-Free Polymer Hole-Transporting Materials for Perovskite Solar Cells. *ACS Applied Energy Materials*. American Chemical Society November 23, 2020, pp 10282–10302. https://doi.org/10.1021/acsaem.0c01917.

(84) Wang, K.; Olthof, S.; Subhani, W. S.; Jiang, X.; Cao, Y.; Duan, L.; Wang, H.; Du, M.; Liu, S. (Frank). Novel Inorganic Electron Transport Layers for Planar Perovskite Solar Cells: Progress and Prospective. *Nano Energy*. Elsevier Ltd February 1, 2020. https://doi.org/10.1016/j.nanoen.2019.104289.

(85) Abrusci, A.; Stranks, S. D.; Docampo, P.; Yip, H. L.; Jen, A. K. Y.; Snaith, H. J. High-Performance Perovskite-Polymer Hybrid Solar Cells via Electronic Coupling with Fullerene Monolayers. *Nano Lett* **2013**, *13* (7), 3124–3128. https://doi.org/10.1021/nl401044q.

(86) Said, A. A.; Xie, J.; Zhang, Q. Recent Progress in Organic Electron Transport Materials in Inverted Perovskite Solar Cells. *Small*. Wiley-VCH Verlag July 5, 2019. https://doi.org/10.1002/smll.201900854.

(87) Zhong, Y.; Hufnagel, M.; Thelakkat, M.; Li, C.; Huettner, S. Role of PCBM in the Suppression of Hysteresis in Perovskite Solar Cells. *Adv Funct Mater* **2020**, *30* (23). https://doi.org/10.1002/adfm.201908920.

(88) Jiang, Q.; Tong, J.; Xian, Y.; Kerner, R. A.; Dunfield, S. P.; Xiao, C.; Scheidt, R. A.; Kuciauskas, D.; Wang, X.; Hautzinger, M. P.; Tirawat, R.; Beard, M. C.; Fenning, D. P.; Berry, J. J.; Larson, B. W.; Yan, Y.; Zhu, K. Surface Reaction for Efficient and Stable Inverted Perovskite Solar Cells. *Nature* **2022**, *611* (7935), 278–283. https://doi.org/10.1038/s41586-022-05268-x.

(89) Zahran, R.; Hawash, Z. Fullerene-Based Inverted Perovskite Solar Cell: A Key to Achieve Promising, Stable, and Efficient Photovoltaics. *Advanced Materials Interfaces*. John Wiley and Sons Inc December 12, 2022. https://doi.org/10.1002/admi.202201438.

(90) Nielsen, C. B.; Holliday, S.; Chen, H. Y.; Cryer, S. J.; McCulloch, I. Non-Fullerene Electron Acceptors for Use in Organic Solar Cells. *Acc Chem Res* **2015**, *48* (11), 2803–2812. https://doi.org/10.1021/acs.accounts.5b00199.

(91) Li, X.; Wang, W.; Huang, P.; Yang, L.; Hu, J.; Wei, K.; Gao, L.; Jiang, Y.; Sun, K.; Du, G.; Cai, X.; Liu, C.; Tang, W.; Zhang, J. Fluorinated Naphthalene Diimides as Buried Electron Transport Materials Achieve Over 23% Efficient Perovskite Solar Cells. *Advanced Science* **2024**. https://doi.org/10.1002/advs.202403735.

(92) Miao, J.; Hu, Z.; Liu, M.; Umair Ali, M.; Goto, O.; Lu, W.; Yang, T.; Liang, Y.; Meng, H. A Non-Fullerene Small Molecule Processed with Green Solvent as an Electron Transporting Material for High Efficiency p-i-n Perovskite Solar Cells. *Org Electron* **2018**, *52*, 200–205. https://doi.org/10.1016/j.orgel.2017.10.028.

(93) Bai, H.; Wang, Y.; Cheng, P.; Wang, J.; Wu, Y.; Hou, J.; Zhan, X. An Electron Acceptor Based on Indacenodithiophene and 1,1-Dicyanomethylene-3-Indanone for Fullerene-Free Organic Solar Cells. *J Mater Chem A Mater* **2015**, *3* (5), 1910–1914. https://doi.org/10.1039/c4ta06004k.

(94) Li, X.; Wang, W.; Huang, P.; Yang, L.; Hu, J.; Wei, K.; Gao, L.; Jiang, Y.; Sun, K.; Du, G.; Cai, X.; Liu, C.; Tang, W.; Zhang, J. Fluorinated Naphthalene Diimides as Buried Electron Transport Materials Achieve Over 23% Efficient Perovskite Solar Cells. *Advanced Science* **2024**. https://doi.org/10.1002/advs.202403735.

(95) Jameel, M. A.; Yang, T. C. J.; Wilson, G. J.; Evans, R. A.; Gupta, A.; Langford, S. J. Naphthalene Diimide-Based Electron Transport Materials for Perovskite Solar Cells. *Journal of Materials Chemistry A*. Royal Society of Chemistry December 28, 2021, pp 27170–27192. https://doi.org/10.1039/d1ta08424k.

(96) Krishna, B. G.; Ghosh, D. S.; Tiwari, S. Hole and Electron Transport Materials: A Review on Recent Progress in Organic Charge Transport Materials for Efficient, Stable, and Scalable Perovskite Solar Cells. *Chemistry of Inorganic Materials* **2023**, *1*, 100026. https://doi.org/10.1016/j.cinorg.2023.100026.

(97) Chen, W.; Shi, Y.; Wang, Y.; Feng, X.; Djurišić, A. B.; Woo, H. Y.; Guo, X.; He, Z. N-Type Conjugated Polymer as Efficient Electron Transport Layer for Planar Inverted Perovskite Solar Cells with Power Conversion Efficiency of

20.86%. *Nano Energy* **2020**, *68*. https://doi.org/10.1016/j.nanoen.2019.104363.

(98) Hu, Q.; Liu, Y.; Li, Y.; Ying, L.; Liu, T.; Huang, F.; Wang, S.; Huang, W.; Zhu, R.; Gong, Q. Efficient and Low-Temperature Processed Perovskite Solar Cells Based on a Cross-Linkable Hybrid Interlayer. *J Mater Chem A Mater* **2015**, *3* (36), 18483–18491. https://doi.org/10.1039/c5ta04695e.

(99) Shao, S.; Chen, Z.; Fang, H. H.; Ten Brink, G. H.; Bartesaghi, D.; Adjokatse, S.; Koster, L. J. A.; Kooi, B. J.; Facchetti, A.; Loi, M. A. N-Type Polymers as Electron Extraction Layers in Hybrid Perovskite Solar Cells with Improved Ambient Stability. *J Mater Chem A Mater* **2016**, *4* (7), 2419–2426. https://doi.org/10.1039/c5ta10696f.

(100) Yan, W.; Wang, Z.; Gong, Y.; Guo, S.; Jiang, J.; Chen, J.; Tang, C.; Xia, R.; Huang, W.; Xin, H. Naphthalene-Diimide Selenophene Copolymers as Efficient Solution-Processable Electron-Transporting Material for Perovskite Solar Cells. *Org Electron* **2019**, *67*, 208–214. https://doi.org/10.1016/j.orgel.2019.01.040.

(101) Sun, C.; Wu, Z.; Yip, H. L.; Zhang, H.; Jiang, X. F.; Xue, Q.; Hu, Z.; Hu, Z.; Shen, Y.; Wang, M.; Huang, F.; Cao, Y. Amino-Functionalized Conjugated Polymer as an Efficient Electron Transport Layer for High-Performance Planar-Heterojunction Perovskite Solar Cells. *Adv Energy Mater* **2016**, *6* (5). https://doi.org/10.1002/aenm.201501534.

(102) Valero, S.; Cabrera-Espinoza, A.; Collavini, S.; Pascual, J.; Marinova, N.; Kosta, I.; Delgado, J. L. Naphthalene Diimide-Based Molecules for Efficient and Stable Perovskite Solar Cells. *European J Org Chem* **2020**, *2020* (33), 5329–5339. https://doi.org/10.1002/ejoc.202000287.

(103) Wang, H.; Zhang, C.; Yao, Y.; Cheng, C.; Wang, K. Non-Fullerene Organic Electron Transport Materials toward Stable and Efficient Inverted Perovskite

Photovoltaics. *Small*. John Wiley and Sons Inc October 24, 2024. https://doi.org/10.1002/smll.202403193.

(104) Liu, H.; Huang, Z.; Wei, S.; Zheng, L.; Xiao, L.; Gong, Q. Nano-Structured Electron Transporting Materials for Perovskite Solar Cells. *Nanoscale*. Royal Society of Chemistry March 28, 2016, pp 6209–6221. https://doi.org/10.1039/c5nr05207f.

(105) Zhang, T.; He, Q.; Yu, J.; Chen, A.; Zhang, Z.; Pan, J. Recent Progress in Improving Strategies of Inorganic Electron Transport Layers for Perovskite Solar Cells. *Nano Energy*. Elsevier Ltd December 15, 2022. https://doi.org/10.1016/j.nanoen.2022.107918.

(106) Lian, J.; Lu, B.; Niu, F.; Zeng, P.; Zhan, X. Electron-Transport Materials in Perovskite Solar Cells. *Small Methods*. John Wiley and Sons Inc October 1, 2018. https://doi.org/10.1002/smtd.201800082.

(107) Sánchez, S.; Pfeifer, L.; Vlachopoulos, N.; Hagfeldt, A. Rapid Hybrid Perovskite Film Crystallization from Solution. *Chemical Society Reviews*. Royal Society of Chemistry June 21, 2021, pp 7108–7131. https://doi.org/10.1039/d0cs01272f.

(108) Wang, Z.; Lin, Q.; Chmiel, F. P.; Sakai, N.; Herz, L. M.; Snaith, H. J. Efficient Ambient-Air-Stable Solar Cells with 2D-3D Heterostructured Butylammonium-Caesium-Formamidinium Lead Halide Perovskites. *Nat Energy* **2017**, *2* (9). https://doi.org/10.1038/nenergy.2017.135.

(109) Zhang, Y.; Xi, J.; Deng, Y.; Liu, W.; Li, Z.; Liu, C.; Guo, W. The Crucial Role of Organic Ligands on 2D/3D Perovskite Solar Cells: A Comprehensive Review. *Advanced Energy Materials*. John Wiley and Sons Inc 2024. https://doi.org/10.1002/aenm.202403326.

(110) Palei, S.; Murali, G.; Kim, C. H.; In, I.; Lee, S. Y.; Park, S. J. A Review on Interface Engineering of MXenes for Perovskite Solar Cells. *Nano-Micro*

*Letters*. Springer Science and Business Media B.V. December 1, 2023. https://doi.org/10.1007/s40820-023-01083-9.

(111) Deng, W.; Liang, X.; Kubiak, P. S.; Cameron, P. J. Molecular Interlayers in Hybrid Perovskite Solar Cells. *Advanced Energy Materials*. Wiley-VCH Verlag January 5, 2018. https://doi.org/10.1002/aenm.201701544.

(112) Choi, J.; Kamaraj, E.; Park, H.; Jeong, B. H.; Baac, H. W.; Park, S.; Park, H. J. Defect-Passivation of Organometal Trihalide Perovskite with Functionalized Organic Small Molecule for Enhanced Device Performance and Stability. *Dyes and Pigments* **2021**, *189*. https://doi.org/10.1016/j.dyepig.2021.109255.

(113) He, S.; Wang, B.; Wang, P.; Wang, Y.; Cheng, Y.; Lv, Y.; Li, Y. Interfacial Defects Passivation and Energy Level Alignment with Small Molecule Pyridine Material for Efficient and Stable Inverted Perovskite Solar Cells. *Surfaces and Interfaces* **2024**, *46*. https://doi.org/10.1016/j.surfin.2024.104031.

(114) Liu, J.; He, J.; Wu, W. Molecular Symmetry of Small-Molecule Passivating Agents Improves Crystal Quality of Perovskite Solar Cells. *ChemSusChem* **2024**, *17* (10). https://doi.org/10.1002/cssc.202301458.

(115) Zhang, W.; Yuan, M.; Han, L.; Luo, G.; Zhang, L.; He, H.; Lin, P.; Xu, L.; Wu, X.; Zhu, X.; Yu, X.; Wang, P.; Cui, C. Perovskite Surface Passivation Using Thiophene-Based Small Molecules for Efficient and Stable Solar Cells. *ACS Appl Energy Mater* **2023**, *6* (13), 7003–7013. https://doi.org/10.1021/acsaem.3c00549.

(116) Wu, M.; Duan, Y.; Yang, L.; You, P.; Li, Z.; Wang, J.; Zhou, H.; Yang, S.; Xu, D.; Zou, H.; Liu, Z. Multifunctional Small Molecule as Buried Interface Passivator for Efficient Planar Perovskite Solar Cells. *Adv Funct Mater* **2023**, *33* (22). https://doi.org/10.1002/adfm.202300128.

(117) Liu, X.; Zhang, Y.; Shi, L.; Liu, Z.; Huang, J.; Yun, J. S.; Zeng, Y.; Pu, A.; Sun, K.; Hameiri, Z.; Stride, J. A.; Seidel, J.; Green, M. A.; Hao, X. Exploring Inorganic Binary Alkaline Halide to Passivate Defects in Low-Temperature-Processed Planar-Structure Hybrid Perovskite Solar Cells. *Adv Energy Mater* **2018**, *8* (20). https://doi.org/10.1002/aenm.201800138.

(118) He, S.; Wang, B.; Wang, P.; Wang, Y.; Cheng, Y.; Lv, Y.; Li, Y. Interfacial Defects Passivation and Energy Level Alignment with Small Molecule Pyridine Material for Efficient and Stable Inverted Perovskite Solar Cells. *Surfaces and Interfaces* **2024**, *46*. https://doi.org/10.1016/j.surfin.2024.104031.

(119) Choi, J.; Kamaraj, E.; Park, H.; Jeong, B. H.; Baac, H. W.; Park, S.; Park, H. J. Defect-Passivation of Organometal Trihalide Perovskite with Functionalized Organic Small Molecule for Enhanced Device Performance and Stability. *Dyes and Pigments* **2021**, *189*. https://doi.org/10.1016/j.dyepig.2021.109255.

(120) He, Z.; Zhou, Y.; Xu, C.; Su, Y.; Liu, A.; Li, Y.; Gao, L.; Ma, T. Mechanism of Enhancement in Perovskite Solar Cells by Organosulfur Amine Constructed 2D/3D Heterojunctions. *Journal of Physical Chemistry C* **2021**, *125* (30), 16428–16434. https://doi.org/10.1021/acs.jpcc.1c04343.

(121) Wu, M.; Duan, Y.; Yang, L.; You, P.; Li, Z.; Wang, J.; Zhou, H.; Yang, S.; Xu, D.; Zou, H.; Liu, Z. Multifunctional Small Molecule as Buried Interface Passivator for Efficient Planar Perovskite Solar Cells. *Adv Funct Mater* **2023**, *33* (22). https://doi.org/10.1002/adfm.202300128.

(122) Liu, J.; He, J.; Wu, W. Molecular Symmetry of Small-Molecule Passivating Agents Improves Crystal Quality of Perovskite Solar Cells. *ChemSusChem* **2024**, *17* (10). https://doi.org/10.1002/cssc.202301458.

(123) Zhang, W.; Yuan, M.; Han, L.; Luo, G.; Zhang, L.; He, H.; Lin, P.; Xu, L.; Wu, X.; Zhu, X.; Yu, X.; Wang, P.; Cui, C. Perovskite Surface Passivation

Using Thiophene-Based Small Molecules for Efficient and Stable Solar Cells. *ACS Appl Energy Mater* **2023**, *6* (13), 7003–7013. https://doi.org/10.1021/acsaem.3c00549.

(124) Liu, C.; Yang, Y.; Chen, H.; Xu, J.; Liu, A.; R Bati, A. S.; Zhu, H.; Grater, L.; Sudhakar Hadke, S.; Huang, C.; Sangwan, V. K.; Cai, T.; Shin, D.; Chen, L. X.; Hersam, M. C.; Mirkin, C. A.; Chen, B.; Kanatzidis, M. G.; Sargent, E. H. *Bimolecularly Passivated Interface Enables Efficient and Stable Inverted Perovskite Solar Cells*. https://www.science.org.

(125) Min Park, S.; Wei, M.; Xu, J.; Atapattu, H. R.; Eickemeyer, F. T.; Darabi, K.; Grater, L.; Yang, Y.; Liu, C.; Teale, S.; Chen, B.; Chen, H.; Wang, T.; Zeng, L.; Maxwell, A.; Wang, Z.; Rao, K. R.; Cai, Z.; Zakeeruddin, S. M.; Pham, J. T.; Risko, C. M.; Amassian, A.; Kanatzidis, M. G.; Graham, K. R.; Grätzel, M.; Sargent, E. H. *Engineering Ligand Reactivity Enables High-Temperature Operation of Stable Perovskite Solar Cells*. https://www.science.org.

(126) Zhang, F.; Yeon Park, S.; Yao, C.; Lu, H.; Dunfield, S. P.; Xiao, C.; Uličná, S.; Zhao, X.; Du Hill, L.; Chen, X.; Wang, X.; Mundt, L. E.; Stone, K. H.; Schelhas, L. T.; Teeter, G.; Parkin, S.; Ratcliff, E. L.; Loo, Y.-L.; Berry, J. J.; Beard, M. C.; Yan, Y.; Larson, B. W.; Zhu, K. *Metastable Dion-Jacobson 2D Structure Enables Efficient and Stable Perovskite Solar Cells*. https://www.science.org.

(127) Zheng, L.; Shen, L.; Fang, Z.; Song, P.; Tian, W.; Chen, J.; Liu, K.; Luo, Y.; Xu, P.; Yang, J.; Tian, C.; Xie, L.; Wei, Z. Reducing the Surface Reactivity of Alkyl Ammonium Passivation Molecules Enables Highly Efficient Perovskite Solar Cells. *Adv Energy Mater* **2023**, *13* (36). https://doi.org/10.1002/aenm.202301066.

(128) Xu, J.; Qiao, H.; Chen, Z.; Wang, X. L.; Yao, Y. F. Construction of a 3D/2D Heterojunction Based on a Fluorinated Cyclohexylamine 2D Ruddlesden-

Popper Perovskite for Highly Efficient and Stable Perovskite Solar Cells. *APL Mater* **2023**, *11* (4). https://doi.org/10.1063/5.0142995.

(129) Liu, S.; Guan, X.; Xiao, W.; Chen, R.; Zhou, J.; Ren, F.; Wang, J.; Chen, W.; Li, S.; Qiu, L.; Zhao, Y.; Liu, Z.; Chen, W. Effective Passivation with Size-Matched Alkyldiammonium Iodide for High-Performance Inverted Perovskite Solar Cells. *Adv Funct Mater* **2022**, *32* (38). https://doi.org/10.1002/adfm.202205009.

(130) Zhang, F.; Yeon Park, S.; Yao, C.; Lu, H.; Dunfield, S. P.; Xiao, C.; Uličná, S.; Zhao, X.; Du Hill, L.; Chen, X.; Wang, X.; Mundt, L. E.; Stone, K. H.; Schelhas, L. T.; Teeter, G.; Parkin, S.; Ratcliff, E. L.; Loo, Y.-L.; Berry, J. J.; Beard, M. C.; Yan, Y.; Larson, B. W.; Zhu, K. *Metastable Dion-Jacobson 2D Structure Enables Efficient and Stable Perovskite Solar Cells*. https://www.science.org.

(131) Xu, J.; Qiao, H.; Chen, Z.; Wang, X. L.; Yao, Y. F. Construction of a 3D/2D Heterojunction Based on a Fluorinated Cyclohexylamine 2D Ruddlesden-Popper Perovskite for Highly Efficient and Stable Perovskite Solar Cells. *APL Mater* **2023**, *11* (4). https://doi.org/10.1063/5.0142995.

(132) Zhao, W.; Wu, M.; Liu, Z.; Yang, S.; Li, Y.; Wang, J.; Yang, L.; Han, Y.; Liu, S. Orientation Engineering via 2D Seeding for Stable 24.83% Efficiency Perovskite Solar Cells. *Adv Energy Mater* **2023**, *13* (14). https://doi.org/10.1002/aenm.202204260.

(133) Lee, J. W.; Tan, S.; Seok, S. Il; Yang, Y.; Park, N. G. Rethinking the A Cation in Halide Perovskites. *Science (1979)* **2022**, *375* (6583). https://doi.org/10.1126/science.abj1186.

(134) Peng, S.; Yang, Z.; Sun, M.; Yu, L.; Li, Y. Stabilizing Metal Halide Perovskites for Solar Fuel Production: Challenges, Solutions, and Future Prospects. *Advanced Materials*. John Wiley and Sons Inc November 9, 2023. https://doi.org/10.1002/adma.202304711.

(135) Zhao, J.; Zhang, Z.; Li, G.; Aldamasy, M. H.; Li, M.; Abate, A. Dimensional Tuning in Lead-Free Tin Halide Perovskite for Solar Cells. *Advanced Energy Materials*. John Wiley and Sons Inc April 6, 2023. https://doi.org/10.1002/aenm.202204233.

(136) Zhou, T.; Xu, Z.; Wang, R.; Dong, X.; Fu, Q.; Liu, Y. Crystal Growth Regulation of 2D/3D Perovskite Films for Solar Cells with Both High Efficiency and Stability. *Advanced Materials* **2022**, *34* (17). https://doi.org/10.1002/adma.202200705.

(137) Li, Y.; Wu, J.; Zhang, Y.; Zhang, L.; Zhou, X.; Hu, B.; Jiang, Z.; Zeng, J.; Wang, D.; Liu, Y.; Chen, S.; Liu, Z.; Liu, C.; Wang, X.; Xu, B. Whether Organic Spacer Cations Induced 2D/3D or Quasi-2D/3D Mixed Dimensional Perovskites? *Chemical Engineering Journal* **2022**, *450*. https://doi.org/10.1016/j.cej.2022.137887.

(138) Zhong, Y.; Liu, G.; Su, Y.; Sheng, W.; Gong, L.; Zhang, J.; Tan, L.; Chen, Y. Diammonium Molecular Configuration-Induced Regulation of Crystal Orientation and Carrier Dynamics for Highly Efficient and Stable 2D/3D Perovskite Solar Cells. *Angewandte Chemie - International Edition* **2022**, *61* (5). https://doi.org/10.1002/anie.202114588.

(139) Wu, T.; Li, X.; Qi, Y.; Zhang, Y.; Han, L. Defect Passivation for Perovskite Solar Cells: From Molecule Design to Device Performance. *ChemSusChem*. John Wiley and Sons Inc October 20, 2021, pp 4354–4376. https://doi.org/10.1002/cssc.202101573.

(140) Cheng, H.; Liu, C.; Zhuang, J.; Cao, J.; Wang, T.; Wong, W. Y.; Yan, F. KBF4 Additive for Alleviating Microstrain, Improving Crystallinity, and Passivating Defects in Inverted Perovskite Solar Cells. *Adv Funct Mater* **2022**, *32* (36). https://doi.org/10.1002/adfm.202204880.

(141) Abdi-Jalebi, M.; Andaji-Garmaroudi, Z.; Cacovich, S.; Stavrakas, C.; Philippe, B.; Richter, J. M.; Alsari, M.; Booker, E. P.; Hutter, E. M.; Pearson,

A. J.; Lilliu, S.; Savenije, T. J.; Rensmo, H.; Divitini, G.; Ducati, C.; Friend, R. H.; Stranks, S. D. Maximizing and Stabilizing Luminescence from Halide Perovskites with Potassium Passivation. *Nature* **2018**, *555* (7697), 497–501. https://doi.org/10.1038/nature25989.

(142) Correa-Baena, J.-P.; Saliba, M.; Buonassisi, T.; Grätzel, M.; Abate, A.; Tress, W.; Hagfeldt, A. *Promises and Challenges of Perovskite Solar Cells*. https://www.science.org.

(143) Li, D.; Zhang, D.; Lim, K. S.; Hu, Y.; Rong, Y.; Mei, A.; Park, N. G.; Han, H. A Review on Scaling Up Perovskite Solar Cells. *Advanced Functional Materials*. John Wiley and Sons Inc March 1, 2021. https://doi.org/10.1002/adfm.202008621.

(144) Charles, R. G.; Doolin, A.; García-Rodríguez, R.; Villalobos, K. V.; Davies, M. L. Circular Economy for Perovskite Solar Cells - Drivers, Progress and Challenges. *Energy and Environmental Science*. Royal Society of Chemistry July 26, 2023, pp 3711–3733. https://doi.org/10.1039/d3ee00841j.

(145) Cai, M.; Wu, Y.; Chen, H.; Yang, X.; Qiang, Y.; Han, L. Cost-Performance Analysis of Perovskite Solar Modules. *Advanced Science* **2017**, *4* (1). https://doi.org/10.1002/advs.201600269.

(146) Qu, S.; Tian, H. Diketopyrrolopyrrole (DPP)-Based Materials for Organic Photovoltaics. *Chemical Communications* **2012**, *48* (25), 3039–3051. https://doi.org/10.1039/c2cc17886a.

(147) Bronstein, H.; Chen, Z.; Ashraf, R. S.; Zhang, W.; Du, J.; Durrant, J. R.; Shakya Tuladhar, P.; Song, K.; Watkins, S. E.; Geerts, Y.; Wienk, M. M.; Janssen, R. A. J.; Anthopoulos, T.; Sirringhaus, H.; Heeney, M.; McCulloch, I. Thieno[3,2- b]Thiophene-Diketopyrrolopyrrole-Containing Polymers for High-Performance Organic Field-Effect Transistors and Organic Photovoltaic Devices. *J Am Chem Soc* **2011**, *133* (10), 3272–3275. https://doi.org/10.1021/ja110619k.

(148) Kim, M.; Ryu, S. U.; Park, S. A.; Choi, K.; Kim, T.; Chung, D.; Park, T. Donor–Acceptor-Conjugated Polymer for High-Performance Organic Field-Effect Transistors: A Progress Report. *Advanced Functional Materials*. Wiley-VCH Verlag May 1, 2020. https://doi.org/10.1002/adfm.201904545.

(149) Li, Y.; Sonar, P.; Murphy, L.; Hong, W. High Mobility Diketopyrrolopyrrole (DPP)-Based Organic Semiconductor Materials for Organic Thin Film Transistors and Photovoltaics. *Energy and Environmental Science*. June 2013, pp 1684–1710. https://doi.org/10.1039/c3ee00015j.

(150) Wang, T.; Deng, W.; Cao, J.; Yan, F. Recent Progress on Heterojunction Engineering in Perovskite Solar Cells. *Advanced Energy Materials*. John Wiley and Sons Inc September 1, 2023. https://doi.org/10.1002/aenm.202201436.

(151) Guo, Z.; Jena, A. K.; Kim, G. M.; Miyasaka, T. The High Open-Circuit Voltage of Perovskite Solar Cells: A Review. *Energy and Environmental Science*. Royal Society of Chemistry June 20, 2022, pp 3171–3222. https://doi.org/10.1039/d2ee00663d.

(152) Krishna, A.; Gottis, S.; Nazeeruddin, M. K.; Sauvage, F. Mixed Dimensional 2D/3D Hybrid Perovskite Absorbers: The Future of Perovskite Solar Cells? *Advanced Functional Materials*. Wiley-VCH Verlag February 21, 2019. https://doi.org/10.1002/adfm.201806482.

(153) Burschka, J.; Pellet, N.; Moon, S. J.; Humphry-Baker, R.; Gao, P.; Nazeeruddin, M. K.; Grätzel, M. Sequential Deposition as a Route to High-Performance Perovskite-Sensitized Solar Cells. *Nature* **2013**, *499* (7458), 316–319. https://doi.org/10.1038/nature12340.

(154) Campos, T.; Dally, P.; Gbegnon, S.; Blaizot, A.; Trippé-Allard, G.; Provost, M.; Bouttemy, M.; Duchatelet, A.; Garrot, D.; Rousset, J.; Deleporte, E. Unraveling the Formation Mechanism of the 2D/3D Perovskite Heterostructure for Perovskite Solar Cells Using Multi-Method

Characterization. *Journal of Physical Chemistry C* **2022**, *126* (31), 13527–13538. https://doi.org/10.1021/acs.jpcc.2c04957.

(155) Thrithamarassery Gangadharan, D.; Ma, D. Searching for Stability at Lower Dimensions: Current Trends and Future Prospects of Layered Perovskite Solar Cells. *Energy Environ Sci* **2019**, *12* (10), 2860–2889. https://doi.org/10.1039/c9ee01591d.

(156) Qin, Y.; Zhong, H.; Intemann, J. J.; Leng, S.; Cui, M.; Qin, C.; Xiong, M.; Liu, F.; Jen, A. K. Y.; Yao, K. Coordination Engineering of Single-Crystal Precursor for Phase Control in Ruddlesden–Popper Perovskite Solar Cells. *Adv Energy Mater* **2020**, *10* (16). https://doi.org/10.1002/aenm.201904050.

(157) Zhou, N.; Zhou, H. Spacer Organic Cation Engineering for Quasi-2D Metal Halide Perovskites and the Optoelectronic Application. *Small Structures*. John Wiley and Sons Inc July 1, 2022. https://doi.org/10.1002/sstr.202100232.

(158) Gao, P.; Bin Mohd Yusoff, A. R.; Nazeeruddin, M. K. Dimensionality Engineering of Hybrid Halide Perovskite Light Absorbers. *Nature Communications*. Nature Publishing Group December 1, 2018. https://doi.org/10.1038/s41467-018-07382-9.

(159) Hu, F.; Lou, Y. H.; Wang, Z. K. Functional 2D Phases in Mixed Dimensional Perovskite Photovoltaics. *Advanced Functional Materials*. John Wiley and Sons Inc November 2, 2023. https://doi.org/10.1002/adfm.202304848.

(160) Gunes, U.; Bag Celik, E.; Akgul, C. C.; Koc, M.; Ameri, M.; Uzuner, B. E.; Ghasemi, M.; Sahiner, M. C.; Yildiz, İ.; Kaya, H. Z.; Yerci, S.; Gunbas, G. A Thienothiophene-Based Cation Treatment Allows Semitransparent Perovskite Solar Cells with Improved Efficiency and Stability. *Adv Funct Mater* **2021**, *31* (42). https://doi.org/10.1002/adfm.202103130.

(161) Fu, C.; Gu, Z.; Tang, Y.; Xiao, Q.; Zhang, S.; Zhang, Y.; Song, Y. From Structural Design to Functional Construction: Amine Molecules in High-

Performance Formamidinium-Based Perovskite Solar Cells. *Angewandte Chemie - International Edition*. John Wiley and Sons Inc May 2, 2022. https://doi.org/10.1002/anie.202117067.

(162) Metcalf, I.; Sidhik, S.; Zhang, H.; Agrawal, A.; Persaud, J.; Hou, J.; Even, J.; Mohite, A. D. Synergy of 3D and 2D Perovskites for Durable, Efficient Solar Cells and Beyond. *Chemical Reviews*. American Chemical Society August 9, 2023, pp 9565–9652. https://doi.org/10.1021/acs.chemrev.3c00214.

(163) Zhou, Q.; Xiong, Q.; Zhang, Z.; Hu, J.; Lin, F.; Liang, L.; Wu, T.; Wang, X.; Wu, J.; Zhang, B.; Gao, P. Fluoroaromatic Cation-Assisted Planar Junction Perovskite Solar Cells with Improved $V_{OC}$ and Stability: The Role of Fluorination Position. *Solar RRL* **2020**, *4* (7). https://doi.org/10.1002/solr.202000107.

(164) Hu, J.; Oswald, I. W. H.; Stuard, S. J.; Nahid, M. M.; Zhou, N.; Williams, O. F.; Guo, Z.; Yan, L.; Hu, H.; Chen, Z.; Xiao, X.; Lin, Y.; Yang, Z.; Huang, J.; Moran, A. M.; Ade, H.; Neilson, J. R.; You, W. Synthetic Control over Orientational Degeneracy of Spacer Cations Enhances Solar Cell Efficiency in Two-Dimensional Perovskites. *Nat Commun* **2019**, *10* (1). https://doi.org/10.1038/s41467-019-08980-x.

(165) Su, H.; Zhang, L.; Liu, Y.; Hu, Y.; Zhang, B.; You, J.; Du, X.; Zhang, J.; Ren, X.; Gou, J.; Liu, S. (Frank). Polarity Regulation for Stable 2D-Perovskite-Encapsulated High-Efficiency 3D-Perovskite Solar Cells. *Nano Energy* **2022**, *95*. https://doi.org/10.1016/j.nanoen.2022.106965.

(166) Ren, X.; Zhang, B.; Zhang, L.; Wen, J.; Che, B.; Bai, D.; You, J.; Chen, T.; Liu, S. Deep-Level Transient Spectroscopy for Effective Passivator Selection in Perovskite Solar Cells to Attain High Efficiency over 23%. *ChemSusChem* **2021**, *14* (15), 3182–3189. https://doi.org/10.1002/cssc.202100980.

(167) Wang, Z.; Wei, Q.; Liu, X.; Liu, L.; Tang, X.; Guo, J.; Ren, S.; Xing, G.; Zhao, D.; Zheng, Y. Spacer Cation Tuning Enables Vertically Oriented and

Graded Quasi-2D Perovskites for Efficient Solar Cells. *Adv Funct Mater* **2021**, *31* (5). https://doi.org/10.1002/adfm.202008404.

(168) Lee, H. B.; Kumar, N.; Tyagi, B.; Ko, K. J.; Kang, J. W. Dimensionality and Defect Engineering Using Fluoroaromatic Cations for Efficiency and Stability Enhancement in 3D/2D Perovskite Photovoltaics. *Solar RRL* **2021**, *5* (3). https://doi.org/10.1002/solr.202000589.

(169) Zhao, S.; Xie, J.; Cheng, G.; Xiang, Y.; Zhu, H.; Guo, W.; Wang, H.; Qin, M.; Lu, X.; Qu, J.; Wang, J.; Xu, J.; Yan, K. General Nondestructive Passivation by 4-Fluoroaniline for Perovskite Solar Cells with Improved Performance and Stability. *Small* **2018**, *14* (50). https://doi.org/10.1002/smll.201803350.

(170) Pan, H.; Zhao, X.; Gong, X.; Shen, Y.; Wang, M. Atomic-Scale Tailoring of Organic Cation of Layered Ruddlesden-Popper Perovskite Compounds. *Journal of Physical Chemistry Letters* **2019**, *10* (8), 1813–1819. https://doi.org/10.1021/acs.jpclett.9b00479.

(171) Gozukara Karabag, Z.; Karabag, A.; Gunes, U.; Gao, X. X.; Syzgantseva, O. A.; Syzgantseva, M. A.; Varlioglu Yaylali, F.; Shibayama, N.; Kanda, H.; Rafieh, A. I.; Turnell-Ritson, R. C.; Dyson, P. J.; Yerci, S.; Nazeeruddin, M. K.; Gunbas, G. Tuning 2D Perovskite Passivation: Impact of Electronic and Steric Effects on the Performance of 3D/2D Perovskite Solar Cells. *Adv Energy Mater* **2023**, *13* (45). https://doi.org/10.1002/aenm.202302038.

(172) Lin, T.; Dai, T.; Li, X. 2D/3D Perovskite: A Step toward Commercialization of Perovskite Solar Cells. *Solar RRL*. John Wiley and Sons Inc April 1, 2023. https://doi.org/10.1002/solr.202201138.

(173) Gunes, U.; Yaylali, F. V.; Gozukara Karabag, Z.; Gao, X.-X.; Syzgantseva, O. A.; Karabag, A.; Yildirim, G. B.; Tsoi, K.; Shibayama, N.; Kanda, H.; Rafieh, A. I.; Zhong, L.; Züttel, A.; Dyson, P. J.; Yerci, S.; Nazeeruddin, M. K.; Gunbas, G. Drastic Influence of Substituent Position on Orientation of 2D

Layers Enables Efficient and Stable 3D/2D Perovskite Solar Cells. *Cell Rep Phys Sci* **2023**, 101380. https://doi.org/10.1016/j.xcrp.2023.101380.

(174) Perdew, J. P.; Burke, K.; Ernzerhof, M. *Generalized Gradient Approximation Made Simple*; 1996.

(175) Grimme, S.; Antony, J.; Ehrlich, S.; Krieg, H. A Consistent and Accurate Ab Initio Parametrization of Density Functional Dispersion Correction (DFT-D) for the 94 Elements H-Pu. *Journal of Chemical Physics* **2010**, *132* (15). https://doi.org/10.1063/1.3382344/926936.

(176) Vande Vondele, J.; Hutter, J. Gaussian Basis Sets for Accurate Calculations on Molecular Systems in Gas and Condensed Phases. *Journal of Chemical Physics* **2007**, *127* (11). https://doi.org/10.1063/1.2770708/295855.

(177) Goedecker, S.; Teter, M.; Hutter, J. *Separable Dual-Space Gaussian Pseudopotentials*; 1996.

(178) Kühne, T. D.; Iannuzzi, M.; Del Ben, M.; Rybkin, V. V.; Seewald, P.; Stein, F.; Laino, T.; Khaliullin, R. Z.; Schütt, O.; Schiffmann, F.; Golze, D.; Wilhelm, J.; Chulkov, S.; Bani-Hashemian, M. H.; Weber, V.; Borštnik, U.; Taillefumier, M.; Jakobovits, A. S.; Lazzaro, A.; Pabst, H.; Müller, T.; Schade, R.; Guidon, M.; Andermatt, S.; Holmberg, N.; Schenter, G. K.; Hehn, A.; Bussy, A.; Belleflamme, F.; Tabacchi, G.; Glöß, A.; Lass, M.; Bethune, I.; Mundy, C. J.; Plessl, C.; Watkins, M.; VandeVondele, J.; Krack, M.; Hutter, J. CP2K: An Electronic Structure and Molecular Dynamics Software Package -Quickstep: Efficient and Accurate Electronic Structure Calculations. *Journal of Chemical Physics*. American Institute of Physics Inc. May 21, 2020. https://doi.org/10.1063/5.0007045.

(179) Momma, K.; Izumi, F. VESTA 3 for Three-Dimensional Visualization of Crystal, Volumetric and Morphology Data. *J Appl Crystallogr* **2011**, *44* (6), 1272–1276. https://doi.org/10.1107/S0021889811038970.

(180) Humphrey, W.; Dalke, A.; Schulten, K. *VMD: Visual Molecular Dynamics*; 1996.

(181) Karabağ, A. *A Systematıc Research On Ratıonal Desıgn And Synthesıs of Innovatıve Materıals For Developıng Hıgh-Performance Perovskıte Solar Cells*

(182) Li, D.; Lai, W. Y.; Zhang, Y. Z.; Huang, W. Printable Transparent Conductive Films for Flexible Electronics. *Advanced Materials*. Wiley-VCH Verlag March 8, 2018. https://doi.org/10.1002/adma.201704738.

(183) Li, M. H.; Yeh, H. H.; Chiang, Y. H.; Jeng, U. S.; Su, C. J.; Shiu, H. W.; Hsu, Y. J.; Kosugi, N.; Ohigashi, T.; Chen, Y. A.; Shen, P. S.; Chen, P.; Guo, T. F. Highly Efficient 2D/3D Hybrid Perovskite Solar Cells via Low-Pressure Vapor-Assisted Solution Process. *Advanced Materials* **2018**, *30* (30). https://doi.org/10.1002/adma.201801401.

(184) Abbas, M. S.; Hussain, S.; Zhang, J.; Wang, B.; Yang, C.; Wang, Z.; Wei, Z.; Ahmad, R. Orientationally Engineered 2D/3D Perovskite for High Efficiency Solar Cells. *Sustain Energy Fuels* **2019**, *4* (1), 324–330. https://doi.org/10.1039/c9se00817a.

(185) Cho, K. T.; Paek, S.; Grancini, G.; Roldán-Carmona, C.; Gao, P.; Lee, Y.; Nazeeruddin, M. K. Highly Efficient Perovskite Solar Cells with a Compositionally Engineered Perovskite/Hole Transporting Material Interface. *Energy Environ Sci* **2017**, *10* (2), 621–627. https://doi.org/10.1039/c6ee03182j.

(186) Zhou, T.; Lai, H.; Liu, T.; Lu, D.; Wan, X.; Zhang, X.; Liu, Y.; Chen, Y. Highly Efficient and Stable Solar Cells Based on Crystalline Oriented 2D/3D Hybrid Perovskite. *Advanced Materials* **2019**, *31* (32). https://doi.org/10.1002/adma.201901242.

(187) Proppe, A. H.; Johnston, A.; Teale, S.; Mahata, A.; Quintero-Bermudez, R.; Jung, E. H.; Grater, L.; Cui, T.; Filleter, T.; Kim, C. Y.; Kelley, S. O.; De

Angelis, F.; Sargent, E. H. Multication Perovskite 2D/3D Interfaces Form via Progressive Dimensional Reduction. *Nat Commun* **2021**, *12* (1). https://doi.org/10.1038/s41467-021-23616-9.

(188) Liu, C.; Yang, Y.; Rakstys, K.; Mahata, A.; Franckevicius, M.; Mosconi, E.; Skackauskaite, R.; Ding, B.; Brooks, K. G.; Usiobo, O. J.; Audinot, J. N.; Kanda, H.; Driukas, S.; Kavaliauskaite, G.; Gulbinas, V.; Dessimoz, M.; Getautis, V.; De Angelis, F.; Ding, Y.; Dai, S.; Dyson, P. J.; Nazeeruddin, M. K. Tuning Structural Isomers of Phenylenediammonium to Afford Efficient and Stable Perovskite Solar Cells and Modules. *Nat Commun* **2021**, *12* (1). https://doi.org/10.1038/s41467-021-26754-2.

(189) Quintero-Bermudez, R.; Gold-Parker, A.; Proppe, A. H.; Munir, R.; Yang, Z.; Kelley, S. O.; Amassian, A.; Toney, M. F.; Sargent, E. H. Compositional and Orientational Control in Metal Halide Perovskites of Reduced Dimensionality. *Nat Mater* **2018**, *17* (10), 900–907. https://doi.org/10.1038/s41563-018-0154-x.

(190) Wang, F.; Jiang, X.; Chen, H.; Shang, Y.; Liu, H.; Wei, J.; Zhou, W.; He, H.; Liu, W.; Ning, Z. 2D-Quasi-2D-3D Hierarchy Structure for Tin Perovskite Solar Cells with Enhanced Efficiency and Stability. *Joule* **2018**, *2* (12), 2732–2743. https://doi.org/10.1016/j.joule.2018.09.012.

(191) Wu, G.; Liang, R.; Ge, M.; Sun, G.; Zhang, Y.; Xing, G. Surface Passivation Using 2D Perovskites toward Efficient and Stable Perovskite Solar Cells. *Advanced Materials*. John Wiley and Sons Inc February 1, 2022. https://doi.org/10.1002/adma.202105635.

(192) Lv, Y.; Song, X.; Yin, Y.; Feng, Y.; Ma, H.; Hao, C.; Jin, S.; Shi, Y. Hexylammonium Iodide Derived Two-Dimensional Perovskite as Interfacial Passivation Layer in Efficient Two-Dimensional/Three-Dimensional Perovskite Solar Cells. *ACS Appl Mater Interfaces* **2020**, *12* (1), 698–705. https://doi.org/10.1021/acsami.9b17930.

(193) Zouhair, S.; Yoo, S. M.; Bogachuk, D.; Herterich, J. P.; Lim, J.; Kanda, H.; Son, B.; Yun, H. J.; Würfel, U.; Chahboun, A.; Nazeeruddin, M. K.; Hinsch, A.; Wagner, L.; Kim, H. Employing 2D-Perovskite as an Electron Blocking Layer in Highly Efficient (18.5%) Perovskite Solar Cells with Printable Low Temperature Carbon Electrode. *Adv Energy Mater* **2022**, *12* (21). https://doi.org/10.1002/aenm.202200837.

(194) Choi, H. S.; Kim, H. S. 3D/2D Bilayerd Perovskite Solar Cells with an Enhanced Stability and Performance. *Materials*. MDPI AG September 1, 2020. https://doi.org/10.3390/ma13173868.

(195) Chen, P.; Bai, Y.; Wang, S.; Lyu, M.; Yun, J. H.; Wang, L. In Situ Growth of 2D Perovskite Capping Layer for Stable and Efficient Perovskite Solar Cells. *Adv Funct Mater* **2018**, *28* (17). https://doi.org/10.1002/adfm.201706923.

(196) Zhuang, J.; Mao, P.; Luan, Y.; Yi, X.; Tu, Z.; Zhang, Y.; Yi, Y.; Wei, Y.; Chen, N.; Lin, T.; Wang, F.; Li, C.; Wang, J. Interfacial Passivation for Perovskite Solar Cells: The Effects of the Functional Group in Phenethylammonium Iodide. *ACS Energy Lett* **2019**, *4* (12), 2913–2921. https://doi.org/10.1021/acsenergylett.9b02375.

(197) Yue, X.; Zhao, X.; Fan, B.; Yang, Y.; Yan, L.; Qu, S.; Huang, H.; Zhang, Q.; Yan, H.; Cui, P.; Ji, J.; Ma, J.; Li, M. Surface Regulation through Dipolar Molecule Boosting the Efficiency of Mixed 2D/3D Perovskite Solar Cell to 24%. *Adv Funct Mater* **2023**, *33* (4). https://doi.org/10.1002/adfm.202209921.

(198) Mahmud, M. A.; Pham, H. T.; Duong, T.; Yin, Y.; Peng, J.; Wu, Y.; Liang, W.; Li, L.; Kumar, A.; Shen, H.; Walter, D.; Nguyen, H. T.; Mozaffari, N.; Tabi, G. D.; Andersson, G.; Catchpole, K. R.; Weber, K. J.; White, T. P. Combined Bulk and Surface Passivation in Dimensionally Engineered 2D-3D Perovskite Films via Chlorine Diffusion. *Adv Funct Mater* **2021**, *31* (46). https://doi.org/10.1002/adfm.202104251.

(199) Kim, H.; Lee, S. U.; Lee, D. Y.; Paik, M. J.; Na, H.; Lee, J.; Seok, S. Il. Optimal Interfacial Engineering with Different Length of Alkylammonium Halide for Efficient and Stable Perovskite Solar Cells. *Adv Energy Mater* **2019**, *9* (47). https://doi.org/10.1002/aenm.201902740.

(200) Tan, S.; Zhou, N.; Chen, Y.; Li, L.; Liu, G.; Liu, P.; Zhu, C.; Lu, J.; Sun, W.; Chen, Q.; Zhou, H. Effect of High Dipole Moment Cation on Layered 2D Organic–Inorganic Halide Perovskite Solar Cells. *Adv Energy Mater* **2019**, *9* (5). https://doi.org/10.1002/aenm.201803024.

(201) Tan, H.; Lyu, Q.; Xie, Z.; Li, M.; Wang, K.; Wang, K.; Xiong, B.; Zhang, L.; Zhu, J. Metallosupramolecular Photonic Elastomers with Self-Healing Capability and Angle-Independent Color. *Advanced Materials* **2019**, *31* (6). https://doi.org/10.1002/adma.201805496.

(202) Grancini, G.; Nazeeruddin, M. K. Dimensional Tailoring of Hybrid Perovskites for Photovoltaics. *Nature Reviews Materials*. Nature Publishing Group January 1, 2019, pp 4–22. https://doi.org/10.1038/s41578-018-0065-0.

(203) Zhou, Q.; Liu, B.; Shai, X.; Li, Y.; He, P.; Yu, H.; Chen, C.; Xu, Z.-X.; Wei, D.; Chen, J. Precise Modulation Strategies of 2D/3D Perovskite Heterojunctions in Efficient and Stable Solar Cells. *Chemical Communications* **2023**. https://doi.org/10.1039/d2cc07048k.

(204) Chen, C.; Liang, J.; Zhang, J.; Liu, X.; Yin, X.; Cui, H.; Wang, H.; Wang, C.; Li, Z.; Gong, J.; Lin, Q.; Ke, W.; Tao, C.; Da, B.; Ding, Z.; Xiao, X.; Fang, G. Interfacial Engineering of a Thiophene-Based 2D/3D Perovskite Heterojunction for Efficient and Stable Inverted Wide-Bandgap Perovskite Solar Cells. *Nano Energy* **2021**, *90*. https://doi.org/10.1016/j.nanoen.2021.106608.

(205) Qin, Z.; Xue, H.; Qin, M.; Li, Y.; Wu, X.; Wu, W. R.; Su, C. J.; Brocks, G.; Tao, S.; Lu, X. Critical Influence of Organic A′-Site Ligand Structure on 2D

Perovskite Crystallization. *Small* **2023**. https://doi.org/10.1002/smll.202206787.

(206) Liang, L.; Luo, H.; Hu, J.; Li, H.; Gao, P. Efficient Perovskite Solar Cells by Reducing Interface-Mediated Recombination: A Bulky Amine Approach. *Adv Energy Mater* **2020**, *10* (14). https://doi.org/10.1002/aenm.202000197.

(207) Hansch, C.; Leo, A.; Taft, R. W. *A Survey of Hammett Substituent Constants and Resonance and Field Parameters*; 1991; Vol. 91. https://pubs.acs.org/sharingguidelines.

(208) Wang, Y.; Zhang, Y.; Zhang, P.; Zhang, W. High Intrinsic Carrier Mobility and Photon Absorption in the Perovskite CH3NH3PbI3. *Physical Chemistry Chemical Physics* **2015**, *17* (17), 11516–11520. https://doi.org/10.1039/c5cp00448a.

(209) Eperon, G. E.; Stranks, S. D.; Menelaou, C.; Johnston, M. B.; Herz, L. M.; Snaith, H. J. Formamidinium Lead Trihalide: A Broadly Tunable Perovskite for Efficient Planar Heterojunction Solar Cells. *Energy Environ Sci* **2014**, *7* (3), 982–988. https://doi.org/10.1039/c3ee43822h.

(210) Yang, Y.; Yang, M.; Li, Z.; Crisp, R.; Zhu, K.; Beard, M. C. Comparison of Recombination Dynamics in CH3NH3PbBr3 and CH3NH3PbI3 Perovskite Films: Influence of Exciton Binding Energy. *Journal of Physical Chemistry Letters* **2015**, *6* (23), 4688–4692. https://doi.org/10.1021/acs.jpclett.5b02290.

(211) Miyata, A.; Mitioglu, A.; Plochocka, P.; Portugall, O.; Wang, J. T. W.; Stranks, S. D.; Snaith, H. J.; Nicholas, R. J. Direct Measurement of the Exciton Binding Energy and Effective Masses for Charge Carriers in Organic-Inorganic Tri-Halide Perovskites. *Nat Phys* **2015**, *11* (7), 582–587. https://doi.org/10.1038/nphys3357.

(212) Wang, D.; Wright, M.; Elumalai, N. K.; Uddin, A. Stability of Perovskite Solar Cells. *Solar Energy Materials and Solar Cells*. Elsevier April 1, 2016, pp 255–275. https://doi.org/10.1016/j.solmat.2015.12.025.

(213) Philippe, B.; Park, B. W.; Lindblad, R.; Oscarsson, J.; Ahmadi, S.; Johansson, E. M. J.; Rensmo, H. Chemical and Electronic Structure Characterization of Lead Halide Perovskites and Stability Behavior under Different Exposures-A Photoelectron Spectroscopy Investigation. *Chemistry of Materials* **2015**, *27* (5), 1720–1731. https://doi.org/10.1021/acs.chemmater.5b00348.

(214) Im, H.-S.; Seo, J.-Y.; Park, N.-G. Material and Device Stability in Perovskite Solar Cells. *ChemSusChem* **2016**, *9*, 2528–2540. https://doi.org/10.1002/cssc.v9.18/issuetoc.

(215) Domanski, K.; Correa-Baena, J. P.; Mine, N.; Nazeeruddin, M. K.; Abate, A.; Saliba, M.; Tress, W.; Hagfeldt, A.; Grätzel, M. Not All That Glitters Is Gold: Metal-Migration-Induced Degradation in Perovskite Solar Cells. *ACS Nano* **2016**, *10* (6), 6306–6314. https://doi.org/10.1021/acsnano.6b02613.

(216) Zheng, H.; Xu, H.; Zheng, F.; Liu, G.; Xu, X.; Xu, S.; Zhang, L.; Pan, X. The Effect of Constituent Ratios and Varisized Ammonium Salts on the Performance of Two-Dimensional Perovskite Materials. *ChemSusChem* **2020**, *13* (1), 252–259. https://doi.org/10.1002/cssc.201901948.

(217) Zhou, N.; Zhou, H. Spacer Organic Cation Engineering for Quasi-2D Metal Halide Perovskites and the Optoelectronic Application. *Small Structures*. John Wiley and Sons Inc July 1, 2022. https://doi.org/10.1002/sstr.202100232.

(218) Chen, Y.; Sun, Y.; Peng, J.; Tang, J.; Zheng, K.; Liang, Z. 2D Ruddlesden–Popper Perovskites for Optoelectronics. *Advanced Materials*. Wiley-VCH Verlag January 11, 2018. https://doi.org/10.1002/adma.201703487.

(219) Huang, W.; Bu, T.; Huang, F.; Cheng, Y. B. Stabilizing High Efficiency Perovskite Solar Cells with 3D-2D Heterostructures. *Joule*. Cell Press May 20, 2020, pp 975–979. https://doi.org/10.1016/j.joule.2020.04.009.

(220) Leung, T. L.; Ahmad, I.; Syed, A. A.; Ng, A. M. C.; Popović, J.; Djurišić, A. B. Stability of 2D and Quasi-2D Perovskite Materials and Devices. *Commun Mater* **2022**, *3* (1). https://doi.org/10.1038/s43246-022-00285-9.

(221) Yao, H.; Zhu, W.; Hu, J.; Wu, C.; Wang, S.; Zhao, X.; Niu, X.; Ding, L.; Hao, F. Halogen Engineering of 2D/3D Tin Halide Perovskite for Enhanced Structural Stability. *Chemical Engineering Journal* **2023**, *455*. https://doi.org/10.1016/j.cej.2022.140862.

(222) Zhou, Q.; Xiong, Q.; Zhang, Z.; Hu, J.; Lin, F.; Liang, L.; Wu, T.; Wang, X.; Wu, J.; Zhang, B.; Gao, P. Fluoroaromatic Cation-Assisted Planar Junction Perovskite Solar Cells with Improved $V_{OC}$ and Stability: The Role of Fluorination Position. *Solar RRL* **2020**, *4* (7). https://doi.org/10.1002/solr.202000107.

(223) Zhuang, J.; Mao, P.; Luan, Y.; Yi, X.; Tu, Z.; Zhang, Y.; Yi, Y.; Wei, Y.; Chen, N.; Lin, T.; Wang, F.; Li, C.; Wang, J. Interfacial Passivation for Perovskite Solar Cells: The Effects of the Functional Group in Phenethylammonium Iodide. *ACS Energy Lett* **2019**, *4* (12), 2913–2921. https://doi.org/10.1021/acsenergylett.9b02375.

(224) Xu, H.; Liu, G.; Xu, X.; Xu, S.; Zhang, L.; Chen, X.; Zheng, H.; Pan, X. Hydrophobic 2D Perovskite-Modified Layer with Polyfunctional Groups for Enhanced Performance and High Moisture Stability of Perovskite Solar Cells. *Solar RRL* **2020**, *4* (12). https://doi.org/10.1002/solr.202000647.

(225) Meng, F.; Shang, X.; Gao, D.; Zhang, W.; Chen, C. Functionalizing Phenethylammonium by Methoxy to Achieve Low-Dimensional Interface Defects Passivation for Efficient and Stable Perovskite Solar Cells. *Nanotechnology* **2022**, *33* (6). https://doi.org/10.1088/1361-6528/ac33d5.

(226) Fu, W.; Liu, H.; Shi, X.; Zuo, L.; Li, X.; Jen, A. K. Y. Tailoring the Functionality of Organic Spacer Cations for Efficient and Stable Quasi-2D

Perovskite Solar Cells. *Adv Funct Mater* **2019**, *29* (25). https://doi.org/10.1002/adfm.201900221.

(227) Min, H.; Lee, D. Y.; Kim, J.; Kim, G.; Lee, K. S.; Kim, J.; Paik, M. J.; Kim, Y. K.; Kim, K. S.; Kim, M. G.; Shin, T. J.; Il Seok, S. Perovskite Solar Cells with Atomically Coherent Interlayers on SnO2 Electrodes. *Nature* **2021**, *598* (7881), 444–450. https://doi.org/10.1038/s41586-021-03964-8.

(228) Varlıoğlu Yaylalı, F., *Development of Dopant-Free Hole Transport and Passıvatıon Materıals For Hıgh-Performance Perovskıte Solar Cells*

(229) Long, C.; Huang, K.; Chang, J.; Zuo, C.; Gao, Y.; Luo, X.; Liu, B.; Xie, H.; Chen, Z.; He, J.; Huang, H.; Gao, Y.; Ding, L.; Yang, J. Creating a Dual-Functional 2D Perovskite Layer at the Interface to Enhance the Performance of Flexible Perovskite Solar Cells. *Small* **2021**, *17* (32). https://doi.org/10.1002/smll.202102368.

(230) Chen, P.; Bai, Y.; Wang, S.; Lyu, M.; Yun, J. H.; Wang, L. In Situ Growth of 2D Perovskite Capping Layer for Stable and Efficient Perovskite Solar Cells. *Adv Funct Mater* **2018**, *28* (17). https://doi.org/10.1002/adfm.201706923.

(231) Cho, K. T.; Paek, S.; Grancini, G.; Roldán-Carmona, C.; Gao, P.; Lee, Y.; Nazeeruddin, M. K. Highly Efficient Perovskite Solar Cells with a Compositionally Engineered Perovskite/Hole Transporting Material Interface. *Energy Environ Sci* **2017**, *10* (2), 621–627. https://doi.org/10.1039/c6ee03182j.

(232) Peng, W.; Yin, J.; Ho, K. T.; Ouellette, O.; De Bastiani, M.; Murali, B.; El Tall, O.; Shen, C.; Miao, X.; Pan, J.; Alarousu, E.; He, J. H.; Ooi, B. S.; Mohammed, O. F.; Sargent, E.; Bakr, O. M. Ultralow Self-Doping in Two-Dimensional Hybrid Perovskite Single Crystals. *Nano Lett* **2017**, *17* (8), 4759–4767. https://doi.org/10.1021/acs.nanolett.7b01475.

(233) Wu, J.; Zhang, W.; Wang, Q.; Liu, S.; Du, J.; Mei, A.; Rong, Y.; Hu, Y.; Han, H. A Favored Crystal Orientation for Efficient Printable Mesoscopic

Perovskite Solar Cells. *J Mater Chem A Mater* **2020**, *8* (22), 11148–11154. https://doi.org/10.1039/d0ta04589f.

(234) Li, Y.; Zhang, J.; Xiang, J.; Hu, H.; Zhong, H.; Shi, Y. A Novel 4,4'-Bipiperidine-Based Organic Salt for Efficient and Stable 2D-3D Perovskite Solar Cells. *ACS Appl Mater Interfaces* **2022**, *14* (19), 22324–22331. https://doi.org/10.1021/acsami.1c23115.

(235) Chen, J.; Yang, Y.; Dong, H.; Li, J.; Zhu, X.; Xu, J.; Pan, F.; Yuan, F.; Dai, J.; Jiao, B.; Hou, X.; K-Y Jen, A.; Wu, Z. *Highly Efficient and Stable Perovskite Solar Cells Enabled by Low-Dimensional Perovskitoids*; 2022; Vol. 8. https://www.science.org.

(236) Koh, T. M.; Shanmugam, V.; Guo, X.; Lim, S. S.; Filonik, O.; Herzig, E. M.; Müller-Buschbaum, P.; Swamy, V.; Chien, S. T.; Mhaisalkar, S. G.; Mathews, N. Enhancing Moisture Tolerance in Efficient Hybrid 3D/2D Perovskite Photovoltaics. *J Mater Chem A Mater* **2018**, *6* (5), 2122–2128. https://doi.org/10.1039/c7ta09657g.

(237) Zhang, T.; Long, M.; Qin, M.; Lu, X.; Chen, S.; Xie, F.; Gong, L.; Chen, J.; Chu, M.; Miao, Q.; Chen, Z.; Xu, W.; Liu, P.; Xie, W.; Xu, J. bin. Stable and Efficient 3D-2D Perovskite-Perovskite Planar Heterojunction Solar Cell without Organic Hole Transport Layer. *Joule* **2018**, *2* (12), 2706–2721. https://doi.org/10.1016/j.joule.2018.09.022.

(238) Yang, B.; Suo, J.; Di Giacomo, F.; Olthof, S.; Bogachuk, D.; Kim, Y.; Sun, X.; Wagner, L.; Fu, F.; Zakeeruddin, S. M.; Hinsch, A.; Gratzel, M.; Di Carlo, A.; Hagfeldt, A. Interfacial Passivation Engineering of Perovskite Solar Cells with Fill Factor over 82% and Outstanding Operational Stability on N-i-p Architecture. *ACS Energy Lett* **2021**, *6* (11), 3916–3923. https://doi.org/10.1021/acsenergylett.1c01811.

(239) Zhou, J.; Li, M.; Wang, S.; Tan, L.; Liu, Y.; Jiang, C.; Zhao, X.; Ding, L.; Yi, C. 2-CF3-PEAI to Eliminate Pb0 Traps and Form a 2D Perovskite Layer to

Enhance the Performance and Stability of Perovskite Solar Cells. *Nano Energy* **2022**, *95*. https://doi.org/10.1016/j.nanoen.2022.107036.

(240) Mahmud, M. A.; Pham, H. T.; Duong, T.; Yin, Y.; Peng, J.; Wu, Y.; Liang, W.; Li, L.; Kumar, A.; Shen, H.; Walter, D.; Nguyen, H. T.; Mozaffari, N.; Tabi, G. D.; Andersson, G.; Catchpole, K. R.; Weber, K. J.; White, T. P. Combined Bulk and Surface Passivation in Dimensionally Engineered 2D-3D Perovskite Films via Chlorine Diffusion. *Adv Funct Mater* **2021**, *31* (46). https://doi.org/10.1002/adfm.202104251.

(241) Mahmud, M. A.; Duong, T.; Yin, Y.; Peng, J.; Wu, Y.; Lu, T.; Pham, H. T.; Shen, H.; Walter, D.; Nguyen, H. T.; Mozaffari, N.; Tabi, G. D.; Liu, Y.; Andersson, G.; Catchpole, K. R.; Weber, K. J.; White, T. P. In Situ Formation of Mixed-Dimensional Surface Passivation Layers in Perovskite Solar Cells with Dual-Isomer Alkylammonium Cations. *Small* **2020**, *16* (49). https://doi.org/10.1002/smll.202005022.

(242) Tan, S.; Zhou, N.; Chen, Y.; Li, L.; Liu, G.; Liu, P.; Zhu, C.; Lu, J.; Sun, W.; Chen, Q.; Zhou, H. Effect of High Dipole Moment Cation on Layered 2D Organic–Inorganic Halide Perovskite Solar Cells. *Adv Energy Mater* **2019**, *9* (5). https://doi.org/10.1002/aenm.201803024.

(243) Zhao, T.; Chueh, C. C.; Chen, Q.; Rajagopal, A.; Jen, A. K. Y. Defect Passivation of Organic-Inorganic Hybrid Perovskites by Diammonium Iodide toward High-Performance Photovoltaic Devices. *ACS Energy Lett* **2016**, *1* (4), 757–763. https://doi.org/10.1021/acsenergylett.6b00327.

(244) Perdew, J. P.; Burke, K.; Ernzerhof, M. *Generalized Gradient Approximation Made Simple*; 1996.

(245) Grimme, S.; Antony, J.; Ehrlich, S.; Krieg, H. A Consistent and Accurate Ab Initio Parametrization of Density Functional Dispersion Correction (DFT-D) for the 94 Elements H-Pu. *Journal of Chemical Physics* **2010**, *132* (15). https://doi.org/10.1063/1.3382344.

(246) Gratia, P.; Zimmermann, I.; Schouwink, P.; Yum, J. H.; Audinot, J. N.; Sivula, K.; Wirtz, T.; Nazeeruddin, M. K. The Many Faces of Mixed Ion Perovskites: Unraveling and Understanding the Crystallization Process. *ACS Energy Lett* **2017**, *2* (12), 2686–2693. https://doi.org/10.1021/acsenergylett.7b00981.

(247) Liu, C.; Yang, Y.; Rakstys, K.; Mahata, A.; Franckevicius, M.; Mosconi, E.; Skackauskaite, R.; Ding, B.; Brooks, K. G.; Usiobo, O. J.; Audinot, J. N.; Kanda, H.; Driukas, S.; Kavaliauskaite, G.; Gulbinas, V.; Dessimoz, M.; Getautis, V.; De Angelis, F.; Ding, Y.; Dai, S.; Dyson, P. J.; Nazeeruddin, M. K. Tuning Structural Isomers of Phenylenediammonium to Afford Efficient and Stable Perovskite Solar Cells and Modules. *Nat Commun* **2021**, *12* (1). https://doi.org/10.1038/s41467-021-26754-2.

(248) Kanda, H.; Shibayama, N.; Huckaba, A. J.; Lee, Y.; Paek, S.; Klipfel, N.; Roldán-Carmona, C.; Queloz, V. I. E.; Grancini, G.; Zhang, Y.; Abuhelaiqa, M.; Cho, K. T.; Li, M.; Mensi, M. D.; Kinge, S.; Nazeeruddin, M. K. Band-Bending Induced Passivation: High Performance and Stable Perovskite Solar Cells Using a Perhydropoly(Silazane) Precursor. *Energy Environ Sci* **2020**, *13* (4), 1222–1230. https://doi.org/10.1039/c9ee02028d.

(249) Gao, F.; Zhao, Y.; Zhang, X.; You, J. Recent Progresses on Defect Passivation toward Efficient Perovskite Solar Cells. *Advanced Energy Materials*. Wiley-VCH Verlag April 1, 2020. https://doi.org/10.1002/aenm.201902650.

(250) Sidhik, S.; Wang, Y.; De Siena, M.; Asadpour, R.; Torma, A. J.; Terlier, T.; Ho, K.; Li, W.; Puthirath, A. B.; Shuai, X.; Agrawal, A.; Traore, B.; Jones, M.; Giridharagopal, R.; Ajayan, P. M.; Strzalka, J.; Ginger, D. S.; Katan, C.; Alam, M. A.; Even, J.; Kanatzidis, M. G.; Mohite, A. D. *Deterministic Fabrication of 3D/2D Perovskite Bilayer Stacks for Durable and Efficient Solar Cells*. https://www.science.org.

(251) Vaynzof, Y. The Future of Perovskite Photovoltaics—Thermal Evaporation or Solution Processing? *Adv Energy Mater* **2020**, *10* (48). https://doi.org/10.1002/aenm.202003073.

(252) Rao, P. S.; Gupta, A.; Srivani, D.; Bhosale, S. V.; Bilic, A.; Li, J.; Xiang, W.; Evans, R. A.; Bhosale, S. V. An Efficient Non-Fullerene Acceptor Based on Central and Peripheral Naphthalene Diimides. *Chemical Communications* **2018**, *54* (40), 5062–5065. https://doi.org/10.1039/c8cc01779d.

(253) Lai, Y. Y.; Huang, V. H.; Lee, H. T.; Yang, H. R. Stacking Principles on π- and Lamellar Stacking for Organic Semiconductors Evaluated by Energy Decomposition Analysis. *ACS Omega* **2018**, *3* (12), 18656–18662. https://doi.org/10.1021/acsomega.8b02713.

(254) Svirskaite, L. M.; Mandati, S.; Spalatu, N.; Malinauskiene, V.; Karazhanov, S.; Getautis, V.; Malinauskas, T. Asymmetric NDI Electron Transporting SAM Materials for Application in Photovoltaic Devices. *Synth Met* **2022**, *291*. https://doi.org/10.1016/j.synthmet.2022.117214.

(255) Mohanraj, J.; Samanta, B.; Almora, O.; Escalante, R.; Marsal, L. F.; Jenatsch, S.; Gadola, A.; Ruhstaller, B.; Anta, J. A.; Caspary Toroker, M.; Olthof, S. $NiO_x$ Passivation in Perovskite Solar Cells: From Surface Reactivity to Device Performance. *ACS Appl Mater Interfaces* **2024**, *16* (32), 42835–42850. https://doi.org/10.1021/acsami.4c06709.

(256) Cao, Y.; Li, Y.; Morrissey, T.; Lam, B.; Patrick, B. O.; Dvorak, D. J.; Xia, Z.; Kelly, T. L.; Berlinguette, C. P. Dopant-Free Molecular Hole Transport Material That Mediates a 20% Power Conversion Efficiency in a Perovskite Solar Cell. *Energy Environ Sci* **2019**, *12* (12), 3502–3507. https://doi.org/10.1039/c9ee02983d.

(257) Li, J.; Xia, R.; Qi, W.; Zhou, X.; Cheng, J.; Chen, Y.; Hou, G.; Ding, Y.; Li, Y.; Zhao, Y.; Zhang, X. Encapsulation of Perovskite Solar Cells for Enhanced Stability: Structures, Materials and Characterization. *Journal of Power*

*Sources*. Elsevier B.V. February 15, 2021. https://doi.org/10.1016/j.jpowsour.2020.229313.

(258) Jones, D. (Mac); An, Y.; Hidalgo, J.; Evans, C.; Vagott, J. N.; Correa-Baena, J. P. Polymers and Interfacial Modifiers for Durable Perovskite Solar Cells: A Review. *Journal of Materials Chemistry C*. Royal Society of Chemistry October 7, 2021, pp 12509–12522. https://doi.org/10.1039/d1tc01243f.

(259) Yang, J.; Xiong, S.; Qu, T.; Zhang, Y.; He, X.; Guo, X.; Zhao, Q.; Braun, S.; Chen, J.; Xu, J.; Li, Y.; Liu, X.; Duan, C.; Tang, J.; Fahlman, M.; Bao, Q. Extremely Low-Cost and Green Cellulose Passivating Perovskites for Stable and High-Performance Solar Cells. *ACS Appl Mater Interfaces* **2019**, *11* (14), 13491–13498. https://doi.org/10.1021/acsami.9b01740.

(260) Han, Y.; Meyer, S.; Dkhissi, Y.; Weber, K.; Pringle, J. M.; Bach, U.; Spiccia, L.; Cheng, Y. B. Degradation Observations of Encapsulated Planar CH3NH3PbI3 Perovskite Solar Cells at High Temperatures and Humidity. *J Mater Chem A Mater* **2015**, *3* (15), 8139–8147. https://doi.org/10.1039/c5ta00358j.

(261) Chaudhary, B.; Kulkarni, A.; Jena, A. K.; Ikegami, M.; Udagawa, Y.; Kunugita, H.; Ema, K.; Miyasaka, T. Poly(4-Vinylpyridine)-Based Interfacial Passivation to Enhance Voltage and Moisture Stability of Lead Halide Perovskite Solar Cells. *ChemSusChem* **2017**, *10* (11), 2473–2479. https://doi.org/10.1002/cssc.201700271.

(262) Wu, T.; Wang, Y.; Li, X.; Wu, Y.; Meng, X.; Cui, D.; Yang, X.; Han, L. Efficient Defect Passivation for Perovskite Solar Cells by Controlling the Electron Density Distribution of Donor-π-Acceptor Molecules. *Adv Energy Mater* **2019**, *9* (17). https://doi.org/10.1002/aenm.201803766.

(263) Fu, Q.; Liu, H.; Gao, Y.; Cao, X.; Li, Y.; Yang, Y.; Wang, J.; Chen, Y.; Yao, Z.; Liu, Y. Tunable Molecular Packing of Dopant-Free Hole-Transport

Polymers for Perovskite Solar Cells. *ACS Energy Lett* **2023**, *8* (7), 2878–2885. https://doi.org/10.1021/acsenergylett.3c00855.

(264) Kranthiraja, K.; He, W.; Yu, H. W.; Feng, Z.; Nozaki, N.; Matsumoto, H.; Yu, M. H.; Li, Y.; Manzhos, S.; Andersson, M. R.; Chueh, C. C.; Michinobu, T.; Sonar, P. Diketopyrrolopyrrole-Dioxo-Benzodithiophene-Based Multifunctional Conjugated Polymers for Organic Field-Effect Transistors and Perovskite Solar Cells. *Solar RRL* **2024**, *8* (14). https://doi.org/10.1002/solr.202400185.

(265) Huang, B.; Fu, Q.; Ai, Q.; Tan, L.; Chen, L.; Chen, Y. Optimization of Perovskite by 3D Twisted Diketopyrrolopyrrole for Efficient Perovskite Solar Cells. *Mater Chem Front* **2017**, *1* (6), 1179–1184. https://doi.org/10.1039/c6qm00210b.

(266) Qin, P. L.; Yang, G.; Ren, Z. W.; Cheung, S. H.; So, S. K.; Chen, L.; Hao, J.; Hou, J.; Li, G. Stable and Efficient Organo-Metal Halide Hybrid Perovskite Solar Cells via π-Conjugated Lewis Base Polymer Induced Trap Passivation and Charge Extraction. *Advanced Materials* **2018**, *30* (12). https://doi.org/10.1002/adma.201706126.

(267) Sadoughi, G.; Starr, D. E.; Handick, E.; Stranks, S. D.; Gorgoi, M.; Wilks, R. G.; Bär, M.; Snaith, H. J. Observation and Mediation of the Presence of Metallic Lead in Organic-Inorganic Perovskite Films. *ACS Appl Mater Interfaces* **2015**, *7* (24), 13440–13444. https://doi.org/10.1021/acsami.5b02237.

(268) Wu, Z.; Jiang, M.; Liu, Z.; Jamshaid, A.; Ono, L. K.; Qi, Y. Highly Efficient Perovskite Solar Cells Enabled by Multiple Ligand Passivation. *Adv Energy Mater* **2020**, *10* (10). https://doi.org/10.1002/aenm.201903696.

(269) Wang, K.; Liu, J.; Yin, J.; Aydin, E.; Harrison, G. T.; Liu, W.; Chen, S.; Mohammed, O. F.; De Wolf, S. Defect Passivation in Perovskite Solar Cells by Cyano-Based π-Conjugated Molecules for Improved Performance and

Stability. *Adv Funct Mater* **2020**, *30* (35). https://doi.org/10.1002/adfm.202002861.

# APPENDICES

## A. NMR DATA

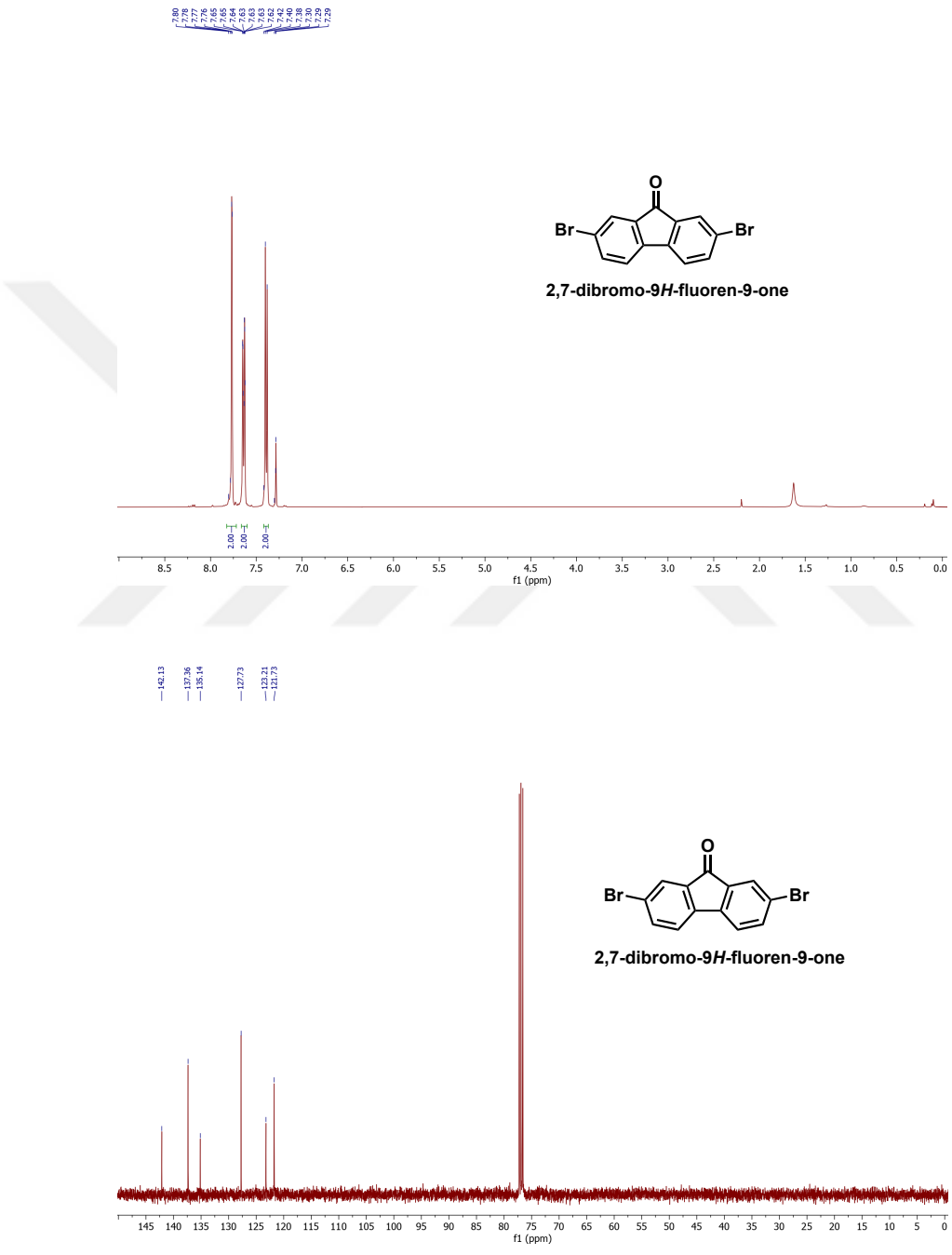



**Figure A 1.** $^{1}H$ and $^{13}C$ NMR spectra of **2,7-dibromo-9*H*-fluorene-9-one** in $CDCl_3$

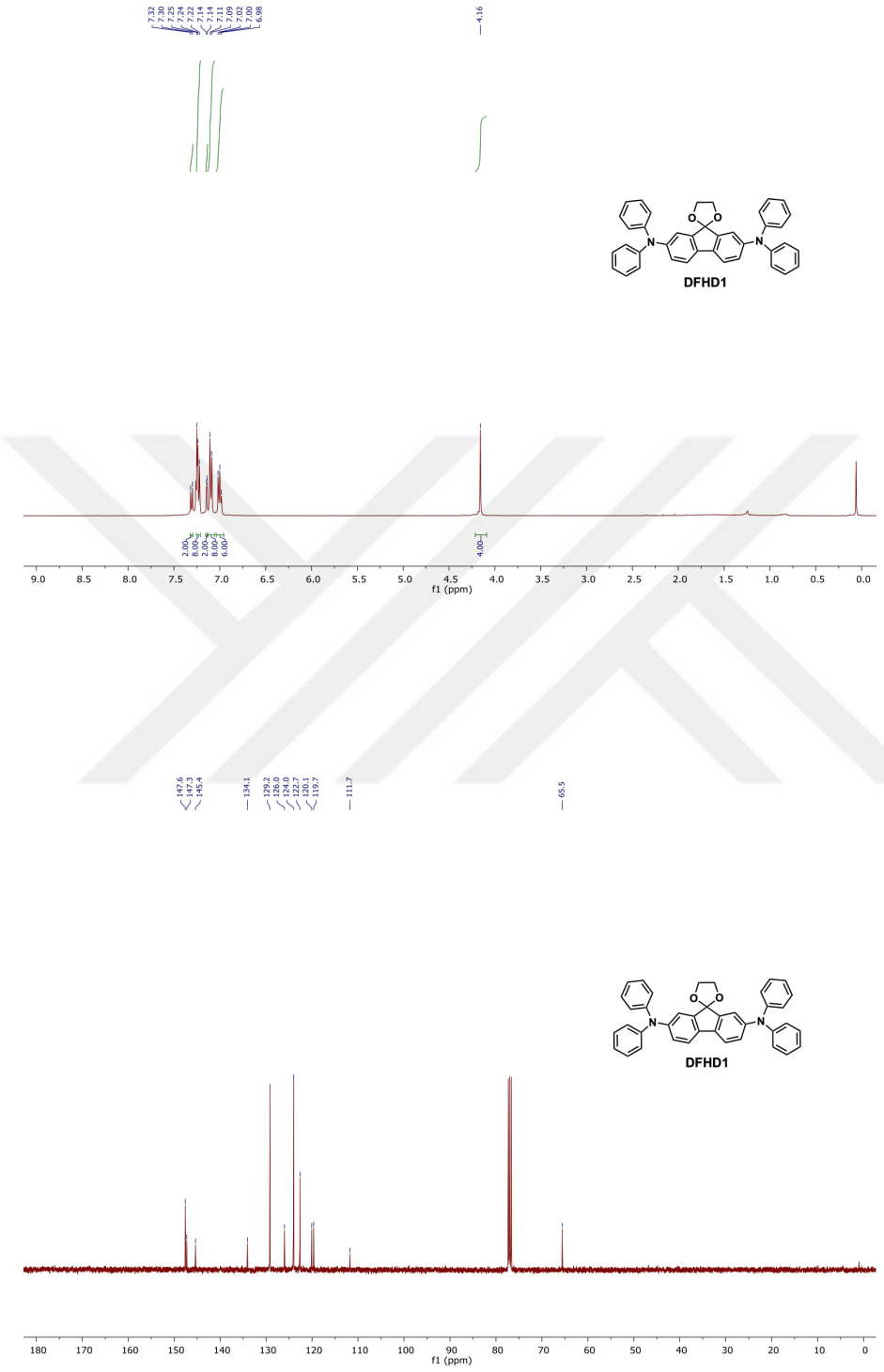



**Figure A 2.** $^{1}H$ and $^{13}C$ NMR spectra of **DFHD1** in $CDCl_3$

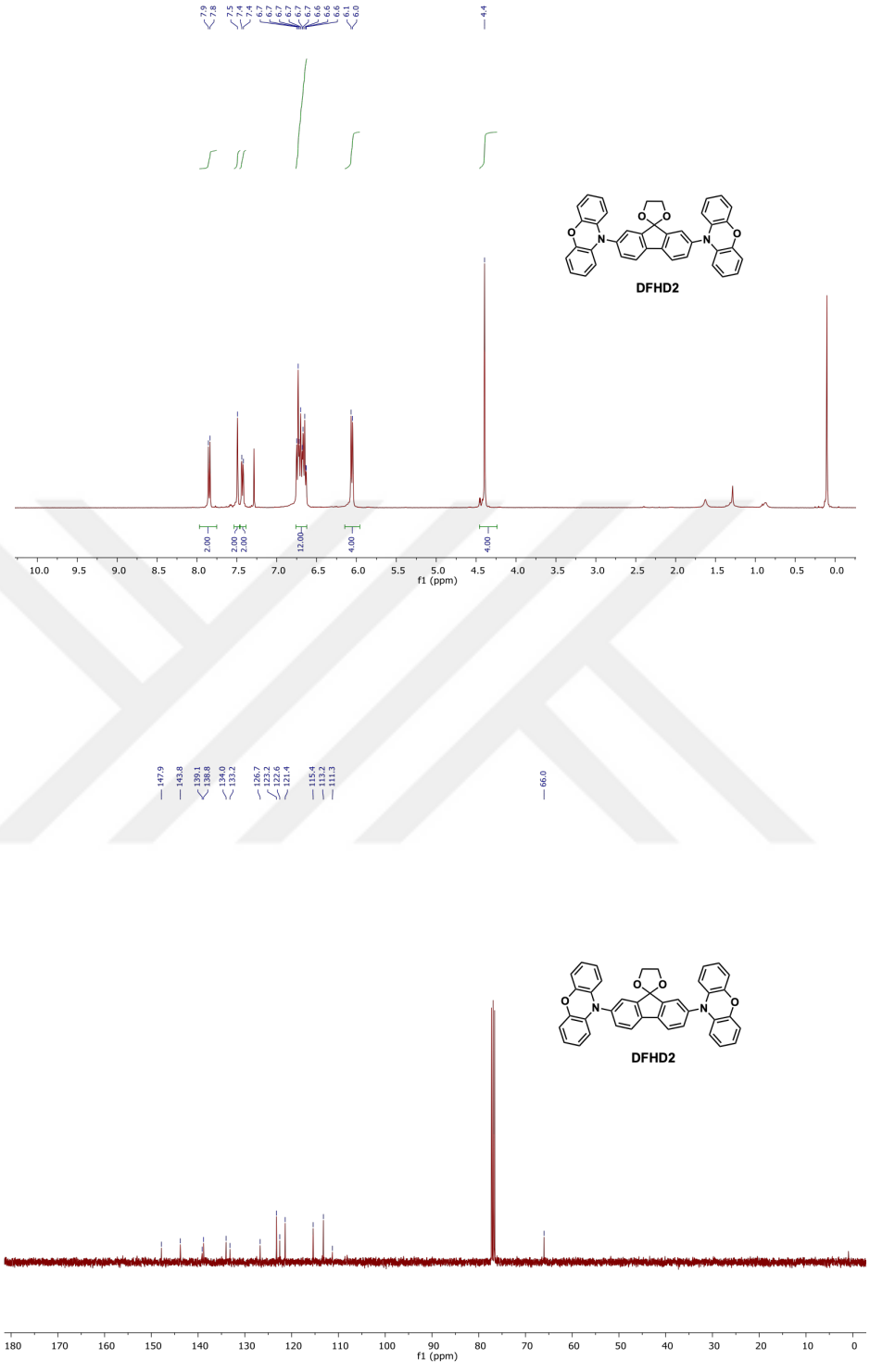



**Figure A 3.** $^{1}H$ and $^{13}C$ NMR spectra of **DFHD2** in $CDCl_3$

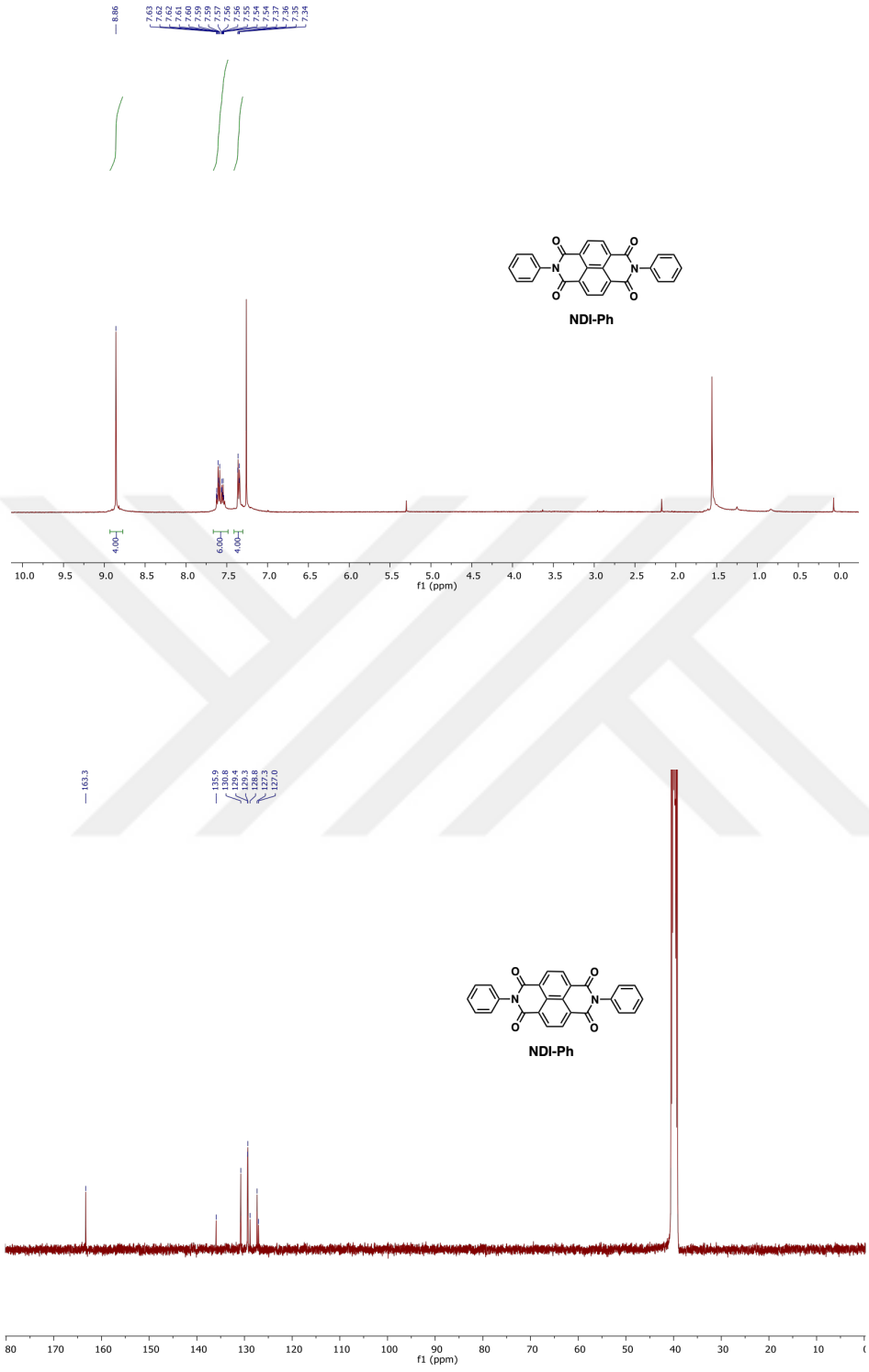



**Figure A 4.** $^{1}H$ and $^{13}C$ NMR spectra of **NDI-Ph** in $CDCl_3$ and DMSO-$d_6$, respectively

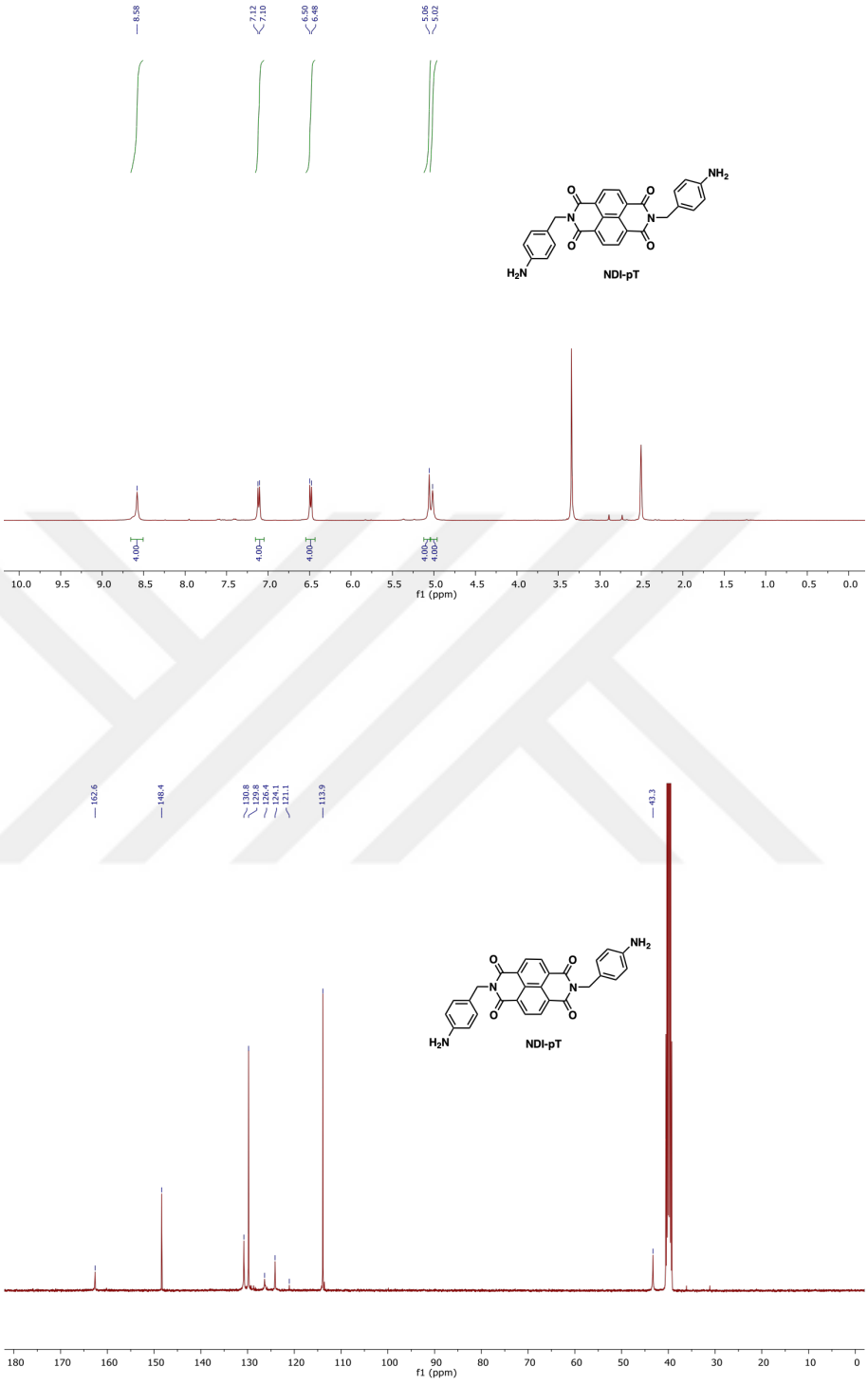



**Figure A 5.** $^{1}H$ and $^{13}C$ NMR spectra of **NDI-pT** in DMSO.

## CURRICULUM VITAE

Gözükara Karabağ, Zeynep

### EDUCATION

| Degree | Institution | Year of Graduation |
|---|---|---|
| MS | METU, Chemistry | 2019 |
| BS | METU, Chemistry | 2017 |
| High School | Etlik Anadolu High School, Ankara | 2011 |

### FOREIGN LANGUAGES

Advanced English, Beginner Deutsch

### PERSONAL QUALITIES

Researcher, Self-Motivated, Fast Learner, Adaptable, Hardworking, Creative, Energetic, Problem-Solving.

### RESEARCH AREA

Material Design and Synthesis, π-Conjugated Semiconductors, Large Bulky Organic Cations, Characterization and Purification Methods, Photovoltaics, Perovskite Solar Cells, Characterization Techniques

### COMPUTER SKILLS

Microsoft Office Programs (Advanced), ChemDraw (Advanced), MestreNova (Advanced), OriginPro (Advanced).

### TECHNICAL SKILLS

Materials Development, NMR Spectroscopy (Advanced), Mass Spectroscopy (Advanced), Column Chromatography (Advanced), Thin Layer Chromatography (Advanced), Perovskite Solar Cells Fabrication, Spin-Coating, Thermal

Evaporation, Spray Coating, CV, Uv-vis, UPS, XPS, FTIR, XRD, PL, AFM, TEM, SEM, ToF-SIMS, GIWAXS

**RESEARCH EXPERIENCE**

2022 – 2024 Effect of Polymeric Additives on the Efficiency and Stability of n-i-p Structured Perovskite Solar Cells

2020 – 2022 2D Perovskite Passivation Studies by Implementing Methoxy and Halogen Units on PEAI Ring for the Fabrication of High Performance and Stable n-i-p-Based 3D Perovskite Solar Cells

2019 – 2020 Design and Synthesis of NDI-Based Electron Transport Layers and Fluorene-based $NiO_x$ Passivation Layers for the Fabrication of Thermally Evaporated p-i-n Type Perovskite Solar Cell

2017 – 2019 Asymmetric Synthesis of Pyridine Substituted Pyrrolidine Derivatives

**WORK EXPERIENCE**

2023 – 2024 Senior Researcher in the Perovskite Photovoltaics area at ODTÜ-GÜNAM, METU, Ankara, Türkiye

2021 – 2022 Collaborative Visiting Researcher at EPFL, Sion, Switzerland

2019 – 2023 Chemical Designer for ODTÜ-GÜNAM, METU, Ankara, Türkiye

**PROJECTS AND SCHOLARSHIPS**

2018 – 2019 TÜBİTAK Project Scholarship, **118Z414**, National

''Development of New Chiral Catalysts for the Asymmetric Synthesis of Heteroaryl Substituted Pyrrolidine Derivatives''

2019 – 2024 TÜBİTAK Project Scholarship, **118C063**, National

''New Generation Photovoltaic Energy Glasses''

2020 – 2023 **TÜBİTAK 2244** – Industrial PhD Fellowship Programme

2020 – 2024 TÜBİTAK Performance Scholarship

''**BIDEB 2250** – Graduate Fellowship Performance Program for Ph.D. Students''

2024 – 2026 TÜBİTAK Project Contribution, **123F373**, National

''Developing Functional Phenylethylammonium-Based Materials for Dual Passivation of Inverted (p-i-n) Perovskite Solar Cells and Mini-modules with High Performance and Stability''

2022 – 2025 TÜBİTAK Project Contribution, **121C250**, National

''Towards the Discovery of Structure-Activity Relationship for Polymer Additives in Perovskite Solar Cells''

**PUBLICATIONS**

1. Beksultanova, N., **Gozukara, Z.**, Araz, M., Bulut, M., Polat-Cakir, S., Aygun, M., & Dogan, O. *Chirality* **2021**, *33*(*8*), 465-478.

2. Gunes, U., Varlioglu Yaylali, F., **Gozukara Karabag, Z.**, Gao, X. X., Syzgantseva, O. A., Karabag, A., ... & Gunbas, G. *Cell Rep. Phys. Sci.*, **2023**, *4*(*5*), 101380.

3. **Gozukara Karabag, Z.**, Karabag, A., Gunes, U., Gao, X. X., Syzgantseva, O. A., Syzgantseva, M. A., ... & Gunbas, G. *Adv. Energy Mater.*, **2023**, *13*(*45*), 2302038.